seit 1558

Statistical modelling of resolved debris discs

DISSERTATION

zur Erlangung des akademischen Grades
Doctor Rerum Naturalium (Dr.rer.nat)

vorgelegt dem Rat der Physikalisch-Astronomischen Fakultät
der Friedrich-Schiller-Universität Jena

von M.Sc. Nicole Pawellek
geboren am 06. Dezember 1988 in Meiningen

Erster Gutachter: Prof. Dr. Alexander Krivov
Astrophysikalisches Institut und Universitätssternwarte
Friedrich-Schiller-Universität Jena

Zweiter Gutachter: Prof. Dr. Sebastian Wolf
Institut für theoretische Physik und Astrophysik
Christian-Albrechts-Universität Kiel

Dritter Gutachter: Prof. Dr. Jean-Charles Augereau
Institut de Planétologie et d'Astrophysique de Grenoble (IPAG)
Grenoble, France

Tag der öffentlichen Verteidigung: 17. November 2016

Gewidmet dem Wissenschaftsoffizier der Enterprise.

Contents

Danksagung

Auf dem Weg zu meiner Promotion haben mich zahlreiche Menschen begleitet und unterstützt, ohne die die vorliegende Dissertation nicht möglich gewesen wäre. Allen voran möchte ich mich bei meinem Doktorvater, Professor Alexander „Sascha“ Krivov, bedanken, der mir zu jeder Zeit mit Rat und Tat zur Seite stand und immer einen rettenden Einfall hatte. Ohne seine montäglichen Anrufe wäre es kein Montag gewesen. Des Weiteren danke ich Dr. Katharina Schreyer, Dr. Torsten Löhne, Herrn Christian Schüppler, Dr. Christian Vitense, Dr. Martin Reidemeister und Herrn Fabian Geiler für die vielen produktiven Diskussionen, wie auch Frau Monika Müller, Dr. Frank Gießler und Herrn Jürgen Weiprecht für die technische und bürokratische Unterstützung. Auch die Kollegen von anderen Instituten, wie Dr. Attila Moór, Dr. Steve Ertel, Dr. Jonathan Marshall und Dr. Benjamin Montesinos, waren mir mit ihrem Wissen und ihren Ideen eine große Hilfe. Nicht zuletzt möchte ich mich bei meinen Physik- und Mathematiklehrern, Herrn Wolgang Fiedler, Frau Bianca Krämer, Dr. Winfried Zappe und Dr. Eberhard Koch bedanken, die ihre Begeisterung für die Astronomie und Physik auf mich übertragen haben.

Neben der fachlichen Unterstützung dürfen natürlich auch nicht die vielen anderen Menschen vergessen werden, die mir einen Ausgleich zum Arbeitsalltag geschaffen haben. Zunächst sei meiner Familie gedankt, besonders meinen Eltern Kerstin und Frank, die mich bereits in jungen Jahren zur Astrophysik gebracht und das gesamte Studium überhaupt erst ermöglicht haben. Mein Bruder Markus erklärte mir die Grundlagen des Programmierens und meine Großeltern Ingrid und Alfred sorgten dafür, dass ich immer mit ausreichend Essen versorgt war. Ohne meine Musiklehrer, Frau Ingeborg und Herr Christian Glöckner, die mich von frühester Kindheit an unterrichtet haben, sowie Herr Martin Meier und Frau Regine Seifert, die später dazu kamen, wäre ich vermutlich an mancher Stelle verzweifelt und so möchte ich auch sie alle an dieser Stelle erwähnen. Ebenso bin ich dankbar für die guten Freunde, die immer ein offenes Ohr für meine Probleme hatten: Anne und Oliver Schwartz und Katrin Richter sowie die Mitwirkenden bei den sonntäglichen Andachten: Schwester Kati, Herr Klaus Genieser, Frau Maria Glöckner-Latour und Frau Marita Krüger.

Kurzfassung

In dieser Arbeit wurde eine Stichprobe von 39 räumlich aufgelösten Trümmerschreiben um AFGKM-Sterne mit der Absicht untersucht, Korrelationen zwischen den Zentralsternparametern der Trümmerscheibensysteme und den Scheibenparametern an sich zu finden. Eine Hürde war dabei die Entartung zwischen den Staubteilchengrößen und der Entfernung des Staubes vom Zentralstern. Kleine Partikel in einer großen Entfernung lieferten ähnliche Ergebnisse wie große Teilchen näher am Stern. Jedoch konnten durch die räumliche Auflösung der Scheiben deren Radien mittels einer neuen Methode bestimmt und so die Entartung gebrochen werden. Die gewählte Stichprobe stellt die bis dato größte analysierte Sammlung von räumlich aufgelösten Scheiben dar, wobei die Modellierung der spektralen Energieverteilung (SED) die Grundlage der Analyse bildete.

Es wurden zwei verschiedene Modelle für die Anpassung der SEDs genutzt, zum einen der modifizierte Schwarzkörper (MBB) und zum anderen die Staubgrößenverteilung (SD). Der Vergleich der beiden verdeutlichte, dass sie zu ähnlichen Korrelationen der verschiedenen Parameter führen, jedoch auch Unterschiede bei individuellen Scheiben sichtbar sind. Da die Teilchengröße und die Staubsorte ebenfalls entartet sind, wurden fünf verschiedene Staubarten für die Modellierung verwendet: reines Astrosilikat und reiner Kohlenstoff sowie Mischungen von Astrosilikat mit Eis, Kohlenstoff und Vakuum. Die Verwendung all dieser Sorten führte gleichfalls zu ähnlichen Korrelationen.

Im Ergebnis zeigte sich, dass die neue Methode der Radienbestimmung auf einen Großteil der Trümmerschreiben anwendbar ist, unabhängig von deren Entfernung oder dem Spektraltyp des Zentralsterns. Des Weiteren wurde eine große Streuung der Radien über den gesamten Bereich der stellaren Leuchtkraft festgestellt. Daher scheint die entgültige Form der Scheibe nicht von temperaturabhängigen Prozessen abhängig zu sein. Unter der Annahme, dass eine Scheibe aus Planck'schen Strahlern besteht, lässt sich ein Schwarzkörperradius ableiten. Die Untersuchung des „wahren“ Scheibenradius im Verhältnis zu diesem Schwarzkörperradius zeigte einen Abfall mit zunehmender stellarer Leuchtkraft, was es nun erlaubt, den Radius von unaufgelösten Trümmerschreiben zu schätzen.

Die Scheibentemperatur zeigt einen Anstieg mit zunehmender stellarer Leuchtkraft, wobei sie in Einheiten der Schwarzkörpertemperatur abnimmt. Die dominante Teilchengröße steigt leicht mit der stellaren Leuchtkraft an, jedoch ist dieser Anstieg auch mit einer konstanten Teilchengröße von $(5 \pm 3)\,\mu\mathrm{m}$ vereinbar. Die Theorie sagt einen wesentlich steileren Anstieg, bedingt durch den zunehmenden Strahlungsdruck des Zentralsterns, vorher. Dadurch ist ein Abfall der dominanten Teilchengröße in Einheiten der Ausstoßgröße erkennbar, der zudem die stärkste Korrelation dieser Arbeit darstellt und robust gegenüber den verschiedenen Staubsorten und Kollisionsmodellierungen ist. Es wurden mehrere Erklärungen für diesen Abfall untersucht. Neben rein technischen oder statistischen wurden auch physikalische Effekte, wie ein endliches Reservoir an Oberflächenenergie für die kleinsten Staubteilchen und die Rolle der dynamischen Anregung der Scheibe analysiert. Ersterer scheint jedoch nur von untergeordneter Bedeutung zu sein. Letzterer hingegen deutet darauf hin, dass die dynamische Anregung mit der stellaren Leuchtkraft zunimmt. Scheiben um Sterne früherer Spektraltypen könnten daher möglicherweise massereichere Planeten oder Planetesimale besitzen.

1 Introduction and motivation

"It is difficult to understand the universe
if you only study one planet."

based on Miyamoto Musashi (1645)

The science of planetary system formation and evolution is a famous field of interest, since it tries to address the fundamental questions: "What are the origins of Earth (and humankind)?" and "Are we alone in the Universe?". In the course of time different phenomena were discovered, inspiring the enquiring human mind. These discoveries, beginning with the identification of planets by ancient Greeks and discovery of asteroids in the 19th century after the advent of the telescope, followed by the more recent detection of the Vega phenomenon and protoplanetary discs in the late 20th century and the serendipity of the first exoplanet found around the main-sequence star 51 Peg, help us to better understand the processes and mechanisms that drive the formation and evolution of planets. However, up to now we do not completely understand how a planetary system forms or evolves and thus we would like to contribute to the previous knowledge with this piece of work. Our thesis concentrates on the succesors to protoplanetary discs, namely debris discs, which represent leftovers of planet formation and evolution processes. In the following sections we will briefly describe the nature of debris discs and the aims of this work.

1.1 Debris discs

1.1.1 Solar system

In 1766 Johann Titius formulated an empirical equation describing the regular spacing between the orbits of the six known planets at that time. Shortly after, Johann Bode claimed that this equation predicted a planet lying between Mars and Jupiter that had not yet been discovered. Hence, a search for this object started (Bode, 1772) leading to the discovery of the first asteroid (1) Ceres in 1801 (Piazzi, 1802). The first represenative of the Asteroid belt was rapidly followed by the discovery of many other similar objects[1]. The Asteroid belt is a part of our Solar system's debris disc which is the succesor of a protoplanetary disc. It is an optically thin and gas-poor disc composed of planetesimal belts where colliding and growing solids are situated (Wyatt, 2008; Krivov, 2010). While the smallest dust particles of the debris disc are produced by collisions of planetesimals and are expelled from the system by direct stellar radiation pressure (e.g., Burns et al., 1979; Müller et al., 2010), the larger bodies are more influenced by stellar gravity and other processes such as stirring by planets or Poynting-Robertson drag (e.g., Kenyon and Bromley, 2001; Mustill and Wyatt, 2009). Another fact is that debris discs can be made of one or more distinct material rings. In case of our Solar system the Asteroid belt is the inner ring whereas the Edgeworth-Kuiper-belt (Edgeworth, 1943, 1949; Kuiper, 1951) with its famous dwarf planet Pluto (Leonard, 1930; Tombaugh, 1946) is the outer one. In Figure 1.1 a scheme of a typical planetary system is depicted including terrestrial and giant planets,

---

[1] Today, 713968 asteroids (numbered and unnumbered) are known in the main Asteroid belt. (Yeomans, Donald K.: "JPL Small-Body Database Search Engine". NASA JPL, retrieved 9th May 2016)

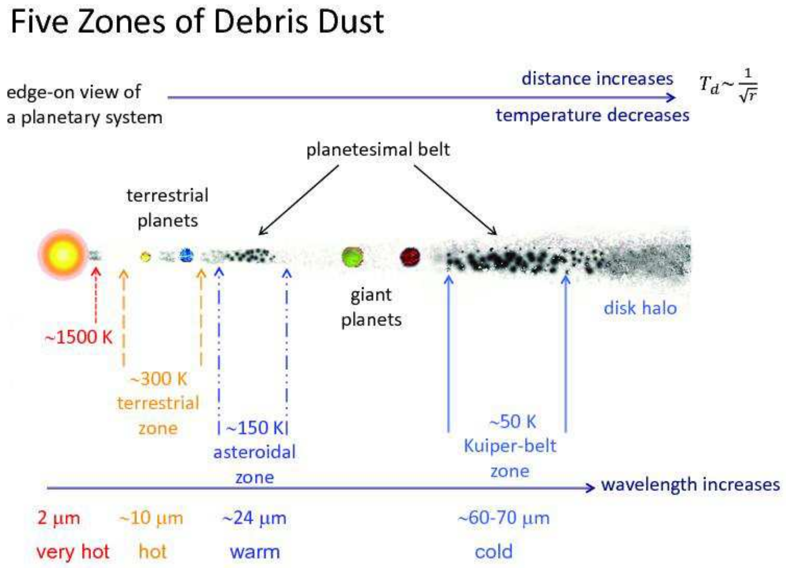

Figure 1.1: Edge-on view of a planetary system as function of observational wavelength from Matthews et al. (2014b). Courtesy: Kate Su.

asteroidal and Edgeworth-Kuiper belt zones as well as a hot dust component close to the host star and a disc halo.

As described above the Asteroid belt is known since the late 19th century, whereas the Edgeworth-Kuiper belt was a theory from the 1940s and 50s (Edgeworth, 1943, 1949; Kuiper, 1951) and only confirmed in the 1990s (Jewitt et al., 1992). Therefore, they were not interpreted as parts of the Solar system's debris disc at first. The first debris disc known as such was observed around Vega in the 1980s (Aumann et al., 1984).

1.1.2 Investigation methods

Since the large planetesimals – the parent bodies of debris disc dust – possess only a small total cross section they cannot be detected by current observational techniques. Thus, the investigation of dust produced by collisions of these planetesimals is necessary. The total cross section of the small dust particles is much higher compared to the parent bodies and their thermal emission much easier to detect. The observation of dust allows conclusions about the parent body population to be drawn and potentially the indirect detection of planets in the circumstellar system offering insight into planet formation and evolution processes. The study of debris disc spectral energy distributions (SEDs) is among other methods, such as imaging and infrared spectroscopy, an important tool to gather information and will be the basis of this work. SEDs reflect debris disc properties, such as disc temperature, typical dust grain sizes, and the amount of disc material. However, the modelling of them is difficult, since a degeneracy between disc radius and typical dust grain sizes exists (e.g., Krist et al., 2010; Ertel et al., 2011; Churcher et al., 2011b; Löhne et al., 2012; Booth et al., 2013; Morales et al., 2013). That means that large grains at a small distance from the star can produce a similar SED as small grains at a large distance and thus disentangling both, distance from the star and grain size, is not possible. Only resolved discs, such as Fomalhaut (Acke et al., 2012) and β Pictoris

(Vandenbussche et al., 2010) offer a solution, since their radii could be derived from images.

Over the last years the frequency of discs was studied by several groups (e.g., Su et al., 2006; Eiroa et al., 2013; Chen et al., 2014; Thureau et al., 2014; Marshall et al., 2016). Eiroa et al. (2013) found that nearly 20% of FGK-stars own a debris disc, whereas Thureau et al. (2014) analysed more luminous A-stars of which approximately 24% possess a disc. These results do not mean that more discs can be found around A-stars than around K-stars, since the frequencies are statistically indistinguishable (Trilling et al., 2008; Eiroa et al., 2013). Furthermore, the structure of discs was investigated. As known from our Solar system, debris discs might not only possess Edgeworth-Kuiper belts, but also Asteroid belts. Thus it is not surprising that a recent study of Spitzer/IRS mid-infrared specra (Chen et al., 2014) revealed that nearly 66% of known debris discs seem to be confined into two rings, similar to the Solar system. To the present day nearly 100 discs could be resolved in one way or another (e.g., MacGregor et al. (2015); Choquet et al. (2016), Table C.1) and so the large number of discs offers a possibility for statistical analyses and the search for correlations between different debris disc parameters derived from SED modelling and stellar parameters, such as stellar luminosity or temperature.

1.2 Aims of this work

In this work we will investigate a sample of 39 resolved debris discs and their SEDs, breaking the degeneracy of disc radii and typical dust grain sizes, in order to find correlations between disc and stellar properties. This will allow conclusions about system parameters of unresolved discs to be made, providing a deeper insight in the disc physics and formation and evolution processes.

The dust size distribution and therefore the typical grain size will be of special interest here. As Krivov et al. (2000) stated, several processes influence the size distribution. Besides radiation pressure and collisions, transport processes and erosion mechanisms (Wyatt et al., 2011) play an important role. Hence, the derived size distribution allows conclusions about these processes. When the size distribution is steep enough (which is the case for most of the discs), particles just above a certain minimum grain size are the most abundant and thus carry the largest part of the particle cross section. As a matter of fact, these particles are easy to detect in thermal emission in mid- and far infrared and can be referred to as particles with a typical dust grain size. Grains smaller than the radiation pressure blowout limit are expelled and it is expected that the typical grain size is close to this limit. The ratio of minimum grain size and blowout limit is influenced by the dynamical excitation of the dust producing planetesimals, as shown by dynamical simulations. If the average eccentricity of the dust parent planetesimals is low, meaning that the disc is dynamically cold, the ratio is expected to be much larger than unity (e.g., Thébault and Wu, 2008; Krivov et al., 2013). On the other hand, for high dynamical excitation, the ratio should be slightly above unity (e.g., Krivov et al., 2006; Thébault and Augereau, 2007). Thus, the grain size ratio allows conclusions not only about the dynamical excitation itself but about processes that alter it, e.g., stirring by planets or planetesimals. Of course, the typical grain size depends on other parameters besides the dynamical excitation as well. The dust properties, both optical and mechanical, the disc radius and the system's age are only a few examples for that. So if the disc is spatially resolved and the systems age could be inferred from the host star, conclusions about dust properties will be possible.

We will begin this thesis in Chapter 2 with the question of how a debris disc can be described and will explain the basic terms used for that, e.g., fractional luminosity or blowout grain size. Since the modelling of SEDs is an essential part here as well, a short introduction into the technical aspect of SED fitting is given in Chapter 3. Then it is discussed which resolved debris discs are appropriate for a statistical analysis (Chapter 4) and how their radii can be derived (Chapter 5). This is followed by a presentation of the fitting results (Chapter 6) whereas a detailed analysis of the grain size – stellar luminosity trend is given in Chapter 7. The trend found between disc-to-blackbody radius ratio and stellar luminosity is investigated in Chapter 8. A summary can be found in Chapter 9.

2 Theoretical foundations

At the beginning of this work we would like to concentrate on the question how a debris disc can be observed, described and analysed. Therefore, we will start with an introduction to spectral energy distributions, which are the basis of our debris disc analysis. Then an explanation of the basic terms of a debris disc system such as blowout grain size or fractional luminosity will follow. This chapter will end with the description of the statistical methods used for analysing a sample of debris discs.

2.1 Spectral energy distributions

A debris disc is composed of gas, dust and planetesimal belts. While the gas component may be a remnant of the predecessing protoplanetary disc (Moór et al., 2013b) the circumstellar dust is short-lived and thus the existence of dust-producing planetesimals is evident. The disc material is confined to rings which contain growing and crushed solid material with sizes ranging from serveral tens of kilometres (planetesimals) to sub-micrometres (dust) (e.g., Stern, 1996; Sitko et al., 1998; Thébault et al., 2003; Greaves et al., 2004; Fitzgerald et al., 2007). The micron sized dust particles can most effectively be traced by their thermal emission and therefore it is not astonishing that the first debris disc was found by the so-called infrared excess emission in the spectral energy distribution (SED) (Aumann et al., 1984). This infrared excess is indeed the common evidence for the presence of a debris disc and thus the SED is the basis for any debris disc analysis and needs to be explained in more detail. In Figure 2.1 a typical infrared excess is shown. Obviously, the flux density of the circumstellar system measured at infrared wavelengths is higher than what is expected from the star alone. In order to describe this emission physically we will begin with an explanation of the optical parameters of dust

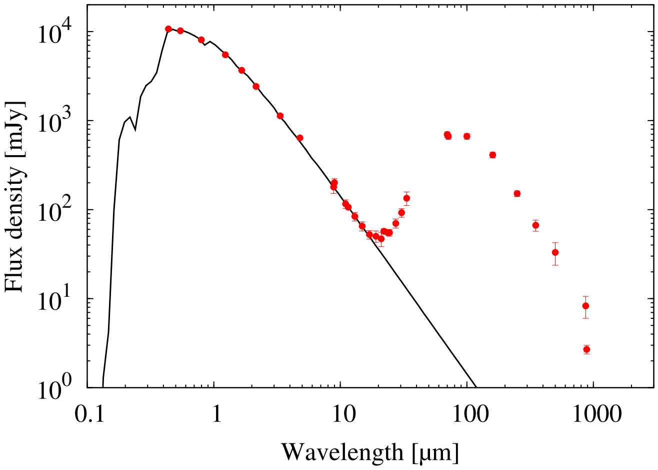

Figure 2.1: Flux density as a function of wavelength for HD 21997 (Moór et al., 2013b). Black solid line shows emission of stellar photosphere. Red filled circles with error bars show observational measurements.

particles. This is followed by an introduction of different radiation models starting with blackbody radiation.

2.1.1 Optical parameters of dust particles

Different radiation processes occur in a debris disc, namely absorption, reemission and scattering of stellar radiation by the dust grains. The basics of these processes were treated by Bohren and Huffman (1983) using Mie theory and here the most important parameters will be explained.

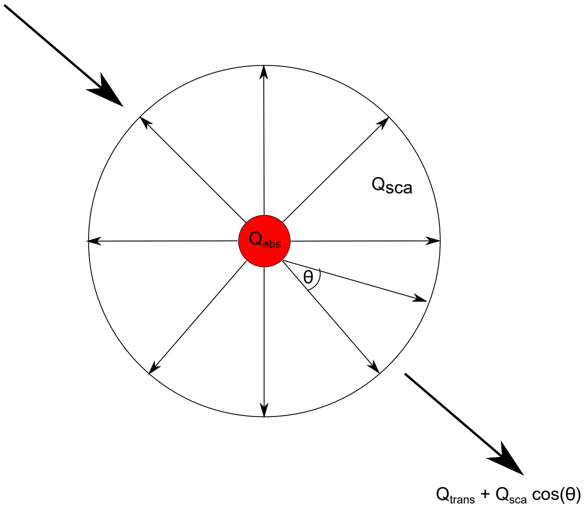

Figure 2.2: Optical efficiency factors as explained by Burns et al. (1979). Black arrows represent directional vectors of electromagnetic waves.

Compact spherical particles with a geometrical cross section A are assumed and in Figure 2.2 such a particle is depicted as a red circle. When an electromagnetic wave with a certain energy approaches the particle it is subject to the above mentioned radiation processes. The parameter Q_{abs} gives the part of the energy which is absorbed, while Q_{sca} represents the part of scattered and Q_{trans} the part of transmitted energy. The scattered part contains a momentum of $Q_{\mathrm{sca}} \times \cos(\theta)$, which is sent in the forward direction. The parameter $\langle\cos(\theta)\rangle$ is the weighted average of the angular dependence of the scattered radiation (Burns et al., 1979) and called the asymmetry factor. It is given by

$$\langle\cos(\theta)\rangle \equiv \int_{4\pi} f(\theta)\cos\theta \, d\Omega, \tag{2.1}$$

where θ is the scattering angle, Ω the solid angle and $f(\theta)$ the phase function computed by Mie theory (Bohren and Huffman, 1983). For the particle with cross section A this means that on an area $C_{\mathrm{abs}} = A \times Q_{\mathrm{abs}}$ the incoming energy will be absorbed while on $C_{\mathrm{sca}} = A \times Q_{\mathrm{sca}}$ it will be scattered. These areas are called the absorption or scattering cross section, respectively. The parameter Q_{pr} is the radiation pressure efficiency. It is defined as

$$Q_{\mathrm{pr}} \equiv Q_{\mathrm{abs}} + Q_{\mathrm{sca}}(1 - \langle\cos(\theta)\rangle). \tag{2.2}$$

If the whole energy were scattered in forward direction, Q_{pr} would be equal to Q_{abs}. In case of perfect back-scattering Q_{pr} would be $Q_{\mathrm{abs}} + 2Q_{\mathrm{sca}}$. And if the energy were scattered isotropically Q_{pr} would be the sum of Q_{abs} and Q_{sca}.

Now we assume a blackbody particle in equilibrium conditions. The energy emitted by the grain must be the same as the absorbed energy. Using Kirchhoff's law of absorption and emission it can be shown that $Q_{\rm abs}$ = Emissivity and furthmore $Q_{\rm abs} \equiv 1$ for a blackbody. Here, $Q_{\rm abs}$ is independent of the wavelength of the electromagnetic wave, but in general all the above mentioned efficiencies are functions of it.

2.1.2 Blackbody radiation

In the last section we saw that blackbodies are ideal absorbers with an absorption efficiency of unity. Thus, the easiest model to describe the emission of the dust particles is the blackbody radiation. This model was first described and derived by Max Planck (Planck, 1900) and is the basis of many debris disc analyses.

Planck's law

The Planck law can be written in terms of wavelength or frequency:

$$B_\lambda(\lambda,T)d\lambda = \frac{2\;h\;c^2}{\lambda^5\;\left[\exp\left(\frac{h\;c}{\lambda\;k\;T}\right)-1\right]}\;d\lambda, \qquad B_\nu(\nu,T)d\nu = \frac{2\;h\;\nu^3}{c^2\;\left[\exp\left(\frac{h\;\nu}{k\;T}\right)-1\right]}\;d\nu. \tag{2.3}$$

Here, ν is the frequency, λ the wavelength, c the speed of light, h the Planck constant, k the Stefan-Boltzmann constant and T the temperature. In the field of debris discs another form of this law is used, since the flux density for a certain frequency interval is measured in units of Jansky ([Jy] = 10^{-26}W/(Hz m^2)), but the wavelength is a more common and intuitive parameter. Therefore,

$$B_\nu(\lambda,T)d\nu = \frac{2\;h\;c}{\lambda^3}\;\left[\exp\left(\frac{h\;c}{\lambda\;k\;T}\right)-1\right]^{-1}\;d\nu \tag{2.4}$$

is often used. At long wavelengths the Planck curve can be reduced to the Rayleigh-Jeans approximation given by

$$B_\nu^{\rm RJ}(T)d\nu = \frac{2\nu^2}{c^2}\;kT\;d\nu = \frac{2kT}{\lambda^2}\;d\nu. \tag{2.5}$$

Modified blackbody radiation

In order to describe the infrared excess emission first found around Vega and therefore called the Vega phenomenon, Backman and Paresce (1993) developed the modified blackbody (MBB) as a model for thermal emission by dust grains. They assumed a constant absorption efficiency $Q_{\rm abs} = 1$ up to a certain critical wavelength λ_0. For wavelengths larger than λ_0 the absorption efficiency decreases with $(\lambda/\lambda_0)^{-\beta_{\rm mod}}$, where $\beta_{\rm mod}$ is the opacity index. This leads to

$$B_\nu^{\rm mod}(\lambda,T) = B_\nu(\lambda,T)\left[H(\lambda_0-\lambda) + H(\lambda-\lambda_0)\left(\frac{\lambda}{\lambda_0}\right)^{-\beta_{\rm mod}}\right] \tag{2.6}$$

as the resulting blackbody function and

$$Q_{\rm abs}(\lambda,s) = \begin{cases} 1, & \lambda \le \lambda_0 \\ (\lambda/\lambda_0)^{-\beta_{\rm mod}}, & \lambda > \lambda_0 \end{cases}, \tag{2.7}$$

as the function of the absorption efficiency, where s represents the grain size and $H(\lambda)$ the Heaviside step function. The wavelength λ_0 can be interpreted as a kind of characteristic grain size. Backman and

Paresce (1993) stated that depending on the grain optical properties $\lambda_0 = 2\pi s$ for strongly absorbing materials. For weakly absorbing materials the relation turns out to be $\lambda_0 = s/(2\pi)$ and for moderate absorbing material $\lambda_0 = s$ is a good approximation. Nevertheless, information on the dust material can also be inferred from the parameter β_{mod}. While a value of ~ 1 should be appropriate for amorphous materials, a value of ~ 2 represents crystalline materials or metals (Witt, 1989). A value of ~ 1.5 was found to characterise the grains in the interstellar medium (ISM) (e.g., Planck Collaboration et al., 2015).

2.1.3 Mie radiation

The blackbody description of the dust emission is simple, but it only treats dust particles in an idealised way. In reality, the dust grains have an absorption efficiency that as described above depends on the emission wavelength, the grain size and the optical indices (e.g., refractive indices) of the dust material. Thus, it is necessary to know the composition of dust and the grain sizes in order to get a more physical approach to the dust modelling.

Spectra of debris discs reveal solid features arising from different dust compositions (e.g. Chen et al., 2006; Lisse et al., 2007; Fujiwara et al., 2012, 2013; Donaldson et al., 2013; Riviere-Marichalar et al., 2014; Mittal et al., 2015). Nevertheless, the composition of dust (volume fractions of each component) remains unknown in most of the cases since solid state features are only present in debris disc systems with hot dust emitting in the infrared (Matthews et al., 2014b). This work concentrates on the three most often detected compositions, namely silicate, carbon and water ice and several mixtures of them.

Astronomical silicate

Draine and Lee (1984) proposed the artificially generated material *astronomical silicate* or *astrosilicate* which is one of the most prominent dust compositions describing the emission of the ISM. The basis for this material are lab measurements of crystalline olivine in order to construct a dielectric function. This function is used to derive the optical parameters (Q_{abs}, Q_{sca}, etc.) of the dust. It was improved over the years by Laor and Draine (1993) and Draine (2003b) who among other things extended the wavelength range used. Figure 2.3 shows the optical parameters Q_{abs} and Q_{sca} for different dust grain sizes. The efficiencies decrease with increasing wavelength, whereas for small particles this decrease

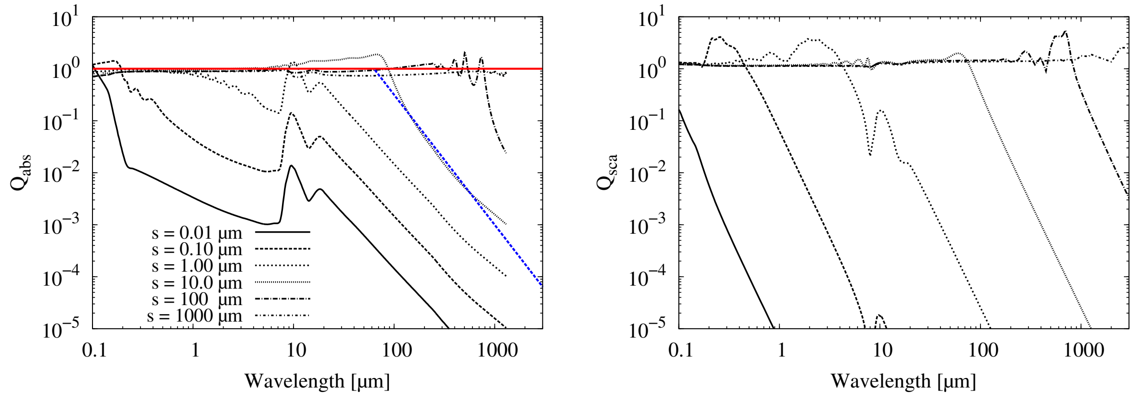

Figure 2.3: Absorption and scattering efficiency as a function of wavelength for astronomical silicate and different dust grain sizes ranging from 0.01 μm to 1000 μm. Red solid line: blackbody conditions; blue dashed line: modified blackbody conditions for $s = 10\,\mu\text{m}$ using $\lambda_0 = 2\pi s$ and $\beta_{\text{mod}} = 2.5$.

starts at shorter wavelengths than for large particles. Large particles have nearly constant values equal to unity, which means that they behave more like blackbodies. A comparison with the MBB model shows that the assumptions of $\lambda_0 = 2\pi s$ and $\beta_{\mathrm{mod}} \sim 2$ for crystalline materials are in good agreement with the slope of Q_{abs} for a grain size larger than 10 µm. For smaller particle sizes the absorption efficiency is not as well approximated by the MBB model.

Carbon

Another dust component often used is carbon, many kinds of which exist and different optical parameters are available. In this work the amorphous carbon dust of Zubko et al. (1996) ("ACAR") is used. Since many debris discs are modelled with this kind of dust (e.g., Donaldson et al., 2013; Lebreton et al., 2012), the modelling results of this work are comparable to them. The optical parameters of carbon and astronomical silicate look similar as shown in Figures 2.3 and 2.4. In the shorter wavelength range between 0.1 µm and 10 µm the values for Q_{abs} of astronomical silicate are decreasing faster than those for carbon. Furthermore, there is no peak at ~ 10 µm for the carbon material, since this emission feature is typical for silicate. The MBB approximation is as well in good agreement with the depicted shape of Q_{abs} for particles larger than 10 µm. The opacity index is smaller compared to astrosilicate what was expected for amorphous materials (Witt, 1989), however it is larger than unity.

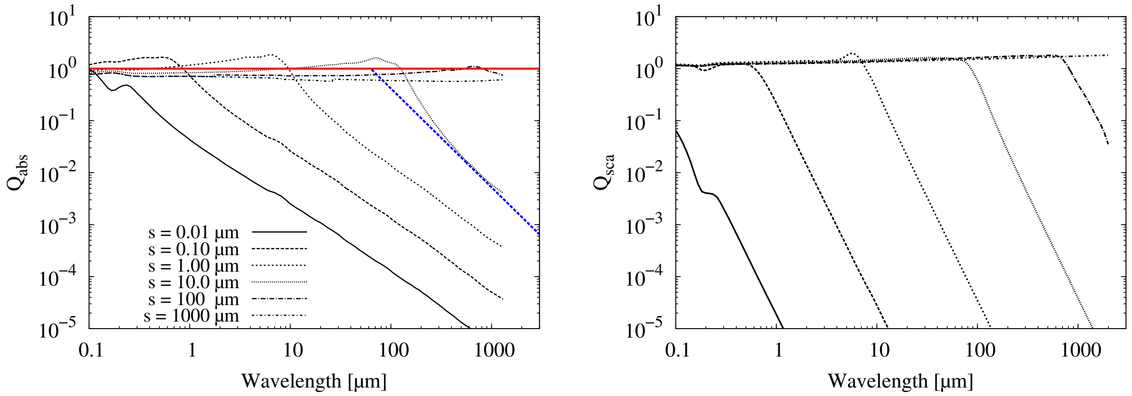

Figure 2.4: Same as Figure 2.3, but for amorphous carbon. $\beta_{\mathrm{mod}} = 1.9$.

Water ice

The third component used in this work is water ice proposed by Li and Greenberg (1998). Here, the dust particles are assumed to have a silicate core with a layer of H_2O dominated ice accreted in dense molecular clouds (Greenberg, 1978). Figure 2.5 reveals that between 0.1 µm and 1 µm the ice particles have a very small $Q_{\mathrm{abs}} \sim 10^{-10}$. This means that the grains do not absorb much energy in this wavelength area. But the decrease of Q_{abs} with increasing wavelength can be seen here as well, although it begins at longer wavelengths ($\sim$ 100 µm). Compared to astrosilicate and carbon the absorption efficiency of water ice shows many peaks at several wavelengths and therefore its shape is not as smooth as for the other two materials. Hence, a comparison to the MBB approximation is difficult. However, Greenberg (1978) stated that water ice is a moderately absorbing material and thus $\lambda_0 = s$ was used for illustration.

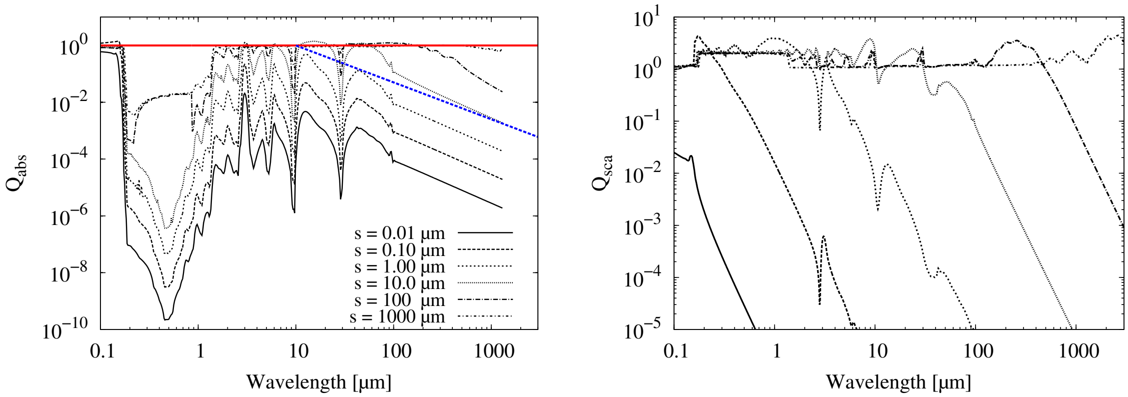

Figure 2.5: Same as Figures 2.3-2.4. MBB conditions: $\lambda_0 = s = 10\,\mu\mathrm{m}$ and $\beta_{\mathrm{mod}} = 1.3$.

Mixtures

To generate the optical parameters of the mixtures used in this work the Bruggeman (1935, 1936) mixing rule was applied. Its advantage against other mixing rules is that it treats each component in the same way and not as environmental part or inclusional part. It is completely symmetric. Since the volume fractions of dust components in debris discs are not known, they were equally distributed in the mixtures. The dust compositions used in this work are given in Table 2.1.

Table 2.1: Dust compositions and their bulk densities.

Dust composition	ϱ [g/cm^3]
50% astrosilicate + 50% vacuum	1.65
50% astrosilicate + 50% ice	2.25
100% astrosilicate	3.30
50% astrosilicate + 50% carbon	2.63
100% carbon	1.95

Dust grain temperatures

As said before, the absorption efficiency depends on the wavelength and the dust grain size (see Figures 2.3 - 2.5). The general shape of Q_{abs} with increasing wavelength stays the same, but there are differences for the dust compositions used. As a consequence of that, not only the temperatures of the grain sizes vary, but also the temperatures of same sized particles of different compositions do (see Figure 2.6). For the calculation of the temperature the balance of absorbed stellar radiation and thermal reemission is assumed (Equations 2.25-2.27). Obviously, grains with a size smaller than 10 µm are warmer than blackbody, while particles of approximately 10 µm have temperatures close to the blackbody temperature. Between a size of 0.1 µm and 1 µm lie the hottest particles. Grains smaller than 0.1 µm or larger than 1 µm are colder (Krivov et al., 2006).

In Figure 2.7 the temperature of the dust grains is given as a function of grain size and disc radius. The wavelength λ_0 can be interpreted as a grain size. Since astronomical silicate is a strongly absorbing material the relation $\lambda_0 = 2\pi s_{\mathrm{min}}$ is assumed. The temperature isolines of MBB and SD method show a different behaviour. While for MBB particles the temperature increases with decreasing grain size,

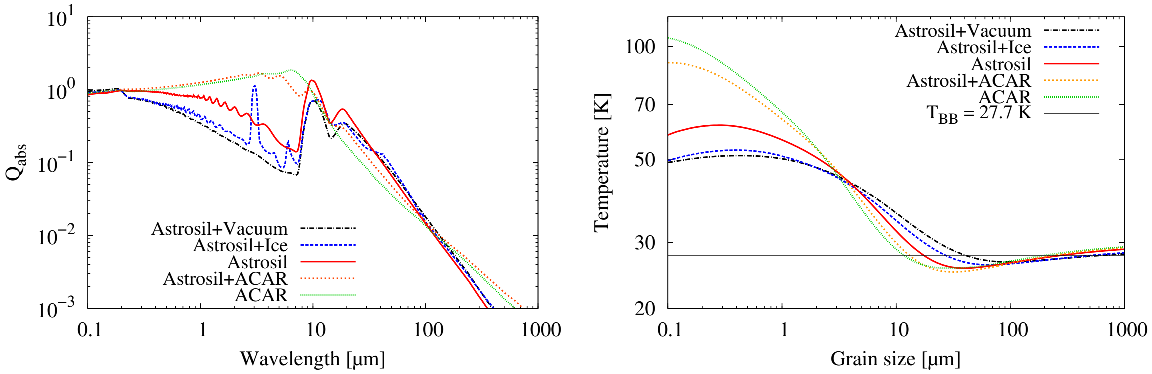

Figure 2.6: Left: absorption efficiency as a function of wavelength for different dust compositions. The particle used has a grain size of $s = 1$ µm. right: dust grain temperature $T_\mathrm{d}(s)$ for a star with $1L_\odot$ at a radius of 100 AU for different dust compositions. T_BB is the blackbody temperature.

the smallest SD grains ($s = 0.1\,\mu\mathrm{m}$) turn out to be cooler than grains with a size of $s = 0.5\,\mu\mathrm{m}$, which was explained already in Figure 2.6. It is obvious as well that grains with a certain size are warmer closer to the star than grains farther out.

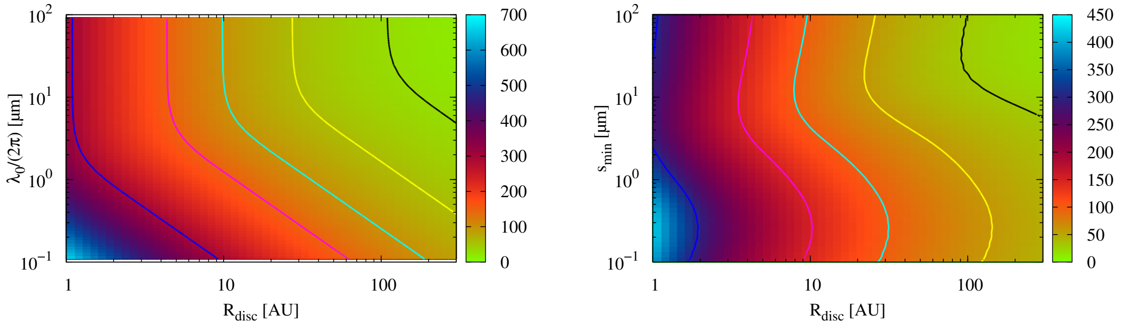

Figure 2.7: The temperature of dust particles as a function of characteristic grain size and disc radius. Left: modified blackbody, right: size distribution. Solid lines show temperature isolines for 30 K (black), 60 K (yellow), 100 K (cyan), 150 K (pink) and 300 K (blue).

2.2 Disc parameters

After having a look at SEDs and optical parameters of dust, it is now necessary to introduce key parameters of a debris disc system. Without these the modelling of a SED would not be possible. Therefore, we will explain the most common terms.

2.2.1 Basic definitions

Dust particles in a debris disc are distributed in several ways. On the one hand they are size distributed, meaning that there is a certain number $N(s)$ of grains with a certain grain size s. On the other hand, the particles have a spatial distribution as well. At a distance r from the star a certain number of grains, $N(r)$, exists. Debris discs are optically thin and thus, the thermal emission of all particles irrespective of their position can be seen in the SED. Therefore, no conclusions about the azimuthal or vertical distribution can be drawn. Thus, the disc is assumed azimuthally symmetrical with no vertical extension while the particles have a size and a radial distribution, $N(r, s)$.

Surface number density $N(r, s)$

The surface number density, $N(r, s)ds$, represents the number of dust particles in an annulus per total area of the annulus and per grain size interval $[s, s + ds]$. The easiest assumption for $N(r, s)$ is a power law for both, the radial distribution and the grain size distribution with the shape

$$N(r, s) = N_0 \left(\frac{r}{R_0}\right)^{-p} \left(\frac{s}{s_0}\right)^{-q}, \tag{2.8}$$

where N_0, R_0 and s_0 are arbitrary normalisation parameters for the number of particles, the radius and the grain size, while p and q are the radial distribution index or the size distribution index, respectively. Using the geometrical optical depth τ, the parameter N_0 can be calculated with

$$\tau = \frac{A}{A_{\text{disc}}} = \frac{A}{\pi(R_{\max}^2 - R_{\min}^2)} = \frac{2\pi}{R_{\max}^2 - R_{\min}^2} \int\limits_{R_{\min}}^{R_{\max}} \int\limits_{s_{\min}}^{s_{\max}} N(r, s)\ s^2\ ds\ r\ dr. \tag{2.9}$$

Here, A is the cross section of the dust particles, A_{disc} the area of the disc, $R_{\min}$ and $R_{\max}$ the inner and outer radius of the disc, and $s_{\min}$ and $s_{\max}$ certain minimum and maximum grain sizes. Thus, N_0 becomes

$$N_0 = \frac{A(2-p)(3-q)}{2\pi^2 R_0^2 s_0^3} \left[\left(\frac{R_{\max}}{R_0}\right)^{2-p} - \left(\frac{R_{\min}}{R_0}\right)^{2-p}\right]^{-1} \left[\left(\frac{s_{\max}}{s_0}\right)^{3-q} - \left(\frac{s_{\min}}{s_0}\right)^{3-q}\right]^{-1}, \tag{2.10}$$

if $p \neq 2$ and $q \neq 3$ are assumed. In case of $p < 2$ the largest part of the particle cross section, A, is located in the outer region of the disc (closer to $R_{\max}$), while for $p > 2$ it is closer to the inner region. Considering the grain sizes, A is dominated by small particles if $q > 3$, while the large particles contribute more in case of $q < 3$. Assuming the limiting case of $p = 2$ and $q = 3$, the normalisation parameter N_0 changes to

$$N_0 = \frac{A}{2\pi^2 R_0^2 s_0^3} \left[\ln\left(\frac{R_{\max}}{R_{\min}}\right) \ln\left(\frac{s_{\max}}{s_{\min}}\right)\right]^{-1}. \tag{2.11}$$

Here, the dust is equally distributed over the whole annulus and all grain sizes contribute the same fraction to the total cross section.

Dust mass M_{dust}

Knowing the surface number density $N(r, s)$, the dust mass is given by

$$M_{\text{dust}} = \frac{4 s_0 A \varrho}{3}\ \frac{3-q}{4-q}\ \frac{\left(\frac{s_{\max}}{s_0}\right)^{4-q} - \left(\frac{s_{\min}}{s_0}\right)^{4-q}}{\left(\frac{s_{\max}}{s_0}\right)^{3-q} - \left(\frac{s_{\min}}{s_0}\right)^{3-q}}, \tag{2.12}$$

with ϱ being the bulk density of the grain material and assuming $q \neq 4$. If $q < 4$ the mass is dominated by the largest dust particles, while the smallest particles contribute the most for $q > 4$. In case of $q = 4$ the dust mass is given by

$$M_{\text{dust}} = \frac{4A\varrho}{3} \ \ln\left(\frac{s_{\text{max}}}{s_{\text{min}}}\right) \ \left[\frac{1}{s_{\text{min}}} - \frac{1}{s_{\text{max}}}\right]^{-1}, \tag{2.13}$$

and is equally distributed over the whole grain size range, meaning that every size interval contributes the same fraction.

2.2.2 Radiation pressure and blowout grain size s_{blow}

Dust particles in debris discs are subject to several mechanisms, e.g., stellar radiation pressure, which acts to remove dust grains below a certain size from the system, and alters the orbital motion of larger grains by transfer of momentum. In the stellar gravitational field dust particles are attracted to the star while they move in elliptical or circular orbits around it. This motion can be derived from Newton's gravitational law:

$$\overrightarrow{F_{\text{G}}} = -\frac{4\pi}{3} s^3 \ \varrho \ G \ M_{\text{star}} \frac{\overrightarrow{r}}{r^3}, \tag{2.14}$$

where G is the gravitational constant, M_{star} the stellar mass and $\overrightarrow{r}$ the radial vector. On the other hand, the dust is repelled by direct stellar radiation pressure:

$$\overrightarrow{F_{\text{rad}}} = \frac{L_{\text{star}} \ \pi s^2 \ Q_{\text{pr}}}{4\pi \ c} \frac{\overrightarrow{r}}{r^3}. \tag{2.15}$$

Here, compact spherical particles are assumed. The parameter Q_{pr} is the radiation pressure efficiency averaged over the stellar spectrum and c the speed of light. The radiation pressure efficiency is explained in Section 2.1. Burns et al. (1979) defined the ratio of graviational force and radiation pressure as β:

$$\beta \equiv \frac{|\overrightarrow{F_{\text{rad}}}|}{|\overrightarrow{F_{\text{G}}}|} = \frac{3L_{\text{star}}}{16\pi G M_{\text{star}} c} \frac{Q_{\text{pr}}}{\varrho s}. \tag{2.16}$$

This ratio is independent of the distance to the star, r, and since it is proportional to the inverse grain size, $1/s$, it is obvious that for large particles β is small and for small particles β is large. Furthermore, the dependence of $Q_{\text{pr}}(s)$ is neglected. Due to the radial independence of β it is possible to write $\overrightarrow{F_{\text{rad}}} = -\beta \ \overrightarrow{F_{\text{G}}}$. The effective "photogravitational force" (Krivov, 2010) is then

$$\overrightarrow{F_{\text{PG}}} = \overrightarrow{F_{\text{G}}} + \overrightarrow{F_{\text{rad}}} = \overrightarrow{F_{\text{G}}} \ (1-\beta) = -\frac{4\pi}{3} s^3 \ \varrho \ G \ M_{\text{star}} \ (1-\beta) \frac{\overrightarrow{r}}{r^3}. \tag{2.17}$$

This means that as a result of stellar radiation pressure the particle seems to be attracted by a central object of mass $M_{\text{star}} \ (1-\beta)$ instead of the original stellar mass M_{star}.

Now a large planetesimal is assumed for which β is close to zero. It moves around the central star on an elliptical orbit with eccentricity e and semi-major axis a. Its specific orbital energy is then given by

$$E_{\text{pl}} = \frac{v^2}{2} - \frac{GM_{\text{star}}}{r} \equiv -\frac{GM_{\text{star}}}{2a}, \tag{2.18}$$

where v is the planetesimal velocity. If the planetesimal is located at the pericentre, r is given by $r_{\text{pc}} = a \ (1-e)$ and the velocity reduces to

$$v_{\text{pc}}^2 = \frac{GM_{\text{star}}}{a} \frac{1+e}{1-e}. \tag{2.19}$$

If a small dust grain with a large value of β is released from the planetesimal, due to a collision for instance, it has an orbital energy of

$$E_{\text{grain}} = \frac{v^2}{2} - \frac{GM_{\text{star}}(1-\beta)}{r} \equiv -\frac{GM_{\text{star}}(1-\beta)}{2a}. \tag{2.20}$$

To eject this small grain from the circumstellar system, its energy, E_{grain} must be larger than zero. Knowing the grain velocity, which is the same as the planetesimal velocity, and the distance from the star, β is given in the pericentre as

$$\beta \geq \frac{1-e}{2}. \tag{2.21}$$

If a particle moves on a circular orbit with $e = 0$, the parameter β must be larger than 1/2 in order to expel the grain from the circumstellar system. Using Equation (2.16), the grain size s corresponding to $\beta = 1/2$ is called the *blowout size* s_{blow}. In this work we will not take into account a possible eccentricity of the parent bodies. Hence, the blowout grain size will allways be the grain size for which $\beta = 1/2$. In Figure 2.8 the grain orbits as a function of β are depicted. If this parameter is smaller than 1/2 the particles stay in bound orbits around the star. In case of $1/2 < \beta < 1$ the grains are ejected on hyperbolic orbits and in case of $\beta > 1$ the ejection orbits will be anomalous hyperbolas.

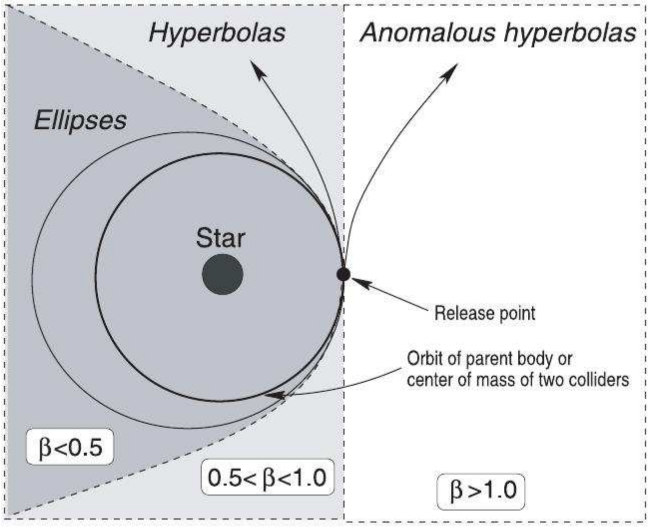

Figure 2.8: Particle orbits as a function of β from Krivov et al. (2006).

2.2.3 Collisional evolution

Due to eccentric orbits of the debris mutual collisions are inevitable. Indeed, destructive collisions are a dominant process in known debris disc systems. The relative velocities between two colliding objects need to have a certain minimum level (e.g., Kenyon and Bromley, 2004b; Krivov et al., 2006; Löhne et al., 2008; Thébault and Augereau, 2007; Wyatt et al., 2007b) in order to be destructive. While in protoplanetary discs these relative velocities are damped by the dense ambient gas, in debris discs this damping process is not effective, since these discs are gas-poor. But in order to reach the high velocities necessary for destructive collisions, the low damping is not sufficient. When a protoplanetary disc evolves to a debris disc it looses the primordial gas and the solid particles should preserve the low velocity dispersion they had previously. Hence, some kind of "stirring mechanism" must ignite the destructive collisions (Wyatt, 2008). One possibility is self-stirring by largest ($\sim$ 1000 km sized) planetesimals as stated by Kenyon and Bromley (2004a) or the stirring by planets orbiting the inner gap of the disc (Wyatt, 2005; Mustill and Wyatt, 2009). Another possible mechanism to ignite a cascade of collisions is e.g., perturbation by binary companion (e.g., Faramaz et al., 2014).

When the collisional cascade in a disc starts the solid material is broken to dust sizes and the smallest particles for which $\beta \gtrsim 0.5$, are expelled from the system by direct radiation pressure. In the dust size range ($<$ 1 mm) stirring is not necessary, as typical eccentricities of the grains are of the same order as the β-ratio (Burns et al., 1979) and the impact velocities are sufficiently high due to radiation pressure.

In order to describe the collisions several parameters are necessary. An important one is the critical specific energy for disruption and dispersal, $Q_{\mathrm{D}}^{\star}$, which is defined as the impact energy per unit target mass. If the objects are small $Q_{\mathrm{D}}^{\star}$ does only depend on the material strength, while for larger objects with sizes of $\sim$ 100 m it is determined by the gravitational binding energy. Therefore, $Q_{\mathrm{D}}^{\star}$ is often described as the sum of two power laws (e.g., Davis et al., 1985; Benz and Asphaug, 1999; Kenyon and Bromley, 2004b; Stewart and Leinhardt, 2009):

$$Q_{\mathrm{D}}^{\star} = Q_{\mathrm{strength}} \left(\frac{s}{1\ \mathrm{m}}\right)^{-b_{\mathrm{strength}}} + Q_{\mathrm{gravity}} \left(\frac{s}{1\ \mathrm{km}}\right)^{b_{\mathrm{gravity}}} . \tag{2.22}$$

The values for Q_{strength} and Q_{gravity} are of the order of $\sim 10^5 - 10^7$ erg/g, while b_{strength} lies between 0 and 0.5 and b_{gravity} between 1 and 2 (Benz and Asphaug, 1999). A minimum of $\sim 10^4 - 10^6$ erg/g of the critical energy is reached at sub-kilometre sizes, while at dust sizes $Q_{\mathrm{D}}^{\star}$ should be of the order of $\sim 10^8$ erg/g. When the relative velocity of two colliders reaches or exceeds a critical value of

$$v_{\mathrm{critical}} = \sqrt{\frac{2(m_{\mathrm{target}} + m_{\mathrm{projectile}})^2}{m_{\mathrm{target}} m_{\mathrm{projectile}}} Q_{\mathrm{D}}^{\star}}, \tag{2.23}$$

where m represents the masses of the colliders, the two colliders are disrupted (e.g., Krivov et al., 2005). Assuming particles of the same size, they will be destroyed if their velocity is larger than $\sqrt{8Q_{\mathrm{D}}^{\star}}$. Considering two dust grains, the critical velocity lies at several hundred metres per second. If they are situated at several tens of AU away from the star they would have an eccentricity of ~ 0.1. As mentioned before, the eccentricity is in the same order as the β-ratio and thus particles with $\beta \sim 0.1$ could naturally attain such eccentricities.

However, the collisions in debris discs influence a size range of $\sim$ 12 orders of magnitude and take place at different velocities. There are two important outcomes of collisions, namely the complete disruption and the cratering, which means partial destruction of one or both colliders with and without reaccumulation of fragments (Thébault and Augereau, 2007; Müller et al., 2010).

2.2.4 Grain sizes

In this work we use different terms for grain sizes, whereas most of them are connected to different methods of disc modelling:

1. Blowout grain size
   In Section 2.2.2 it was mentioned, that if the β-parameter of a dust grain is 1/2, the grain is of blowout size. Smaller grains which possess a larger value of β are expelled from the system by direct radiation pressure.
2. Dominant or typical grain size
   This size is used for collisional modelling and corresponds to the largest cross section of dust in the

debris disc system.

3. Minimum grain size

   This size represents the lower cutoff of a power law size distribution.

4. Characteristic grain size

   Considering the MBB method, no dust grains are assumed during the SED fitting. Thus, the characteristic grain size proposed by Backman and Paresce (1993) is used. We assume the relation $\lambda_0 = s/(2\pi)$ in order to compare the characteristic grain size with the minimum grain size of the power law size distribution.

An illustration for them is given in Figure 2.9, where two different size distributions are depicted, one generated by collisional modelling and the other a power law distribution.

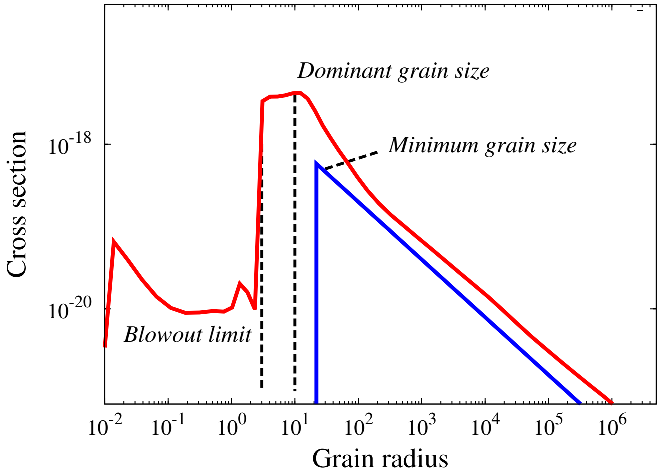

Figure 2.9: Cross section of dust as a function of grain radius. The red solid line represents a size distribution generated by collisional modelling, the blue solid line a power law size distribution. For more detailed explanations see text.

2.2.5 Flux density of a circumstellar debris disc

A debris disc is an optically thin disc (e.g., Zuckerman et al., 1995; Thi et al., 2001; Wolf and Hillenbrand, 2003). Hence, multiple scattering of radiation and heating of dust caused by dust reemission are negligible and the only radiation processes considered are absorption, reemission and scattering of stellar radiation by dust grains. The direct stellar radiation is the only source for the heating of dust particles.

Luminosities

The monochromatic luminosity of a star with the radius R_{star} and the effective temperature T_{star} at the wavelength λ is given by

$$L_{\lambda,\text{star}} = 4\pi R_{\text{star}}^2 \pi B_\lambda(T_{\text{star}}) \tag{2.24}$$

with $B_\lambda(T_{\text{star}})$ being the Planck function. Then a dust particle of size s, with a temperature T_{grain} at a distance r from the star absorbs

$$L_{\lambda,\text{grain}}^{\text{abs}} = L_{\lambda,\text{star}}\ Q_\lambda^{\text{abs}}\ \frac{\pi s^2}{4\pi r^2}, \tag{2.25}$$

and it reemitts

$$L_{\lambda,\mathrm{grain}}^{\mathrm{em}} = 4\pi s^2 Q_\lambda^{\mathrm{abs}}\ \pi B_\lambda(T_{\mathrm{grain}}(r)). \tag{2.26}$$

Here Q_λ^{abs} is the absorption efficiency which is explained in Section 2.1. For the sake of energy conservation, the absorbed luminosity must be the same as the emitted one, meaning

$$\int\limits_0^\infty L_{\lambda,\mathrm{grain}}^{\mathrm{em}}\ d\lambda = \int\limits_0^\infty L_{\lambda,\mathrm{grain}}^{\mathrm{abs}}\ d\lambda. \tag{2.27}$$

If a particle's temperature $T_{\mathrm{grain}}(r)$ is known, Equations (2.25) – (2.27) allow the derivation of the distance r of this particle from the star with

$$r(T_{\mathrm{grain}}) = \frac{R_{\mathrm{star}}}{2}\left[\frac{\int\limits_0^\infty Q_\lambda^{\mathrm{abs}}(s) B_\lambda(T_{\mathrm{star}})\ d\lambda}{\int\limits_0^\infty Q_\lambda^{\mathrm{abs}}(s) B_\lambda(T_{\mathrm{grain}}(r))\ d\lambda}\right]^{1/2}. \tag{2.28}$$

In case of blackbody grains, $Q_\lambda^{\mathrm{abs}}(s)$ is equal to unity and not depending on the grain size s. The integral of $B_\lambda(T)$ is given by the Stefan-Boltzmann law $\int \pi B_\lambda(T) = \sigma\ T^4$, where σ is the Stefan-Boltzmann constant. Therefore, Equation (2.28) can be reduced to the blackbody radius

$$R_{\mathrm{BB}}(T_{\mathrm{grain}}) = \left(\frac{L_{\mathrm{star}}}{16\pi\sigma}\right)^{1/2}\ \left(\frac{1}{T_{\mathrm{grain}}}\right)^2. \tag{2.29}$$

The parameter L_{star} is the stellar luminosity. The blackbody radius R_{BB} is only a function of the particle's temperature and the stellar luminosity and is wavelength independent.

Flux densities

The luminosities given in Section 2.2.5 can be converted into flux densities, which are measurable parameters. An observer at a distance d from the star measures a flux density of

$$f_\lambda(r) = \frac{L_{\lambda,\mathrm{grain}}^{\mathrm{em}}}{4\pi d^2} = \pi B_\lambda(T_{\mathrm{grain}}(r))\left(\frac{s}{d}\right)^2 Q_\lambda^{\mathrm{abs}} \tag{2.30}$$

for one single dust grain. Assuming an annulus with an area of $2\pi r\ dr$ and the resulting total number of dust particles $2\pi r N(r,s)\ ds\ dr$ in it, the flux density of the whole disc is given by

$$F_\lambda(r,s)\ dr\ ds = \frac{2\pi^2}{d^2} B_\lambda(T_{\mathrm{grain}}(r)) Q_\lambda^{\mathrm{abs}} N(r,s)\ r\ dr\ s^2\ ds. \tag{2.31}$$

2.2.6 Fractional luminosity f_{d}

The fractional luminosity, f_{d}, is defined as the ratio of disc luminosity and stellar luminosity i.e.

$$f_{\mathrm{d}} = \frac{L_{\mathrm{disc}}}{L_{\mathrm{star}}}, \tag{2.32}$$

whereas Equation (2.31), using the relation $L_{\mathrm{disc}} = 4\pi d^2 \int\int\int F_\lambda(r,s)\ d\lambda\ ds\ dr$, changes it to

$$f_{\mathrm{d}} = \frac{8\pi^3}{L_{\mathrm{star}}}\int\int\int Q_\lambda^{\mathrm{abs}}(s)\ B_\lambda(T_{\mathrm{grain}}(r))\ r\ s^2\ N(r,s)\ d\lambda\ ds\ dr. \tag{2.33}$$

Using again the blackbody conditions, f_d is reduced to

$$f_\mathrm{d} = \frac{8\pi^2\sigma}{L_\mathrm{star}} \int\limits_{R_\mathrm{min}}^{R_\mathrm{max}} \int\limits_{s_\mathrm{min}}^{s_\mathrm{max}} \left(T_\mathrm{grain}(r)\right)^4 \; r \; s^2 \; N(r,s) \; ds \; dr. \tag{2.34}$$

With Equations (2.8) and (2.29) further transformation is possible. Assuming an infinitesimal ring width, the size distribution is only a function of the grain size: $N(s) \sim (s/s_0)^{-q}$. In that case, f_d is given by

$$f_\mathrm{d} = \frac{4\pi\sigma}{L_\mathrm{star}} \; T^4_\mathrm{grain}(r) \int\limits_{s_\mathrm{min}}^{s_\mathrm{max}} N(s) \; s^2 \; ds = \frac{A}{4\pi R^2_\mathrm{disc}}. \tag{2.35}$$

Thus, the fractional luminosity represents the ratio of the dust's total cross section and the surface area of the sphere with the radius R_disc of the disc. In case of blackbody discs, the grain sizes are irrelevant and only the particle cross section is taken into account.

Minimum fractional luminosity

The fractional luminosity can be used as limiting case for observations, since there is a minimum necessary for a detection by a telescope. This minimum is calculated as follows. Using Equation (2.30), we assume the flux density of the dust to be

$$F_\nu = N_0 \times f_\nu, \tag{2.36}$$

where N_0 is the number of particles and f_ν the flux density measured for one particle at a certain frequency, ν. For this purpose no radial or size distribution of the grains, but a constant particle number is used. Furthermore, this particle number can be expressed by the dust mass, given by

$$M_\mathrm{dust} = \frac{4\pi\varrho s_0^3 N_0}{3}, \tag{2.37}$$

with s_0 being the grain size of a spherical particle. Now, the telescope has a minimum flux density, F_ν^min, measureable at a certain frequency. Hence, there is a minimum dust mass at a certain disc radius necessary for a detection and due to the Planck law (see Equation (2.4)) the dust mass can be written as

$$M_\mathrm{dust} = \frac{2\varrho\lambda^3 d^2 F_\nu^\mathrm{min} s_0}{3hc} \left[\exp\left(\frac{hc}{\lambda kT}\right) - 1\right]. \tag{2.38}$$

The fractional luminosity is calculated by Equation (2.32), where the luminosity of the disc is expressed by $L_\mathrm{disc} = 4\pi d^2 F$, with F being the measured flux and d the distance from the observer. The flux is calculated by

$$F = \int\limits_0^\infty F_\lambda d\lambda = \int\limits_0^\infty \left(\frac{s_0}{d}\right)^2 \pi B_\lambda(T) N_0 d\lambda = \left(\frac{s_0}{d}\right)^2 \sigma T^4_\mathrm{BB} N_0. \tag{2.39}$$

Now, we use Equation (2.29) and express the minimum fractional luminosity with

$$f_\mathrm{d}^\mathrm{min} = \frac{4\pi d^2 F}{L_\mathrm{star}} = \frac{\lambda^3 d^2 F_\nu^\mathrm{min}}{8\pi hc \times r^2} \left[\exp\left(\frac{hc}{\lambda k}\left(\frac{16\pi\sigma}{L_\mathrm{star}}\right)^{1/4} r^{1/2}\right) - 1\right]. \tag{2.40}$$

Obviously, $f_\mathrm{d}^\mathrm{min}$ is independent of the grain size and the density of the dust material and does only depend on the distance, the stellar luminosity and the disc radius. Since the detectable F_ν^min of the telescope is different for each wavelength band, the wavelength is, besides the minimum flux density, an important parameter. In this work the *Herschel*/PACS instrument (Pilbratt et al., 2010; Poglitsch et al., 2010) is often used. It has a detectable minimum flux density of $F_\nu^{\mathrm{min}} = 5.5$ mJy in the 100 µm band[1]. Assuming a Sun-like star at a distance of 10 pc from the observer and with a debris disc radius of 100 AU the minimum fractional luminosity necessary for detection of the disc is $f_\mathrm{d}^{\mathrm{min}} \approx 8 \times 10^{-7}$. In comparison the Edgeworth-Kuiper belt of the Solar system has a fractional luminosity of $f_\mathrm{d} = 1.2 \times 10^{-7}$ (Vitense et al., 2012). Therefore, analogues of this belt around other host stars would be undetectable with PACS.

Maximum fractional luminosity

In the last section we described the fractional luminosity being a limiting case for observations and called it the minimum fractional luminosity. Now, the collisional evolution of a debris disc gives another limiting case, that of a maximum fractional luminosity.

In a collisional cascade particles with a maximum diametre, D_c, are destroyed in collisions and replaced by smaller objects. Hence, the removal of objects with the highest mass in the collisional cascade determines the long-timescale evolution and as a consequence the total mass and the fractional luminosity decrease with the decreasing number of planetesimals of size D_c. Furthermore, the initial disc mass does not influence the disc mass of later times, since the mass of more massive discs is processed faster (Wyatt et al., 2007a). And so there is a maximum disc mass or maximum fractional luminosity, f_max, respectively at a given disc age, t_age, which can be used as an upper limiting case. As given by Wyatt et al. (2007a) the maximum fractional luminosity can be described by

$$f_\mathrm{d}^{\mathrm{max}} = 0.58 \times 10^{-9} \times r^{7/3} \times \frac{dr}{r} \times D_\mathrm{c}^{0.5} \times {Q_\mathrm{D}^\star}^{5/6} \times e^{-5/3} \times M_\mathrm{star}^{-5/6} \times L_\mathrm{star}^{-0.5} \times \frac{1}{t_\mathrm{age}}. \tag{2.41}$$

Using values given by Benz and Asphaug (1999), we assume for the critical energy $Q_\mathrm{D}^\star = 2000$ J/kg, for the planetesimal size $D_\mathrm{c} = 2$ km and for the ring width $dr = 10$ AU. Furthermore, we use an eccentricity, e, of 0.1, which is comparable to that of the classical Edgeworth-Kuiper belt where $e \approx 0.08$ (e.g., Elliot et al., 2005; Vitense et al., 2010).

However, the model proposed by Wyatt et al. (2007a) contains two simplifications. At first, it is assumed that the debris disc is in collisional equilibrium for all sizes ranging from dust up to the largest planetesimals. The second assumption is related to the minimum specific energy necessary to disrupt the colliding objects. In reality this energy depends on the sizes of the colliders, but here, it is independent of them. An improvement of the model was done by Löhne et al. (2008) who lifted these simplifications, but as a consequence, the maximum fractional luminosity is still determined by the initial disc mass here. Therefore, we decided to use the easier model proposed by Wyatt et al. (2007a). It is possible that the fractional luminosity of an observed debris disc is higher than the predicted maximum fractional luminosity (e.g., Wyatt et al., 2007b) caused by simplifications used. In such cases an adaption of the parameter values ($Q_\mathrm{D}^\star$, e, t_age or D_c) is possible or the usage of the improved model proposed by Löhne et al. (2008). However, if the measured f_d is much higher than $f_\mathrm{d}^{\mathrm{max}}$ it is assumed that the disc did not produce dust from the beginning, but started the production at a later time. In Figure 2.10 both the minimum and maximum fractional luminosity are depicted considering a debris disc around a solar-type star.

---

[1] PACS Observer's Manual, Version 2.5.1; http://herschel.esac.esa.int/Docs/PACS/html/pacs_om.html

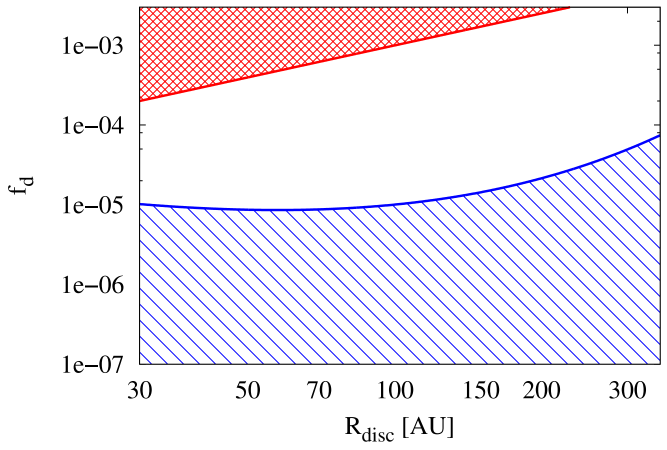

Figure 2.10: Fractional luminosity as function of disc radius. Red solid line: maximum fractional luminosity for a debris disc around a solar-type star with an age of 100Myr. Blue solid line: minimum fractional luminosity for a debris disc around a solar-type star at a distance of 35pc at 100 µm using *Herschel*/PACS. Red squared and blue lined areas show regions where no debris disc is detectable with the parameters (distance, age, …) used.

2.3 Statistical basics

2.3.1 Correlation coefficients

This work is concentrating on statistical analysis of debris discs and as such is looking for correlations between circumstellar system parameters, e.g., stellar luminosity and disc radius. In order to prove the statistical significance of these correlations, we will use the correlation coefficients of Pearson and Spearman.

The Pearson coefficient requires a linear correlation between the two parameters compared and is given by

$$r_{\text{Pearson}} = \frac{\sum\limits_{i=1}^{N_{\text{data}}} (x_i - \bar{x})(y_i - \bar{y})}{\sqrt{\sum\limits_{i=1}^{N_{\text{data}}} (x_i - \bar{x})^2 \sum\limits_{i=1}^{N_{\text{data}}} (y_i - \bar{y})^2}}, \tag{2.42}$$

where x_i and y_i are the values of the data points of both parameters, $\bar{x}$ and $\bar{y}$ the arithmetic mean values of the data points and N_{data} the number of data points (e.g., Hedderich and Sachs, 1968). The coefficient is normalised and can vary between -1 and 1. To check whether the calculated value represents a significant correlation it is necessary to calculate the t-value of the Student's t-distribution and to choose a significance level, which we will set to 1%. The t-value is given by

$$t = r_{\text{Pearson}} \cdot \sqrt{\frac{N_{\text{data}} - 2}{1 - r^2_{\text{Pearson}}}}. \tag{2.43}$$

Using the significance level chosen before, there is a critical value of t, namely t_{critical}, depending on the number of data points. It is listed in the literature, e.g. Hedderich and Sachs (1968) and Bronstein et al. (1977). The correlation is significant, if t is larger than this critical value. In terms of r_{Pearson}

this means the correlation is significant for

$$|r_{\text{critical}}| > \frac{t_{\text{critical}}}{\sqrt{t^2_{\text{critical}} + N_{\text{data}} - 2}}. \tag{2.44}$$

The Pearson correlation coefficient has the disadvantage of requiring a linear correlation between the parameters compared. Furthermore, it is highly influenced by possible outliers of the data sets, which could lead to wrong conclusions. Therefore, we will use the Spearman rank correlation coefficient as well, since this coefficient does not require linearity and is not influenced by outliers. Here, both parameter data sets are transformed into rows of rank numbers, e.g., the lowest value gets rank number 1 and the highest rank number N_{data}. Afterwards, the difference, D, of the two rank numbers is calculated and the correlation coefficient is given by Hedderich and Sachs (1968) as

$$r_{\text{Spearman}} = 1 - \frac{6 \sum\limits_{i=1}^{N_{\text{data}}} D^2}{N_{\text{data}}(N^2_{\text{data}} - 1)}. \tag{2.45}$$

2.3.2 k-sample tests

Another part of the statistical analysis are k-sample tests which shall prove whether two subsamples stem from the same population or not. The selection criteria for one or another subsample are chosen from the system parameters. For example the targets can be sorted by their fractional luminosity, which results in a subsample with low and in one with high fractional luminosity objects. Then it is tested whether the two subsamples follow the same correlations between different system parameters. There are many different testing methods for this case, e.g. the Student's t-test, the Kolmogorov-Smirnov test and the Anderson-Darling test. If the sorting parameter values were distributed normally, the Student's t-test would be the easiest way of checking. However, we do not expect these parameters to be distributed normally and so this test is not an appropriate solution. On the other hand the Kolmogorov-Smirnov test (e.g., Kolmogorov, 1933; Smirnov, 1939, 1948; Massey, 1951) is independent of a specific distribution or the sample size, so it seems to be the most sensitive test for the problem mentioned in this work. Nevertheless, this test holds some disadvantages. It is only appropriate if the empirical distribution functions (EDFs) of the samples do not cross each other and if their difference is large near the centre of the distribution. If the EDFs have their largest difference at the beginning or the end of the distribution this test is insensitive (Hedderich and Sachs, 1968). In order to overcome these two disadvantages the Anderson-Darling test (AD test) was developed (e.g., Anderson and Darling, 1952, 1954; Darling, 1957; Scholz and Stephens, 1987; Feigelson and Babu, 2012) and was applied to the case of this work. The AD test provides the testing value A^2, which is given for two samples by

$$A^2 = \frac{1}{n_1 + n_2} \sum_{i=1}^{k} \frac{1}{n_i} \sum_{j=1}^{n_1+n_2-1} \frac{((n_1 + n_2)M_{ij} - jn_i)^2}{j(n_1 + n_2 - j)}. \tag{2.46}$$

Here, n_i is the size of the i-th sample, $k = 2$ the number of samples and M_{ij} the number of data points in the i-th sample smaller than the data point Z_j of the pooled ordered sample ($Z_1 < ... < Z_{n_1+n_2}$). The A^2 parameter is standardised to

$$T \equiv \frac{A^2 - (k - 1)}{\sigma}, \tag{2.47}$$

where σ is the standard deviation of A^2. The null hypothesis is rejected at a significance level α if $T \geq t_{k-1}(\alpha)$. For $k = 2$ and a significance level of $\alpha = 0.05$, the critical percentile value is $t_1 = 1.960$, while it is $t_1 = 3.752$ for $\alpha = 0.01$ (Scholz and Stephens, 1987).

3 Technical aspects of fitting spectral energy distributions

After introducing the basic terms of a debris disc system and the methods of describing a SED we now come to the question of how we can model such a SED and thus we will explain the technical execution of SED fitting.

3.1 Fitting algorithm

3.1.1 Functionality

The SEDUCE code (Müller et al., 2010) was first designed to calculate SEDs of optically-thin circumstellar discs. With given input parameters, such as minimum grain size $s_{\min}$ or disc radius R_{disc}, the SED can be derived directly with this code. Therefore, information on these parameters have to be taken from the literature or catalogues, but in most of the cases the values are unknown. Furthermore, the shape of the SED is known in general since the flux densities at certain wavelengths can be measured, but the parameters leading to the measured flux densities are not. So the real problem is of indirect nature, actually – which parameter values lead to the observed photometric data points of the SED? To solve this problem a fitting tool is necessary. This tool should minimise the deviation of the model-SED from the observed data points. A common parameter to express the quality of the fit is the χ^2-parameter. It is given as

$$\chi^2 = \sum_{i=1}^{N_{\mathrm{data}}} \left(\frac{F_{\mathrm{i}}^{\mathrm{observed}} - F_{\mathrm{i}}^{\mathrm{model}}}{\sigma_{\mathrm{i}}^{\mathrm{observed}}} \right)^2 , \tag{3.1}$$

where in case of this work N_{data} is the number of photometric data points, F_{i} the observed and modelled flux densities and σ_{i} the uncertainties of the observed flux densities. Since the value of this parameter is larger for a larger number of data points it has to be normalised in order to compare fitting results of different objects. Hence, the reduced χ^2 is used, which is given as

$$\chi^2_{\mathrm{red}} = \frac{\chi^2}{N_{\mathrm{data}} - N_{\mathrm{parameter}} - 1} . \tag{3.2}$$

Here, the value of this parameter is less or equal to unity for a good fit and thus, the problem of fitting is to minimise χ^2.

There are several methods of finding global minima, for example rasterising the parameter space, the Downhill simplex or the Powell method (Press et al., 2002), which all have their advantages and disadvantages. we chose the “simulated annealing” method, since it is an easy algorithm to implement and in addition, it does not require knowledge of the shape of the χ^2-function. The simulated annealing makes use of the analogy with the thermodynamical freezing processes of liquids. The molecules of a liquid move freely at high temperatures, but they loose their ability of moving during the cooling process. If this cooling process is slow, the molecules are able to form a crystal and get to the minimum energy state of the system. If the process passes fast, the minimum energy state cannot be reached. The molecules form an amorphous or a polycrystalline system, which has a higher energy. Analogue to that the global minimum is found by a slow approach. Figure 3.1 shall illustrate this. The diagram shows a function with two minima. While the minimum on the left side is just local, the minimum on the right is both a local and a global one and so the one we are looking for. In order to get the minimum we have to start at an arbitrary point ("Start"). It is given by a set of default parameter values. Then a new set of parameter values is chosen at random and therefore, a maximum step size *step*$_{\max}$ is defined for each parameter. The randomly chosen step sizes lie between $[-step_{\max}, +step_{\max}]$ and thus, the new parameter values increase or decrease by this summand. This leads to a new function value χ^2. For instance this point could be one of the circles numbered with 1, 2 or 3. Now, the function value of the starting point and the new value are compared. In case of circle 1 the parameter χ^2 is lower than the starting value and so we are approaching a minimum. The set of parameters which led to this point is taken as the temporary parameter set of the minimum. For circle 2 the χ^2 value is larger and therefore we took the wrong direction in parameter space. Here, the parameter values of the starting point stay as the temporary parameter set of the minimum.

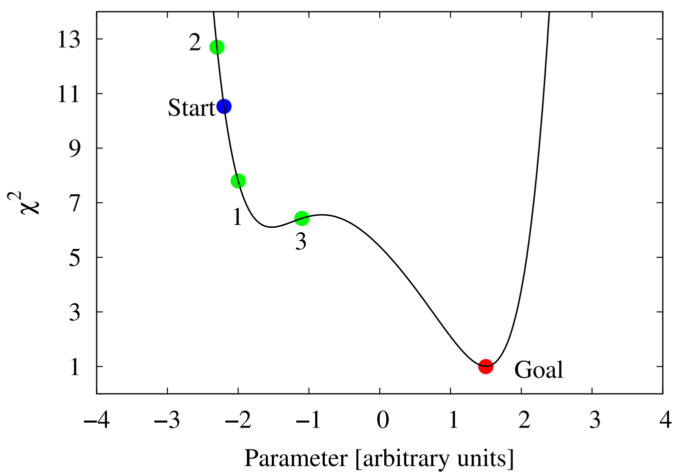

Figure 3.1: Objective function for the simulated annealing. Blue filled circle: starting point for fitting iteration; green filled points: iteration progress points; red filled circle: global minimum and goal of fitting process. See text for further details.

The value of χ^2 may be larger, but there is a possibility for a further minimum. Circle 3 illustrates this. On the left side of it the χ^2-values decrease and lead to a minimum. On its right side the values increase, but as it is shown another minimum (the goal) can be reached. This is the problem, where the simulated annealing method takes place. The probability of not reaching a minimum after increasing values of χ^2 is not constant. It follows the slow annealing process with the shape of

$$P(\chi^2) \sim \exp\left(-\frac{\chi^2 - \chi^2_{\mathrm{start}}}{T}\right), \tag{3.3}$$

where χ^2_{start} is the value of χ^2 of the starting set of parameter values and T the so called annealing function. The acceptance threshold $P(\chi^2)$ is picked from $[0, 1]$ by a random generator and then compared to the value of the right side of Equation (3.3). In case of $P(\chi^2)$ being larger than the right side, the parameter values are reset to the values of the starting point and the annealing function T decreases. This means, the finding of another minimum in this direction of parameter space is unlikely. The other case is $P(\chi^2)$ being smaller than the ride side of Equation (3.3). Here, the values are accepted as the new starting point for the next χ^2-calculation and the annealing function does not change. When the annealing function finally reaches a fixed minimum, since there are no better χ^2-values reachable, the set of parameter values found for the temporary minimum of χ^2 is taken as the global minimum parameter set.

3.1.2 Advantages and disadvantages

As we mentioned before, each algorithm holds several advantages and disadvantages and so does the simulated annealing. As an iterative improvement algorithm the simulated annealing finds always a local minimum during the fitting process, but whether this minimum is the global one or not cannot be said since there is no information on that. Furthermore, the result of the fitting process depends on the input parameter values and therefore the starting point. In general there are no constraints for them, but in this work physical expectations can be used as a first guess. For instance, the minimum grain size should lie at several microns and thus a starting value of one metre would not be appropriate. And last but not least the computation time of the whole process cannot be estimated in general and in the worst case the fitting can be an open problem (Laarhoven and Aarts, 1987).

On the other hand, the simulated annealing can be applied to general problems without knowledge of the function to minimise, which is the case for the χ^2-function of this work. In addition it is an easy algorithm to implement and the computation time for one iteration is small. There are also possibilities to avoid some of the disadvantages mentioned above, for example the usage of a sample of starting points.

All in all, despite some disadvantages this algorithm is a good choice for the χ^2-minimisation, since it can easily be adapted to special problems and therefore offers a high degree of flexibility necessary in this work.

3.2 Fitting procedure

3.2.1 Criteria for one- and two-component systems

Images reveal that debris discs may possess several rings comparable to the Asteroid and the Edgeworth-Kuiper belt in our Solar system (e.g., Roberge et al., 2013; Donaldson et al., 2013; Su et al., 2015; Matthews et al., 2015). Hence, SEDs of debris disc systems may contain several components as well. Figure 3.2 shows, that in the visual and near infrared range the stellar radiation dominates, whereas in the mid-infrared the radiation of the debris disc dust gains more influence on the measured flux densities. Finally, the far-infrared is dominated by the disc's radiation and the star is nearly negligible. Thus the SED can contain a warm component (an "Asteroid belt") for instance, which has more influence in the mid-infrared, and a cold one (an "Edgeworth-Kuiper belt"), which dominates the far-infrared region (see Figure 3.2 left panel). So, in order to fit a SED properly, it has to be proved whether a warm dust component is present in the system or not. Unfortunately, the majority of the observed images cannot reveal or resolve a warm component. Hence, we have to use selection criteria given by the SED itself.

At first, we start to fit the far-infrared photometric points beginning at a wavelength of 70 µm. Here, the near-infrared and mid-infrared photometry is not included in the fitting process, since we want to test, whether the data can be fit well with just one component or not. An examplary result for such a fit is given in Figure 3.2 in the left panel. There is a clear deviation of the mid-infrared photometry from the model data, which indicates the existence of a second, warmer component shown

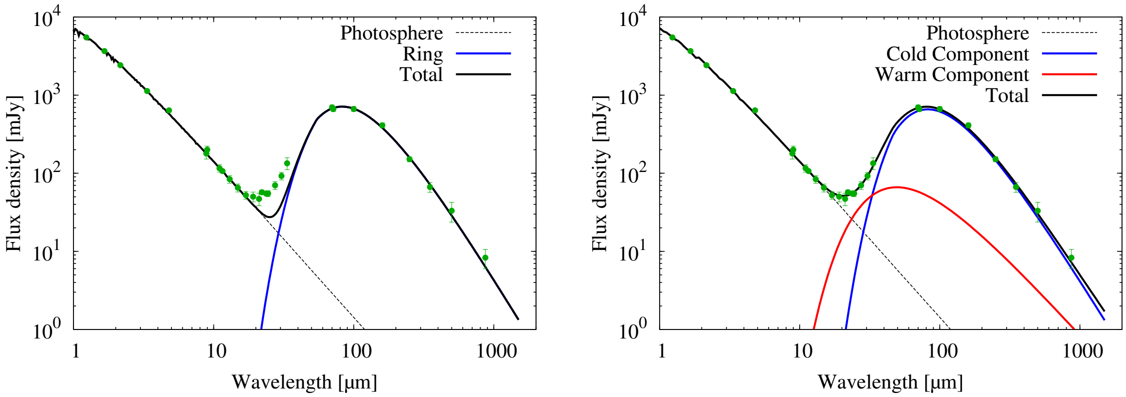

Figure 3.2: Left panel: Typical SED of a debris disc system fitted with one dust ring (cold component shown in blue). Green filled circles show observational points with error bars. Deviation of model values and observational points in the MIR region indicate the existence of a second dust ring (warm component). Right panel: Typical SED of a debris disc system fitted with two dust rings (cold component shown in blue, warm component shown in red.)

in the right panel. In order to prove this assumption the mid-infrared model flux densities of the best fit are compared to the mid-infrared photometric points measured for each disc. Here, the measuring instruments are the InfraRed Spectrograph (IRS)[1] and the Multiband Imaging Photometer (MIPS)[2] of the *Spitzer* Space Telescope as well as the Wide-Field Infrared Survey Explorer (WISE, Wright et al. (2010)) (see Section 4.3.1 for details). We use the parameter $\sigma \equiv (F_\mathrm{i}^\mathrm{observed} - F_\mathrm{i}^\mathrm{model})/\sigma_\mathrm{i}^\mathrm{observed}$ to quantify the significance of an excess. If there is a significant excess at the mid-infrared bands of *Spitzer* IRS/22, WISE/22, *Spitzer* MIPS/24 and *Spitzer* IRS/31, meaning the measured flux densities deviate more than 3σ from the derived model flux densities, then an excess is assumed. Otherwise the second component is refused and the system is fitted with one dust component.

Now, it has to be checked, whether the fit with a second component has a significant better quality than the fit with one component. Therefore, the χ^2 of the one-component fit (shown in the left panel of Figure 3.2) is calculated including the mid-infrared data points starting at 10 μm. At this wavelength the measured flux densities of our sample start to deviate from the pure photospheric spectrum of the host star. The resulting χ^2-value is compared to the χ^2-value of the two-component fit, which has included the mid-infrared points as well. If the quality of the two-component fit is three times better than that of the one-component fit, meaning if $\chi^2_\mathrm{one}/\chi^2_\mathrm{two} > 3$, than the second component is confirmed. The same criterion was used by Ballering et al. (2013)

The third criterion includes the physical parameters of the warm component. Since the dust is fit with a certain material, such as astronomical silicate or carbon, a sublimation temperature exists, for which the material changes from a solid to a gaseous state. If the warm component would be set too close to the star, the ring temperature would reach the sublimation temperature of the material. In this case the dust particles would disappear and no thermal emission could be measured. The fitting tool uses the disc radius as input parameter and calculates then the temperature of the grains. Hence, the radius of the ring must be larger than the sublimation radius, for which the sublimation temperature is reached.

Finally, if all three of the before mentioned criteria are fulfilled, a second dust component is assumed

---

[1] IRS Instrument Handbook, Version 5.0;
http://irsa.ipac.caltech.edu/data/SPITZER/docs/irs/irsinstrumenthandbook/home/

[2] MIPS Instrument Handbook, Version 3;
http://irsa.ipac.caltech.edu/data/SPITZER/docs/mips/mipsinstrumenthandbook/home/

for the debris disc system. In all other cases it is refused and the system is assumed to have just one ring component.

3.2.2 Fitting of one-component systems

A debris disc system is fit with one dust component, if at least one of the above mentioned criteria is missed. In this case all photometric points starting at a wavelength of 10 µm are included in the fitting process. As explained before, the SED fitting of debris discs can be done by using different methods, e.g., the blackbody (BB), the modified blackbody (MBB) or the size distribution (SD) method. Each has its advantages and disadvantages and hence it is not possible to say generally that one method is better than the other one. For statistical analysis of large samples with hundreds of discs it is necessary that the fitting process is fast and that all discs can be modelled without much effort. Therefore, the blackbody method is often chosen (e.g., Ballering et al., 2013; Chen et al., 2014; Kennedy and Wyatt, 2014), since for this method only the amount of dust material and the dust temperature of the disc have to be fit. Obviously, the simplicity of this kind of modelling does not allow conclusions about the properties of the dust grains, such as particle size or composition, but predictions about dust temperatures or the existence of a second component dust ring are possible. The purpose of this work is to statistically investigate the dust properties of debris discs. Therefore, the BB-method is not appropriate for this problem and other methods have to be applied. As could be seen in Chapter 2.1, we will concentrate on the MBB and SD method.

MBB method

The MBB method makes use of the simplicity of the blackbody fitting, but here, conclusions about dust grain sizes can be made as well. Since the number of modelling parameters is increased to three (amount of dust material, cut-off wavelength and opacity index) compared to the BB method, the process is not as fast as for the BB fitting, but statistical analysis of moderately large samples can be easily done (e.g., Moór et al., 2006; Booth et al., 2013; Donaldson et al., 2013; Pawellek et al., 2014; Moór et al., 2015). An example for a SED using the MBB method is given in Figure 3.3. The artificial "knee" generated by the cut-off wavelength λ_0 can be seen easily. Furthermore, the influence of β_{mod} in the far-infrared region is shown. The larger β_{mod} is, the steeper is the decrease.

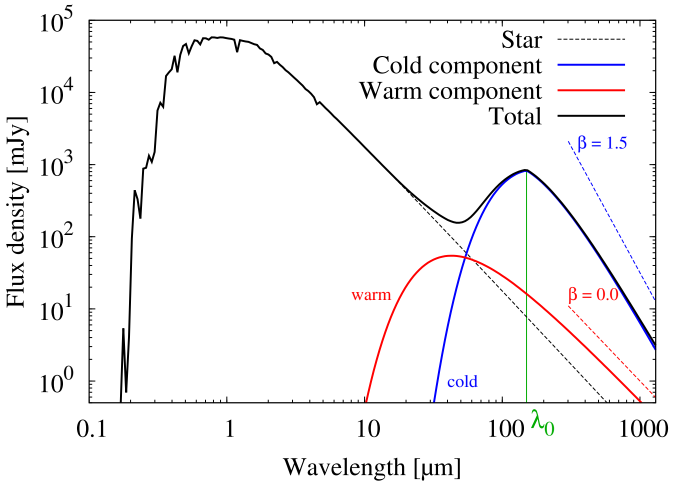

Figure 3.3: SED generated with the MBB method.

SD method

The SD method follows another idea. Here, a more realistic modelling of the dust material is foregrounded at the expense of the fitting fastness. The modelling parameters are now the amount of dust material, the size distribution parameters (e.g., minimum and maximum grain size, size distribution index), the radial parameters (e.g., minimum and maximum radius of the disc, radial distribution index) and the dust composition parameters (e.g., absorption efficiency, density). A statistical analysis of a large or even a moderately large sample of discs with this method is very time expensive and therefore impossible, if there are no fixed parameters or parameter constraints. In Figure 3.4 an example for a SED generated with the SD method is given. While the minimum grain size of the size distribution has its largest influence in the mid-infrared region ($\sim 30-50\,\mu\mathrm{m}$), the size distribution index, q shows a similar behaviour than the β_{mod} of the MBB method. The larger q is, the steeper the decrease at far-infrared wavelengths.

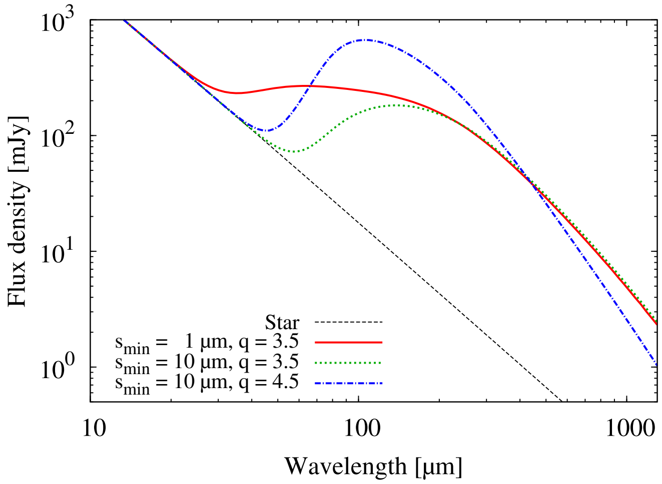

Figure 3.4: SED generated with the SD method for fixed radial parameters. Only the grain size parameters are varied.

The first part in the fitting process for both methods is to calculate the dust optical properties (e.g., Q_{abs}) of each grain size and then determine the absorbing and emitting luminosity (see Equations (2.25) and (2.26)). Assuming energy conservation (Equation (2.27)) the distance of the dust particle to the star can be determined (Equation (2.28)) through numerical integration. At each fitting step (see Section 3.2) the fitting parameter values are randomly selected within the valid range, while the resulting model flux densities are calculated including a normalisation to the measured photometric points in height, which represents an adaption of the dust mass (see Equation (2.12)). This means, that there are at least three free parameters and therefore, five photometric data points are necessary in order to fit the SED properly (see Equation (3.2)). Otherwise, the fitting process cannot uniquely constrain the system parameters given the complexity of the model.

3.2.3 Fitting of two-component systems

The fitting procedure of a two-component debris disc system is similar to the fit of the one-component system. Here, the first step is to fit the SED only with the cold component just including the far-infrared points ($\lambda \gtrsim 70\,\mu\mathrm{m}$). Then, the best fit parameters of the cold component are fixed and the warm component is added and fit assuming a pure blackbody model, now including the mid-infrared points ($\lambda \gtrsim 10\,\mu\text{m}$) as well. After that, the warm component parameters are fixed and the cold component is adapted again. This iteration process is repeated until no further improvement of the SED model is possible, i.e. the χ^2 cannot be reduced anymore. In order to fit a two-component system, at least seven photometric data points are necessary since five free parameters do exist.

3.3 Degeneracy of fit parameters

The fitting of a SED bears the problem that the radial parameters are degenerated with the grain size parameters. This means, that a SED can be fit either with large grains at a small distance to the star or with small grains at a larger distance. The reason for this effect is given in Figure 2.7 for instance. The dust grains of different sizes have different temperatures at the same stellocentric distance. In general, large grains are colder at a certain distance than small ones. Furthermore, the dust composition plays a role in the degeneracy as well, which can be seen in Figure 2.6 in the right panel. Dust grains of the same size but made of different materials have different temperatures, too.

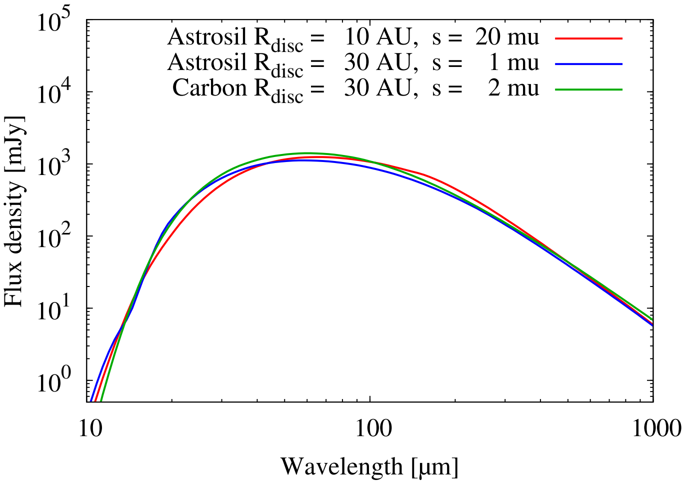

Figure 3.5: SED of a debris disc for different disc radii, grain sizes and dust materials.

Figure 3.5 does explain this in more detail. The same SED can be reproduced by using different parameters. For astronomical silicate we can either use a disc of 10AU and a minimum grain size of 20 µm or a larger radius of 30AU and a small grain size of 1 µm. If we change the dust composition to carbon and set the radius to 30AU as well the minimum grain size changes to 2 µm.

As a consequence, it is necessary to find constraints on the radial parameters or the grain size parameters in order to get reliable results from the SED fit. Using resolved debris discs, which is the basic idea of this work, and assuming a narrow annulus for each disc component, the radial parameters can be fixed and the degeneracy between disc radius and dust grain size can be broken.

3.4 Determination of error bars

After fitting the SED, it is useful to know, how reliable the results are. Therefore, it is necessary to calculate the uncertainties of the fit parameters. The method used was suggested by Steve Ertel (Steward Obervatory, University of Arizona; Ertel (2012)) and is done the following way. Considering the parameter space, the initial point of the calculation of the fit uncertainties is the point of the best fit parameter values. From here, a new annealing process is started, with the difference that Equation (3.3) is changed to

$$P(\chi^2) \sim \exp\left(\chi^2_{\text{start}} - \chi^2\right), \tag{3.4}$$

and no annealing temperature is assumed in order to avoid weighting effects. In the next step it is counted how often a certain parameter value is reached. Therefore, all values are grouped into equal-sized bins. The resulting distribution in the parameter space represents an estimate of the probability distribution of the parameters and is the basis for the calculation of the confidence interval of the parameters. Such a probability distribution is given in Figure 3.6. It is obvious that the most counts are situated between 3 and 3.5 of the minimum grain size and between 3.55 and 3.57 of the size distribution index. Assuming a normal distribution here, the standard deviation for a fit parameter can be calculated by

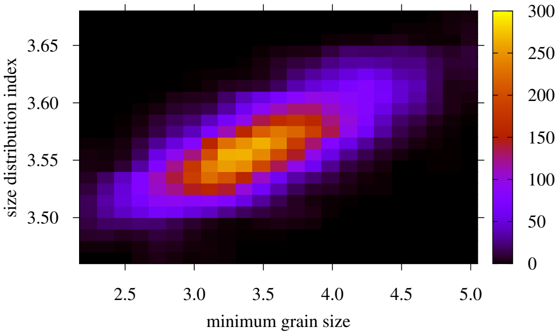

Figure 3.6: Probability distribution in the parameter space of minimum grain size and size distribution index in arbitrary units. The colour range gives the absolute frequencies of the pairs of parameter values.

$$s_{\text{parameter}} = \sqrt{\frac{1}{N}\sum_{i=1}^{N}(x_i - \bar{x})^2}, \tag{3.5}$$

where N is the total number of the counted parameter values, x_i the values theirselves and $\bar{x}$ the mean value of the parameter. In the following parts of this work the standard deviation is taken as the uncertainty of the fit parameter, thus we use the 1σ confidence interval.

One important point is the width of the parameter grid in the fitting process. If the width of the grid nodes is too broad, the uncertainty is overestimated and increases with increasing grid width. So the grid must be fine enough in order to avoid that effect. On the other hand, if the width of the grid nodes is to narrow no normal distribution can be reached in an adequate time. Figure 3.7 shows the resulting probability distribution for different grid widths. In the left panel the grid has a very small width and thus no normal distribution is visible. In the right panel the grid width is chosen very large and the normal distribution is broadened. Hence, the uncertainties are overestimated here. The panel in the middle represents the best choice for the grid width.

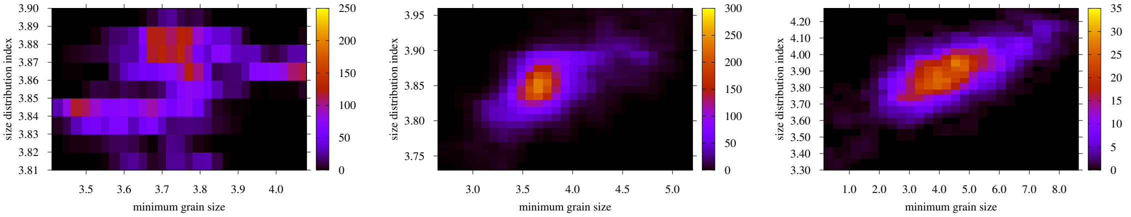

Figure 3.7: Probability distribution in the parameter space of minimum grain size and size distribution index in arbitrary units. The colour range gives the absolute frequencies of the pairs of parameter values. The grid width varies from $\Delta s = 0.01$ and $\Delta q = 0.001$ (left) over $\Delta s = 0.1$ and $\Delta q = 0.01$ (middle) and $\Delta s = 1.0$ and $\Delta q = 0.1$ (right) with Δs being the width of the grain size grid and Δq the grid of the size distribution index.

4 Sample

In the previous chapters we gave an introduction to the description of debris discs and explained the technical way of modelling a SED. Since the theory is known now, it is time to choose the appropriate targets for the SED fitting.

4.1 Resolved debris discs

In Chapter 3.3, we described the problem of degeneracy between the radial, grain size and dust composition parameters of debris discs. In order to model a SED it is necessary to break these degeneracies and one possibility is given by resolved debris discs. Here, the disc radii are known and so the grain sizes can be calculated for given dust compositions. Over the last years many debris discs were found around a wide range of spectral types and could be resolved in one or more wavelength bands with different instruments. At this time nearly one hundred spatially resolved discs are known around stars with spectral types ranging from B to M (see Table C.1). Thus we have the opportunity to select the most appropriate discs.

4.1.1 Selection criteria

In this work we are going to derive statistical correlations between disc parameters and stellar properties. Therefore, it is necessary that the selected discs fulfill several requirements in order to minimise the uncertainties in the statistical results.

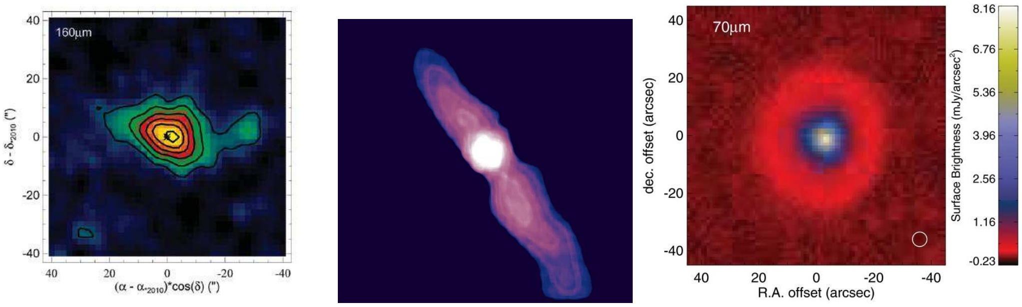

Figure 4.1: Stellar systems revealing peculiarities. Left panel: 61 Vir (Wyatt et al., 2012), middle panel: β Pic (Lagage and Pantin, 1994), right panel: ε Eri (Greaves et al., 2014b).

Every instrument observing discs has its own properties and data reduction system. To avoid possible biases caused by different instruments, we chose discs which were all resolved with *Herschel* Photoconductor Array Camera and Spectrometre (PACS) (Pilbratt et al., 2010; Poglitsch et al., 2010). Furthermore, the selection of photometric data points which are the basis of SED fitting is important. Reliable fitting results are only possible with a reliable set of data points including a wide wavelength range. As a result each disc chosen for this work must have at least two high signal-to-noise flux densities in the PACS bands (70 µm, 100 µm, 160 µm).

Considering the statistical purpose of our thesis the homogeneity of the sample is important as well. Hence, we excluded discs revealing peculiarities such as substantial asymmetries in the resolved image (e.g. β Pic; Golimowski et al. (2006)) or nearby galaxies contaminating the disc image (e.g. 61 Vir; Wyatt et al. (2012)). We excluded discs with central peaks (e.g. ϵ Eri; Backman et al. (2009)) as well, since the determination of the disc radius identified with the location of the maximum surface brightness(see Chapter 5) would lead to wrong values in such cases. In Figure 4.1 examples for such peculiar discs are depicted.

4.1.2 Resulting sample

Using the criteria mentioned above, there are 39 objects out of ~100 chosen for this work and Table 4.1 lists the resulting selection. The objects are distributed over a broad range of spectral types (M to B). Figure 4.2 shows the frequency of objects as a function of spectral type and stellar age. Most of the host stars of the discs chosen have spectral type A (20 targets) or F (7 objects). There are 7 K-type stars, two G and two M-stars and one B-type star. Besides targets of luminosity class V the sample contains class III and IV stars as well. The stellar ages vary between 15 Myr and 2500 Myr and show an equal distribution over the range. The sample does not claim completeness and could be biased in several ways. In order to check it for possible biases we made additional tests which are explained in Chapter 5.

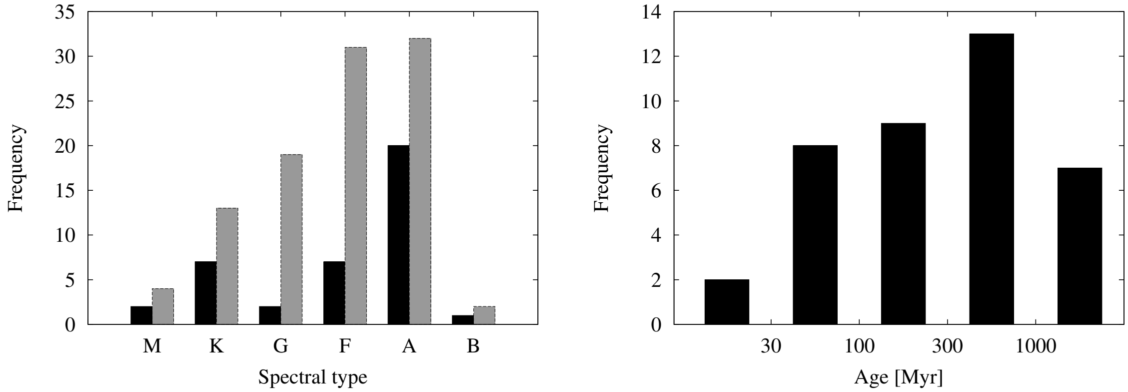

Figure 4.2: Left: Frequency of resolved debris discs as function of spectral type. Black bars represent the selected sample of 39 resolved objects and gray bars the whole number of 100 objects. Right: Frequency of resolved discs of the 39-disc-sample as function of stellar age. For each star with more than one age reference, the age given is the geometric mean value reported in those papers (see Table (4.2).

4.2 Stellar parameters

Knowing the influence of the host star(s) of a debris disc is necessary in order to compute the excess emission and to fit a SED properly. Therefore, it is essential to derive the photosphere from the stellar parameters. In this work these parameters were collected from the literature. If different values were given for one target, the arithmetic mean value was taken, except for the stellar ages where the geometric mean was used. In Table 4.2 the resulting values are listed.

Table 4.1: Sample of resolved debris discs

HD	HIP	Name	Program	Ref
166	544	-	a	1
10647	7978	q^1 Eri	a	2
23484	17439	-	a	3
48682	32480	56 Aur	a	1
131511	72848	DE Boo	a	1
207129	107649	-	a	4
95418	53910	β Uma	b	5
102647	57632	β Leo	b	5
109085	61174	η Crv	b	5
13161	10064	β Tri	b	6
14055	10670	γ Tri	b	6
20320	15197	ζ Eri	b	6
71155	41307	30 Mon	b	6
110411	61960	ϱ Vir	b	6
125162	69732	λ Boo	b	6
139006	76267	α CrB	b	6
188228	98495	ϵ Pav	b	6
-	74995	GJ 581	b	7
27290	19893	γ Dor	b	8
218396	114189	HR 8799	c	9
172167	91262	Vega	d	10
197481	102409	AU Mic	d	11
216956	113368	Fomalhaut	d	12
9672	7345	49 Cet	e	13
10939	8241	q^2 Eri	f	14
17848	13141	ν Hor	f	14
21997	16449	HR 1082	f	15
50571	32775	HR 2562	f	14
95086	53524	-	f	16
161868	87108	γ Oph	f	14
170773	90936	HR 6948	f	14
182681	95619	HR 7380	f	14
195627	101612	φ^1 Pav	f	14
92945	52462	V419 Hya	g	19
104860	58876	-	g	17
142091	77655	κ CrB	h	18
71722	41373	HR 3341	i	17
128311	71395	HN Boo	j	-
192263	99711	V1703 Aql	j	-

Programmes:
[a] DUNES; [b] DEBRIS; [c] OT1_bmatthew_4; [d] KPGT_golofs01_1; [e] GASPS; [f] OT1_pabraham_2; [g] OT1_gbryden_1; [h] OT1_abonsor_1; [i] OT2_fmorales_3 [j] OT1_amoromar_1.

References:
[1] Eiroa et al. (2013); [2] Liseau et al. (2010); [3] Ertel et al. (2014); [4] Marshall et al. (2011); [5] Matthews et al. (2010); [6] Booth et al. (2013); [7] Lestrade et al. (2012); [8] Broekhoven-Fiene et al. (2013); [9] Matthews et al. (2014a); [10] Sibthorpe et al. (2010); [11] Matthews et al. (in prep.); [12] Acke et al. (2012); [13] Roberge et al. (2013); [14] Moór et al. (2015); [15] Moór et al. (2013b); [16] Moór et al. (2013a); [17] Morales et al. (2013); [18] Bonsor et al. (2013); [19] Stapelfeldt et al. (2013).

Stellar photospheres

The stellar photospheres were modelled by Benjamin Montesinos (Departamento de Astrofísica, CAB, CSIC-INTA) in the following way. With the stellar parameters the synthetic spectra were calculated by interpolating the PHOENIX/GAIA model grid (Brott and Hauschildt, 2005). The two stars HD 182681 and HD 188228 have stellar temperatures above 10000K. Since the PHOENIX grid does not go beyond this temperature, these models were replaced by ATLAS9 models (Castelli and Kurucz, 2004).

The SEDs were built using the optical and near-infrared data from different catalogues. The Hipparcos catalogue (CDS catalogue `I/239/hip_main`) provided the Johnson BV and the Cousins I_c

photometry, and Cutri et al. (2003) (CDS catalogue `II/246`) the 2MASS JHK_s photometry. The photometric points were given in magnitudes, so a transformation to flux densities was necessary. Therefore, the calibrations by Bessell (1979) (BVI_c) and Cohen et al. (2003) (JHK_s) were used. Then the generated model photospheres for each star were normalised to the given photometry by taking the I_c flux density as reference. The 2MASS data were not used for normalisation since for a number of targets these data were of poor quality. The object GJ 581 was an exeption since here, the 2MASS K_s data were used. This was done in order to reach a better fit to the photometry points in the near-infrared.

Correction for extinction

Another aspect is the possibility that distant objects are affected by extinction. If that is the case, the stellar photospheres have to be corrected in order to get a realistic result for the stellar influence. All of the targets of the sample are located in the Local Bubble ($d < 100$pc), where the extinction in the optical band is $A_v \lesssim 0.1$mag (e.g., Frisch et al., 2011; Reis et al., 2011). The uncertainties in the measured magnitudes are of the same order. We assume $A_v = 0.2$mag as the worst case, as well as an extinction ratio $A(I_c)/A_v \approx 0.5$ refering to the I_c band to which the stellar photospheres were normalised (Rieke and Lebofsky, 1985). Hence, the extinction for the objects should be of the order of $\lesssim 0.1$mag. Without dereddening the true photospheric flux density would be underestimated by $\lesssim 10\%$ in that case. Considering the mid-infrared, where the excess flux densities lie only slightly above the photospheric ones, there would be an overestimate of the excess by the same 10%, which is the highest possible uncertainty only reachable for the largest extinction and excess flux densities close to the photospheric ones. Refering to the sample chosen for this work the uncertainty due to extinction lies at several percent and is comparable to the measurement uncertainties in the mid-infrared.

Nine stars which were all observed by the OT1_pabraham_2 programme were checked for possible extinction, including the most distant objects of the sample, HD 21997 ($d = 71.9$pc) and HD 95086 ($d = 90.4$pc). Only HD 21997 revealed reddening, where A_v was found to be ≈ 0.16mag, and hence $A(I_c) = 0.08$mag. The flux density at 24 µm is 2.2 times the photospheric flux density and therefore, the estimated uncertainty due to reddening is 4%. Looking at the far-infrared region the excess flux densities are one to three orders of magnitude higher than the photospheric ones and hence the extinction effect is negligible here.

4.3 Photometry

4.3.1 Mid-infrared photometry

We used flux densities at wavelengths longwards of 10 µm in the SED modelling, including *WISE*/12 and /22 (*WISE* All-Sky Release Catalog; Wright et al. (2010)), *AKARI*/18 (*AKARI* All-Sky Catalogue; Ishihara et al. (2010)), measurements taken with MIPS/24 (e.g., Su et al., 2006; Chen et al., 2012) and IRS of the *Spitzer* Space Telescope. (e.g., *Spitzer* Heritage Archive; Chen et al. (2014) and CASSIS archive[1], Lebouteiller et al. (2011); Werner et al. (2004)). In some cases Gemini/MICHELLE data were provided (Churcher et al., 2011a) as well as MMT/BLINC (Stock et al., 2010) and Keck/MIRLIN (Wahhaj et al., 2007). We took the photometric data from the literature, if they were given. In cases where no values were reported there, we took them from the above mentioned catalogues, which we accessed through Vizier and NASA/IPAC Infrared Science Archive. All photometric data can be found in Table A.1.

---

[1] http://cassis.sirtf.com/atlas/query.shtml

Table 4.2: Stellar Parameters Sorted by Stellar Luminosity

HD	HIP	Name	d [pc]	SpT	$L/L_\odot$	$T_{\rm eff}$/K	$M/M_\odot$	log(g)	[Fe/H]	Ref	Age/Myr^f	Age ref
-	74995	GJ 581	6.2	M5V	0.012	3498	0.31	4.90	0.00	1	3996	1, 2, 3
197481	102409	AU Mic	9.9	M1Ve	0.062	3600	0.48	4.60	0.00	2	17	4, 5, 6
128311	71395	HD Boo	16.6	K3V	0.29	4965	1.32	4.83	0.20	3	310	7
192263	99711	V1703 Aql	19.9	K1/2V	0.31	4975	0.83	4.60	0.05	3	2090	8
92945	52462	V419 Hya	21.6	K1V	0.36	5183	1.18	4.76	0.13	3	300	7
23484	17439	-	16.0	K2V	0.41	5166	0.79	4.44	0.05	4	930	9
131511	72848	DE Boo	11.5	K0V	0.49	5335	0.97	4.60	0.17	3	700	9
166	544	V439 And	13.7	K0V	0.61	5577	0.96	4.58	0.18	3	320	9
104860	58876	-	45.5	F8	1.16	5930	1.04	4.39	-0.26	5, 6, 7	200	10
207129	107649	-	16.0	G2V	1.25	5912	1.06	4.44	-0.01	4	2499	9, 11, 12
10647	7978	q1 Eri	17.4	F9V	1.52	6155	1.12	4.48	-0.04	4	1307	9, 12, 13, 14
48682	32480	56 Aur	16.7	G0V	1.83	6086	1.17	4.35	0.09	4	1380	9
50571	32775	HR 2562	33.6	F5VFe+0.4	3.17	6490	1.35	4.23	-0.01	5, 6, 7, 8	449	13, 14, 15
170773	90936	HR 6948	37.0	F5V	3.44	6590	1.38	4.29	-0.05	5, 6, 7, 9	574	7, 13, 15
218396	114189	HR 8799	39.4	A5V	4.81	7380	1.51	4.29	-0.50	5, 7, 9	71	13, 16, 17
109085	61174	η Crv	18.2	F2V	4.87	6950	1.53	4.14	-0.08	10	1768	18, 19, 20
27290	19893	γ Dor	20.5	F1V	6.27	7070	1.62	4.10	-0.13	5, 7, 8	896	17, 19
95086	53524	-	90.4	A8III	7.04	7530	1.70^b	4.29	0.00	5, 7	15	15, 21
195627	101612	ϕ1 Pav	27.8	F0V	7.36	7200	1.69	4.05	-0.12	5, 7, 8	842	7, 15
20320	15197	ζ Eri	33.6	kA4hA9mA9V^a	10.3	7575	1.85	4.05	0.04	5, 7, 8	800	19
21997	16449	HR 1082	71.9	A2IV/V	11.2	8325	1.89	4.30	0.00	5, 7, 11	44	15, 17, 22
110411	61960	ϱ Vir	36.3	A0V	11.7	8710	1.91	4.18	-1.10	5, 7, 9	71	19, 23
142091	77655	κ CrB	30.5	K1IVa	12.5	4815	1.80^c	3.12	-0.09	5, 7, 9	2345	24, 25
102647	57632	β Leo	11.0	A3Va	13.2	8490	1.97	4.26	0.00	5, 7, 9	82	19, 23, 26, 27
125162	69732	λ Boo	30.4	A0p	15.4	8550	2.05	4.11	-1.86	5, 7, 9	301	19, 23
216956	113368	Fomalhaut	7.7	A4V	15.5	8195	2.06	4.17	0.10	5, 7, 8	200	28
17848	13141	ν Hor	50.5	A2V	15.7	8400	2.07	4.20	0.00	5, 7, 11	261	14, 15, 29
9672	7345	49 Cet	59.4	A1V	16.0	9000	2.07	4.30	0.10	12	36	13, 15, 29, 30
71722	41373	HR 3341	71.7	A0V	18.5	8925	2.16	4.29	0.00	13	100	10
182681	95619	HR 7380	69.9	B9V	24.9	10000	2.33	4.30	0.00	5, 7	73	15
14055	10670	γ Tri	34.4	A1Vnn	25.0	9350	2.33	4.19	0.00	5, 7	160	19
161868	87108	γ Oph	31.5	A0V	26.0	9020	2.36	4.12	-0.81	5, 7, 9	276	15, 17, 23
188228	98495	ϵ Pav	32.2	A0Va	26.6	10190	2.37	4.23	-0.04	5, 7, 8	50	19, 23
10939	8241	q2 Eri	62.0	A1V	31.3	9200	2.47	4.17	0.00	5, 7, 11	352	7, 15, 31
71155	41307	30 Mon	37.5	A0V	35.7	9770	2.56	4.06	-0.44	5, 7, 9	169	19, 23
172167	91262	Vega	7.7	A0V	51.8	9530	2.83	3.93	-0.43	5, 7, 9	265	23, 32
139006	76267	α CrB	23.0	A0V	57.7	9220	3.50^d	3.77	0.00	5, 7, 9	291	19, 23
95418	53910	β UMa	24.4	A1IVps	58.2	9130	2.70^e	3.76	0.06	5, 7, 9	305	19, 23
13161	10064	β Tri	38.9	A5III	73.8	8010	4.90^d	3.62	0.20	5, 7, 9	730	19

Notes:
The effective temperatures, metallicities and gravities are averaged over the listed literature values. ^{a}Gray-Corbally notation. See App. A2 in Trilling et al. (2007) for its explanation. The stellar masses were taken from the literature or computed from the luminosities by means of a standard relation $M \propto L^{1/3.8}$ if no mass value was given. Exceptions for other luminosity classes or close binaries are the following: ^{b}stellar mass from Moór et al. (2013a) (giant); ^{c} stellar mass from Bonsor et al. (2012) (subgiant); ^{d}sum of the stellar masses from Kennedy et al. (2012a) (close binaries); ^{e}stellar mass from Booth et al. (2013) (subgiant); ^{f}For each star with more than one age reference, the age given is the geometric mean of the values reported in those papers.

References:
[1] von Braun et al. (2011); [2] Torres (2010); [3] Valenti and Fischer (2005); [4] Eiroa et al. (2013) and references therein; [5] Gray (1992); [6] Holmberg et al. (2009); [7] Allende Prieto et al. (1999); [8] Gray et al. (2006); [9] Gray et al. (2003); [10] Duchêne et al. (2014); [11] Paunzen et al. (2006); [12] Roberge et al. (2013); [13] Morales et al. (2013).

Age references:
[1] Lestrade et al. (2012); [2] Engle and Guinan (2011); [3] Selsis et al. (2007); [4] Zuckerman et al. (2001); [5] Ortega et al. (2004); [6] Mamajek and Bell (2014); [7] Chen et al. (2014); [8] Dragomir et al. (2012); [9] Eiroa et al. (2013); [10] Morales et al. (2013); [11] Löhne et al. (2012); [12] Trilling et al. (2008); [13] Moór et al. (2006); [14] Rhee et al. (2007); [15] Moór et al. (2015); [16] Marois et al. (2010); [17] Chen et al. (2006); [18] Duchêne et al. (2014); [19] Vican (2012); [20] Beichman et al. (2006); [21] Moór et al. (2013a); [22] Moór et al. (2011); [23] Su et al. (2006); [24] Bonsor et al. (2012); [25] Bonsor et al. (2014); [26] Churcher et al. (2011a); [27] Song et al. (2001); [28] Acke et al. (2012); [29] Nielsen et al. (2013); [30] Roberge et al. (2013); [31] Morales et al. (2011); [32] Sibthorpe et al. (2010).

4.3.2 Far-infrared and sub-mm photometry

For the majority of targets in the sample the *Herschel*/PACS and SPIRE[2] (Griffin et al., 2010) fluxes were derived in the original papers, cited in Table 4.1. In contrast to Pawellek et al. (2014) this work includes five additional K-stars, whose data were not all published yet. Furthermore, there are different

---

[2] Spectral and Photometric Imaging Receiver

reduction methods employed by different groups and so the photometric data had to be derived for the first time or cross-checked. This was done by Jonathan Marshall (University of New South Wales) the following way. The data were reduced by using the *Herschel* Interactive Processing Environment (HIPE, Ott, 2010), user release 10.0.0 and PACS calibration version 45. From the Herschel Science Archive (HSA) the level 1 data, which means basic calibrated data, were obtained and processed by using the standard pipeline script with a pixel fraction of 1.0, a pixel size of $1''$ at 70 and 100 µm and $2''$ at 160 µm, respectively. Furthermore, it was adopted that the high pass filters had a width of 15, 20 and 25 frames. In order to avoid the skewing of the background measurement, a region with a radius of $20''$, which was centered on the expected star location, and other sources with a SNR ≥ 5 (as measured by sextractor in the observation's level 2 scan from the HSA), were masked from the high pass filtering process. The performance of the deglitching was done by the second level deglitching task which is appropriate for bright sources. If a target was observed with the two channel combinations of 70/160 and 100/160 the final mosaic was produced by the combination of the four 160 µm scans.

The usage of an IDL script based on the APER photometry routine from the IDL astronomy library[3] allowed the measuring of the flux densities. The radius of the flux aperture varied in the PACS images. This depended on the extent of the disc, which lied typically between $15''$–$20''$. The apertures were corrected in the way provided by Table 2 of Balog et al. (2013). For $15''$ aperture radius these are 0.829 at 70 µm, 0.818 at 100 µm, and 0.729 at 160 µm. For $20''$ aperture radius the correction factors are 0.863, 0.847 and 0.800, respectively. The sky background and the r.m.s. variation had to be estimated as well. This was done by the calculation of the mean and standard deviation of five square apertures with sizes which matched the same area as the apertures of the flux densities at each wavelength and for each target. At distances of $30''$–$60''$ from the source peak the sky apertures were now randomly scattered, whereas for Vega (HD 172167) and HR 8799 (HD 218396) these distances were larger since they have very extended discs. This was done in order to avoid the central region where the target disc lay and in order to avoid any identified background sources in the image. The apertures of $35''$ for sky boxes are many times bigger than a single native pixel of $3.2''$ and $6.4''$ at 100 µm and 160 µm, respectively. Therefore, a correction factor for correlated noise is not required and in addition there are sufficient numbers of apertures. Details of the noise measurement using multiple apertures can be found in Eiroa et al. (2013). For all three PACS bands a calibration uncertainty of 5% was assumed (Müller et al., 2011). It dominates in nearly all cases the total measured uncertainty of the target. An exception are the faintest sources with a flux density of less than ~ 150 mJy at 100 µm. Here, the sky noise can make a larger contribution to the total uncertainty in some cases.

The SPIRE flux densities were measured with aperture radii of $22''$at 250 µm, $30''$at 350 µm and $42''$at 500 µm. In contrast to the PACS instrument the sky background and r.m.s. were estimated by the usage of a sky annulus between $60''$–$90''$, which was centered in the source position, while a calibration uncertainty of 7.5%[4] was assumed for the three SPIRE bands.

As mentioned above, the resulting flux densities were compared with the ones reported in the literature if they were available. They agree within a $\sim 10\%$ range and thus, the derived flux densities of the K-stars, where no literature values exist can be used reasonably well. For all other targets the values were taken from the literature, since they are the result of detailed individual analysis rather than this more general approach given here. The photometric data can be found in Table A.2.

---

[3] idlastro.gsfc.nasa.gov

[4] Taken from SPIRE observer's manual, Sect. 5.2.12

5 Resolved disc radii

In the last chapter we selected 39 well resolved debris discs which shall form the basis of our statistical analysis. Nevertheless, we cannot start the SED modelling, since we do not know the disc radii. These are necessary to break the notorious degeneracy between radial and dust grain size parameters and thus we use the resolved images of each disc and identify the disc radii with the location of the maximum surface brightness. Furthermore, we assume that each disc ring is confined to a narrow annulus with an eccentricity equal to zero and a width of ±1% of the derived radius. For an Edgeworth-Kuiper-belt like dust ring (see Figure 1.1) the small width is understandable, since the region of the underlying planetesimal belt shelters the most emitting dust and is expected to be relatively narrow (e.g., Kennedy and Wyatt, 2010). In case of the warm component this assumption is necessary, since the flux densities and the photospheric subtraction in the mid-infrared possess large uncertainties.

The question now is what kind of images and which wavelength band should be taken to derive the disc radii. The decision fell on the *Herschel*-PACS[1] images (Poglitsch et al., 2010), since many debris discs could be resolved in at least one PACS band. This is important for the statistical purpose of this work, which requires homogeneity in terms of observational technique in order to avoid systematic discrepancies.

5.1 PACS images

The PACS instrument of *Herschel* (Pilbratt et al., 2010) allows the usage of three different wavelength bands, namely 70 µm, 100 µm and 160 µm. An example for a typical image is given in Figure 5.1, where the object HD 218396 (HR 8799) is shown in all three bands. From 70 µm to 160 µm the beam size is increasing, which means that the best angular resolution can be reached at 70 µm. At this band the disc radii can be derived with the best accuracy possible with PACS. On the other hand the 160 µm band can detect colder dust particles, refering to Wien's displacement law (Wien, 1896). Due to the size dependence of the grain temperature (see Figure 2.6) the colder particles are assumed to be larger in size. The larger grains are less affected by stellar radiation and have a low β value (see Section 2.2.2). Thus they better trace their parent planetesimals. We finally chose the 100 µm wavelength band, since it is the best compromise between the best angular resolution at 70 µm and the possibility of detecting the largest grains at 160 µm. Furthermore, for most of the discs the peak of the excess emission lies in the wavelength range of 100 µm. This minimises the stellar influence of the measured flux densities in this band. For the objects HD 9672 (49 Cet),HD 92945, HD 128311, HD 192263, HD 197481 (AU Mic) and HD 216956 (Fomalhaut) no *Herschel*/PACS images were taken at 100 µm. Therefore, 70 µm images are used to derive the disc radii for these targets.

The location of the maximum surface brightness is inferred from the peak of the source brightness profile measured by fitting a two dimensional Gaussian to the target. The values of FWHM are often given in the literature, but for this work they were recalculated. One reason for the recalculation is the care for comparability and homogeneity of the results by treating all objects the same way. A second reason is the lack of FWHM-values for some debris discs in the literature. At time of this writing some objects had no published data and in addition some data were only given in a reduced way. For

---

[1] Photodetector Array Camera and Spectrometer

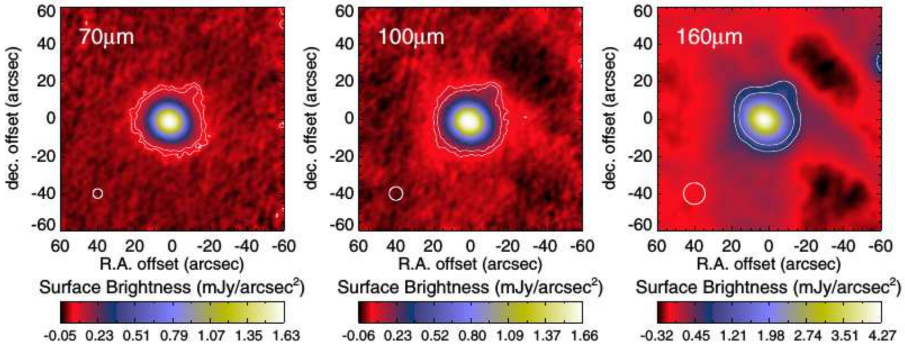

Figure 5.1: PACS images of HD 218396 in the 70 µm band (left), the 100 µm band (middle) and the 160 µm (right). The white circles in the bottom left corner of each panel show the beam size of the PACS bands. The pixel size is 1″ for 70 µm and 100 µm and 2″ for 160 µm. From: Matthews et al. (2014a).

instance, the point spread function (PSF) of PACS was already subtracted from the image and the method to derive the disc radii described in the next section would subtract the PSF for a second time and thus lead to wrong results.

5.2 Method description

The method to derive the disc radii from the resolved (PACS-) images was invented by Alexander Krivov (University of Jena) and Jonathan Marshall and works in the following way. A grid of fiducial discs is considered at a distance $d = 20$ pc from the observer. The outer disc radii vary between 10 and 210 AU with all in all 11 different values. The model ring width is supposed to be 10 AU, which is roughly consistent with the assumption of ±2% ring width for the sample (e.g., Strubbe and Chiang, 2006; Chen et al., 2006; Thébault and Augereau, 2007). Two extreme inclinations are assumed, namely face-on (0°) and edge-on (90°), but in general, the inclination of a disc is not well constrained (e.g., Booth et al., 2013; Greaves et al., 2014a). Therefore the chosen ones will deliver an upper and lower limit of the discs radii.

The signal-to-noise ratio (SNR) of the source influences the measured extent of the disc models in the grid. In order to test its degree of influence, the fiducial disc images are combined with a Gaussian noise component, covering a SNR-range from 5 to 100 considering the peak of the source. The lower SNR value represents the minimum necessary for the detection of the disc, whereas the upper value is chosen to mimic an “infinite” SNR which is limited by calibration uncertainties of the absolute flux density. It lies at $\sigma \sim 5\%$ for PACS (Balog et al., 2013). Using the definition of SNR $= F_\nu/\sigma$ the calibration uncertainty corresponds to a SNR of 20. On the other hand, the relative brightness of the disc compared to the root mean square of the background can be higher than 20. Hence, to cover all plausible disc extents, the upper value is set to 100.

Now, synthetic images of the discs at 100 µm are produced, for which the total disc flux density is set to 0.5 Jy. Looking at the flux densities of the sample of 39 resolved discs this is a good estimate, but here, we are using the brightest discs, i.e. the top end of the brightness distribution of debris discs and thus the model value chosen is not a typical value. The Edgeworth-Kuiper belt for instance is expected to have a flux density of 0.2 mJy at 100 µm which is an order of magnitude less than 0.5 Jy (e.g., Vitense et al., 2012; Bryden et al., 2009; Moro-Martín et al., 2015). However, since the effects of

SNR and the star-to-disc relative brightness are of interest and not the absolute brightness, the total disc flux density is not of importance.

The next step is the convolution of the disc models with the PSF of the PACS/100 band calibrated with the star α Boo. Furthermore, a stellar contribution is added at different $F_{\rm star}/F_{\rm dust}$ levels at 100 µm between 0 and 1. The resulting source brightness profiles are fit with a 2D Gaussian profile in order to find the FWHMs of the convolved synthetic images in the long-axis direction.

The final result is a grid of fiducial discs giving the FWHM as a function of $R_{\rm disc}/d$, orientation (edge-on or face-on), SNR and $F_{\rm star}/F_{\rm d}$. It is shown in Figure 5.2. Obviously, the SNR has only a small influence on the FWHM. The largest deviation of FWHM for SNR=5 and larger SNR lies within 3%. Hence, we will neglect it here. For small disc radii (up to 50 AU) the FWHM is dominated by the PSF of PACS and shows no significant increase with the disc radius. For larger disc radii the FWHM increases linear with it. In order to fit both, the constant and the linear part, we fit the FWHM with a quadratic function, which is shown in the right panel.

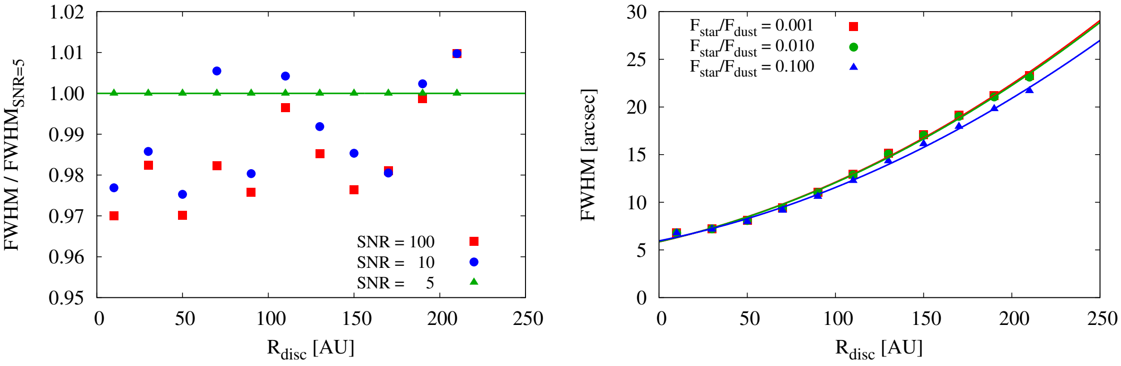

Figure 5.2: Resulting grid of fiducial discs. Left panel: FWHM divided by FWHM at SNR=5 as function of disc radius. Red squares represent SNR=100, blue circles SNR=10 and green triangles SNR=5. The green solid line shows the trend line through the green triangles. Right panel: FWHM as function of disc radius in the edge-on case for different values of $F_{\rm star}/F_{\rm dust}$: red squares $F_{\rm star}/F_{\rm dust} = 0.001$; green circles $F_{\rm star}/F_{\rm dust} = 0.010$; blue triangles $F_{\rm star}/F_{\rm dust} = 0.100$. Coloured solid lines show the best quadratic fit through the same coloured symbols.

After preparing the grid of fiducial discs, the observed 100 µm disc images of the 39 targets of the sample are fit by a 2D Gaussian profile. The resulting FWHM of the long axis is compared to the model FWHM of the grid (see Figure 5.2), which has the selected orientation (face- or edge-on) and the $F_{\rm star}/F_{\rm dust}$- ratio at 100 µm derived from the SED. Now, the inferred disc radius is corrected for the appropriate distance d stemming from HIPPARCOS catalogue (van Leeuwen, 2007). The inclinations of the observed discs vary between face-on and edge-on. Therefore, the mean value of the disc radii for both of these orientations is taken as the "physical" radius of the disc.

5.3 Results

In this section we are going to analyse the results of the method described above and applied to the sample of 39 resolved disc in order to identify possible biases or method constraints. Furthermore, we will investigate the accuracy of this method.

5.3.1 FWHM for major axes

As shown in Figure 5.3 and refering to the sample of 39 debris discs chosen for this work, more luminous stars tend to lie at larger distances from the observer than less luminous stars, while the FWHM of the discs around more luminous stars tend to be smaller than around less luminous stars. A consequence is that discs around A- or F-type stars are often less well resolved than discs around G-type stars, since they are smaller in angular size and therefore the determination of the disc radius could be more uncertain for them.

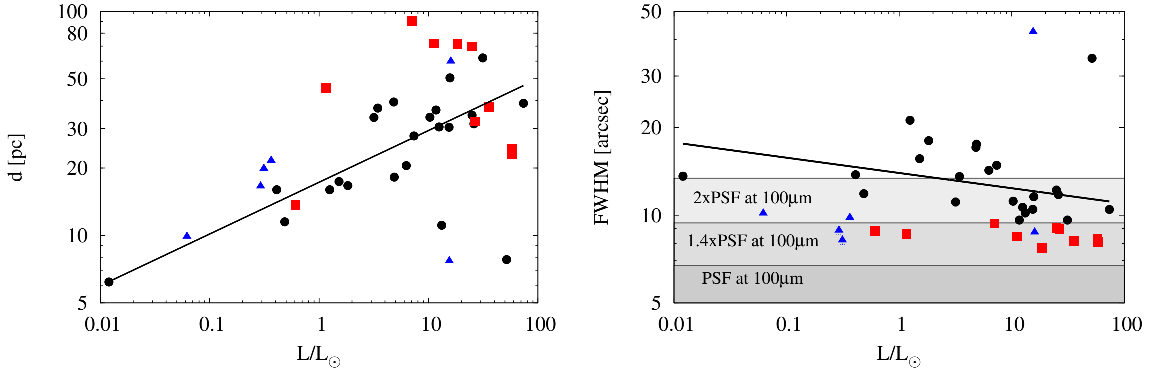

Figure 5.3: Distance to target (left panel) and long-axis FWHM at 100 µm (right panel) as function of stellar luminosity. Black circles represent well resolved discs, i.e. discs with FWHM $>$ 1.4 PSF; red squares show discs with FWHM $<$ 1.4 PSF; blue triangles show objects, where 70 µm images were used to derive the FWHM. Grey-shaded areas correspond to 1.0, 1.4 and 2.0 times the beam size of PACS at 100 µm. Here, 6.7″ is assumed for the PSF (PACS Observer's Manual[3]). Tilted straight lines are log-log best fits through the symbols.

5.3.2 Disc radii

The results of the radius derivation are listed in Table 5.1. The radii are compared with values given in the literature. In general, the derived disc radii are in good agreement with the literature values.

Possible biases

Figure 5.4 depicts the model results which are close to the values reported in the literature. Exceptions are GJ 581, HD 10647 (q^1 Eri), HD 27290 (γ Dor), HD 102647 (β Leo) and HD 172167 (Vega), since here, $R_{\rm disc}$ and $R_{\rm disc}^{\rm ref}$ (data from the literature) differ by more than 20%. We now consider a sample size of 37 targets, ignoring HD 166 and HD 192263 which only possess blackbody radii reported in the literature. Hence, the critical value of the correlation coefficient lies at 0.42 (see Chapter 2.3). Values larger than that show a statistically significant correlation. The comparison between radius deviation and stellar luminosity shows no significant trend ($r_{\rm Pearson}$ = 0.00 and $r_{\rm Spearman}$ = +0.21). The same applies to the correlations between radius deviation and FWHM ($r_{\rm Pearson}$ = 0.06 and $r_{\rm Spearman}$ = −0.03) or distance ($r_{\rm Pearson}$ = −0.06 and $r_{\rm Spearman}$ = −0.01), respectively.

This leads to the conclusion that the model does not invoke systematic biases by determining the debris disc radius and therefore it can be used without further constraints on resolved debris discs.

---

[3] http://herschel.esac.esa.int/Docs/PACS/html/ch03.html#sec-characteristics-photometer

Table 5.1: FWHM of sample objects derived from PACS images.

HD	Band	$L/L_\odot$	d [pc]	FWHM [arcsec]	$F_{\rm star}/F_{\rm d}$	$R_{\rm disc}$ [AU]	$R_{\rm disc}^{\rm ref}$ [AU]	Ref.
GJ 581	100	0.012	6.2	13.60 ± 0.41	0.150	38	31	1
197481	70	0.062	9.9	10.15 ± 0.05	0.000*	37	40	2
128311	70	0.29	16.6	8.87 ± 0.30	0.000*	58	52	3
192263	70	0.31	19.9	8.21 ± 0.25	0.000*	53	11**	4
92945	70	0.37	21.6	9.81 ± 0.04	0.000*	72	59	5
23484	100	0.41	16.0	13.76 ± 0.14	0.050	93	92	6
131511	100	0.49	11.5	11.85 ± 0.27	0.500	74	70	7,8
166	100	0.61	13.7	8.81 ± 0.09	0.150	40	8**	9
104860	100	1.16	45.5	8.63 ± 0.05	0.003	113	122	10
207129	100	1.25	16.0	21.15 ± 0.08	0.030	144	163	11
10647	100	1.52	17.4	15.62 ± 0.03	0.008	114	85	12
48682	100	1.83	16.7	18.01 ± 0.07	0.030	129	130	13
50571	100	3.17	33.6	11.09 ± 0.05	0.010	139	153	14
170773	100	3.44	37.0	13.57 ± 0.02	0.003	203	217	14
218396	100	4.81	39.4	17.08 ± 0.02	0.003	282	300	15
109085	100	4.87	18.2	17.51 ± 0.21	0.080	142	164	16
27290	100	6.27	20.5	14.25 ± 0.16	0.100	129	190	17
95086	100	7.04	90.4	9.35 ± 0.02	0.001	272	270	18
195627	100	7.36	27.8	14.83 ± 0.04	0.010	171	179	14
20320	100	10.3	33.7	11.16 ± 0.22	0.080	149	128	19
21997	100	11.2	71.9	8.46 ± 0.02	0.001	170	175	14
110411	100	11.7	36.3	9.62 ± 0.08	0.030	118	109	19
142091	100	12.5	30.5	10.64 ± 0.03	0.100	127	140	20
102647	100	13.2	11.1	10.17 ± 0.03	0.150	44	70	21
125162	100	15.4	30.4	10.47 ± 0.06	0.030	116	100	19
216956	70	15.5	7.7	42.57 ± 0.02	0.000*	127	138	22
17848	100	15.7	50.5	11.57 ± 0.07	0.010	223	232	14
9672	70	16.0	59.9	8.74 ± 0.01	0.000*	170	196	14
71722	100	18.5	71.7	7.71 ± 0.09	0.010	128	138	10
182681	100	24.9	69.9	9.03 ± 0.02	0.003	195	200	14
14055	100	25.0	34.4	12.19 ± 0.02	0.010	164	148	19
161868	100	26.0	31.5	11.76 ± 0.01	0.010	143	152	14
188228	100	26.6	32.2	8.97 ± 0.26	0.200	102	128	19
10939	100	31.3	62.0	9.62 ± 0.03	0.008	199	208	14
71155	100	35.7	37.5	8.15 ± 0.12	0.100	85	84	19
172167	100	51.8	7.8	34.51 ± 0.02	0.080	108	85	23
139006	100	57.7	23.0	8.28 ± 0.04	0.250	61	53	19
95418	100	58.2	24.5	8.09 ± 0.05	0.300	62	52	19
13161	100	73.8	38.9	10.46 ± 0.03	0.080	154	129	19

Notes:
Band gives the wavelength of the PACS image in microns and $F_{\rm star}/F_{\rm d}$ gives the flux density ratio at the wavelength used. Flux density ratios marked with (*) are set to zero, since for 70 µm no model with stellar influence exists. The disc radii $R_{\rm disc}$ are mean values of the face-on and edge-on values for each star while $R_{\rm disc}^{\rm ref}$ are the values reported in the literature cited under References. Radii marked with (**) are blackbody radii. Here, no "true" disc radii are given in the literature.

References:
[1] Lestrade et al. (2012); [2] Schüppler et al. (2015); [3] Moro-Martín et al. (2010); [4] Janson et al. (2013); [5] Schneider et al. (2014); [6] Ertel et al. (2014); [7] Kennedy (2015); [8] Marshall et al. (2014a); [9] Moro-Martín et al. (2015); [10] Morales et al. (2013); [11] Löhne et al. (2012); [12] Liseau et al. (2010); [13] Stapelfeldt et al. (in prep.); [14] Moór et al. (2015); [15] Matthews et al. (2014a); [16] Duchêne et al. (2014); [17] Broekhoven-Fiene et al. (2013); [18] Moór et al. (2013a); [19] Booth et al. (2013); [20] Bonsor et al. (2012); [21] Churcher et al. (2011a); [22] Acke et al. (2012); [23] Sibthorpe et al. (2010)

Radius correlations

The upper left panel of Figure 5.5 suggests that the disc radius is increasing with increasing distance to the host star with a slope of ∼ 1.3. It is understandable, that discs around distant stars and with a small radius cannot be resolved, since their angular size would be smaller than the beam size of the telescope. Hence, the empty right bottom area can be explained by an observational bias. On the other hand, the empty upper left area is not as easy to explain, since the discs in this area should be

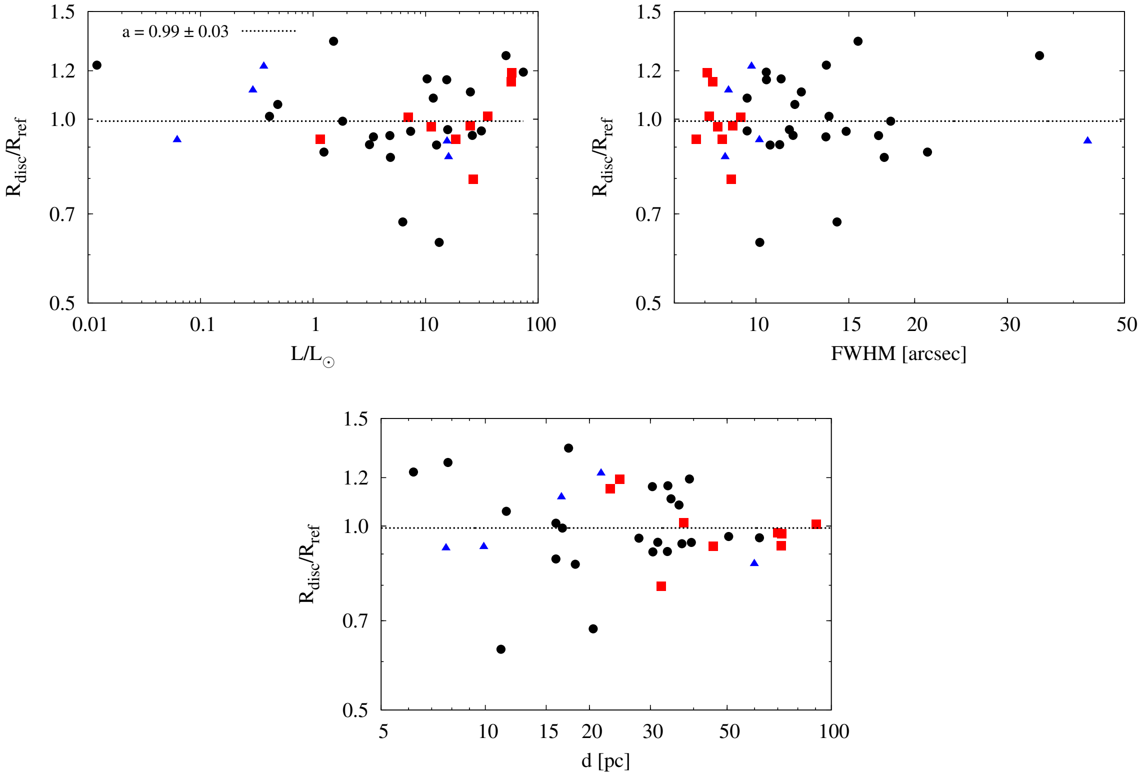

Figure 5.4: Upper left panel: The derived disc radius compared to the literature value as a function of stellar luminosity. Upper right panel: The derived disc radius compared to the literature value as a function of FWHM at 100 µm. Lower panel: The derived disc radius compared to the literature value as a function of distance. The straight dotted lines represent the constant fit to the symbols and the factor a gives the value for this line. Symbols are the same as in Figure (5.3). The objects HD 166 and HD 192263 were excluded here, since only the blackbody radii of the discs were given.

close to the Sun, should be larger in radius and therefore, should be easily resolvable. A possibility for the lack of such discs is given in the upper right panel of Figure 5.5. Most of the discs in the sample used have a size between 100 AU and 150 AU. Discs with larger radii are rare. So the probability of having discs with large radii in a short distance is very small and the empty area could be explained by a statistical effect due to a small sample size. Another possibility is that stars at a short distance (up to 20 pc) tend towards smaller stellar luminosities, which is shown in Figure 5.3. Hence, there are more low-luminosity stars with large discs in the solar neighbourhood. For such disc images the flux per pixel is too small to be recognised by the telescope, so these discs have too low a surface brightness for detection and therefore, the empty area is explainable by another kind of observational bias.

An interesting correlation is shown as well in the lower panel of Figure 5.5. Here, the inferred disc radii are shown as function of stellar luminosity. They vary between ≈ 40 AU and ≈ 280 AU, but no systematic increase exists. Indeed, the straight dotted line increases with stellar luminosity, however this result strongly depends on a few outliers, such as the two M-stars GJ 581 and AU Mic. The correlation coefficients confirm statistical insignificance ($r_{\text{Pearson}} = 0.52$ and $r_{\text{Spearman}} = 0.32$).

Considering the protoplanetary disc phase, it is assumed that a disc can be roughly divided into three regions: terrestrial planet formation (0-5 AU), giant planet formation (5-20 AU) and Edgeworth-Kuiper belt formation (> 20 AU). In addition, the first two regions are characterisable by condensation

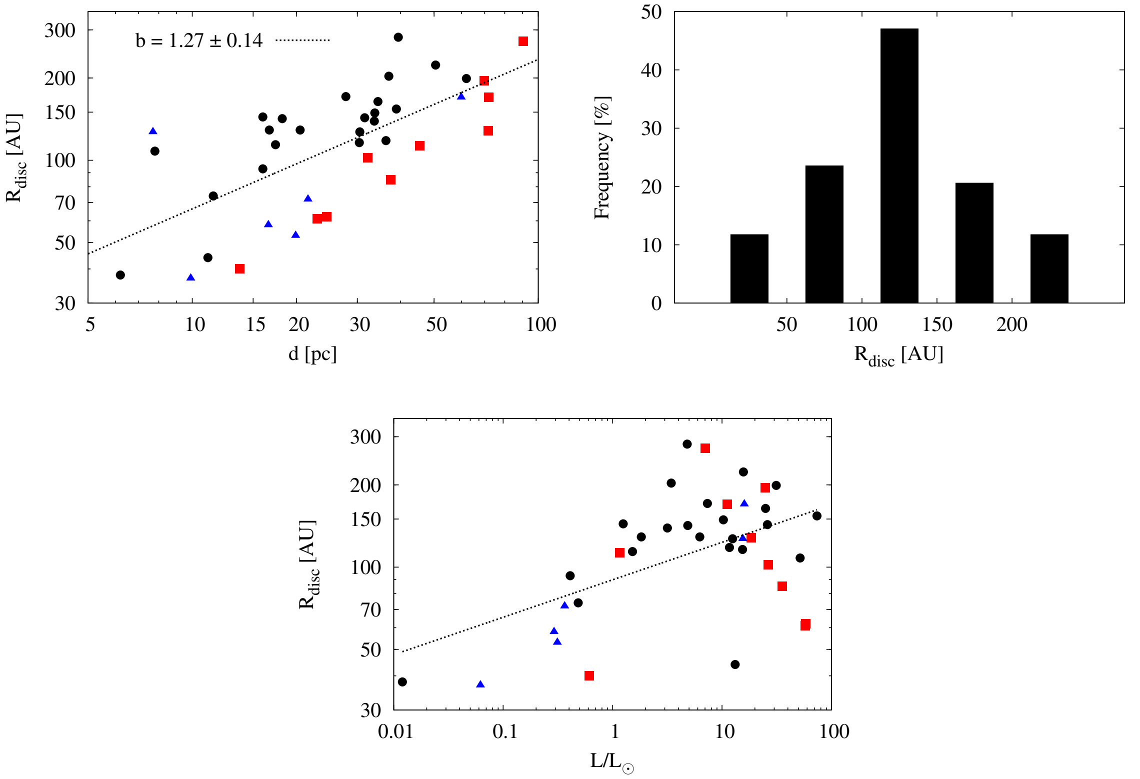

Figure 5.5: Upper left panel: Derived disc radius as a function of distance. Upper right panel: Frequency of the derived disc radii. Lower panel: Derived disc radius as a function of stellar luminosity. The straight dotted lines represent the best log-log fit to the symbols and the factor *b* gives the value for the slope. Symbols are the same as in Figure (5.3).

fronts (Pontoppidan et al., 2014, and references therein). Therefore, the formation of planets seems to be connected to the location of volatiles and snow-lines. This is supported by our own solar system, where the dry terrestrial planets lie close to the Sun while the icy giant planets are located further out. Hence, temperature-driven processes might play an important role for the planet forming regions, but refering to the absence of a correlation between disc radius and stellar luminosity it seems that the Edgeworth-Kuiper belt region and its final shape in the remaining debris disc depends on more dynamical processes. For instance a detailed collisional modelling of e.g., HD 207129 (Löhne et al., 2012) or Vega (Müller et al., 2010) showed their compatibility with a steady-state collisional cascade in a narrow planetesimal belt (Matthews et al., 2014a). This is supported by many discs giving evidence of narrow dust producing planetesimal rings (Strubbe and Chiang, 2006; Lestrade and Thilliez, 2015; Lagrange et al., 2016). Another dynamical process is the sculpting by planets which causes asymmetries in the disc emission, such as inclined warps, dense clumps or eccentric offsets (Matthews et al., 2014b). The discs around β Pic and Fomalhaut are an example for that. For both, the presence of a planet was predicted (Heap et al., 2000; Kalas et al., 2005; Quillen, 2006) based on their discs asymmetries, while the real planets were found later (Lagrange et al., 2010; Kalas et al., 2008). Furthermore, the proposed dominance of dynamical processes in shaping debris discs is consistent with Marshall et al. (2014b), who find that correlations between stars, discs and planets could be ascribed to dynamical effects rather than initial composition.

Caveats

Due to the large scatter of the disc radii no correlation between the disc radius and the stellar luminosity could be found in the sample. Nonetheless, a weak correlation found in earlier studies is possible (e.g., Eiroa et al., 2013). The scatter seems to be larger for more luminous stars, which may be explained by the fact that for the sample of this work more luminous stars are more distant on average (see Figure 5.3) and hence are less well resolved.

Besides the large scatter, the discs are approximated by a narrow ring with a single radius. This assumption could be too rough for some discs, which have an extended dust distribution. Analysing the disc width of a small sample of large and bright discs in scattered light images, Krist et al. (2012) found the width to vary between 20% and 60% of the ring radius. Furthermore, detailed studies of especially A-stars, such as Vega (Su et al., 2006) or HR 8799 (Matthews et al., 2014a), which were observed in several wavelength bands, reveal the presence of huge halos. These halos are probably composed of small dust grains in weakly bound orbits (Su et al., 2009; Sibthorpe et al., 2010; Löhne et al., 2012; Matthews et al., 2014a) and could lead to an incorrect measurement of the radius of the dust-producing planetesimal belt.

5.3.3 Estimation of errors

The derivation of the debris disc radii is subject to several uncertainties. At first, many debris discs are unresolved in the minor axis direction due to the relatively low spatial resolution of *Herschel* (at 100 µm the PSF is $6.7''$). In case of the 39 resolved discs chosen in this work, 12 objects have a FWHM of the minor axis smaller than 1.2 PSF. Therefore, a disc which is closer to edge-on could be mistaken as a face-on disc. In order to avoid this kind of problem we used the radius average between both cases of inclination, since the probability of a discs inclination being between 0° and 90° is much higher than being exactly 0° or 90°, respectively. On average the difference between face- and edge-on radius lies at 10%. Taking only the uncertainty of FWHM into account, the uncertainty of the derived radius is found to be $\sim 1\%$ on average. Another point is the SNR. It has only a little effect on the derivation of the disc radius and for all the discs of the sample it lies above 9 for flux densities at the 100 µm wavelength band. Hence, the uncertainty in the radius derivation due to SNR is $< 1\%$ (see Figure 5.2). The largest influence on the disc radius has the spectral fractional luminosity at 100 µm, which can be seen in Figure 5.2 as well. For most of the targets, it lies above 10, but for 5 objects this value is smaller. If we compare the resulting disc radii of a model with and without the spectral fractional luminosity the uncertainty is found to be $\sim 4\%$ on average.Including the measurement error of the FHWM at 100 µm of $\sim 4\%$ (Kennedy et al., 2012a) and totalising the before mentioned uncertainties of the stellar influence ($\sim 4\%$) and the SNR ($< 1\%$), the estimate of the radius accuracy is $\sim 8\%$.

In Figure 5.4 the derived disc radii show a deviation of $\approx 20\%$ from the values given in the literature. The question is whether this is consistent with an estimated radius accuracy of $\sim 8\%$. Therefore, we assume an uncertainty of the reference disc radii of $\sim 5\%$ based on values given by Booth et al. (2013). This seems appropriate since only a minority of radii stemming from the literature is given with uncertainties and the largest part of it was analysed by Booth et al. (2013) with 9 discs. Now, we compute the largest possible difference of the estimated and the reference radius. Assuming the reference radius is smaller compared to the derived one, than the reference radius is scaled down by 5% while the derived one is scaled up by 8%. The resulting new deviation of derived and reference radius lies on average at $\sim 26\%$, which is consistent with Figure 5.4.

6 Fitting results using the modified black-body and size distribution method

In the last chapter we analysed the debris disc sample considering the resolved disc radii. This part did not include any fitting of SEDs. On this we will catch up in this chapter. The beginning is made by the occurrence of one- and two-component systems. Then, we investigate possible correlations between the stellar luminosity and the disc temperature, the dominant grain size and the size distribution index or the opacity index, respectively. The best fit parameter values for the sample are given in the Tables 6.3 and 6.4 (SD method assuming pure astrosilicate).

Statistical values

In the further analyis of correlations between different debris disc parameters the number of resolved discs can variate. For example, the blowout grain size does not exist for all 39 targets chosen and so only 32 objects are taken into account in case of astrosilicate. Since we will use the correlation coefficients as a criterion for significant correlations Table 6.1 gives the critical values for different sample sizes.

Table 6.1: Critical values for statistical significance with a significance level of 0.01

Sample size	t_{critical}	r_{critical}
39	2.7154	0.408
37	2.7238	0.418
32	2.7500	0.449
31	2.7564	0.456
25	2.7969	0.504

6.1 Systems with one or two components

The Solar systems debris disc possesses not only the Edgeworth-Kuiper belt, but also the warmer Asteroid belt. Therefore, it is possible that discs around other stars are composed of two components as well. This work is concentrating on the outer Edgeworth-Kuiper belt like component though it is necessary to identify possible second asteroid belt like components in order to fit the disc SEDs properly. Using the criteria given in Chapter 3, Table 6.2 shows the results of this analysis. Pure astrosilicate is used as SD dust composition. A sublimation temperature of 1300 K is assumed as third criterion for both, the MBB dust material and the astrosilicate for reasons of comparability (e.g., Lamy, 1974; Defrère et al., 2011; Kobayashi et al., 2011).

In the sample of 39 resolved debris discs 23 discs reveal a second, warm dust component using the MBB method, whereas 21 discs do that using the SD method. These are roughly 59% or 54% of the sample respectively, which is in agreement with similar studies done before (e.g., Ballering et al., 2013; Chen et al., 2014). Figure 6.1 shows that a warm component can be present around low-luminosity

Table 6.2: Identification of the warm component

		MBB							SD						
		Excess				$\frac{\chi^2_{\rm one}}{\chi^2_{\rm two}}$	$R_{\rm warm}$	Warm comp.?	Excess				$\frac{\chi^2_{\rm one}}{\chi^2_{\rm two}}$	$R_{\rm warm}$	Warm comp.?
HD	$R_{\rm sub}$ [AU]	IRS22 [σ]	WISE22 [σ]	MIPS24 [σ]	IRS31 [σ]		[AU]		IRS22 [σ]	WISE22 [σ]	MIPS24 [σ]	IRS31 [σ]		[AU]	
GJ 581	0.01	-0.1	0.4	...	0.4	...	...	N	-0.1	0.4	...	0.3	...	...	N
197481	0.01	...	1.0	5.0	...	6.9	1	Y	...	0.7	1.4	...	...	...	N
128311	0.02	0.9	1.0	0.1	1.2	...	...	N	0.8	1.0	0.1	0.8	...	...	N
192263	0.03	-0.5	-0.7	-0.5	0.1	...	...	N	-0.8	-1.2	-1.1	-1.6	...	...	N
92945	0.03	0.8	2.3	0.1	0.8	...	...	N	0.8	2.8	0.0	0.3	...	...	N
23484	0.03	0.4	1.8	1.2	3.1	3.0	6	Y	0.4	1.8	1.2	0.8	...	...	N
131511	0.03	...	4.1	2.3	...	2.7	< 0.01	N	...	4.6	1.6	...	1.5	< 0.01	N
166	0.04	4.4	5.3	3.2	0.1	10.2	0.2	Y	5.2	6.1	3.4	-0.1	12.9	0.2	Y
104860	0.05	0.9	1.5	1.0	0.4	...	...	N	0.9	1.5	1.0	0.5	...	...	N
207129	0.05	2.4	2.2	-1.7	1.7	...	...	N	2.5	2.3	-1.4	3.6	1.3	14	N
10647	0.06	...	8.9	5.7	1.9	3.1	5	Y	...	-0.2	6.3	1.7	4.0	5	Y
48682	0.06	2.6	3.9	-1.1	3.6	1.1	9	N	2.3	3.7	-1.7	0.1	1.1	6	N
50571	0.08	0.04	1.3	-0.4	-0.9	...	...	N	0.0	1.4	-0.3	0.4	...	...	N
170773	0.08	1.3	2.6	1.7	2.1	...	...	N	1.3	2.6	1.7	2.4	...	...	N
218396	0.10	12.7	12.0	19.6	10.9	14.5	2	Y	12.8	12.1	19.9	13.8	17.4	3	Y
109085	0.10	7.6	...	13.4	...	37.4	3	Y	7.3	...	12.5	...	40.2	3	Y
27290	0.11	2.6	3.9	7.1	0.2	3.4	< 0.1	N	2.4	3.7	6.2	-0.4		< 0.1	N
95086	0.12	...	8.2	7.6	0.3	14.3	7	Y	...	8.9	9.3	0.5	12.5	7	Y
195627	0.12	6.6	6.6	1.3	6.2	9.0	1	Y	6.5	6.5	1.2	5.1	7.8	1	Y
20320	0.15	3.9	...	4.6	7.7	36.8	3	Y	3.9	...	4.6	7.8	45.9	7	Y
21997	0.15	...	7.2	12.3	5.0	34.8	24	Y	...	6.7	10.7	2.4	20.7	24	Y
110411	0.16	5.8	...	6.4	-0.7	4.7	6	Y	6.2	...	7.5	-0.5	5.5	6	Y
142091	0.16	...	-1.9	0.7	...	...	...	N	...	-4.6	-5.2	...	...	...	N
102647	0.17	8.3	...	10.6	...	48.3	1	Y	9.6	...	12.2	...	59.9	3	Y
125162	0.18	16.4	...	35.0	19.1	71.8	9	Y	13.6	...	23.6	6.7	32.4	9	Y
216956*	0.18	1.9	...	2.8	...	...	...	N	1.7	...	2.5	...	...	...	N
17848	0.18	1.6	8.7	7.6	3.7	9.9	19	Y	1.6	8.6	7.6	3.4	7.2	20	Y
9672	0.18	...	5.97	13.5	...	52.6	12	Y	...	5.2	0.6	...	5.2	12	Y
71722	0.20	15.7	12.5	17.4	23.4	205	5	Y	15.9	12.8	17.9	25.6	178	5	Y
182681	0.23	...	26.7	...	...	45.6	1	Y	...	24.8	...	...	145	1	Y
14055	0.23	17.1	...	15.3	26.1	41.7	26	Y	17.3	...	15.8	28.6	87.8	11	Y
161868	0.23	4.9	19.0	15.0	11.1	33.2	21	Y	4.3	17.3	12.5	4.7	19.9	26	Y
188228	0.24	1.7	...	-8.1	0.4	...	...	N	1.04	...	-22.1	0.0	...	...	N
10939	0.26	6.0	12.3	12.9	9.5	16.2	17	Y	6.2	12.6	13.6	11.4	22.3	17	Y
71155	0.27	7.5	...	15.0	-0.3	40.7	14	Y	8.4	...	17.4	-0.2	45.3	15	Y
172167*	0.33	...	...	8.3	...	1.8	31	N	...	...	11.7	...	2.8	10	N
139006	0.35	2.6	...	5.6	8.1	11.4	16	Y	3.0	...	5.8	0.3	4.1	18	Y
95418	0.35	1.7	-2.1	1.9	0.1	...	...	N	2.5	-1.5	3.3	0.1	1.1	< 0.1	N
13161	0.39	7.9	...	8.7	8.1	15.6	32	Y	8.4	...	9.5	9.7	13.3	51	Y

Notes:
(1) The sublimation radius, $R_{\rm sub}$, and the radius of the warm component, $R_{\rm warm}$, are given in AU. A sublimation temperature of 1300 K is assumed. (2)The columns IRS22, WISE22, MIPS24 and IRS31 give the "excess" in units of σ. That means the observed flux density minus the flux density of the cold component minus the flux density of the stellar photosphere. (3) If there is no significant MIR-excess, the objects were fitted with only a one-component model. For these objects no $\chi^2_{\rm one}/\chi^2_{\rm two}$ and $R_{\rm warm}$ are given. (*) With a more detailed analysis, including the full IRS spectra and other identification criteria than these given here, the object shows a existence of a warm component (Lebreton et al., 2013; Su et al., 2013b).

stars as well as around high-luminosity stars. For the MBB-method, 27% of all GKM-stars, 43% of all F-stars and 81% of all BA-stars analysed in this sample reveal a second component. This is comparable to the result given in Chen et al. (2014), where 45% of GKM-stars analysed, 69% of F-stars and 78% of BA-stars do that. The results given by the SD-method show similar frequencies except for the GKM-stars, where only 9% of the targets were found to reveal a second component with the criteria chosen. The differences between MBB, SD and the results found by Chen et al. (2014) can be explained by the different fit methods (Chen et al. (2014) used the BB method). Furthermore, the sample given by Chen et al. (2014) contains more targets. In general, both (MBB and SD) lead to similar but not identical results, which can be seen in Figure 6.2. Here, the SEDs of a typical one-component system (HD 50571) and a typical two-component system (49 Cet) are shown, for which both methods give equal results.

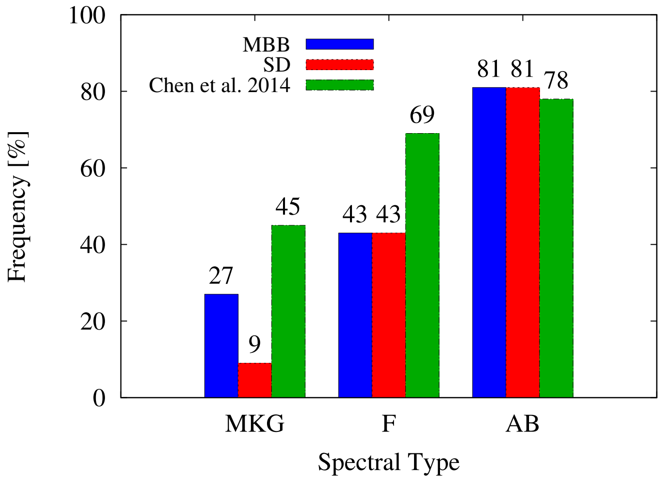

Figure 6.1: Frequency of a second component as a function of stellar spectral type. The sample used in this work contains in total 11 GKM-stars, 7 F-stars and 21 BA-stars. Green bars show results given by Chen et al. (2014), where 117 GKM-stars, 158 F-stars and 218 BA-stars were used.

However, with AU Mic another system is given, where a warm component may be present in case of the MBB method or absent in case of the SD method. An explanation for this is that the shape of the SED depends on the fitting method and shows different responses to the variation of fit parameters. The SED of the MBB model represents a Planck curve for $\lambda < \lambda_0$ while for the Rayleigh-Jeans part, where $\lambda > \lambda_0$, the decrease is steeper than for a normal blackbody. Therefore, a SED generated with MBB is narrower than a SED generated with a pure blackbody model. Furthermore, both wavelength parts are separated at λ_0, where an "artifical knee" can be seen in the SED. On the other hand, the SD model uses different sized particles and thus a temperature distribution and so allows smooth SEDs with both narrower and broader shape than a Planck curve with only one temperature (see Figure 6.2 bottom panels).

6.2 Dust temperatures and disc radii

6.2.1 Dust temperature

Definition

The first question arising from the fit is how to define the temperature of the debris disc in order to analyse possible temperature trends. Although small, the disc has a radial extension and should be warmer at the minimum radius and colder at the outer radius respectively. Furthermore, a size distribution of dust grains is assumed, which leads to different equilibrium temperatures in the stellar radiation field (see Figures 2.6 and 2.7). Hence, in order to describe a disc an effective temperature is necessary, which is in general not the same as the physical temperature of dust grains. The SONATA code (SEDUCE code with fitting tool (Müller et al., 2010)) used for both fitting methods requires the equality of the effective temperature derived from the SED and the dust grain temperature for the MBB method. Therefore, it gives a self-consistent solution in the MBB-case. However, there are several ways to define the disc temperature in case of the SD method. A possibility is using the physical temperature of the dust grains which is averaged over the grain sizes and weighted by the

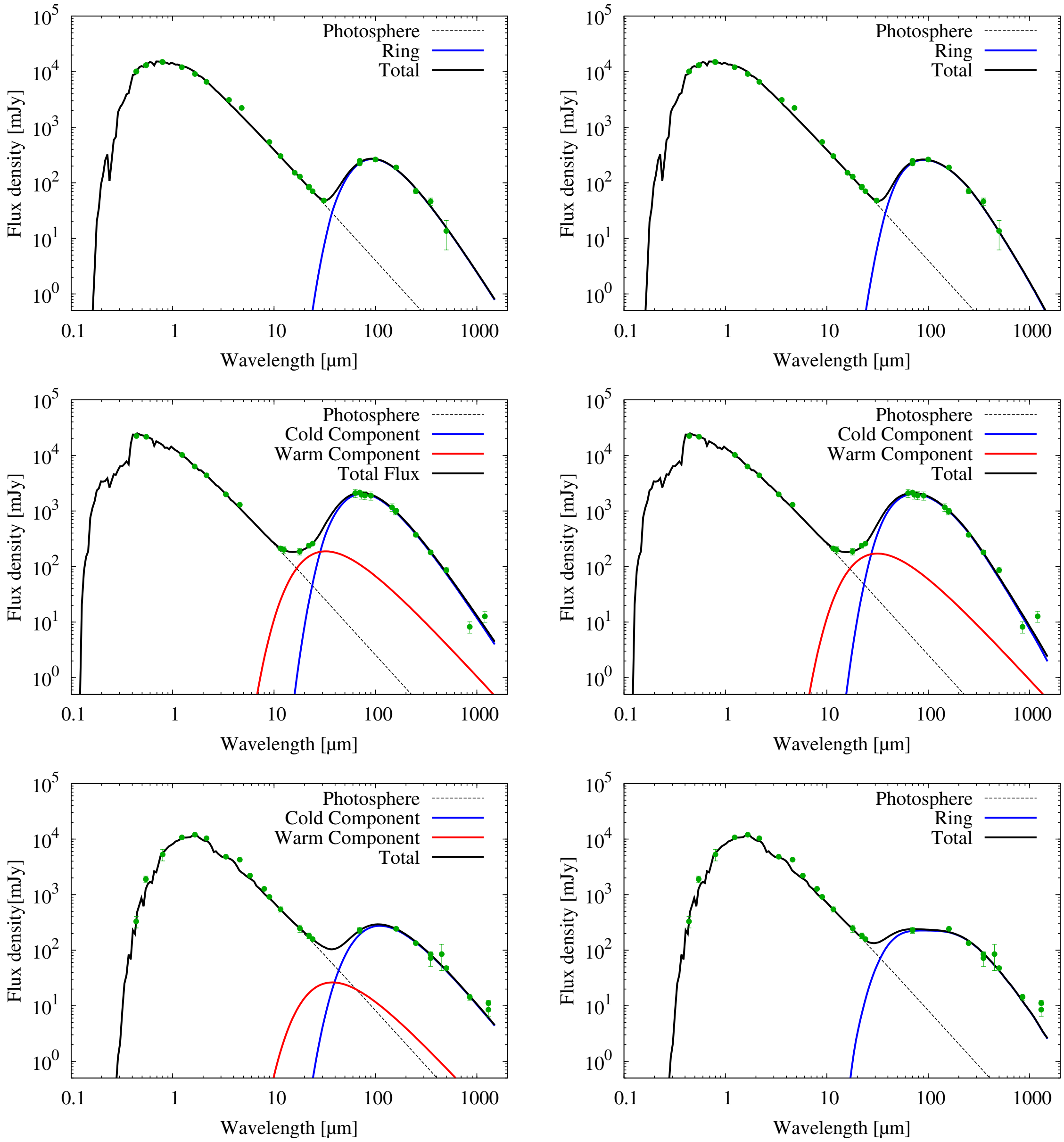

Figure 6.2: SEDs of HD 50571 (top), 49 Cet (middle), and AU Mic (bottom). Left panel: MBB method; right panel: SD method. Green filled circles with error bars show measured flux densities with their uncertainties.

contribution of particles to the total cross section of the disc. Nevertheless, we decided to use another definition in this work. We measure the wavelength of the discs maximum flux density, $\lambda_{\max}$, apply Wien's displacement law (Wien, 1896) and define the disc temperature as $T_{\mathrm{d}} \equiv 5100\ \mathrm{K}(\ \mu\mathrm{m}/\lambda_{\max})$.

Resulting correlation

The dust temperature as function of stellar luminosity is depicted in Figure 6.3 and shows a significant trend ($r_{\mathrm{Pearson}} = 0.70$ and $r_{\mathrm{Spearman}} = 0.70$). For the MBB method it increases from about 30-50 K for low-luminosity stars to 60-100 K for high-luminosity stars. Other *Herschel*-based studies,

Table 6.3: Fitting results for the MBB method

	Cold Component								Warm Component			
HD	R_{disc}	s_{blow}	T_{BB}	$\lambda_0/(2\pi)$	β	T_{d}	$T_{\mathrm{d}}/T_{\mathrm{BB}}$	f_{d}	R_{disc}	T_{d}	f_{d}	χ^2_{red}
GJ 581	38	...	15	0.88 ± 1.59	1.02 ± 0.33	33 ± 3	2.20 ± 0.19	6.62	...	...	...	1.08
197481	37	...	23	0.03 ± 0.25	0.30 ± 0.07	41 ± 2	1.81 ± 0.08	34.8	1	132	10.5	0.49
128311	58	...	27	12.67 ± 1.97	1.16 ± 0.14	31 ± 1	1.15 ± 0.04	2.79	...	...	...	1.70
192263	53	...	28	10.71 ± 1.77	2.14 ± 0.19	35 ± 2	1.23 ± 0.06	2.30	...	...	...	0.19
92945	72	...	25	5.44 ± 1.66	1.09 ± 0.15	35 ± 2	1.36 ± 0.06	58.3	...	...	...	2.72
23484	93	...	23	0.01 ± 0.98	0.24 ± 0.14	36 ± 1	1.59 ± 0.03	6.14	6	90	3.58	0.79
131511	74	...	27	0.01 ± 0.18	0.62 ± 0.13	100 ± 14	3.73 ± 0.54	2.40	...	...	...	7.50
166	40	...	39	5.20 ± 0.34	1.72 ± 0.09	53 ± 5	1.37 ± 0.13	4.61	0.2	512	21.3	1.15
104860	113	0.40	27	7.34 ± 1.37	0.88 ± 0.07	33 ± 1	1.24 ± 0.03	55.4	...	...	...	1.54
207129	144	0.44	24	0.44 ± 0.32	0.66 ± 0.07	44 ± 2	1.78 ± 0.07	8.89	...	...	...	3.87
10647	114	0.48	29	0.27 ± 0.36	0.48 ± 0.07	47 ± 1	1.63 ± 0.04	26.3	5	139	3.48	4.93
48682	129	0.54	28	0.02 ± 0.14	0.38 ± 0.07	52 ± 5	1.84 ± 0.18	6.56	...	...	...	7.71
50571	139	0.85	31	5.90 ± 1.77	0.96 ± 0.11	40 ± 2	1.27 ± 0.05	12.5	...	...	...	1.69
170773	203	0.92	26	4.77 ± 1.00	0.99 ± 0.08	36 ± 1	1.38 ± 0.04	52.3	...	...	...	2.73
218396	282	1.11	24	2.72 ± 0.53	0.92 ± 0.05	37 ± 3	1.52 ± 0.13	28.1	2	271	8.31	7.14
109085	142	1.24	35	21.65 ± 3.82	0.35 ± 0.06	35 ± 2	1.02 ± 0.05	1.48	3	256	14.2	1.78
27290	129	1.36	39	0.00 ± 0.11	0.30 ± 0.04	71 ± 6	1.84 ± 0.16	2.27	...	...	...	10.54
95086	272	1.44	27	0.03 ± 0.16	0.41 ± 0.07	51 ± 2	1.88 ± 0.09	134	7	166	16.3	0.83
195627	171	1.63	35	5.87 ± 0.57	0.97 ± 0.06	43 ± 4	1.24 ± 0.11	9.82	1	387	5.41	2.11
20320	149	2.11	41	5.20 ± 1.59	0.88 ± 0.10	49 ± 2	1.21 ± 0.05	1.40	3	270	1.76	0.54
21997	170	2.10	39	7.46 ± 0.90	0.96 ± 0.05	45 ± 1	1.16 ± 0.01	45.5	24	103	9.53	0.46
110411	118	1.69	47	6.30 ± 0.34	1.34 ± 0.09	57 ± 2	1.21 ± 0.04	4.58	6	208	3.05	4.93
142091	127	2.41	46	0.06 ± 0.49	0.28 ± 0.07	66 ± 4	1.42 ± 0.08	5.40	...	...	...	7.98
102647	44	2.42	80	4.62 ± 0.13	0.94 ± 0.04	89 ± 7	1.11 ± 0.09	2.39	1	465	4.89	16.78
125162	116	2.33	51	4.93 ± 0.39	0.80 ± 0.04	60 ± 1	1.17 ± 0.02	3.55	9	180	2.48	3.90
216956	127	2.76	49	5.51 ± 1.59	0.61 ± 0.12	55 ± 2	1.13 ± 0.03	7.36	...	...	...	3.17
17848	223	2.84	37	11.14 ± 1.18	1.05 ± 0.07	41 ± 1	1.10 ± 0.01	4.15	19	125	1.90	3.38
9672	170	2.78	42	5.09 ± 2.08	0.84 ± 0.07	52 ± 1	1.22 ± 0.02	72.1	12	157	18.2	0.38
71722	128	2.93	48	3.50 ± 0.72	0.74 ± 0.07	60 ± 2	1.26 ± 0.05	9.15	5	244	4.96	1.35
182681	195	3.98	44	1.03 ± 0.31	0.72 ± 0.07	68 ± 10	1.53 ± 0.22	26.0	1	545	7.87	6.18
14055	164	3.35	48	19.39 ± 0.68	1.18 ± 0.07	50 ± 1	1.02 ± 0.01	4.26	26	121	3.45	3.36
161868	143	4.30	52	12.92 ± 1.05	0.92 ± 0.06	55 ± 1	1.06 ± 0.01	5.86	21	137	3.51	2.71
188228	102	3.08	62	0.52 ± 0.88	0.30 ± 0.09	78 ± 2	1.26 ± 0.03	0.44	...	...	...	1.61
10939	199	4.83	46	7.48 ± 1.16	0.60 ± 0.05	51 ± 1	1.10 ± 0.02	7.34	17	161	1.83	4.14
71155	85	4.44	73	9.12 ± 0.24	2.42 ± 0.08	80 ± 1	1.09 ± 0.01	1.64	14	178	1.74	1.46
172167	108	7.84	61	23.24 ± 0.97	1.22 ± 0.05	73 ± 1	1.19 ± 0.01	1.45	...	...	...	6.04
139006	61	5.73	98	12.13 ± 0.53	1.87 ± 0.12	101 ± 1	1.03 ± 0.01	0.97	16	192	0.47	1.87
95418	62	7.50	97	10.89 ± 0.79	1.27 ± 0.17	100 ± 1	1.03 ± 0.01	0.95	...	...	...	5.41
13161	154	5.24	65	22.28 ± 0.67	1.39 ± 0.11	66 ± 1	1.00 ± 0.01	1.65	32	143	1.87	2.75

Notes:
(1) The disc radii are given in AU, the temperatures in K and $\lambda_0/(2\pi)$, s_{blow} in µm, the fractional luminosity in 10^{-5}. (2) For the values of s_{blow} the simplified equation of Burns et al. (1979) (see Equation (2.16)) was used with a material density of $\varrho = 3.3$ g/cm^3 and $Q_{\mathrm{pr}} = 1$. For stars with a luminosity less than 1 $L_\odot$ no blowout size is assumed. (3) The warm component is treated as blackbody. Therefore, the given R_{disc} and T_{d} are blackbody radius or temperature, respectively.

especially Booth et al. (2013) and Thureau et al. (2014), found similar results for A-stars for which the temperatures lie between 70 and 120 K or 40 and 290 K respectively. In contrast to that, Morales et al. (2011) used *Spitzer* data and give a median value for their sample of G-stars of 59 K while their sample of A-stars is given with 62 K. The trend found in this work is stronger compared to Morales et al. (2011), but roughly consistent as well.

In case of the SD method, the temperature increases with increasing stellar luminosity from 20-60 K to 50-120 K, but in contrast to the MBB method, the increase is not as steep, while in general the discs are slightly warmer. Nevertheless, the correlation is significant ($r_{\mathrm{Pearson}} = 0.59$ and $r_{\mathrm{Spearman}} = 0.56$).

6.2.2 Dust-to-blackbody-temperature ratio

Now, the disc temperature, T_{d}, is compared to the temperature a disc made of pure blackbodies would have (T_{BB}). Figure 6.4 shows a clear decrease of the temperature ratio with increasing stellar luminosity. The result of the MBB method shows a linear trend for the whole luminosity range

Table 6.4: Fitting results for the SD method

HD	Cold Component								Warm Component			χ^2_{red}
	R_{disc}	s_{blow}	T_{BB}	s_{min}	q	T_{d}	$T_{\mathrm{d}}/T_{\mathrm{BB}}$	f_{d}	R_{disc}	T_{d}	f_{d}	
GJ 581	38	...	15	1.60 ± 1.03	3.40 ± 0.21	25 ± 7	1.66 ± 0.48	8.46	...	...	...	0.78
197481	37	...	23	0.02 ± 0.26	3.34 ± 0.02	56 ± 9	2.47 ± 0.40	49.3	...	...	...	1.70
128311	58	...	27	2.27 ± 1.80	3.26 ± 0.17	35 ± 3	1.30 ± 0.10	3.19	...	...	...	1.56
192263	53	...	28	7.33 ± 1.32	5.39 ± 0.28	62 ± 7	2.17 ± 0.25	2.37	...	...	...	0.19
92945	72	...	14	5.57 ± 1.07	4.01 ± 0.19	49 ± 2	1.92 ± 0.06	57.4	...	...	...	2.78
23484	93	...	23	1.12 ± 0.82	3.37 ± 0.10	36 ± 3	1.59 ± 0.14	9.73	...	...	...	1.67
131511	74	...	27	0.10 ± 0.45	3.61 ± 0.11	92 ± 11	3.45 ± 0.41	1.19	...	...	...	12.13
166	40	0.32	39	3.32 ± 0.47	4.75 ± 0.32	91 ± 2	2.35 ± 0.06	4.68	0.2	512	20.9	1.12
104860	113	0.54	27	7.05 ± 0.34	3.88 ± 0.03	44 ± 1	1.63 ± 0.04	55.3	...	...	...	1.32
207129	144	0.56	24	4.95 ± 0.18	4.21 ± 0.03	56 ± 1	2.30 ± 0.01	8.33	...	...	...	5.63
10647	114	0.64	29	3.79 ± 0.22	3.85 ± 0.03	56 ± 1	1.95 ± 0.04	26.9	5	142	3.68	5.33
48682	129	0.72	28	2.05 ± 0.19	3.70 ± 0.03	62 ± 2	2.18 ± 0.06	7.23	...	...	...	3.00
50571	139	1.00	31	5.41 ± 0.70	4.00 ± 0.09	56 ± 2	1.79 ± 0.05	12.5	...	...	...	1.84
170773	203	1.05	26	4.97 ± 0.52	3.99 ± 0.05	53 ± 1	2.02 ± 0.05	52.8	...	...	...	3.33
218396	282	1.29	24	4.85 ± 0.25	3.98 ± 0.03	51 ± 1	2.09 ± 0.05	28.8	3	255	7.90	6.37
109085	142	1.34	35	10.90 ± 1.45	2.88 ± 0.09	36 ± 1	1.05 ± 0.03	1.40	3	235	13.1	1.53
27290	129	1.55	39	0.73 ± 0.20	3.36 ± 0.06	59 ± 5	1.53 ± 0.12	2.28	...	...	...	6.43
95086	272	1.65	27	2.73 ± 0.21	3.86 ± 0.04	62 ± 2	2.26 ± 0.05	137	7	170	17.3	1.23
195627	171	1.74	35	4.86 ± 0.20	4.00 ± 0.05	62 ± 1	1.77 ± 0.03	9.97	1	402	5.77	2.25
20320	149	2.18	41	7.07 ± 1.62	4.24 ± 0.27	62 ± 3	1.52 ± 0.08	10.6	7	187	1.37	0.44
21997	170	2.27	39	5.19 ± 0.56	3.97 ± 0.06	62 ± 2	1.59 ± 0.04	45.7	24	103	9.39	0.54
110411	118	2.34	47	4.10 ± 0.13	4.39 ± 0.06	87 ± 1	1.84 ± 0.02	4.50	6	217	3.19	4.90
142091	127	2.76	46	2.60 ± 0.29	3.63 ± 0.07	71 ± 3	1.55 ± 0.06	5.42	...	...	...	7.45
102647	44	2.57	80	4.13 ± 0.18	4.43 ± 0.11	110 ± 1	1.38 ± 0.02	2.11	3	300	2.65	18.38
125162	116	2.85	51	3.57 ± 0.20	3.85 ± 0.05	79 ± 2	1.54 ± 0.03	3.65	9	183	2.43	3.84
216956	127	2.89	49	4.07 ± 0.22	3.60 ± 0.04	65 ± 2	1.33 ± 0.03	7.29	...	...	...	2.80
17848	223	2.89	37	7.15 ± 0.74	4.10 ± 0.09	56 ± 2	1.52 ± 0.05	41.8	20	124	1.93	3.43
9672	170	2.92	42	3.83 ± 1.23	3.86 ± 0.11	71 ± 7	1.68 ± 0.17	75.4	12	161	17.0	0.97
71722	128	3.23	48	3.63 ± 0.19	3.92 ± 0.08	79 ± 2	1.64 ± 0.04	8.98	5	232	5.11	1.72
182681	195	3.94	44	2.24 ± 0.14	3.91 ± 0.06	87 ± 2	1.95 ± 0.05	25.8	1	525	7.47	1.72
14055	164	3.97	48	4.16 ± 0.20	3.64 ± 0.04	68 ± 2	1.41 ± 0.03	6.50	11	187	2.61	1.77
161868	143	4.07	52	6.87 ± 0.87	3.88 ± 0.09	68 ± 2	1.30 ± 0.05	5.23	26	122	4.03	2.87
188228	102	4.11	62	2.21 ± 0.26	3.44 ± 0.09	83 ± 3	1.33 ± 0.05	0.42	...	...	...	1.68
10939	199	4.64	46	4.97 ± 0.32	3.62 ± 0.04	62 ± 1	1.33 ± 0.03	7.35	17	159	1.84	3.34
71155	85	5.08	73	5.65 ± 0.15	6.61 ± 0.19	105 ± 3	1.43 ± 0.03	1.52	15	174	1.91	1.73
172167	108	6.58	61	13.10 ± 0.87	3.86 ± 0.06	59 ± 1	0.96 ± 0.01	1.19	...	...	...	9.12
139006	61	5.97	98	6.99 ± 0.23	5.47 ± 0.07	95 ± 2	0.98 ± 0.02	0.81	18	179	0.72	2.24
95418	62	7.73	97	5.21 ± 0.28	4.41 ± 0.13	110 ± 3	1.13 ± 0.03	1.02	...	...	...	5.34
13161	154	5.53	65	15.90 ± 0.53	5.23 ± 0.22	53 ± 1	0.82 ± 0.01	0.91	51	114	2.45	3.80

Notes:
(1) The disc radii are given in AU, the temperatures in K and s_{min}, s_{blow} in µm and the fractional luminosity in 10^{-5}. (2) For the values of s_{blow} the equation of Burns et al. (1979) (see Equation (2.16)) was used with a material density of $\varrho = 3.3$ g/cm^3. Q_{pr} was averaged over the stellar spectrum. (3) The warm component is treated as blackbody. Therefore, the given R_{disc} and T_{d} are blackbody radius or temperature, respectively.

($r_{\mathrm{Pearson}} = -0.63$ and $r_{\mathrm{Spearman}} = -0.66$), while the SD result reaveals that the trend is flattening for low-luminosity stars ($r_{\mathrm{Pearson}} = -0.59$ and $r_{\mathrm{Spearman}} = -0.66$). This is reported in the literature as well (Booth et al., 2013). The temperature ratios for stars with a stellar luminosity smaller than the Sun's are smaller than expected by the log-log trend chosen, whereas it is a good approximation in the MBB case. A possible reason are the absorption properties of the small astrosilicate grains depicted in Figure 2.3. Here, the absorption efficiency drastically decreases in the visible wavelength range. Hence, the smallest particles become colder (Krivov et al., 2008) than grains slightly larger and in case of low-luminosity stars, such as GJ 581 or HD 128311, this leads to smaller temperature ratios.

6.2.3 Dust-to-blackbody-radius ratio

In Chapter 5, we discussed a possible correlation between the resolved disc radius and the stellar luminosity. Therefore, the disc radius should now be compared to the blackbody radius of a debris disc, analogue to the temperature considerations before. Here, the blackbody radius is the radius

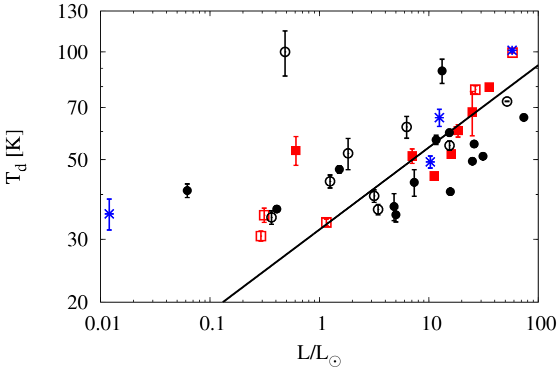

Figure 6.3: Dust temperature as a function of stellar luminosity. Left: MBB method; right: SD method. Open and filled symbols represent one- and two-component disc systems. Circles stand for well-resolved discs, squares for marginally resolved ones. Blue asterisks are objects, where no (sub-) millimetre detections exist. The line shows the best linear log-log-fit to the data points.

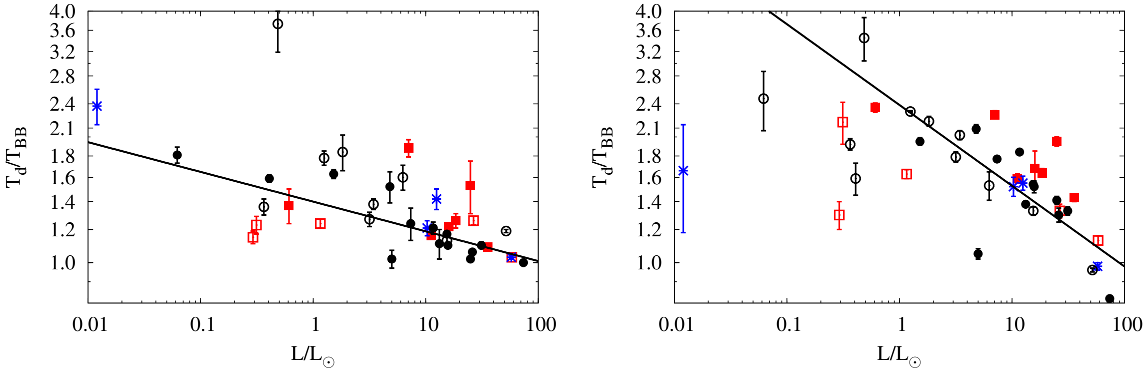

Figure 6.4: Dust to blackbody temperature ratio as a function of stellar luminosity. Left: MBB method; right: SD method. Open and filled symbols represent one- and two-component disc systems. Circles stand for well-resolved discs, squares for marginally resolved ones. Blue asterisks are objects, where no (sub-) millimetre detections exist. The line shows the best linear log-log-fit to the data points.

which a disc at a certain temperature made of pure blackbodies would have.

At the “true” disc radius, $R_{\rm disc}$, the dust has an effective temperature, $T_{\rm d}$. If we assume that the dust can emit like a blackbody, a blackbody temperature, $T_{\rm BB}(R_{\rm disc})$, exists as well. Using Equation (2.29) it is obvious that $R_{\rm disc} \propto T_{\rm BB}^{-2}(R_{\rm disc})$. On the other hand, the dust has a certain effective temperature at a certain disc radius. Assuming blackbody grains again, there is of course a blackbody radius, $R_{\rm BB}(T_{\rm d})$, for which Equation (2.29) is also valid and leads to $R_{\rm BB}(T_{\rm d}) \propto T_{\rm d}^{-2}$. Therefore, by analysing the trend of $T_{\rm d}/T_{\rm BB}$, we can analyse the radius ratio as well since

$$\frac{R_{\rm disc}}{R_{\rm BB}(T_{\rm d})} = \frac{T_{\rm BB}^{-2}(R_{\rm disc})}{T_{\rm d}^{-2}} = \left(\frac{T_{\rm d}}{T_{\rm BB}}\right)^2 \equiv \Gamma. \tag{6.1}$$

The result is that the dust-to-blackbody-radius ratio decreases with increasing stellar luminosity, like the temperature ratio does. A similar study was done at first for A-stars by Booth et al. (2013) who found Γ decreasing from about 2.5 to 1.0 in a luminosity range between 10 and 100 $L_\odot$. This was followed by a study from Morales et al. (2013) who used a larger sample over a broader luminosity range and included the targets from Booth et al. (2013). They found Γ decreasing from about 9 at $L \approx 0.01\ L_\odot$ to 4 at $L \approx 1\ L_\odot$ and 1 at $L \approx 100\ L_\odot$.

Knowing the correlation between Γ and the stellar luminosity, a possibility of estimating the "true" disc radius of an *unresolved* debris disc opens up. The detailed description of this method can be found in Chapter 8.

6.2.4 Fractional luminosities and disc radii

The correlation between fractional luminosity and disc radius was investigated and there seemed be to a trend between both parameters. In order to explain this, the role of fractional luminosity as lower limiting case for observations and as upper limiting case for collisional evolution is taken into account (see Chapter 2). In Figure 6.5 the upper grey areas show the maximum fractional luminosity for three stars of 1 $L_\odot$, 3 $L_\odot$ and 15 $L_\odot$ calculated by Equation (2.41). All three stars are assumed to have an age of 30 Myr. The grey areas show a clear increase with the disc radius and thus, a correlation of fractional luminosity and disc radius could be justified with the model of maximum fractional luminosity. The lower areas give the minimum fractional luminosity necessary in order to detect the debris disc. The same stellar luminosities were used and a minimum flux density of $F_\nu = 5.5$ mJy[1] was assumed for PACS at 100 µm. Here, an increase of the fractional luminosity with increasing disc radius could be justified as well. And indeed, the targets lie in the area between maximum and minimum fractional luminosity. However, the correlation coefficients do not confirm the correlation (MBB: $r_{\text{Pearson}} = 0.34$ and $r_{\text{Spearman}} = -0.37$; SD: $r_{\text{Pearson}} = 0.31$ and $r_{\text{Spearman}} = 0.34$) due to the strong scatter of the stellar luminosity of the targets.

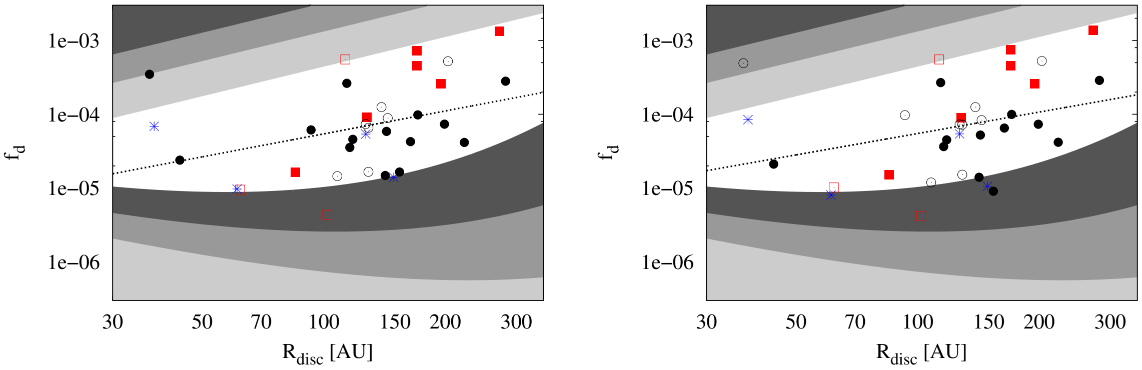

Figure 6.5: Fractional luminosity as a function of disc radius. Left: MBB-method; right: SD-method. Black circles show well resolved objects with an FWHM > 1.4PSF; red squares show objects with an FWHM < 1.4PSF and blue triangles show objects where the radii were derived from 70 µm images. The straight dotted line is the best log-log fit through the data points and the grey areas give the areas for the maximum and minimum fractional luminosity possible for a star of 1 $L_\odot$ (dark grey), 3 $L_\odot$ (middle grey) and 15 $L_\odot$ (light grey). Further explanation see in the text.

Wyatt et al. (2007a) applied their model to a sample of Sun-like stars and found the fractional luminosities measured for these systems to be much higher than the expected maximum fractional

---

[1] PACS Observer's Manual, Version 2.5.1; http://herschel.esac.esa.int/Docs/PACS/html/pacs_om.html

luminosities. An explanation was the transience of dust produced in stochastical processes, e.g., the collision of two massive protoplanets (Song et al., 2005) the sublimation of a supercomet (Beichman et al., 2005) or the sublimation of a swarm of comets (Gomes et al., 2005). In our sample of resolved discs no evidence for such processes could be found since all fractional luminosities lie below the expected maximum fractional luminosities.

6.3 Grain sizes

After analysing the disc temperatures and radii we now come to the grain sizes. We will start with an investigation of the blowout grain size, which is followed by the minimum grain size or characteristic grain size respectively.

6.3.1 Blowout grain size

As defined in Chapter 2, the blowout grain size of a certain dust material is reached, when β of Equation (2.16) is equal to a value of 0.5. The parameter β depends on the stellar luminosity, the stellar mass, the bulk density of the dust material and the radiation pressure efficiency. For low-luminosity stars, β never reaches this value and thus no particles are expelled from the circumstellar system due to radiation pressure. In Figure 6.6 the β-parameter is shown as a function of grain size.

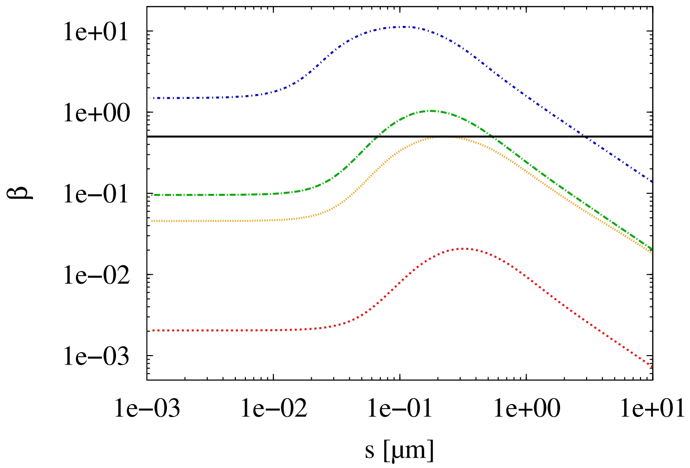

Figure 6.6: β-parameter as a function of grain size. The red dotted line represents GJ 581, the orange small dotted line HD 166, the green dash-dotted line HD 104860 and the blue small dash-dotted line HD 9672. The solid black line lies at a value of 0.5. Pure astrosilicate was used, except for HD 166, where a mixture of astrosilicate and ice was applied.

For all objects represented here, β reaches a maximum value at a certain grain size and becomes constant towards smaller grain sizes. Towards larger sizes it continues to decrease. For GJ 581, the object with the lowest luminosity in the sample, β lies always below 0.5 and thus no blowout grain size exists. In case of HD 104860, which has a luminosity comparable to the Sun, β increases and exceeds the value of 0.5. Then it decreases below 0.5 again. Therefore, two blowout grain sizes exist. The target HD 166 has a smaller luminosity than HD 104860 and here, β reaches 0.5 once at its maximum point. Theoretically, two blowout grain sizes exist here as well, but both lie at the same value. HD 9672 (49 Cet) is a high-luminosity target. The constant value of β at small grain sizes lies above 0.5. Towards larger sizes, it decreases and falls below 0.5 for the first time. As a result, there is only one blowout grain size for this object. In general we can say that objects with lowest luminosities do not owe a blowout grain size, while targets with moderate stellar luminosity possess two of them. In contrast, the high-luminosity objects only have one blowout size. In Figure 6.7 the resulting blowout sizes are given for the sample of 39 resolved debris discs. Some apparent outliers reflect the fact that $s_{\rm blow}$ for any individual star depends on $Q_{\rm abs}$ and $Q_{\rm sca}$ averaged over the stellar photospheric spectrum of that particular star. For example, κ CrB with $L/L_{\odot} = 12.5$ is a K1-subgiant with a temperature twice lower than that of its neighbouring stars in the figure. This results in the larger averaged values of $Q_{\rm abs}$, $Q_{\rm sca}$, and $s_{\rm blow}$ compared to its neighbours. For still other stars and particular grain compositions, the stellar spectrum peaks at the maxima of the resonant oscillations of

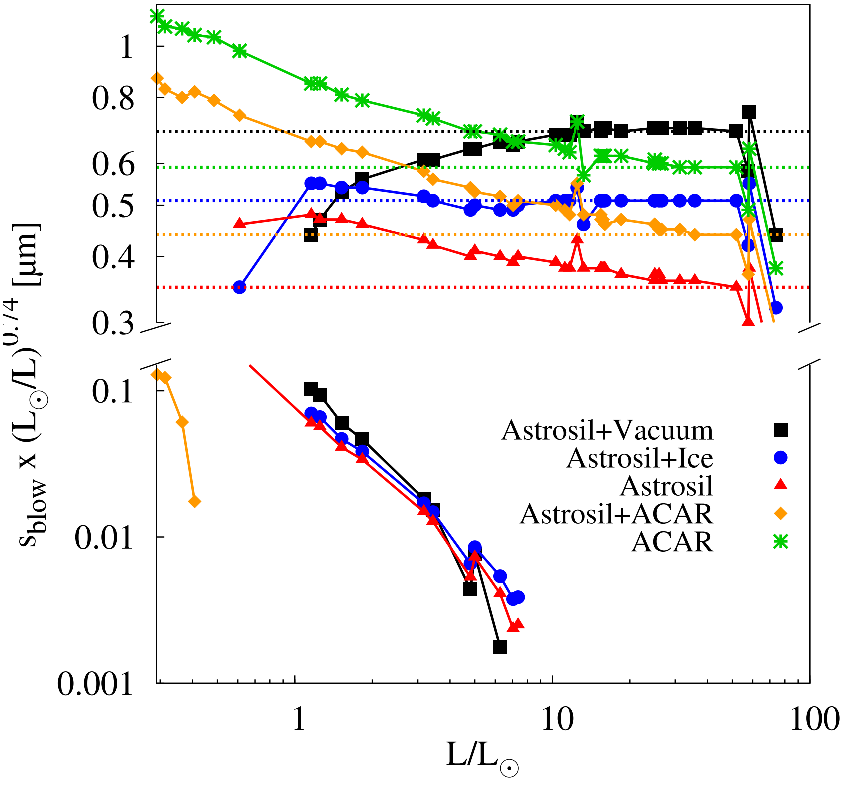

Figure 6.7: Blowout grain size, multiplied with $(M/M_{\odot})/(L/L_{\odot})$ as a function of stellar luminosity. Different colours correspond to different dust compositions, as indicated in the legend. Symbols with connecting solid lines: results for size- dependent $Q_{\rm pr}$ obtained with Mie-theory and for actual stellar masses from Table 4.2; horizontal dashed lines results for $Q_{\rm pr} = 1$ and assuming the main-sequence mass-luminosity relation. The vertical offset between the symbols and lines that represent different compositions is caused by their different bulk densities (see Table 2.1). For stars with $L_{\odot} \lesssim L \lesssim 10L_{\odot}$, except for pure carbon, the second blowout limit appears in the bottom part of the plot. Grains in blowout orbits are those between the upper and lower branches. For the low-luminosity stars in the sample (HD 92945, HD 128311, HD 131511 and HD 192263 with $L < 0.49L_{\odot}$) the upper blowout limit only exists for carbon and the mixture carbon and astrosilicate, while the lower blowout limit does only exist for astrosilicate and carbon. The strongest outliers amongst the symbols are stars with masses departing from the main-sequence mass-luminosity relation. These are the A1-subgiant β UMa with $L/L_{\odot} = 58.2$ and the close binaries α CrB ($L/L_{\odot} = 57.7$) and the A1III-star β Tri ($L/L_{\odot} = 73.8$).

the Mie-calculated $Q_{\rm abs}$ and $Q_{\rm sca}$, which also makes $s_{\rm blow}$ different from that of the adjacent stars. This is particularly the case for β Leo with $L/L_\odot = 13.2$, if the astrosilicate-ice and astrosilicate-carbon mixtures are assumed (Pawellek and Krivov, 2015).

6.3.2 Minimum grain size

The next dust parameter investigated was the minimum grain size or characteristic grain size respectively. Our expectation was that it would increase with increasing stellar luminosity, like the blowout grain size (see Equation (2.16)) does. As shown in Figure 6.8 the results of the MBB method lead to such an increase ($r_{\rm Pearson} = 0.46$ and $r_{\rm Spearman} = 0.47$), whereas the SD method with pure astrosilicate gives a much weaker trend ($r_{\rm Pearson} = 0.54$ and $r_{\rm Spearman} = 0.36$), which is also consistent with a constant grain size of roughly 5 µm.

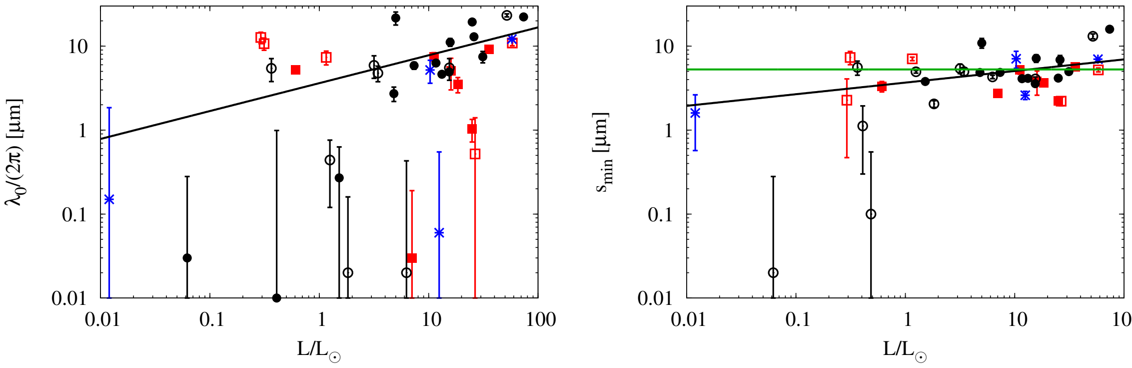

Figure 6.8: Minimum grain size as a function of stellar luminosity. Left: MBB method; right: SD method. Symbols are the same as in Figure 6.3. The green line shows a constant fit to the symbols of the SD method.

Considering the MBB result there are many objects for which the characteristic grain size is smaller than 1 µm and thus smaller than the shortest wavelength of 10 µm used for fitting. It is thinkable that for such objects the λ_0 cannot exactly be determined, since it lies not in the wavelength range of the SED, but nevertheless it is possible. Here, for all wavelengths included in the fitting process, a decrease of the absorption efficiency is assumed due to $Q_{\rm abs} = (\lambda/\lambda_0)^{-\beta_{\rm mod}}$, while λ_0 gives the starting point and $\beta_{\rm mod}$ the steepness of the decrease. Thus, the absorption efficiency is clearly defined for all λ_0, but since the cutoff wavelength lies not in the wavelength range of the disc's SED no artificial "knee" can be seen in it.

We assume the relation $\lambda_0 = 2\pi s_{\rm min}$ given in Backman and Paresce (1993) for the grain sizes derived from the MBB method. To check whether this is a good estimate we compared the dominant grain sizes of both methods with each other (see Figure 6.9). If the characteristic grain size is $0.01\,\mu{\rm m} < \lambda_0/(2\pi) < 0.1\,\mu{\rm m}$ the minimum grain size, $s_{\rm min}$ differs more than one magnitude from the MBB result for most of the targets. This deviation decreases for larger $s_{\rm min}$. This means if the characteristic MBB grain size is smaller than 1 µm the correlation between λ_0 and $s_{\rm min}$ is less reliable.

6.3.3 Minimum-to-blowout grain size ratio

The blowout grain size increases with increasing stellar luminosity (see Equation (2.16)) and it was expected that the dominant dust grain size behaves in a similar way. However, we found that at least

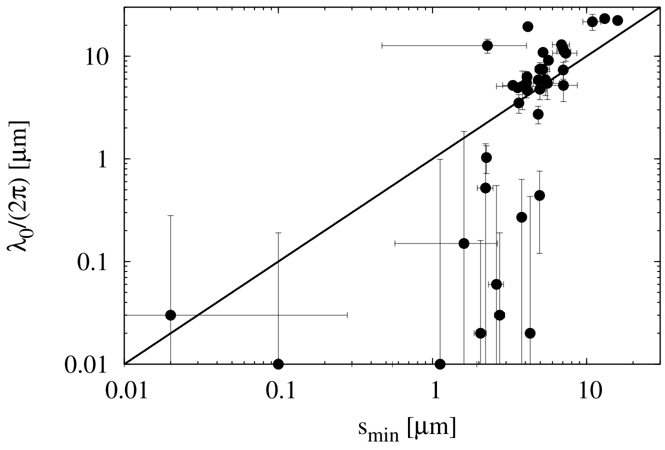

Figure 6.9: Characteristic grain size of the MBB method as a function minimum grain size of the SD method with pure astrosilicate. The solid black line shows where $\lambda_0/2\pi = s_{\mathrm{min}}$.

for the SD method with pure astosilicate the grain size shows a trend which is not as steep as it should be. In Figure 6.10 the ratio of the minimum grain size and the blowout grain size is given as a function of stellar luminosity. Since the blowout grain size does not exist for the low-luminosity targets, the sample contains now 32 objects. There is a clear decrease towards higher luminosities from ~ 10 for solar-type stars to unity for A- and B-type stars in the SD method. Since the MBB method shows a stronger correlation between characteristic grain size and stellar luminosity the trend of the grain size ratio is statistically insignificant ($r_{\mathrm{Pearson}} = -0.04$ and $r_{\mathrm{Spearman}} = -0.13$), while for the SD method it is the strongest correlation found in this work ($r_{\mathrm{Pearson}} = -0.81$ and $r_{\mathrm{Spearman}} = -0.77$). As explained before, there are some objects for which the characteristic grain size of the MBB method is very small and hence a bad estimate for the minimum grain size. If the objects with such small characteristic particle sizes are excluded 25 targets with luminosities between 0.6 $L_{\odot}$ and 74 $L_{\odot}$ remain in the sample and the correlation turns out to be significant now ($r_{\mathrm{Pearson}} = -0.83$ and $r_{\mathrm{Spearman}} = -0.54$). There is

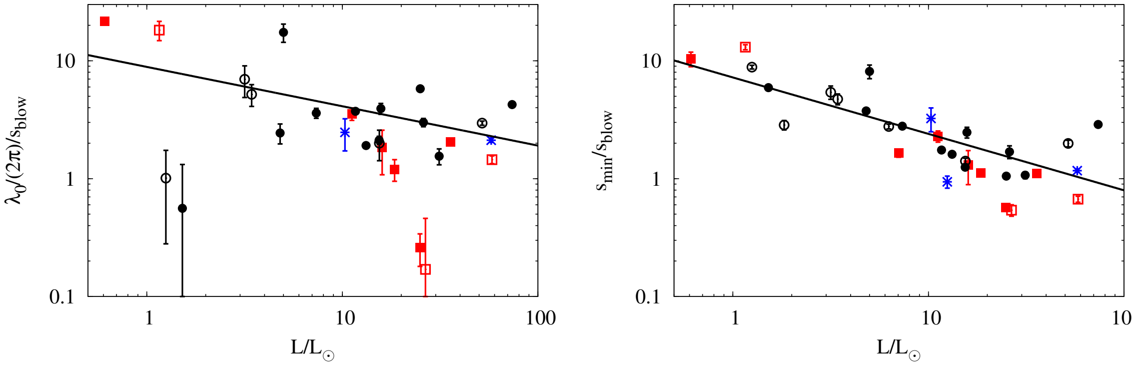

Figure 6.10: Characteristic grain size of the MBB method (left) and minimum grain size of SD method (right) in units of the blowout grain size as a function of stellar luminosity. Symbols are the same as in Figure 6.3.

a trend from ∼ 10 for solar-type stars to unity for A- and B-type stars as well, however the correlation is not as strong as for the SD method.

Although this trend was first reported in Pawellek et al. (2014) previous studies confirm the deviation of the minimum grain size from the blowout grain size for individual debris disc systems (Su et al., 2009; Krist et al., 2010; Golimowski et al., 2011; Kirchschlager and Wolf, 2013; Morales et al., 2013) and even the decrease with increasing stellar luminosity can be found combining the results of the individual systems. Nevertheless, this trend was not expected by theory. Therefore, we investigated several possibilities in order to explain it. These are described in Chapter 7.

6.4 Opacity index and grain size distribution index

We now come to the size distribution index or the opacity index, respectively. In Figure 6.11 these parameters are presented as a function of stellar luminosity. The opacity index varies between 0 and 2.5, while for the most discs it lies between zero and unity. Previous studies (e.g., Williams and Andrews, 2006; Nilsson et al., 2010) show similar results. There seems to be a trend of β_{mod} increasing with the stellar luminosity, However, this is not confirmed by the correlation coefficients ($r_{\mathrm{Pearson}} = 0.21$ and $r_{\mathrm{Spearman}} = 0.26$). As well there seems to be a slight increase of the size distribution index with the stellar luminosity, but here the correlation coefficients do not confirm this as well ($r_{\mathrm{Pearson}} = 0.32$ and $r_{\mathrm{Spearman}} = 0.28$). The q-parameter varies between 2.8 and 6.5, although for most targets it lies between 3 and 4. A value of 3.5 is predicted by theory (Dohnanyi, 1969) and other studies show similar results for individual objects (e.g., Augereau and Beust, 2006; Donaldson et al., 2013; Lebreton et al., 2013). Compared to Pawellek et al. (2014) the largest values of 6.5 are even larger than the 5.5 reported there. The reason is an improvement in the fitting algorithm which led to smaller χ^2. Such large q-values were reported in the literature before (e.g., Ertel et al., 2012; Riviere-Marichalar et al., 2014). Ertel et al. (2012) even found values of 9 for HD 199260 or 10 for HD 206860, respectively. They stated that these debris discs show evidence for a deviation from the standard equilibrium collisional cascade, however, the results depend very much on the photometric data reduction pipeline used.

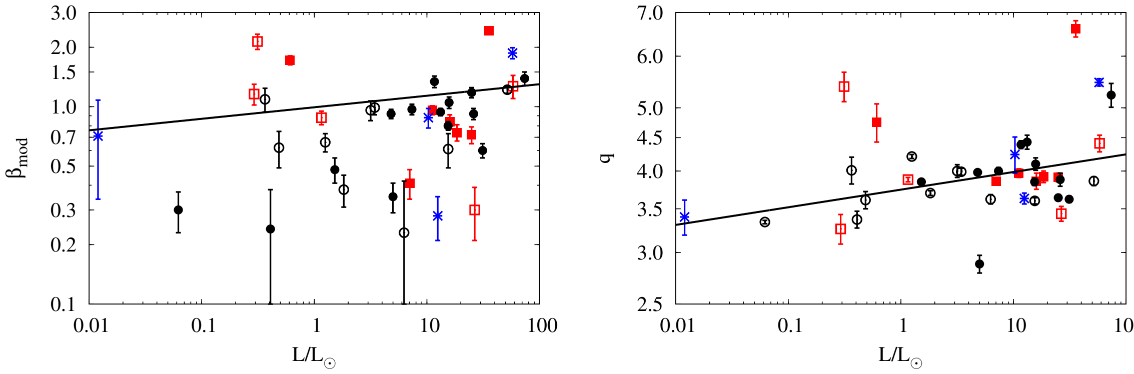

Figure 6.11: Opacity index (left) and size distribution index (right) as a function of stellar luminosity. The symbols are the same as in Figure (6.3).

In order to investigate a possible correlation between the dominant grain size and the size distribution or opacity index respectively, we analysed the fit parameter space and generated χ^2-maps for different objects.

6.5 χ^2-maps

In this section the spatial distribution of χ^2 in the parameter space is analysed. Figure 6.12 gives typical χ^2-maps for stars with different stellar luminosities, which were generated for both, the MBB and SD method. The lines of equal χ^2 are elongated from the bottom left to the top right, which can be explained as follows. If the grain size (λ_0 or $s_{\rm min}$) is larger than the best-fit value, the fitting routine is forced to take a steeper size distribution given by a larger size distribution index ($\beta_{\rm mod}$ or q). As well the shape of the isolines can be understood, while we will concentrate on the SD method here. We assume that the emission of different sized grains is proportional to their cross section as a rough estimate and define an “effective” grain size, s_0. This grain size is the one for which we replace the size distributed grains with the same number of equal-sized grains of radius s_0. Furthermore, we require that the equal-sized grains have the same cross-section as the size distributed ones. This can be described by

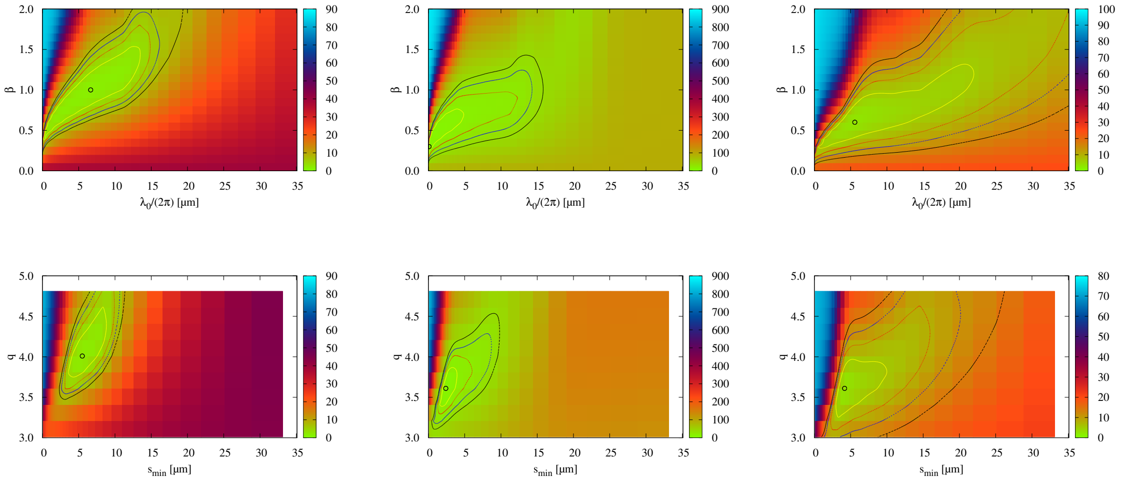

Figure 6.12: χ^2-maps for HD 50571 (left), HD 142091 (middle) and HD 216956 (right) in the MBB (top) and SD (bottom) method. The lines show the $n \times \chi^2_{\rm red}$ isolines for $n = 1$ (small circle), $n = 2$ (yellow line), $n = 3$ (red line), $n = 4$ (blue line) and $n = 5$ (black line), where $\chi^2_{\rm red}$ is the best-fit value.

$$\int_{s_{\rm min}}^{\infty} s^{2-q} ds = s_0^2 \int_{s_{\rm min}}^{\infty} s^{-q} ds. \tag{6.2}$$

Additionally, we assume that $q > 3$ which leads to

$$s_0 \approx s_{\rm min} \sqrt{\frac{q-1}{q-3}}. \tag{6.3}$$

Taking $q = 3.5$ for instance the “effective” grain size would be $\approx 2.2 s_{\rm min}$. An expectation now is that different pairs of $(s_{\rm min}, q)$ with the same s_0 lead to the same SEDs that reproduce the observed one equally well and thus the isolines should roughly follow the equation

$$s_{\rm min} \sqrt{\frac{q-1}{q-3}} = {\rm const}. \tag{6.4}$$

Indeed, this can be seen in Figure 6.12. Here, q rises more steeply for larger $s_{\min}$ and the isoline takes a kind of banana shape. Another fact is that the isolines are tilted to the x-axis, whereas this tilt is becoming smaller for stars with a higher stellar luminosity (see panels from left to right). The reason is that the effective grain size is slightly larger around more luminous stars and hence the derivative $dq/ds_{\min}$ is smaller at the same $s_{\min}$.

6.6 The role of the stellar photosphere

We investigated the stability of the fit results by changing the contribution of the stellar photosphere. Uncertainties of the stellar temperature of ±100 K and the stellar luminosity of ±20% were assumed and new photospheres calculated using the same models as described in Section 4.2. The changes of each photosphere compared to the original photosphere used for fitting are shown in Figure 6.13. Obviously, the strongest deviations can be found between 0.1 and 0.5 microns, whereas in the longer wavelength range the differences lie below 5%.

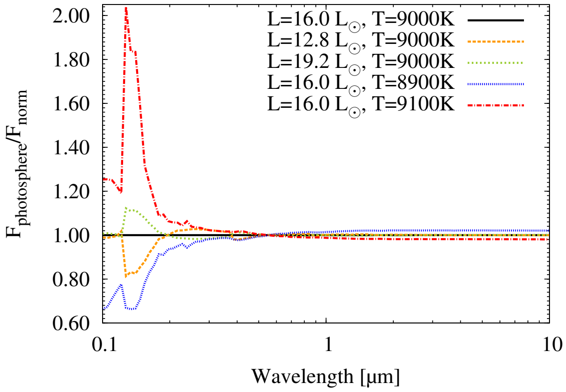

Figure 6.13: Flux density of the stellar photosphere of HD 9672 for different stellar luminosities and temperatures divided by the photosphere used for fitting ($L/L_\odot = 16$ and $T = 9000$ K) as a function of wavelength.

We chose four different targets, where two stars (a low and a high luminosity one) possess a one-component system while the two others (as well a low and a high luminosity one) are composed of two rings. Then we fit the SEDs of all targets with the four new photospheres. The results are listed in Table 6.5. The cold component fit results derived from the new photospheres show only small deviations from the original parameter values and lie in general within the uncertainties of the original fit (see Table 6.4). Considering the high fractional luminosity targets, HD 9672 (49 Cet) and HD 10647 (q^1 Eri) the standard deviations of grain sizes, dust temperatures and fractional luminosities are of the order of 1-3% while with 3-13% it is larger for the low-fractional luminosity objects, HD 48682 and HD 95418 (β UMa). The cold component has the largest influence in the far-infrared, and here, the stellar photosphere emission is several orders of magnitude smaller than the dust emission. Furthermore, the deviations of each new photosphere lies below 5% in this wavelength range. Thus, we can say that large uncertainties of the stellar parameters have not much influence on the cold component parameters.

On the other hand, the warm component radius is affected more strongly looking at a standard deviation of 8-20%. In the mid-infrared, the contribution of the stellar photosphere to the excess emission is comparable to the dust emission and so it has more influence on the warm component

Table 6.5: Fit results for different stellar photospheres.

HD	T [K]	$L/L_\odot$	s_{min} [µm]	T_{d} [K]	R_{disc} [AU]	f_{d}
9672	8900	16.0	3.90	69	12	9.41×10^{-4}
	9000	19.2	3.90	69	14	9.30×10^{-4}
	9000	16.0	3.83	71	12	9.25×10^{-4}
	9000	12.8	3.90	69	12	9.27×10^{-4}
	9100	16.0	3.90	69	12	9.18×10^{-4}
10647	6055	1.5	3.86	57	5	3.16×10^{-4}
	6155	1.8	3.86	57	4	3.19×10^{-4}
	6155	1.5	3.79	56	5	3.06×10^{-4}
	6155	1.2	3.80	57	3	3.21×10^{-4}
	6255	1.5	3.68	57	2	3.30×10^{-4}
48682	5985	1.8	2.69	63	...	6.64×10^{-5}
	6086	2.2	2.41	63	...	6.75×10^{-5}
	6086	1.8	2.05	62	...	7.23×10^{-5}
	6086	1.5	2.36	63	...	6.79×10^{-5}
	6186	1.8	2.04	63	...	6.95×10^{-5}
95418	9030	58.2	5.44	102	...	9.94×10^{-6}
	9130	69.8	5.24	112	...	1.01×10^{-5}
	9130	58.2	5.21	110	...	1.02×10^{-5}
	9130	46.6	5.15	112	...	1.03×10^{-5}
	9230	58.2	4.98	112	...	1.03×10^{-5}

fit results. Nevertheless, the variation of the different stellar photospheres lies below 5% as well. Therefore, the uncertainties of stellar parameters only play a minor role in the SED fitting of debris discs.

7 Analysis of the grain size – stellar luminosity trend

We found a correlation between the dominant grain size in units of the blowout grain size and the stellar luminosity, which is even the strongest trend found in this work (considering the SD method with pure astrosilicate). In order to explain this unexpected result we tried several possibilities starting with a mere fitting effect due to the dust composition used, which is followed by a test for statistical variations of the trend. After checking the possible technical reasons for the correlation found, two physical reasons are tested as well, namely the role of the surface energy constraint and the role of stirring.

7.1 Dust compositions

At first, we analysed the variation of the grain size – stellar luminosity trend by using different dust compositions in order to check the robustness of the resulting trend (see Section 2.1.3). Besides pure astronomical silicate (Draine, 2003a) and pure amorphous carbon (ACAR, Zubko et al. (1996)) we used a 1:1 mixture of astrosilicate and ice (Li and Greenberg, 1998), a 1:1 mixture of astrosilicate and amorphous carbon and a 1:1 mixture of astrosilicate and vacuum, which should mimic porous dust particles. The 1:1 ratios give the volume fraction of each dust component. The sublimation temperatures were assumed to be 1900 K for pure carbon and 130 K for pure ice particles (Kobayashi et al., 2011). However, since the warm component is not well constrained it was assumed as blackbody and we used the original 1300 K of astrosilicate as sublimation temperature for it. Considering the astrosilicate and ice mixture (Table B.1), most of the inner rings should not contain ice particles, since their temperature exceeds the sublimation temperature of ice. This is similar to the Solar system, where the Asteroid belt is located between Mars and Jupiter. Assuming its distance to the Sun of ~ 4 AU and using Equation (8.2) the temperature lies at ~ 140 K and exceeds the ice sublimation temperature as well. If a smaller distance to the Sun is assumed the temperature even increases.

Figure 7.1 shows the resulting temperature and size parameter trends already mentioned in Chapter 6. The steepness of the trends variates with different compositions, but persists in general. This means that for all compositions used the dust gets warmer, the disc radius goes down to the blackbody value, the typical grain size increases not as fast as expected and therefore, the typical grain size in blowout units decreases with increasing stellar luminosity.

Analysing the differences between the dust compositions we recognised the following. For porous particles the $s_{\mathrm{min}}/s_{\mathrm{blow}}$ dependence on the stellar luminosity is flatter than for compact particles. This is explainable by looking at Figure 2.6. Considering particles with sizes $s < 3\,\mu\mathrm{m}$ the temperature of porous grains is the lowest compared to all compositions used and conversely, for porous particles larger than $3\,\mu\mathrm{m}$ the temperature is higher than for other mixtures. Therefore, for discs around early-type stars the temperature of a porous astrosilicate grain of size s_{min} is higher than that of a compact astrosilicate particle of the same size. Thus, the SED of such a disc can only be reproduced, if the porous grains are larger than the compact ones. Conversely, for discs around late-type stars a porous grain with size s_{min} is colder than a compact one and therefore, the porous particles must be smaller

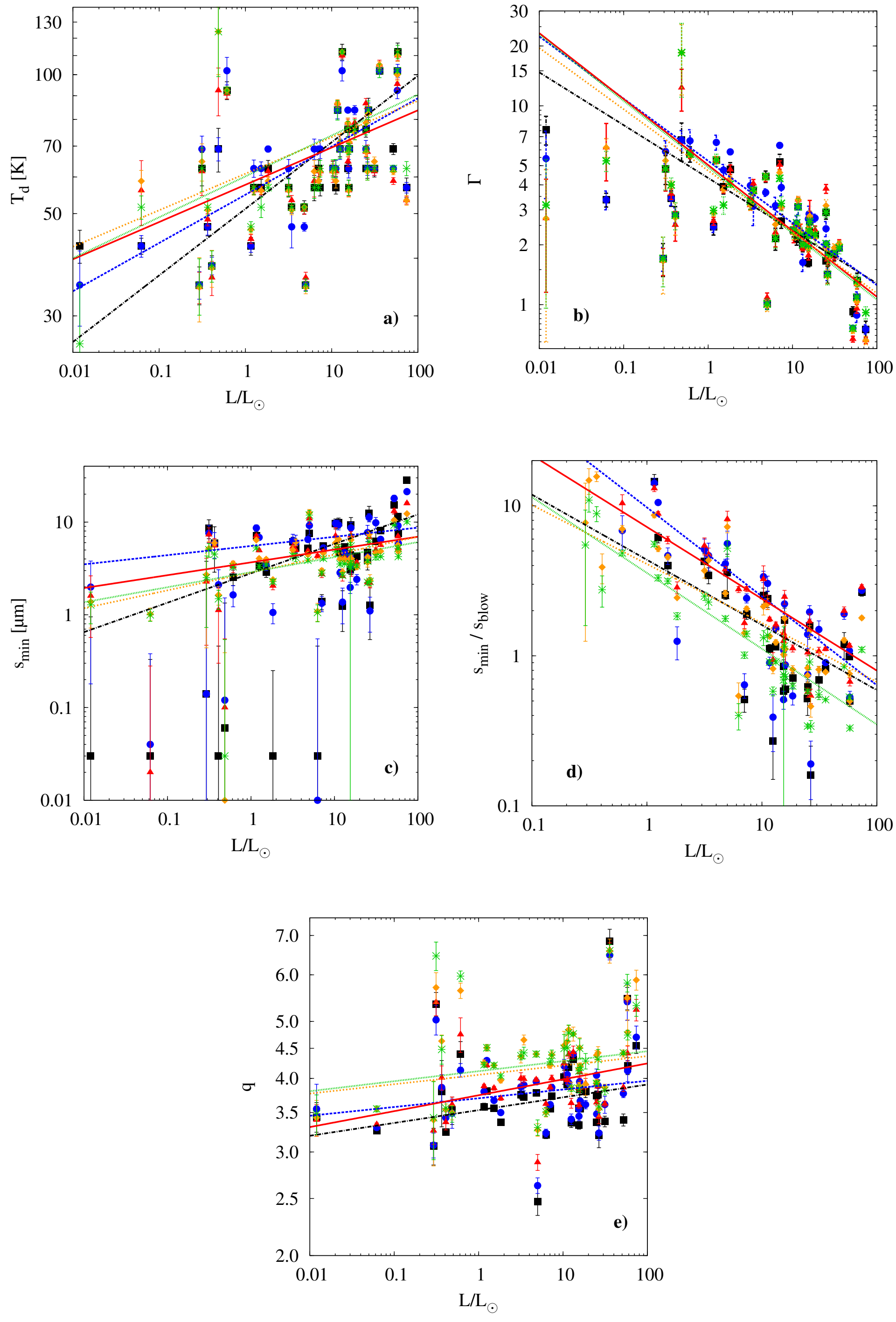

Figure 7.1: Various dust and disc parameters as function of the stellar luminosity for different dust compositions: (a) dust temperature, (b) disc's true radius to its blackbody radius, Γ, (c) minimum grain size s_{min}, (d) grain size ratio, $s_{\mathrm{min}}/s_{\mathrm{blow}}$, (e) size distribution index, q. Different colours denote different dust compositions: astrosilicate+vacuum (black dash-dotted line), astrosilicate+ice (blue dashed line), astrosilicate (red solid line), astrosilicate+carbon (orange dotted line) and carbon (green small-dotted line). Symbols with error bars are fit results for individual discs in the sample. A straight line of a certain colour is a best-fit trend line through the symbols of the same colour.

than the compact ones (Kirchschlager and Wolf, 2013). This results in a steeper trend of the minimum grain size of porous particles with the stellar luminosity, and thus a gentler decrease of the $s_{\mathrm{min}}/s_{\mathrm{blow}}$ ratio, compared to the other dust compositions.

The role of porosity

As a result from the analysis of different dust compositions we found that for a mixture of 50% astrosilicate and 50% vacuum (that means 50% porosity) the decrease of the $s_{\mathrm{min}}/s_{\mathrm{blow}}$ trend with stellar luminosity could be slightly flattened. The idea now was to increase the degree of porosity in order to erase the grain size ratio trend completely. We assumed 10% astrosilicate and 90% vacuum as a dust composition, which represents an extreme case of porosity, and fit the sample of resolved debris discs again. It turned out that for most of the discs the quality of the SED fits, measured by χ^2, gets poorer with the increasing degree of porosity. For example, the disc of HD 50571 yields the reduced $\chi^2 = 1.84$ for a porosity of zero (for pure astrosilicate). If the degree of porosity is increased to 50% , χ^2 increases as well to 1.86 and with 90% to 3.06. Another point is that the statistical scatter of the fit results increases as well and therefore the correlation between $s_{\mathrm{min}}/s_{\mathrm{blow}}$ and the stellar luminosity gets weaker with increasing porosity. Furthermore, the usage of this dust composition seems questionable, since the values of the fit parameters turn out to differ a lot from the typical values of the other compositions. An example is the size distribution index, which lies in general between 3 and 4 (in extreme cases between 4 and 7). For 90% porosity it changes to values around -2 for some targets, and this means that the size distribution contains more large particles than small ones. Considering the theory of collisional evolution of debris disc systems this index value is not compatible with it (e.g., Dohnanyi, 1969; Williams and Wetherill, 1994; Kenyon and Bromley, 2004c; Löhne et al., 2008; Pan and Schlichting, 2012).

Nevertheless, while this correlation is the strongest one for pure astrosilicate in this work it is statistically insignificant for 90% porosity ($r_{\mathrm{Pearson}} = -0.25$ and $r_{\mathrm{Spearman}} = -0.33$).

All in all we conclude that the decrease of the $s_{\mathrm{min}}/s_{\mathrm{blow}}$ ratio with increasing stellar luminosity identified by Pawellek et al. (2014) is pretty robust against the variation of dust composition considering compact dust grains (Pawellek and Krivov, 2015) and the usage of a 90% porosity dust composition is not appropriate for the sample of resolved debris discs.

7.2 Outliers

Since the choice of dust composition does not erase the correlation between grain size ratio and stellar luminosity the influence of individual systems in the resulting trend was investigated in order to check its robustness. Object HD 109085 (η Crv) is an example of such an outlier. By looking at Figure 7.1d it turns out that this target owns a much higher grain size ratio than other objects with comparable stellar luminosities. Furthermore, the uncertainties of HD 109085 are quite small, which could lead to the effect that the resulting best-fit trend line lies above many data points. Other examples for outliers are two of the four most luminous stars, namely HD 172167 (Vega) and HD 13161 (β Tri), as well as HD 104860. These targets have all a high derived minimum grain size and small uncertainties and thus it is possible that they influence the trend of $s_{\mathrm{min}}/s_{\mathrm{blow}}$.

The outliers of the sample were identified in the following way. For the whole sample one data point by one was removed and the best-fit trend line calculated at each time. Then it was analysed which target removal had the largest influence on the regression line. In Figure 7.2 the results for pure astrosilicate are presented. There are three apparent outliers, namely HD 104860, HD 207129

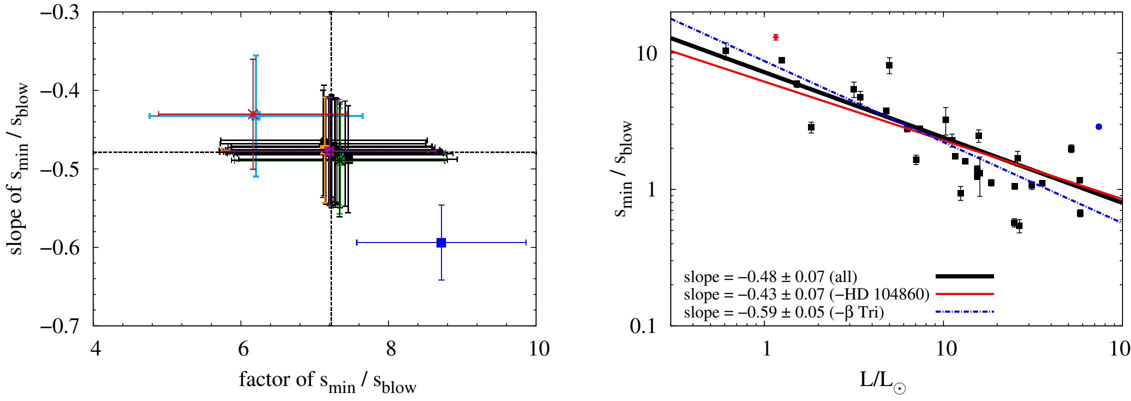

Figure 7.2: Identification of outliers in $s_{\rm min}/s_{\rm blow}(L)$ for pure astrosilicate. Left: the factors A and slopes B of the trend lines in the form $A \ \ (L/L_\odot)^B$, calculated by excluding from the sample one data point at a time. Error bars are uncertainties in A and B returned by the fitting. The "cross-hairs" depict the best fit through the whole sample. The strongest outliers are shown in colour: red is HD 104860, light blue is HD 207129, and blue is β Tri. Right: size ratio versus stellar luminosity for pure astrosilicate with and without outliers. The colour coding is the same as on the left. The black line gives the trend line for the entire sample. The line of a certain colour is the best fit without the object of the same colour. The removal of HD 104860 or HD 207129 lead to similar regression lines. Therefore, only the result for the removal of HD 104860 is shown.

and HD 13161 (β Tri). Removing either HD 104860 or HD 207129 the slope of the trend is changed from -0.48 to -0.43. The difference is 0.05 and lies within the uncertainty of the best-fit trend (0.07). On the other hand, if β Tri is removed, the slope is changed more strongly by 0.11 to a value of -0.59. This is larger than the uncertainty given by the fit. All in all we can say that individual systems can influence the best-fit trend line moderately. Therefore, we decided to exclude β Tri from a further analysis of the sample. This object is the most luminous star of the sample and belongs to the giant class. Furthermore, it is a close binary (Kennedy et al., 2012b). These peculiarities suggest that β Tri might not be representative for the whole sample.

7.3 Subsamples

We investigated the technical robustness of the trend by analysing the influence of different dust compositions and individual targets. Now, we assume that the size ratio may depend on more physical parameters of the system, such as the fractional luminosity or the disc radius and thus we will have a more statistical point of view on the robustness.

7.3.1 Extracting and comparing subsamples

We split the whole sample of 31 objects (all targets with blowout grain sizes, minus β Tri) into two subsamples of sizes n_1 and n_2, where $n = 31 = n_1 + n_2$ according to a physical parameter, P, selected. For instance, one subsample contains objects with a smaller median value of P and the other one all objects larger than the median value of P. In that case, $n_1 = 15$ and $n_2 = 16$. After dividing the sample, we analyse the $s_{\rm min}/s_{\rm blow}(L)$ trend for both subsamples individually and calculate the best-fit log-log regression lines with slopes $b_1 \pm SE(b_1)$ and $b_2 \pm SE(b_2)$. The parameter $SE(x)$ represents the standard error of x. Finally, it has to be checked whether the trends of both subsamples are statistically, significantly different or not. Thus, the null hypothesis is that the two subsamples are not significantly different and the Student's t-score can be applied with

$$t = \frac{|b_1 - b_2|}{SE(b_1 - b_2)} \tag{7.1}$$

and

$$SE(b_1 - b_2) = \sqrt{SE(b_1)^2 + SE(b_2)^2}. \tag{7.2}$$

Then the probability, p, has to be calculated, which proves whether the null hypothesis is true or not with $n_1 + n_2 - 4$ degrees of freedom. The criterion used is that the subsamples are different, if the two-tailed $p < 0.01$.

Since the sample contains a number of 31 objects it is not particularly large. Hence, it is necessary to check the feasibility of this procedure. Therefore, we chose the HD-number of the targets as the parameter P. The number is connected to the right-ascension of the primary stars and as such it is an unphysical parameter, which should lead to an confirmation of the null hypothesis. The visualisation

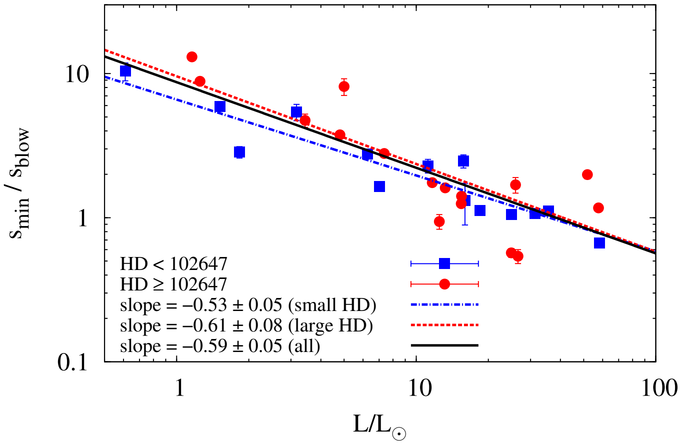

Figure 7.3: The grain size ratio as a function of stellar luminosity for two subsamples. The subsamples are divided by the HD number. Objects with low HD number are shown in blue squares and objects with high HD number are shown in red circles. The blue and red straight lines are the best fit through the blue and red symbols. The black line represents the best fit for the whole sample.

of the results is given in Figure 7.3. The slopes of both subsamples are -0.53 ± 0.05 and -0.61 ± 0.08, which leads to a t-value of 0.85 by using Equations (7.1) and (7.2). With 27 degrees of freedom the probability of the null hypothesis is $p = 0.40$. This is much larger than 0.01 and thus, both subsamples are indistinguishable from each other. So, our expectation is confirmed, the null hypothesis accepted and the usage of subsamples is feasible.

7.3.2 Discs of low and high fractional luminosity

In this section the parameter P is identified with the fractional luminosity of the debris discs. The median value of it is $P_{\text{med}} = 6.50 \times 10^{-5}$, whereas the subsample sizes stay $n_1 = 15$ and $n_2 = 16$. The results are presented in Figure 7.4 for both, the minimum grain size and the grain size ratio as function of stellar luminosity. For reasons of comparability with the size ratio plot, the minimum grain

Table 7.1: Comparing the regressions for $s_{\rm min}/s_{\rm blow}$ in pairs of subsamples for $P < P_{\rm med}$ and $P \geq P_{\rm med}$

P	$b_1 \pm SE(b_1)$	$b_2 \pm SE(b_2)$	t-score	p	Verdict
HD	-0.53 ± 0.05	-0.61 ± 0.08	0.85	0.40	same
$f_{\rm d}$	-0.42 ± 0.10	-0.74 ± 0.06	2.74	0.01	marginally
$R_{\rm disc}$	-0.56 ± 0.07	-0.69 ± 0.07	1.31	0.20	same
$T_{\rm age}$	-0.66 ± 0.10	-0.54 ± 0.05	1.07	0.29	same
F_{100}	-0.45 ± 0.08	-0.75 ± 0.06	3.00	0.006	different
F_{100}/Extent	-0.62 ± 0.06	-0.58 ± 0.08	0.40	0.69	same
FWHM	-0.60 ± 0.08	-0.55 ± 0.07	0.47	0.64	same

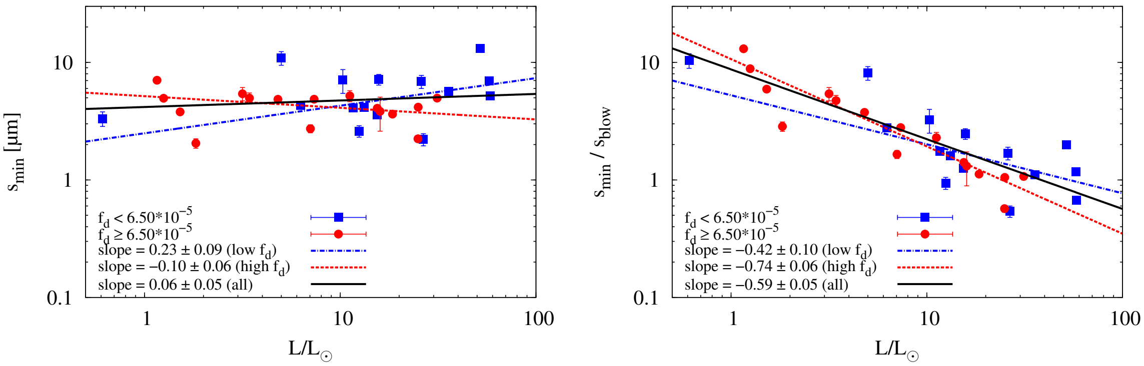

Figure 7.4: Minimum size (left) and size ratio (right) vs. stellar luminosity, assuming pure astrosilicate, for the subsamples of low and high fractional luminosity discs. Blue line and squares: $f_{\rm d} < 6.50 \times 10^{-5}$, red line and circles: $f_{\rm d} \geq 6.50 \times 10^{-5}$, black line: the entire sample.

size plot does only contain the 31 objects mentioned above, although all targets of the sample own a minimum grain size. The subsamples cover a broad stellar luminosity range, the one with low fractional luminosities consists of objects between 0.6 $L_\odot$ and 58 $L_\odot$ while the other one with high fractional luminosity targets covers a range between 1.1 $L_\odot$ and 31 $L_\odot$. Considering the subsample of high fractional luminosity discs, the grain size $s_{\rm min}$ is roughly consistent with a constant value of $\sim 5\,\mu$m and shows only a weak, decreasing correlation with the stellar luminosity which is not statistically significant ($r_{\rm Pearson} = -0.21$ and $r_{\rm Spearman} = -0.24$). The low fractional luminosity subsample shows as well a not significant correlation between the minimum grain size and the stellar luminosity ($r_{\rm Pearson} = 0.27$ and $r_{\rm Spearman} = 0.20$). Applying the t-score, it turns out that $t = 3.05$ and hence, $p = 0.005$. This means, that the subsamples are statistically different from each other. In case of the $s_{\rm min}/s_{\rm blow}$ ratio $t = 2.74$ and $p = 0.011$ which only shows marginally differences. Here, the slope is stronger for high fractional luminosity discs ($r_{\rm Pearson} = -0.93$ and $r_{\rm Spearman} = -0.96$), but both subsamples show a strong correlation (low fractional luminosity: $r_{\rm Pearson} = -0.80$ and $r_{\rm Spearman} = -0.72$). Obviously, the scatter is smaller for the high fractional luminosity subsample which is also reported in Section 6.6. One explanation for the differences between high and low fractional luminosity discs is that with a higher $f_{\rm d}$ the infrared excess is more pronounced and thus the SED fit is more reliable and less uncertain. A confirmation for this assumption is that the scatter of data for high fractional luminosity discs around the regression line is smaller (the correlation between the grain size ratio or the grain size and the stellar luminosity is stronger) than for low fractional luminosity objects. The uncertainties of the trend line parameters in Figure 7.4 show that. While it is 0.10 for the low fractional luminosity sample it is only 0.06 for the high-$f_{\rm d}$ one. Besides this more technical explanation there is also a physical possibility for differences between the two subsamples. It might be that high and low fractional luminosity discs differ in one or another respect. If this is the case, than there should be systematic differences in subsamples of other key parameters (e.g., disc radius or system's age) as well.

7.3.3 Small vs. large discs and young vs. old discs

The differences in the two subsamples of high and low fractional luminosity discs might be explained due to systematic differences in the disc radius or the stellar system's age (e.g., Moór et al., 2006). For example, debris discs are expected to loose dust mass and therefore fractional luminosity during the collisional evolution. In this process planetesimals are ground to dust and particles of sub-blowout size are produced and then expelled from the debris disc system due to stellar radiation pressure (Wyatt et al., 2007a; Löhne et al., 2008). Considering the minimum and maximum fractional luminosity the disc radius is expected to be larger for high fractional luminosity discs than for low fractional luminosity ones (see Figure 2.10).

Considering discs of a fractional luminosity $f_\mathrm{d} < 6.50 \times 10^{-5}$ the average disc radius lies at (110 ± 48) AU, while for discs with $f_\mathrm{d} \geq 6.50{\times}10^{-5}$ it is $(170{\pm}51)$ AU. Hence, the radii of low fractional luminosity discs seem to be smaller. The average ages of both subsamples are (547 ± 666) Myr and (519 ± 685) Myr respectively, which leads to the impression that low fractional luminosity discs might be slightly older (ignoring the large uncertainties). However, the standard deviations in both cases are large and a statistical test is necessary in order to get reliable conclusions. The null hypothesis for the following AD-test (see Chapter 2.3) is given by the disc radii and the ages being indistinguishable for both subsamples. In Chapter 5.3.3, we inferred the uncertainty of the disc radii derived to be 8%, while we assume an uncertainty of 25% in the age of the host stars estimated by $25\% \times \log_{10}(T_\mathrm{age}/\mathrm{Myr})$. The test parameters for the AD-test are given by Equations (2.46) and (2.47), where we use $n_1 = 15$, $n_2 = 16$ as subsample sizes and $k = 2$ as number of the subsamples. In that case, the critical value for the rejection of the null hypothesis is $t_1 = 3.75$ at a significance level of $\alpha = 0.01$ (Scholz and Stephens, 1987). The result for the disc radii is a value of $T = 5.28 \pm 1.05$ which is larger than the critical value. On the other hand, the AD-test for the ages led to a value of $T = -0.20 \pm 0.77$. Therefore, we can say that the radii of low and high fractional luminosity discs may be statistically distinguishable, whereas the ages of the discs are clearly indistinguishable.

In addition we divided the sample into subsamples of small ($R_\mathrm{disc} \leq 129$ AU) and large discs ($R_\mathrm{disc} \geq 129$ AU) as well as into young ($T_\mathrm{age} < 276$ Myr) and old discs ($T_\mathrm{age} \geq 276$ Myr). For both we used the median as separation value. The resulting statistical parameters of the two-sample tests are given in Table 7.1. As listed there, the subsamples of disc radii and stellar age are indistinguishable from each other, since the p-probabilities with 0.20 (disc radii) and 0.29 (stellar age) are much larger than the significance level of 0.01. Hence, the marginal differences between the discs of high and low fractional luminosity seem to originate more in the quality of the fits than in a physical reason.

7.3.4 Faint vs. bright discs

In an additional attempt, we chose the absolute integrated flux from the disc and that flux divided by the disc extent as splitting parameter, P, in order to investigate possible systematic errors stemming from the images. An example for such a systematic would be, that discs with a high absolute flux might be larger, since a larger fraction of the disc would be visible above the noise. We used the absolute *integrated* brightness at 100 µm and the absolute *surface* brightness to generate the two subsamples. The results can be seen in Figure 7.6. Here, the objects HD 9672 (49 Cet), HD 172167 (Vega) and HD 216956 (Fomalhaut) are excluded, since they have no *Herschel*-measured fluxes at 100 µm. Therefore, the size of the subsamples is $n_1 = n_2 = 14$. The two subsamples of both, integrated and

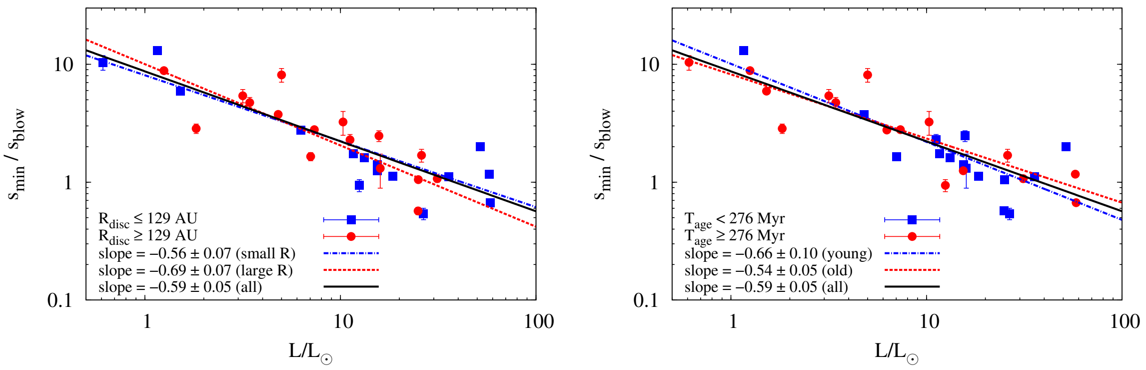

Figure 7.5: Same as Figures 7.3 and 7.4, but for the two subsamples based on the disc radius (left) and the stellar age (right). Left: blue line and squares: $R_{\rm disc} \leq 129$ AU; red line and circles: $R_{\rm disc} \geq 129$ AU; right: blue line and squares: systems younger than 276 Myr; red line and circles: systems older than 276 Myr; both panels: black line: the entire sample.

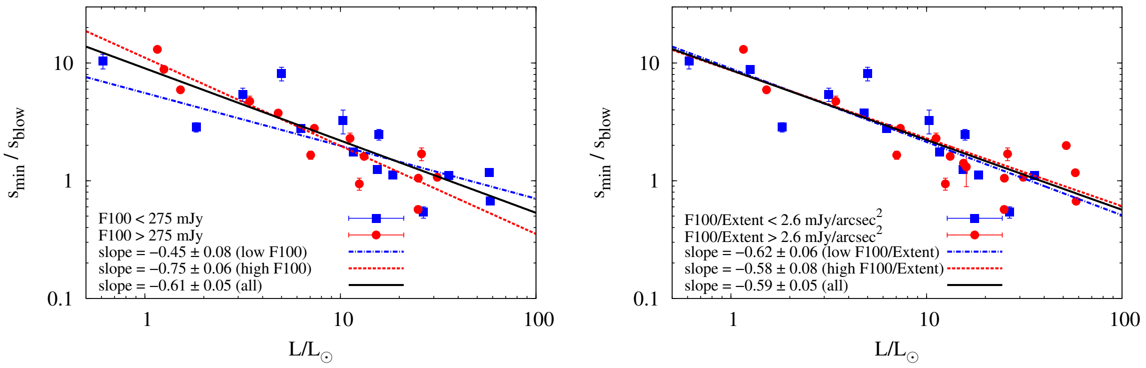

Figure 7.6: Same as Figures 7.3–7.5, but for the two subsamples based on disc's absolute integrated brightness (left) and absolute surface brightness (right). Blue line and squares: faint discs; red line and circles: bright discs; black line: the entire sample.

surface brightness include a wide range of stellar luminosities. The regression lines for the surface brightness show no significant differences which is confirmed by a p-probability of 0.69. On the other hand, there are variations for the integrated brightness ($p = 0.006$, see Table 7.1). Comparing these new results with the result of the chapter before, it seems that the differences in the regression lines are caused by the quality of the SED fit and not by a physical effect. Indeed, Figure 7.7 shows that there is a correlation between the integrated brightness and the fractional luminosity. Since there are no differences in the subsamples divided by surface brightness, systematic uncertainties caused by the images seem not to be the reason for the differences in the subsamples of high and low fractional luminosity.

7.3.5 Marginally-resolved vs well-resolved discs

Another possible explanation for the different trend lines might be the uncertainties of the measured disc radii. We used the discs' FWHM at 100 µm and compared it to the width of the *Herschel*/PACS point-spread function (PSF) at the same wavelength ($6.7''$). The sample was splitted into well resolved discs with an FWHM $\geq 10.6''$ (i.e., FWHM $\geq$ 1.6PSF) and marginally resolved discs with an FWHM $< 10.6''$ (i.e., FWHM $<$ 1.6PSF). The results are shown in Figure 7.8. Most of the marginally

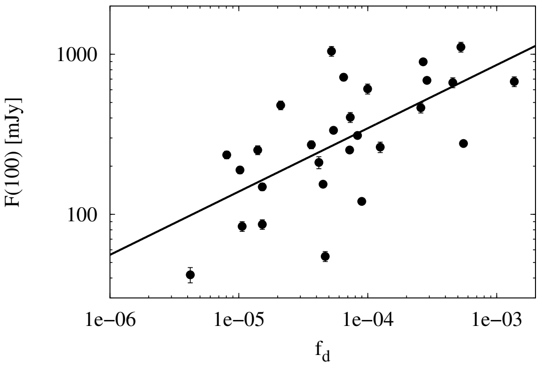

Figure 7.7: Integrated brightness at 100 µm as a function of fractional luminosity. Excluded are 49 Cet, Fomalhaut and Vega, since they do not have integrated brightnesses at 100 µm. The straight solid line shows the best log-log-fit through the symbols.

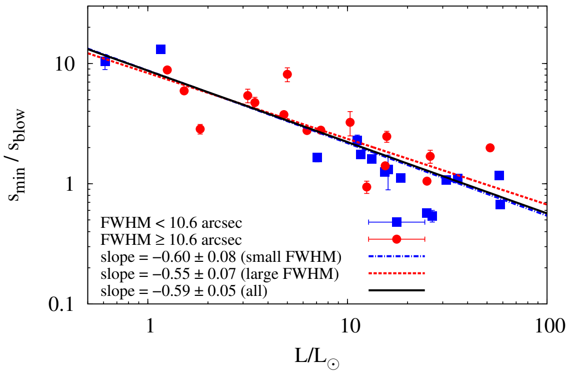

Figure 7.8: Same as Figures 7.3–7.6, but for the two subsamples based on disc's FWHM at 100 µm. Blue line and squares: marginally resolved discs; red line and circles: well-resolved discs; black line: the entire sample.

resolved discs of the sample can be found around high stellar luminosity stars, while the majority of the well resolved discs have lower stellar luminosities. This is in agreement with Figure 5.3. The regression lines of both subsamples reveal no significant differences with $p = 0.64$ (see Table 7.1).

All in all, we can say that the $s_{\rm min}/s_{\rm blow}$ trend with the stellar luminosity persists, although discs with high and low fractional luminosity or high and low integrated brightness reveal small differences in the steepness of the slope. Therefore, a statistical effect causing this trend can be excluded as well and now, physical processes can be investigated.

7.4 The role of the surface energy constraint

The analysis of the $s_{\rm min}/s_{\rm blow}$ trend with stellar luminosity led to the assumption that this correlation does not have a statistical or technical cause. Hence, physical processes have to be investigated in order to explain it.

The model without radiation pressure

The first idea is that it is not possible to produce smaller collisional fragments around low-luminosity stars. The reason was given by Krijt and Kama (2014), who stated that the minimum size of collisional fragments should be connected to the impact energy available. They showed the $s_{\rm min}/s_{\rm blow}$ ratio to be describable by

$$x \equiv \frac{s_{\rm min}}{s_{\rm blow}} = 48A\left(\frac{0.01}{f}\right)^2, \tag{7.3}$$

where

$$A \equiv \left(\frac{R_{\rm disc}}{100\,{\rm AU}}\right)\left(\frac{L_\odot}{L}\right)\left(\frac{0.01}{\eta}\right)\left(\frac{\gamma}{100{\rm erg cm}^{-2}}\right), \tag{7.4}$$

γ the surface energy per unit surface of the material and η the fraction of kinetic energy which is used to create the new surface. The parameter f is given by

$$f = \frac{v_{\rm rel}}{v_{\rm K}} = v_{\rm rel}/\sqrt{\frac{GM_{\rm star}}{R_{\rm disc}}}, \tag{7.5}$$

with $v_{\rm K}$ being the Keplerian orbital velocity and $v_{\rm rel}$ the relative velocity of the colliders. Krijt and Kama (2014) set this velocity ratio equal to the average eccentricity of the dust parent planetesimals, $\langle e\rangle$, which can also called the dynamical excitation.

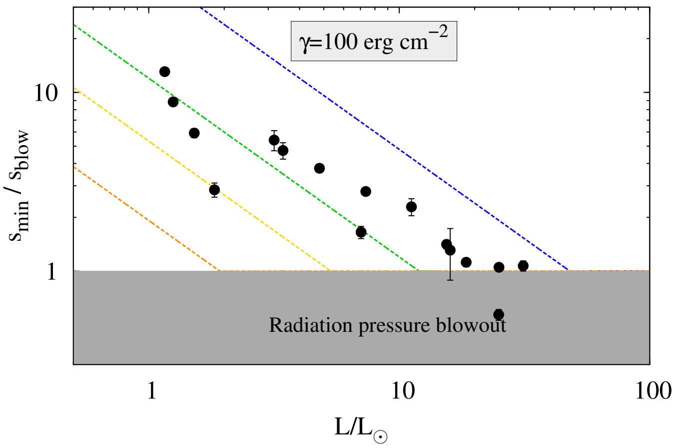

Figure 7.9: The $s_{\rm min}/s_{\rm blow}$ ratio as a function of stellar luminosity, assuming pure astrosilicate grains. Symbols with error bars: discs of our sample with $f_{\rm d} \geq 6.50 \times 10^{-5}$. Gray-shaded area: region of blowout grains. Dashed lines: original model by Krijt and Kama (2014), Equation (7.3). Grains below the dashed lines are excluded by these models, because they should not be produced. Different line colours correspond to different degrees of dynamical excitations: $\langle e\rangle = 0.01$ (blue), $\langle e\rangle = 0.02$ (green), $\langle e\rangle = 0.03$ (yellow), $\langle e\rangle = 0.05$ (orange); $\gamma = 100$ ergcm^{-2}.

In Figure 7.9 the $s_{\rm min}/s_{\rm blow}$ ratio as function of stellar luminosity is presented for the subsample of 16 discs of high fractional luminosities. We chose this subsample since the fit results may be more reliable than for the whole sample, which was explained in Section 7.3. Furthermore, the grain size correlation was found to be stronger for this subsample and hence it is easier to compare the models. Using the Krijt-and-Kama model (Equation (7.3)) and comparing it to the $s_{\rm min}/s_{\rm blow}$-L correlation found for the sample of resolved discs, we got the following results depicted in Figure 7.9. The parameter values were assumed to be $\eta = 0.01$ and $\gamma = 100$ erg cm^{-2}, but they are highly uncertain.

Particles with a size ratio below the dashed lines cannot be produced in a collision, since there would be not enough impact energy to build their surface. On the other hand, smaller grains can be created if their eccentricity is larger. Refering to the sample of resolved discs, the forbidden areas below $\langle e \rangle \approx 0.02$–$0.03$ and below the blowout limit match the region where no data points can be found (except for HD 182681 which lies below the blowout limit).

The model including radiation pressure

Due to the radiation pressure the eccentricities of dust grain orbits are higher than those of their parent planetesimals and hence there is a possibility to improve the above mentioned model, as noted by Krijt and Kama (2014). The parameter f is connected to the average eccentricity of solids, which are the "immediate parents" of the smallest collisional fragments. It is assumed that these particles have a radius of bs_{min} with $b > 1$ being a numerical factor. They have the same dynamical excitation as the planetesimals from which they originate, but the radiation pressure causes an increase in their eccentricities (see Chapter 2.2.2). Now, the parameter f can be adopted as

$$f \approx \sqrt{\langle e \rangle^2 + \left(\frac{\beta}{1-\beta} \right)^2}, \tag{7.6}$$

with β given by Equation (2.16) (e.g., Lissauer and Stewart, 1993). Since Equations (7.3)–(7.4) assume $Q_{\mathrm{pr}} = 1$, this relation is used as well for the sake of simplicity and allows to set $\beta = 1/(2bx)$. With this, Equation (7.3) can be written as

$$x = 48A \left(\frac{0.01}{\langle e \rangle} \right)^2 \left[1 + \frac{1}{\langle e \rangle^2 (2bx-1)^2} \right]^{-1} \tag{7.7}$$

Depending on b the discriminant of this cubic function is smaller than zero for $\langle e \rangle$ smaller than a certain value (e.g., for $b = 10$, the dynamical excitation must be $\langle e \rangle \lesssim 0.04$) and thus three real solutions for $s_{\mathrm{min}}/s_{\mathrm{blow}}$ exist in this case. For larger $\langle e \rangle$ the discriminant is larger than zero and so only one real solution can be obtained while the other two are imaginary. Considering a discriminant smaller than zero, the largest root of the cubic function leads to the $s_{\mathrm{min}}/s_{\mathrm{blow}}$ of interest, while for $b \to \infty$ the simplified equation of Krijt and Kama (2014) can be obtained. The two other roots of Equations (7.7) have a physical meaning as well. If the eccentricities of the parent particles are sufficiently high due to radiation pressure, the fragments with an $s_{\mathrm{min}}/s_{\mathrm{blow}}$ ratio between these roots can be created. A limiting case explaining this is $\langle e \rangle \to 0$. Here, the cubic function can be simplified to a quadratic one with

$$x = 4.8 \times 10^{-3} A \left(2bx - 1 \right)^2 . \tag{7.8}$$

Now, the particles with $s_{\mathrm{min}}/s_{\mathrm{blow}}$ between the two roots of this equation have large radiation pressure-induced eccentricities and therefore, the impact energies are high enough to create these fragments. Considering the parameter ranges used in this work, the two roots are smaller than unity, which means that the minimum grain size, s_{min} is smaller than the blowout limit, s_{blow} and thus, they do not play a physical role in this case. In Figure 7.10 the forbidden areas of the improved model including radiation pressure (using Equation (7.7)) are shown in comparison to the model excluding radiation pressure (using Equation (7.3)). Both models use the same eccentricities $\langle e \rangle$, while the factor b was set to 10. This means that the collisional targets are on average ten times larger than the resulting fragments (See Krivov et al., 2005, for justification of this choice and additional references.).

Comparing the $s_{\mathrm{min}}/s_{\mathrm{blow}}$ trend of the data set with both, the simplified and the improved model the latter one seems to reproduce the data not as well as the original one. Since some parameters,

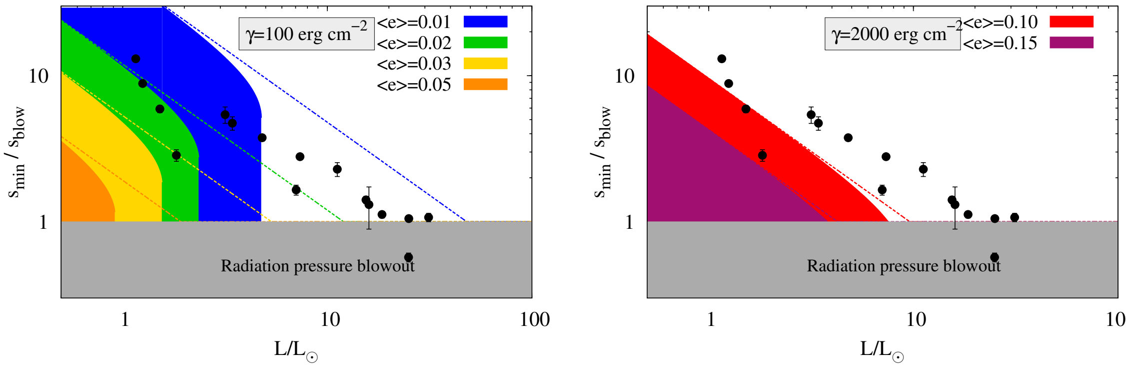

Figure 7.10: The $s_{\mathrm{min}}/s_{\mathrm{blow}}$ ratio as a function of stellar luminosity, assuming pure astrosilicate grains. Symbols with error bars: discs of our sample with $f_{\mathrm{d}} \geq 6.50 \times 10^{-5}$. Gray-shaded area: region of blowout grains. Dashed lines: original model by Krijt and Kama (2014), Eq. (7.3). Filled areas: improved model, Eq. (7.7). Grains below the dashed lines and those in filled areas are excluded by these models, because they should not be produced. Different line and filling colours correspond to different degrees of the dynamical excitation, $\langle e \rangle$. Left: $\gamma = 100$ ergcm^{-2}, symbols represent the full sample; right: $\gamma = 2000$ ergcm^{-2}.

like γ or η, are uncertain a better adaption to the data can be generated by varying these parameters in the given equations. This was done in the right panel of Figure 7.10, where γ was increased from 100 erg/cm^2 to 2000 erg/cm^2. The former value is realistic for icy materials (Wada et al., 2007; Gundlach et al., 2011) whereas the latter one is more appropriate for e.g., silicon (Gilman, 1960). As well, a lower energy fraction might be used. The result is a good match at higher eccentricities, e.g., at $\langle e \rangle \approx 0.10$ the area excluded by the improved model could describe the decrease of $s_{\mathrm{min}}/s_{\mathrm{blow}}$.

However, Thebault (2016) investigated the surface energy contraint in more detail by incorporating it into a statistical code for collisional evolution of debris discs. Here, not only equal-sized colliders (as in Krijt and Kama (2014)) were assumed, but a distribution (s_i, s_j) of them. He found that for all pairs of colliders the energy constraint can be observed, especially around low-mass stars or in discs with low $\langle e \rangle$ it has a significant effect. In general this confirms the results found in Pawellek and Krivov (2015) and in the previous sections of this work, but there are limitations as well. For example, the pairs of colliders for which the surface energy constraint has the largest effect are not the same pairs which produce the most of the dust. Thus, the global influence of the surface energy constraint is relatively small. Only for discs around solar-type stars which have a high dynamical excitation the constraint has a visible effect on the size distribution of dust particles. It was expected that in discs with $\langle e \rangle = 0.01$ the effect should be the strongest, but contrarily no visible effect on the size distribution is detectable here. Thebault (2016) concluded that in such discs another mechanism dominates the size distribution at small sizes, namely the imbalance of a small dust production and destruction rate (Thébault and Wu, 2008) in dynamically cold discs. Mentioning the degree of excitation of debris discs in connection to the surface energy constraint the influence of the stirring level on the grain size ratio - stellar luminosity trend will be the next point of investigation.

7.5 The role of the stirring level

In this section we will have a closer look on the balance between dust production and destruction rate of small particles. It is related to the microphysical effect of the surface energy constraint explained in the last section, but it is controlled by the level of stirring of the larger, macrophysical bodies.

7.5.1 Idea

The grain size distribution depends on the degree of dynamical excitation of the dust producing planetesimals, $\langle e \rangle$ (Thébault and Wu, 2008). To explain this idea, we assume planetesimals with a low dynamical excitation, which is still sufficiently high for collisions to be mostly destructive. In this case the collision velocities between large grains not influenced by stellar radiation pressure are low and therefore, the *production* rate of small grains is decreased compared to the production rate in systems with a higher dynamical excitation.

On the other hand, the *destruction* rate of the small particles is related to their eccentricities and these are set by stellar radiation pressure. Hence, it is independent of the dynamical excitation of the parent bodies and stays the same. Considering the low dynamical excitation, a smaller number of particles is produced, but the same number is destroyed and therefore, a dearth of small particles should be the result leading to a shift of the maximum of the size distribution and the $s_{\rm min}/s_{\rm blow}$ ratio to larger values. This can be seen in Figure 7.11 considering the right maximum of the distribution. The dominant grain size ($s_{\rm min}$) should be the peak of the size distribution. Particles of this size have inherited the eccentricity, $\langle e \rangle$, of their parent planetesimals which is the same as the radiation pressure-induced eccentricity, $\beta/(1-\beta)$, here. Assuming $Q_{\rm pr} = 1$ again, $\beta \approx 0.5(s_{\rm blow}/s_{\rm min})$ and thus,

$$\frac{s_{\rm min}}{s_{\rm blow}} \approx \frac{\langle e \rangle^{-1} + 1}{2} \tag{7.9}$$

can be taken as rough estimate provable by collisional simulations. Pawellek and Krivov (2015) used the collisional code ACE (Krivov et al., 2013) treating the collisional and radiation pressure forces in a more realistic way by including cratering collisions, rebounds and sticking. Furthermore, they considered low-luminosity stars besides A-stars already treated in Thébault and Wu (2008).

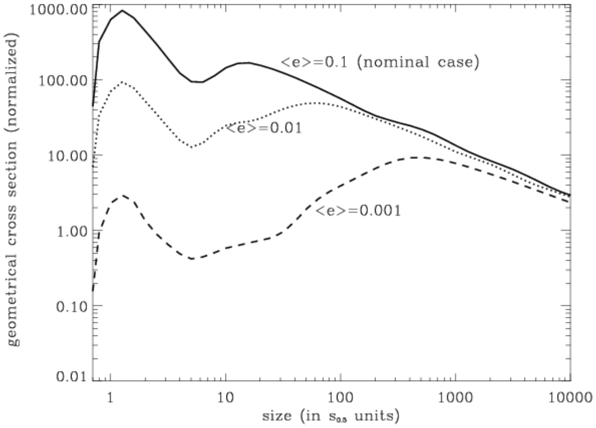

Figure 7.11: Geometrical cross section as a function of grain size for different dynamical excitations. The right maximum shifts towards larger values for lower dynamical excitations. The maximum for the smallest grains on the left side is caused by a lack of even smaller particles which could destroy their parent bodies. From Thébault and Wu (2008).

7.5.2 ACE runs

In order to test the effect in more detail, several ACE runs were necessary. Following Pawellek and Krivov (2015) two different central stars (A2V with 17.4 $L_\odot$ and G2V with 1 $L_\odot$) and two different stirring levels (average planetesimals' eccentricity of 0.1 and 0.01, average inclination according to the energy equipartition) were investigated. The code considered stellar gravity, direct radiation pressure and Poynting-Robertson drag besides the above mentioned possible collisional outcomes (disruptive, cratering, rebounding, and sticking collisions). The initial disc mass was assumed to be 30 $M_\oplus$ (in the bodies of up to 100 km radius), leading to typical fractional luminosities of the dust in the sample of resolved debris discs, while the disc radius was taken as (100 ± 10) AU. The other standard assumptions for the model runs are compact astrosilicate as dust composition (Draine, 2003a) and a critical fragmentation energy from Benz and Asphaug (1999). The collisional evolution run was stopped at a quasi-steady state defined in Löhne et al. (2008).

7.5.3 Results

Size distribution

Figure 7.12 depicts the resulting size distribution from the described ACE runs. Comparing them with Figure 7.11 we can say that both diagrams show similar results. The maximum of the size distribution is shifted to higher values for lower dynamical excitations, $\langle e \rangle$. Furthermore, it is obvious that the size distribution generated with ACE has significant differences comparing to a power law distribution with a sharp cutoff size (see Figure 2.9).

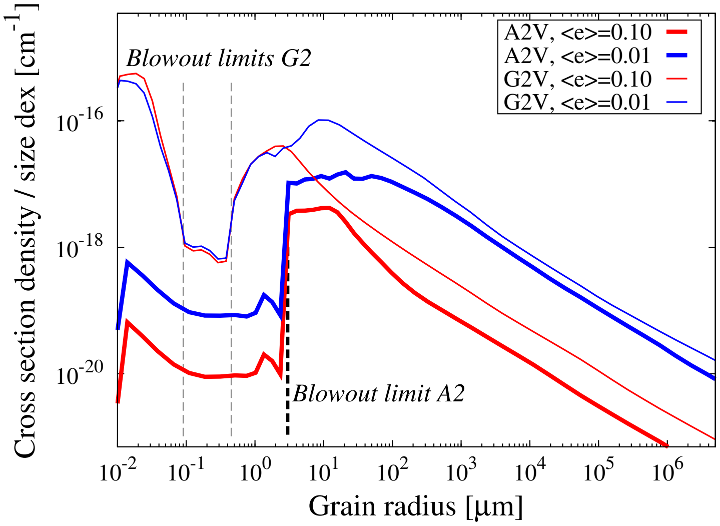

Figure 7.12: Simulated size distributions in the fiducial discs around A2-stars (thick lines) and G2-stars (thin lines) with higher (red) and lower (blue) level of stirring. Plotted is the size distribution in the parent ring, assumed to be located at 100 AU. Vertical dashed lines mark the radiation pressure blowout limit of A2-stars (thick) and G2-stars (thin). Note that two blowout values exist for the G2-stars. The grains in unbound orbits are those between these two.

Beginning with the distribution for the A-star, a "plateau" can be seen between $s_{\text{blow}} = 3.0\,\mu\text{m}$ and a shallow maximum at 12 µm (for $\langle e \rangle = 0.10$). This maximum increases towards 50 µm in case of a dynamically cold disc (i.e. for $\langle e \rangle = 0.01$). There are different-sized grains in the given size area contributing almost equally to the dust cross section. Thus, a geometric mean value between the lower and higher end of the plateau is taken as the minimum or dominant grain size, s_{min}.

The disc around the G2-star has a blowout size of $s_{\text{blow}} = 0.46\,\mu\text{m}$ and a size distribution maximum at 2.6 µm for $\langle e \rangle = 0.10$ or 10 µm for $\langle e \rangle = 0.01$, respectively. Here, a second blowout limit does exist as well, meaning that particles smaller than $\lesssim 0.1\,\mu\text{m}$ are staying in bound orbits and are contributing a large fraction to the dust's total cross section. The absorption efficiency, Q_{abs}, of these "sub-blowout grains" is much lower compared to the larger bound particles (see Figure 2.3) and hence they only play a minor role in the observed emission, which lies at the order of $\sim 10\%$ at all wavelengths. Therefore, the grains do not have a direct relevance to the discussed lower cutoff size of the size distribution, but they do affect the distribution, since they are able to collide with the grains just above the upper blowout limit and thus "erode" these particles.

Grain size ratio

The next step after analysing the size distribution is the investigation of the resulting grain size ratio - stellar luminosity trend depicted in Figure 7.13. Here, the results from the sample of resolved discs are compared to the ACE runs. The expectation was that $s_{\mathrm{min}}/s_{\mathrm{blow}}$ increases with decreasing dynamical excitation, $\langle e\rangle$, and this is confirmed for both stars. It is as well roughly consistent with Equation (7.9). Another interesting result is given by the fact that the lines of constant dynamical excitation are tilted and thus s_{min} becomes closer to s_{blow} for high luminosity stars even if the dynamical excitation stays constant. This effect was not expected before the modelling and it was reported in Pawellek and Krivov (2015) for the first time. Furthermore, it mimics the $s_{\mathrm{min}}/s_{\mathrm{blow}} - L$ trend found for the sample of resolved discs. Comparing the $s_{\mathrm{min}}/s_{\mathrm{blow}}$ - L trend with the lines of equal dynamical excitation it is obvious that the trend does not confirm an assumption of constant $\langle e\rangle$ for the whole stellar luminosity range. In fact, a dynamical excitation between 0.01 and 0.1 for G-stars and $\gtrsim 0.1$ for A-stars seems to be the best approximation of the data. Looking at the results of detailed collisional modelling of several individual objects the increase of dynamical excitation with increasing stellar luminosity is supported by Löhne et al. (2012) and Schüppler et al. (2014) who analysed a G0V-star HD 207129 and a K2V-star HIP 17439 respectively and found $\langle e\rangle$ being at the order of a few per cent. On the other hand the modellings of the A5V-star HR8799 (Matthews et al., 2014a) and the A0V-star Vega

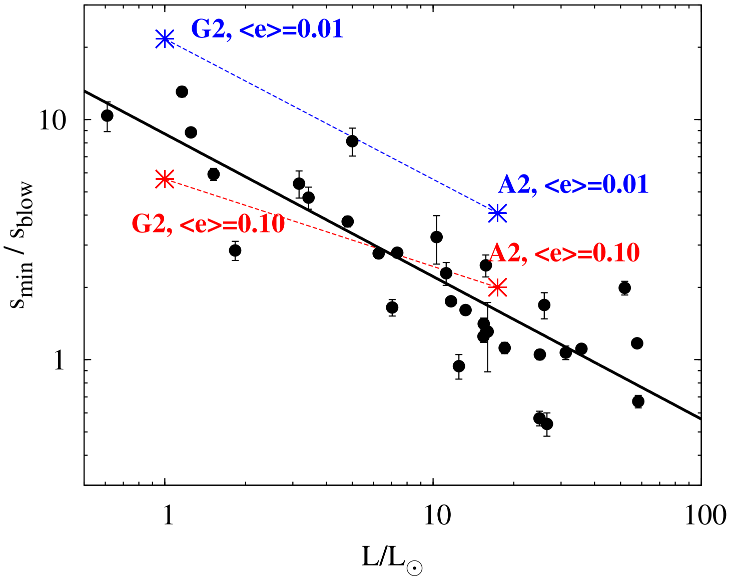

Figure 7.13: Symbols with error bars represent the discs of our sample (assuming pure astrosilicate) and the thick black line is the best-fit through these data. Asterisks mark approximate values of $s_{\mathrm{min}}/s_{\mathrm{blow}}$ extracted from ACE simulations, as described in the text. The pairs of asterisks corresponding to the same dynamical excitation, $\langle e\rangle$, are connected with dashed lines for illustrative purposes.

(Müller et al., 2010) lead to a value of $\langle e \rangle \sim 0.1$. In case of HR 8799 the higher dynamical excitation is expected since a substantial outer halo of small particles is present. However, the increase of dynamical excitation with increasing stellar luminosity is a general statistical trend. Indeed, there is a scatter for individual systems and as well there might be discs which do not follow this trend at all.

Another interesting aspect is the "self-regulation" of the $s_{\text{min}}/s_{\text{blow}}(L)$ dependence which can be explained as follows. The dynamical excitation of discs around more luminous stars is assumed to be stronger and therefore, such discs should possess more pronounced halos. These halos would lead to an overestimation of the disc radii of early-type stars since they were inferred from the images. As a consequence the dust grain sizes would be underestimated (Pawellek et al., 2014). The correction of this effect would lead to a raise of the data points on the right side of Figure 7.13 and thus to a flattening of the $s_{\text{min}}/s_{\text{blow}}(L)$ trend. In case of these discs the level of dynamical excitation would decrease. If $\langle e \rangle$ is lower, the halos are assumed to be weaker which results in a drop down of the data points of more luminous stars in Figure 7.13. The $s_{\text{min}}/s_{\text{blow}}$ ratio is smaller, the $s_{\text{min}}/s_{\text{blow}}(L)$ trend shows a steeper decrease and all is reset to the starting conditions. So this trend seems to be robust considering the uncertainties of the measured disc radii.

It should be also remarked that both, the stirring models and the surface energy models mentioned in section 7.4 depend on each other. Assuming that the stirring level is correlated with the stellar luminosity as proposed here, the surface energy constraint described in section 7.4 will be affected as well, which results in a change of the filled areas depicted in Figure 7.9. A combination of both effects to a single model would be a good way in future works, e.g., the surface energy constraint could be implemented into the above mentioned collisional code ACE, since the collisional simulations shown in this section did not include it.

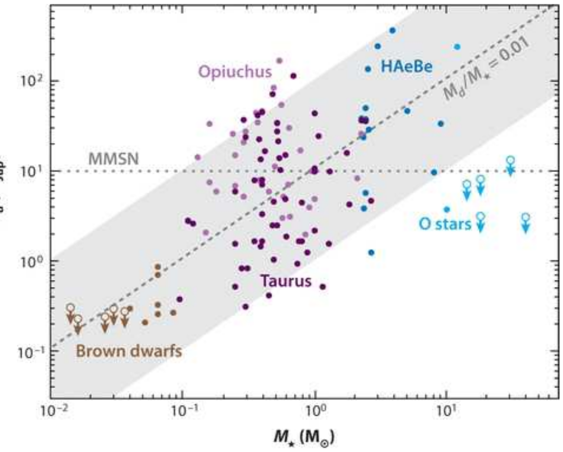

Figure 7.14: Mass of the protoplanetary disc as function of stellar mass. From Williams and Cieza (2011).

The question arises whether the correlation between the dynamical excitation and the stellar luminosity can be expected. For instance, Williams and Cieza (2011) investigated protoplanetary discs which are the progenitors of debris discs. They showed that the submillimeter dust masses in such discs are correlated with the masses of their central stars (see Figure 7.14). So there is a possibility that discs around more massive, high-luminosity stars possess a larger mass and therefore could form a larger number of large planetesimals. In debris discs these large planetesimals could act as stirrers (the so-called "self-stirring scenario", e.g., Wyatt, 2008; Kennedy and Wyatt, 2010), which is supported by simulations of planetesimal accretion (e.g., Kenyon and Bromley, 2008). The protoplanetary discs may not only be more successful in the formation of large planetesimals but also in building more massive giant planets. In the past, these planets could have been subject to scattering or vigorous migration resulting in a higher dynamical excitation of debris discs (the “planetary stirring scenario”, e.g., Mustill and Wyatt, 2009). Supporting results for this theory come from both observational (e.g., Johnson et al., 2010; Reffert et al., 2015) and theoretical investigations (e.g., Ida and Lin, 2005; Kennedy and Kenyon, 2008; Alibert et al., 2011; Mordasini et al., 2012), who concluded that more massive stars possess giant planets more frequently and that the typical planet mass is larger. Nevertheless, the above mentioned possibilities have to be tested further in order to validate them.

8 Application to radii of unresolved discs

In the last chapter we analysed the grain size ratio - stellar luminosity trend and tried to explain its cause by investigating different technical and physical effects. Now we will concentrate on another trend found and described briefly in section 6.2.3, the ratio of the disc radius to the blackbody radius, Γ, as a function of stellar luminosity. It was shown in Figure 7.1b for the whole sample of 39 resolved debris discs and different dust compositions. Its existence allows us to estimate the radii of debris discs which could not be spatially resolved yet. Refering to section 7.3, we will analyse possible outliers at first in order to investigate the influence of individual objects. Then, we will give a recipe for the estimation of the "true" disc radius of unresolved discs followed by an application to resolved discs not included in the sample used in this work.

8.1 Outliers

8.1.1 Low-luminosity stars

As mentioned in sections 6.2.2 and 6.3, the radii ratios for stars with a stellar luminosity smaller than 1 $L_\odot$ are smaller than expected from the trend line, which is partially explainable by the absorption properties of the dust grains. Thus, the correlation found between the radius ratio and the stellar luminosity is not the same for low-luminosity stars as for stars with higher stellar luminosities. In Figure 8.1 the influence of the low-luminosity stars on the trend line is depicted. While the slope

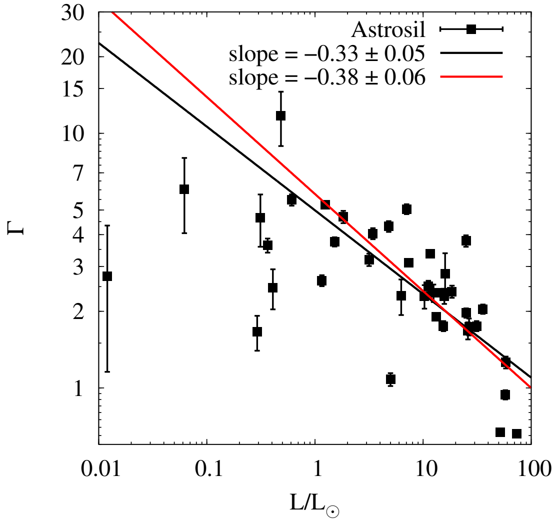

Figure 8.1: Radius ratio as function of stellar luminosity. Black filled squares with error bars show the 39 data points. The black solid line shows the best log-log fit through the symbols. The red solid line shows the best log-log fit for objects with $L > 1\ L_\odot$. Pure astrosilicate was assumed.

for the whole sample is -0.33 ± 0.05 using pure astrosilicate, it is changed to -0.38 ± 0.06 when all stars with $L < 1\ L_{\odot}$ are excluded. Taking the uncertainties of the fit into account both lines show a similar trend. The small influence of the low-luminosity stars on the trend can be explained by larger uncertainties of their radius ratio. In order to get a reliable estimate of the radii of unresolved discs we will exclude all stars with $L < 1\ L_{\odot}$. Hence, 31 objects remain in the sample used for the radius estimate.

8.1.2 Other outliers

After excluding the low-luminosity stars from the sample we investigate the influence of the remaining stars on the trend. Therefore, we will use the same method as described in section 7.2. Figure 8.2 shows the result of this analysis. The influence of individual objects is relatively small. The strongest outliers are HD 104860, Vega, and β Tri. Interestingly, η Crv is an obvious outlier, but causes no significant change in the trend line. This is a slightly different result than reported in Pawellek and Krivov (2015) and can be explained by an improvement of the error analysis of the SED fit process. While in Pawellek and Krivov (2015) η Crv had a small uncertainty compared to the other discs the new calculation led to smaller uncertainties for most of the data points making the trend more robust against the influence of individual systems. This is supported by Figure 8.2 where the slope values of the different trend lines in the right panel show similar results within the uncertainties. In order to make the trend as robust as possible we will exclude all five outliers, namely q^1 Eri, HD 104860, η Crv, Vega and β Tri, which reduces the sample size to 27.

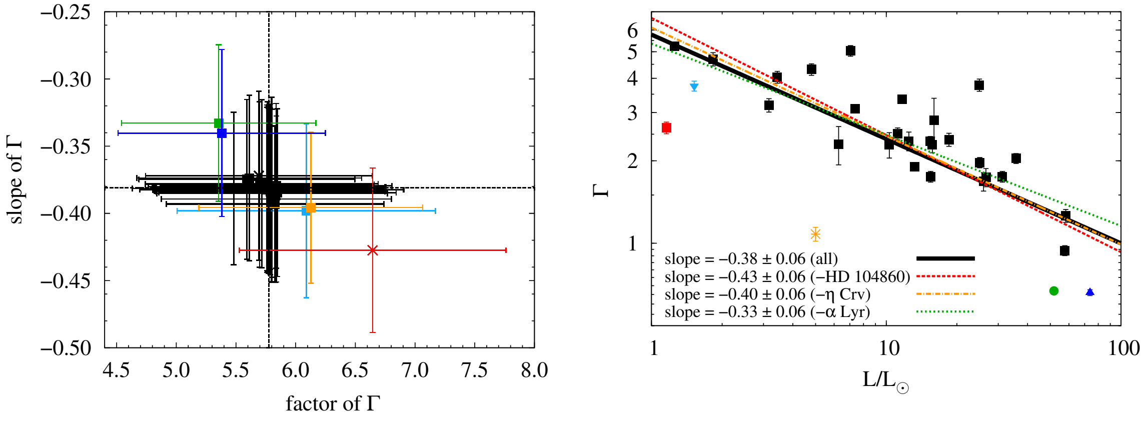

Figure 8.2: Identification of outliers in $s_{\mathrm{min}}/s_{\mathrm{blow}}(L)$ for pure astrosilicate. Left: the factors A and slopes B of the trend lines in the form $A\ (L/L_{\odot})^{B}$, calculated by excluding from the sample one data point at a time. Error bars are uncertainties in A and B returned by the fitting. The "cross-hairs" depict the best fit through the whole sample. The strongest outliers are shown in colour: red is HD 104860, light blue is HD 10647, orange is η Crv, green is Vega, and blue is β Tri. Right: size ratio versus stellar luminosity for pure astrosilicate with and without outliers. The colour coding is the same as on the left. The black line gives the trend line for the entire sample. The line of a certain colour is the best fit without the object of the same colour. The removal of HD 10647 or η Crv lead to similar regression lines as well as the removal of Vega or β Tri. Therefore, only the result for the removal of η Crv and Vega are shown.

8.2 Influence of dust compositions

We assume the best-fit relation between Γ and the stellar luminosity as

$$\Gamma = A\ (L/L_\odot)^B\,. \tag{8.1}$$

The values of the power law coefficients A and B are given in Table 8.1 for the sample of 27 objects. The trend lines for all dust compositions show a similar slope taking the uncertainties into account. While in Pawellek and Krivov (2015) astrosilicate showed the steepest trend with $A = 8.26 \pm 1.27$ and $B = -0.55 \pm 0.04$ it changed to $A = 6.49 \pm 0.86$ and $B = -0.37 \pm 0.05$ in this work. Reasons are the improvement of the error calculation process during the SED fitting and the improvement of the derivation of the true disc radius compared to Pawellek et al. (2014). Now, the composition of astrosilicate and ice possesses the steepest trend with $A = 8.38 \pm 1.20$ and $B = -0.44 \pm 0.05$. Compared to Pawellek and Krivov (2015), where the standard deviation of the slope was 0.07, the trend lines calculated in this work are not as much influenced by the different dust compositions. The standard deviation of the slope is now 0.03.

Table 8.1: Power-law coefficients for the Γ ratio

Dust composition	A	B
50% astrosilicate + 50% vacuum	6.93 ± 0.84	-0.40 ± 0.04
50% astrosilicate + 50% ice	8.38 ± 1.20	-0.44 ± 0.05
100% astrosilicate	6.49 ± 0.86	-0.37 ± 0.05
50% astrosilicate + 50% carbon	6.15 ± 0.76	-0.36 ± 0.05
100% carbon	6.43 ± 0.71	-0.40 ± 0.04

After analysing the radius ratio trend with increasing stellar luminosity we are now going to use the results described above in order to estimate the disc radii of unresolved debris discs.

8.3 Estimation of unresolved disc radii

8.3.1 Calculation recipe

The disc radius gives information about formation processes of planetesimals and planets and thus, it is an important parameter for modelling debris discs. Unfortunately, most of the known debris discs are unresolved and therefore, it is useful to have a possibility to estimate the disc radius of such discs. The correlation between the ratio of true to blackbody radius and stellar luminosity gives us a good chance to do that.

We will use the following steps in order to estimate the disc radius. At first it is necessary to derive the dust temperature T_d of the disc. This can be done by a SED fit of the disc with one or another disc model, for instance, the modified blackbody radiation model (Backman and Paresce, 1993). Another way is to estimate the temperature from the wavelength λ_max of the maximum excess emission by $T_\mathrm{d} = 5100\,\mathrm{K}(1\,\mu\mathrm{m}/\lambda_\mathrm{max})$. After deriving the dust temperature it is possible to calculate the blackbody radius of the disc with help of the bolometric luminosity and

$$R_\mathrm{BB} = \left(\frac{278\,\mathrm{K}}{T_\mathrm{d}}\right)^2 \left(\frac{L}{L_\odot}\right)^{1/2}\ \mathrm{AU}. \tag{8.2}$$

Equation (8.1) was used in the last section to describe the correlation between the radius ratio and the stellar luminosity. Now, it can be used to compute the "true" disc radius by multiplying Γ by R_{BB} with help of the coefficients A and B given in Table 8.1. Since the coefficients depend on the dust composition, the most appropriate should be chosen. The SED fit can give some hints in that case if several dust compositions are tested. The composition delivering the smallest χ^2 value is often assumed as the best choice.

The described recipe for the radius estimation has to be tested in order to check the reliability of it. Therefore, we will use resolved discs which were not included in the sample of this work to derive Γ. The radii of these discs are known and so we have a possibility to compare the radii reported in the literature and measured from the resolved images with the calculated ones.

8.3.2 Application to resolved discs

We arbitrarily chose three discs resolved in scattered light in order to check the reliability of the radius estimation. Since their radii were not inferred from the measurements of the *Herschel*/PACS instrument these discs are the most suitable objects to test the method described above. The discs are around the G2V star HD 107146 (taking the data from Ardila et al., 2004; Williams et al., 2004; Ertel et al., 2011), the F5V star HD 181327 (Schneider et al., 2006; Lebreton et al., 2012), and the A7 star HD 32297 (Kalas, 2005; Schneider et al., 2005; Donaldson et al., 2013). For all discs we calculated the "true" disc radius for all five dust compositions used in this work. The results are listed in Table 8.2. The estimate of the true disc radius gives reasonable results for all three discs. While the recipe leads to a large overestimate in case of the solar-type star, it delivers a value close to the true one for the A-star. The low-luminosity stars show a different behaviour in the Γ-trend due to the absorption properties of their dust. Thus, the radius estimate is not appropriate for these stars. Since HD 107146 has a stellar luminosity close to the cut-off luminosity of 1 $L_\odot$ for this method the estimate is not as good here as for the other two stars with higher stellar luminosities.

Table 8.2: Resolved discs used to test the $\Gamma(L)$ relation.

HD number	$L/L_\odot$	$T_{\mathrm{d}}[K]$	R_{BB}[AU]	Γ_{pred}	R_{pred}[AU]	R_{true}[AU]
107146	1.1	51	31	6.7 (astrosil+vacuum) 8.0 (astrosil+ice) 6.3 (astrosil) 5.9 (astrosil+carbon) 6.2 (carbon)	208 (astrosil+vacuum) 248 (astrosil+ice) 195 (astrosil) 183 (astrosil+carbon) 192 (carbon)	130
181327	3.3	73	26	4.3 (astrosil+vacuum) 5.0 (astrosil+ice) 4.2 (astrosil) 4.0 (astrosil+carbon) 4.0 (carbon)	112 (astrosil+vacuum) 130 (astrosil+ice) 109 (astrosil) 104 (astrosil+carbon) 104 (carbon)	89
32297	5.3	83	26	3.6 (astrosil+vacuum) 4.0 (astrosil+ice) 3.5 (astrosil) 3.4 (astrosil+carbon) 3.3 (carbon)	94 (astrosil+vacuum) 104 (astrosil+ice) 91 (astrosil) 88 (astrosil+carbon) 86 (carbon)	110

At this point it seems that the dust composition of astrosilicate and ice would be a poor choice for the estimation of the true disc radius. But here, the object HD 95086 leads to the large regression parameters A and B. If we remove this data point from the sample, the values of the regression change to $A = 7.00 \pm 0.67$ and $B = -0.39 \pm 0.03$. Using them instead of the values given in Table 8.1 the disc radii of the three resolved discs are 209 AU for HD 107146, 114 AU for HD 181327 and 95 AU for HD 32297. These results are more comparable to the estimation by the composition of astrosilicate and vacuum. These two mixtures are often used in the literature (e.g, Lebreton et al., 2012; Donaldson et al., 2013) instead of pure astrosilicate, but since the derived disc radii for all dust compositions are close to each other the choice of the mixture seems to play a minor role here. On the other hand, the sample size from which the correlation coefficients were calculated is quite small. Therefore, it would be necessary to enlarge the sample and to check whether conclusions about the dust composition are possible.

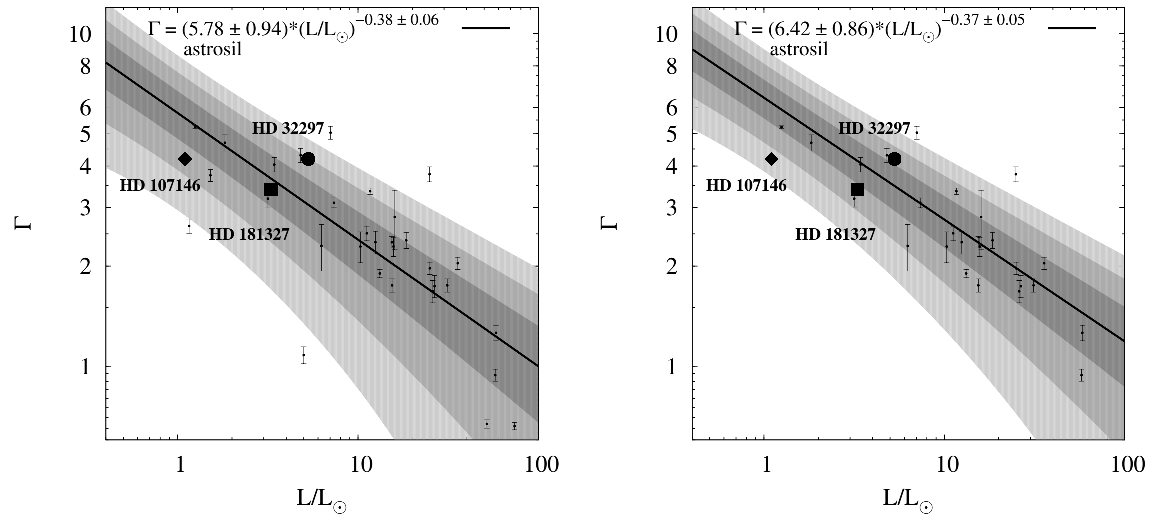

Figure 8.3: The predicted ratio of the true disc radius to the blackbody radius, Γ, for pure astrosilicate. The solid line is the best-fit relation, Eq. (8.1). The areas filled with dark-, medium-, and light-grey are $1\sigma-$, $2\sigma-$, and $3\sigma-$confidence areas for that relation, respectively. The symbols show the actual Γ values (i.e., observed versus blackbody radius) for three selected test discs. Unlabeled small symbols with error bars are fitting results for the discs in our sample, for the same dust composition. These are the same as blue symbols in Fig. 7.1b. Left: the sample excluding stars with $L < 1L_{\odot}$. Right: five outliers (HD 10647, HD 104860, η Crv, Vega, and β Tri) excluded.

In Figure 8.3 the three resolved discs are put onto the Γ-plot of pure astrosilicate, where in addition the confidence levels of $\Gamma(L)$ are given. HD 107146 as worst estimate is a $\approx 3\sigma$-outlier and shows that for low stellar luminosities an over- or underestimate up to 60% is possible. In case of more luminous stars the estimate is more accurate. In the literature the blackbody radius is often used as first guess of the disc radius, but as shown above our proposed method of radius estimation is in any account a better way comparing the results of Table 8.2, where e.g., for HD 32297 $R_{\mathrm{BB}} = 26$ AU while $R_{\mathrm{disc}} = 110$ AU.

9 Conclusions and summary

In this work we analysed a sample of 39 debris discs around AFGKM-type stars with the goal of finding correlations between stellar and disc parameters. All discs of the sample are well resolved and therefore, we were able to derive their disc radii with a newly invented method, which made it possible to break the degeneracy between the dust grain size and the location of dust in SED modelling. At time of this writing the sample chosen was the largest of resolved debris discs ever analysed.

The SEDs were fit with two different methods, the modified blackbody approximation (MBB) where the dominant grain size is assumed to be $\lambda_0/(2\pi)$ and the size distribution (SD) where the dominant grain size is given by s_{min}. Since there is a degeneracy between dust grain size and dust composition as well we were able to break it due to the usage of five different dust compositions, namely pure carbon, pure astrosilicate, mixtures of astrosilicate and ice, astrosilicate and vacuum and astrosilicate and carbon. The results of the analysis are as follows:

Disc radii and radius ratio

A comparison of the results achieved with the above mentioned radius estimation in Chapter 5 and the radius values reported in the literature led to the conclusion that the newly invented method of radius estimation can be applied to all debris discs without constraints to the spectral type or distance to the observer. Even for marginally resolved discs the method led to reasonable results.

The inferred disc radii show a large dispersion over the whole luminosity range of the host stars and we could not find a significant correlation between them and the stellar luminosity. Small disc radii can be found around late- and early type stars as well as large disc radii. Thus, the final shape of a debris disc seems to depend on processes like collisional evolution or sculpting by planets rather than temperature-driven processes which play a more important role during the formation of planetary systems.

Furthermore, we found a decrease of the true to blackbody radius ratio as a function of stellar luminosity. Since the blackbody radius can easily be inferred from the SED the correlation found gives a recipe for the estimation of the true disc radius of unresolved debris discs. With this it is possible to break the degeneracy between the grain size and the dust location.

SED models

We could fit all SEDs with a more or less high goodness of fit for both models (MBB and SD) and found that for statistical analyses of disc temperatures or blackbody radii the fit method only plays a minor role. In terms of grain sizes the MBB method only estimates the dominant particle size, whereas the SD method uses it directly. Therefore, some differences can be found in the correlations, but in general these are robust against both fit methods. For individual discs the fit method is more important since it can make a difference between a one or two component system which was the case for AU Mic for instance.

Dust temperature

We found a systematic increase of the dust temperature with increasing stellar luminosity for both fit methods and for all dust compositions used. The ratio of dust to blackbody temperature decreases towards stars of earlier spectral types which is related to the decrease of the true-to-blackbody-radius ratio with stellar luminosity.

Minimum size of dust grains and grain size ratio

We found a slight increase of the minimum grain size with increasing stellar luminosity, but the assumption of a constant grain size with $s_{\mathrm{min}} \approx (5 \pm 3)\,\mu\mathrm{m}$ is also reasonable. However, theory predicts an even stronger increase of the minimum grain size since the radiation pressure becomes stronger towards more luminous stars. Caused by this small increase, the minimum-to-blowout-grain-size ratio shows a decrease with increasing stellar luminosity. This was the strongest correlation found in this work and it is robust against the variation of dust composition and porosity. It flattens for a higher degree of porosity, but cannot be erased, which was shown by the usage of a 90% porosity composition. The fit results using this extreme composition were unrealistical and the χ^2-values for the SED fit were quite large, so that there was no way in eradicating the grain size ratio trend.

We used subsamples in order to check whether the grain size ratio trend shows a different shape for different disc parameters and investigated therefore discs with lower and higher fractional luminosity, smaller and larger radii, younger and older ages, lower and higher absolute integrated flux density, lower and higher absolute surface brightness, and marginally and well resolution. Except for lower and higher fractional luminosity and lower and higher absolute integrated flux density the subsamples are statistically indistinguishable in terms of $s_{\mathrm{min}}/s_{\mathrm{blow}}(L)$. The differences for fractional luminosity and absolute integrated flux density seem to be more related to SED fit effects than to physical causes and are related to each other.

Since we could not find technical or statistical reasons for the grain size ratio trend we suppose physical causes for it. Hence, the role of the surface energy constraint on the size of smallest collisional fragements and the role of stirring of dust-producing planetesimals were investigated. The former effect may be responsible for a lack of particles with a small $s_{\mathrm{min}}/s_{\mathrm{blow}}$-ratio in discs around late-type stars, but a recent study showed that the global influence of the surface energy constraint is only of small relevance. On the other hand, the $s_{\mathrm{min}}/s_{\mathrm{blow}}(L)$ trend was confirmed by collisional simulations and thus, the degree of stirring may be related to the grain size ratio trend. A conclusion would be that discs around more luminous stars are more strongly excited than around low-luminosity stars and so the protoplanetary discs of more massive young stars may be more efficient in building large planetesimals or planets which act as stirrers at later evolutionary stages.

Both explanations, the microphysical (surface energy) and the macrophysical (stirring) one are related to each other, since they involve small grain dynamics which is set by radiation pressure. Hence, a combination of both could be done in future work in order to improve the analysis of the $s_{\mathrm{min}}/s_{\mathrm{blow}}(L)$ trend.

It might be also possible that alternative explanations for this trend exist. Several fit parameters of the disc, e.g., chemical composition, tensile strength or degree of porosity, could vary with the type of central star, but up to now, there is no observational evidence for such correlations and theoretical expectations do not support this assumption as well. An example are the progenitors of debris discs around early and late-type stars, Herbig Ae/Be stars and T Tau stars. The dust compositions of their cold disc parts show no evidence for systematic differences (e.g., Dutrey et al., 2014).

Size distribution index

The opacity index of the MBB model shows values between 0.3 and 2.0 for the whole sample of resolved debris discs which confirms previous determinations based on sub-mm data. Considering the SD method, the values of the index q lie between 3.0 and 4.5 for most of the debris discs using pure astrosilicate, but there are more extreme values as well (η Crv: $q = 2.9$ and 30 Mon: $q = 6.6$). Considering other dust compositions the variation of q is only minor. In general, q is roughly consistent with results from detailed collisional modelling, but there it changes with the particle size, whereas in the SD method only one q is used for the whole grain size range. Therefore, differences between the results of collisional modelling and SD method are evident.

Dust composition

As mentioned before, the correlations found between disc and stellar parameters are robust against the variation of the dust composition not considering extreme porosity. An extreme mixture of 90% vacuum and 10% astrosilicate led to large χ^2 values in the SED fits and gave unrealistical fit results. Therefore, no conclusions can be made in this case.

On the other hand, the dust composition is important for the modelling of individual systems. Here, astrosilicate was used as a kind of "reference material" for all discs, but it is not the best choice since it is a designed material for the description of observations of the interstellar medium (Draine and Lee, 1984). As such it does not exist in nature and has no justification for the application to circumstellar discs may it a protoplanetary or a debris one. The modelling of individual systems shows that pure astrosilicate fits SEDs more poorly than combinations with ice, carbon and vacuum (e.g., Lebreton et al., 2012; Donaldson et al., 2013; Morales et al., 2013; Schüppler et al., 2014, among many others).

Summary and outlook

One general conclusion of this thesis is that the statistical modelling of debris discs is not as easy as it seems, since each disc is an individual system with its own peculiarities. An example is the star β Tri, which possesses the highest stellar luminosity in the sample, is one of only two giants and a close binary as well. Nevertheless, all these individuals seem to follow general trends, that are robust against the variations of fit method or dust composition.

With 39 well-resolved debris discs the sample chosen for this analysis can be increased by several other resolved discs in future works in order to make the correlations found even more robust. It is also possible to derive an improved "reference material" as dust composition for debris discs, leading to more reliable results in SED fitting of individual discs. Furthermore, the investigation of correlations of a sample of collisionally modelled discs would be interesting. At time of this writing, HIP 17439, AU Mic, HD 207129, q^1 Eri and Vega were modelled with the collisional code ACE, but in the future more discs will be done.

Appendices

AppendixA Photometry of the systems

Table A.1: Mid-IR Photometry Used in Creating the Target SEDs

Target (HD)	Flux [mJy]							
Wavelength	11.56μm	16μm	18μm	22μm	22.09μm	24μm	31μm	Note
Instrument	b	a	c	a	b	d	a	
GJ 581	213 ± 19	108 ± 1	...	58.8 ± 1.0	...	...	31.4 ± 1.3	(3)
197481	543 ± 60	...	246 ± 36	183 ± 21	...	158 ± 3	...	
128311	268.6 ± 3.686	140.0 ± 4.0	...	74.98 ± 2.94	74.20 ± 1.76	61.00 ± 3.000	37.04 ± 1.260	(2)
192263	176.47 ± 2.28	101.7 ± 3.07	...	52.70 ± 2.79	52.41 ± 2.12	43.80 ± 3.000	27.05 ± 3.57	(2)
92945	177.5 ± 2.435	100.2 ± 6.87	...	54.63 ± 10.94	50.12 ± 1.590	39.20 ± 3.89	26.55 ± 3.88	(2)
23484	314.4 ± 5.2	172 ± 6	...	90.3 ± 8.4	90.4 ± 2.0	80.47 ± 5.09	56.6 ± 15.4	(2)
131511	867.6 ± 11.20	...	384.0 ± 18.80	...	240.1 ± 5.033	193.0 ± 3.930	...	
166	708.5 ± 16.13	324 ± 11	273.0 ± 29.40	182 ± 4	187.1 ± 4.258	155.0 ± 3.160	120 ± 4	(2)
104860	81.1 ± 1.1	44.49 ± 2.93	...	24.73 ± 3.53	23.3 ± 1.1	21.54 ± 2.91	13.36 ± 3.10	
207129	635 ± 8	371 ± 5	262 ± 31	197 ± 4	196 ± 5	155 ± 3	114 ± 5	(2)
10647	600.2 ± 7.7	...	315.3 ± 39.7	...	218.1 ± 4.0	184.8 ± 3.8	185.4 ± 7.3	
48682	774 ± 11	425 ± 12	458 ± 17	240 ± 5	246 ± 5	193 ± 4	152 ± 4	(2)
50571	303 ± 4	152 ± 4	129 ± 12	82.7 ± 5.0	85.4 ± 1.9	70.4 ± 2.8	48.0 ± 4.0	(2)
170773	262 ± 3	136 ± 5	...	78.4 ± 5.7	76.4 ± 2.2	65.3 ± 2.6	54.6 ± 6.0	(2)
218396	258 ± 4	140 ± 2	119 ± 80	91.3 ± 2.3	94.7 ± 2.8	86.6 ± 1.7	68.0 ± 2.3	(2)
109085	1460 ± 70	...	820 ± 20	...	680 ± 40	590 ± 20	...	(4)
27290	1269.12 ± 9.35	704.8 ± 12.7	...	263.3 ± 8.9	367.76 ± 7.11	315.6 ± 3.2	...	
95086	62.7 ± 3.0	...	...	46.7 ± 7.3	51.6 ± 3.3	45.6 ± 2.0	96.7 ± 10.0	(1)
195627	761 ± 10	439.6 ± 8.3	325 ± 13	248.5 ± 6.7	237 ± 5	186 ± 7	159.46 ± 4.85	
20320	...	333.5 ± 6.6	263.5 ± 56.0	186.8 ± 5.0	...	162.6 ± 4.2	109.18 ± 2.94	
21997	106.6 ± 5.2	...	...	...	57.2 ± 3.7	55.1 ± 2.2	92.3 ± 10.3	(1)
110411	247.4 ± 7.2	...	204.2 ± 18.3	162.8 ± 6.0	...	149.7 ± 3.9	...	
142091	...	...	...	...	890.4 ± 13.1	800.1 ± 8.0	...	
102647	...	2989 ± 48	...	1724 ± 30	...	1647 ± 33	...	
125162	...	442 ± 5	415.7 ± 15.6	310 ± 6	...	270.8 ± 2.3	276 ± 6	(2)
216956	...	6947 ± 112	5338 ± 81.8	3940 ± 64	...	3502 ± 64	...	(4)
17848	315 ± 4	177.3 ± 3.6	105 ± 10	99.82 ± 2.75	102 ± 2	88.68 ± 2.44	68.26 ± 1.87	
9672	211 ± 21	...	...	...	238 ± 24	259 ± 10	426 ± 1	(1)
71722	141 ± 2	85.67 ± 1.83	...	65.16 ± 1.81	63.4 ± 2.1	62.53 ± 1.73	76.70 ± 1.94	
182681	180 ± 2	...	...	...	123 ± 3	...	...	
14055	...	443 ± 11	372.2 ± 22.1	315 ± 6	...	282.66 ± 6.63	317 ± 6	(2)
161868	1160 ± 15	643.6 ± 12.6	...	463.3 ± 11.4	474 ± 9	438.5 ± 10.9	...	
188228	...	385 ± 12	296.6 ± 31.0	206.8 ± 7.3	...	170.75 ± 0.55	128 ± 14	(2)
10939	322 ± 4	177 ± 4	...	116 ± 5	121 ± 3	104 ± 2	114 ± 5	(2)
71155	...	455 ± 10	398.4 ± 19.5	337 ± 9	...	307 ± 3	296 ± 4	(2)
172167	...	...	...	...	...	8900 ± 89	...	(4)
139006	...	2331 ± 39	1823 ± 38	1375 ± 25	...	1261.63 ± 15.46	964.16 ± 7.07	
95418	3283 ± 27	1770 ± 42	1546 ± 21	1060 ± 31	1167 ± 25	1026 ± 14	743 ± 26	(2)
13161	...	1530 ± 34	1141 ± 31	896 ± 19	...	791.5 ± 16.0	669 ± 24	(2)

Notes:

All values and error bars are taken from the literature as they were published. For instance, *WISE* error bars for different objects may or may not include the calibration uncertainty. (1) For these stars, more photometry points extracted from the IRS spectra have been published. Although not given in the table, these were included in the SED fitting. (2) For these stars, we took the IRS spectra from CASSIS (Lebouteiller et al., 2011). The spectra of objects taken in mapping mode were reduced as in Moór et al. (2013a,b). For those observed in low-resolution staring mode we made additional steps (outlier detection, module stitching) as described in Moor et al. (in prep.). In both cases, we then took averages in the wavelength ranges 15–17, 21–23, and 30-32 microns to extract the photometry points. (3) This object was observed in high resolution staring mode. Since no CASSIS spectrum is available, we used its Spitzer Science Center IRS Enhanced Product, performed the usual post-processing steps, and then extracted the photometry points. (4) For these stars, IRS spectra in different observing modes have been taken (Lebreton et al., 2013; Su et al., 2013b; Chen et al., 2014; Duchêne et al., 2014). However, the resulting fluxes are not given in the literature, except for two photometry points for HD 216956. We decided not to reduce the data by ourselves because of the large spatial extent and brightness of the objects (saturation effects). *Instruments:* (a) *Spitzer*/IRS; (b) *WISE*; (c) *AKARI*; (d)*Spitzer*/MIPS.

References: WISE from Wright et al. (2010); Moór et al. (2013a,b); Bonsor et al. (2013); *Spitzer*/IRS from Moór et al. (2013a,b); Roberge et al. (2013); Chen et al. (2014); AKARI from Ishihara et al. (2010); *Spitzer*/MIPS from Su et al. (2006); Trilling et al. (2007); Chen et al. (2012); Eiroa et al. (2013); Moór et al. (2013a,b); Bonsor et al. (2013).

Table A.2: Far-IR and Sub-mm Photometry Used in Creating the Target SEDs

Target (HD)	Flux [mJy]									
Wavelength	70μm	70μm	100μm	160μm	250μm	350μm	450μm	500μm	850μm	870μm
Instrument	a	b	b	b	c	c	d	c	d	e
GJ 581	20.0 ± 5.3	18.9 ± 1.4	21.5 ± 1.5	22.2 ± 5.0	< 24.0	< 26.0	...	< 27.0	...	...
197481	227 ± 27	231.3 ± 16.3	...	243 ± 17	134 ± 8	84.4 ± 5.4	85 ± 42	47.6 ± 3.8	14.4 ± 1.8	...
128311	21.00 ± 3.200	23.00 ± 5.400	...	25.90 ± 2.000	...	...	...	...	...	...
192263	22.30 ± 5.000	19.50 ± 2.200	...	7.100 ± 1.800	...	...	...	...	...	...
92945	298.0 ± 45.00	267.5 ± 13.40	...	276.5 ± 13.40	...	...	...	...	...	...
23484	99.1 ± 8.4	74.5 ± 3.8	91.3 ± 4.7	91.9 ± 4.9	53.0 ± 10.4	32.2 ± 8.9	...	< 21.6	...	...
131511	42.70 ± 6.700	36.80 ± 3.800	25.00 ± 2.100	14.40 ± 3.200	...	...	...	...	...	...
166	103.0 ± 7.830	96.50 ± 4.800	54.60 ± 3.900	22.20 ± 2.700	...	...	...	...	...	...
104860	183.1 ± 7.4	...	277.0 ± 3.5	243.4 ± 5.2	...	50.1 ± 15.0	47.0 ± 14.0	...	6.8 ± 1.2	...
207129	278.2 ± 21.5	284.0 ± 1.5	311 ± 1	211.0 ± 1.5	113 ± 18	44.3 ± 9.0	...	25.9 ± 8.0	...	5.1 ± 2.7
10647	863.4 ± 58.7	896.2 ± 26.9	897.1 ± 26.9	635.9 ± 31.8	312.3 ± 25.6	179.9 ± 14.6	...	78.4 ± 9.8	...	39.4 ± 4.1
48682	262.8 ± 18.3	264.0 ± 4.1	252.3 ± 3.2	182.1 ± 3.8	90 ± 15	25 ± 8	...	< 24.0	5.5 ± 1.1	...
50571	248.8 ± 18.7	223.9 ± 17.4	262.9 ± 19.7	188.5 ± 16.7	71.1 ± 7.3	46.2 ± 7.0	...	13.6 ± 7.4	...	...
170773	787.9 ± 56.0	806.7 ± 56.8	1109.9 ± 78.3	875.2 ± 61.5	379.1 ± 21.6	167.8 ± 11.2	...	73.9 ± 7.3	...	18.0 ± 5.4
218396	610.0 ± 31.0	537 ± 15	687 ± 20	570 ± 50	309 ± 30	163 ± 30	...	74 ± 30	10.3 ± 1.8	...
109085	198 ± 7	230 ± 13	252 ± 16	231 ± 13	...	...	58 ± 10	...	15.5 ± 1.4	...
27290	170.7 ± 8.1	171.0 ± 8.7	148.4 ± 7.7	134.3 ± 14.1	52.5 ± 6.5	23.5 ± 8.0	...	< 16.7	...	...
95086	654.6 ± 44.4	690.1 ± 48.6	675.1 ± 47.6	462.4 ± 32.7	213.4 ± 12.9	120.3 ± 8.7	...	63.6 ± 10.2	...	41.3 ± 18.4
195627	609.0 ± 60.9	630.0 ± 44.5	607.9 ± 43.5	405.4 ± 29.3	145.9 ± 14.1	70.9 ± 7.7	...	34.1 ± 7.5	...	13.0 ± 7.0
20320	103.0 ± 8.0	93.9 ± 5.8	84.1 ± 5.9	42.1 ± 0.8	...	...	...	...	...	...
21997	663.7 ± 46.0	697.6 ± 49.2	665.4 ± 47.5	410.8 ± 30.0	151.4 ± 11.0	66.7 ± 9.5	...	33.1 ± 9.4	8.3 ± 2.3	...
110411	248.0 ± 2.2	230.1 ± 4.3	154.2 ± 7.0	67.3 ± 7.0	37.9 ± 0.8	22.7 ± 0.5	...	20.3 ± 0.4	...	...
142091	426.2 ± 22.3	...	335.0 ± 16.0	192.0 ± 10.0	...	...	...	...	...	...
102647	743.0 ± 52.0	...	480.0 ± 30.0	215.0 ± 32.0	51.0 ± 12.0	< 39.0	< 50.0	< 15.0	< 6.0	...
125162	364.7 ± 3.9	345.3 ± 17.3	272.1 ± 15.4	142.4 ± 12.1	50.7 ± 5.1	21.3 ± 5.3	...	4.2 ± 4.9	...	...
216956	9057.1 ± 736.4	10800 ± 900	...	6200 ± 600	2700 ± 300	1100 ± 100	595 ± 35	500 ± 50	97 ± 5	...
17848	...	213.8 ± 17.1	210.8 ± 18.1	138.5 ± 11.4	50.9 ± 5.9	28.8 ± 6.4	...	6.8 ± 10.1	...	...
9672	...	2142.0 ± 58.0	...	1004.0 ± 53.0	372.0 ± 27.0	180.0 ± 14.0	...	86.0 ± 9.0	8.2 ± 1.9	...
71722	155 ± 4	...	120.5 ± 4.1	46.9 ± 8.7	...	...	...	...	...	...
182681	...	607.8 ± 42.8	463.2 ± 33.3	243.0 ± 18.2	84.3 ± 7.2	30.1 ± 5.4	...	8.2 ± 7.3	...	...
14055	787.8 ± 157.6	777.6 ± 38.8	718.8 ± 35.5	444.3 ± 10.4	186.6 ± 13.6	78.1 ± 7.2	...	21.8 ± 5.1	5.5 ± 1.8	...
161868	1085.2 ± 217.0	1219.4 ± 85.5	1044.5 ± 73.4	587.8 ± 44.4	177.9 ± 12.8	98.3 ± 10.1	...	57.0 ± 11.6	...	12.8 ± 5.2
188228	69.0 ± 6.1	63.1 ± 4.8	41.9 ± 4.6	23.6 ± 3.2	5.0 ± 3.9	0.7 ± 4.8	...	0.0 ± 4.7	...	...
10939	384.6 ± 16.5	396.3 ± 28.3	403.7 ± 28.8	277.9 ± 20.7	94.9 ± 7.7	43.5 ± 7.0	...	4.0 ± 6.7	...	...
71155	211.7 ± 2.8	206.2 ± 10.5	86.5 ± 5.9	25.5 ± 0.7	7.0 ± 3.4	4.2 ± 4.5	...	< 13.8	...	...
172167	11416.1 ± 2283.2	10120 ± 1180	...	4610 ± 900	1680 ± 260	610 ± 100	...	210 ± 40	45.7 ± 5.4	...
139006	542.0 ± 80.7	515.0 ± 25.2	235.1 ± 12.6	67.6 ± 2.4	...	...	...	...	...	...
95418	421.13 ± 84.23	393.0 ± 19.4	189.2 ± 9.6	58.3 ± 10.5	18.3 ± 3.9	14.1 ± 4.3	...	9.1 ± 4.7	...	...
13161	643.0 ± 51.0	641.2 ± 31.5	481.1 ± 23.4	263.6 ± 0.3	87.1 ± 7.3	34.6 ± 5.6	...	5.1 ± 4.9	...	...

Notes:

All values and error bars are taken from the literature as they were published. This explains, for instance, why non-detections are sometimes given as measured values (4.2 ± 4.9) and sometimes as upper limits (< 15.0).

Instruments:

(a) *Spitzer*/MIPS; (b) *Herschel*/PACS; (c) *Herschel*/SPIRE; (d) JCMT/SCUBA; (e) APEX/LABOCA.

References:

Spitzer/MIPS from Su et al. (2006); Trilling et al. (2007); Eiroa et al. (2013); Moór et al. (2013a,b); Bonsor et al. (2013);
Herschel/PACS and /SPIRE see Table 4.1;
JCMT/SCUBA from Sheret et al. (2004); Najita and Williams (2005); Williams and Andrews (2006);
APEX/LABOCA from Nilsson et al. (2010); Liseau et al. (2008).

AppendixB Fit results for different dust compositions

B.1 Astrosilicate and ice

	Cold Component								Warm Component			
HD	R_{disc}	s_{blow}	T_{BB}	s_{min}	q	T_{d}	$T_{\text{d}}/T_{\text{BB}}$	f_{d}	R_{disc}	T_{d}	f_{d}	χ^2_{red}
GJ 581	38	...	15	1.99 ± 1.81	3.55 ± 0.36	35 ± 7	2.35 ± 0.44	7.73	...	...	...	0.79
197481	37	...	23	0.04 ± 0.34	3.30 ± 0.03	43 ± 2	1.87 ± 0.10	40.5	...	...	...	4.63
128311	58	...	27	0.14 ± 2.29	3.08 ± 0.15	35 ± 2	1.31 ± 0.09	3.20	...	...	...	1.55
192263	53	...	28	7.59 ± 1.62	5.03 ± 0.29	69 ± 5	2.43 ± 0.16	2.43	...	...	...	0.19
92945	72	...	25	5.89 ± 1.81	3.86 ± 0.20	47 ± 2	1.85 ± 0.08	56.4	...	...	...	2.78
23484	93	...	23	2.11 ± 0.95	3.43 ± 0.08	39 ± 2	1.68 ± 0.07	8.49	...	...	...	2.32
131511	74	...	27	0.12 ± 1.40	3.49 ± 0.20	69 ± 4	2.57 ± 0.15	0.80	...	...	...	13.97
166	40	0.24	39	1.64 ± 0.42	4.13 ± 0.11	102 ± 7	2.64 ± 0.18	5.02	0.2	512	19.7	1.04
104860	113	0.61	27	8.64 ± 0.68	3.80 ± 0.05	43 ± 1	1.57 ± 0.05	55.0	...	...	...	1.38
207129	144	0.65	24	6.84 ± 0.16	4.29 ± 0.03	63 ± 3	2.57 ± 0.11	7.71	...	...	...	6.70
10647	114	0.74	29	3.44 ± 0.44	3.67 ± 0.04	63 ± 2	2.17 ± 0.07	26.1	6	123	4.19	4.93
48682	129	0.85	28	1.06 ± 0.26	3.50 ± 0.03	69 ± 1	2.44 ± 0.04	7.12	...	...	...	7.01
50571	139	1.23	31	6.28 ± 1.10	3.87 ± 0.10	63 ± 3	2.00 ± 0.09	12.1	...	...	...	1.87
170773	203	1.28	26	5.97 ± 1.25	3.90 ± 0.09	47 ± 5	1.77 ± 0.18	50.8	...	...	...	3.53
218396	282	1.58	24	6.50 ± 0.46	3.95 ± 0.05	47 ± 1	1.92 ± 0.04	27.3	3	235	7.47	6.84
109085	142	1.64	35	9.19 ± 1.94	2.63 ± 0.08	35 ± 1	1.01 ± 0.03	1.45	3	247	13.8	1.81
27290	129	1.91	39	0.01 ± 0.54	3.23 ± 0.05	69 ± 4	1.79 ± 0.09	2.07	...	...	...	6.92
95086	272	2.07	27	1.33 ± 0.25	3.61 ± 0.04	69 ± 1	2.53 ± 0.04	141	7	171	16.6	1.33
195627	171	2.17	35	5.26 ± 0.37	3.86 ± 0.05	69 ± 3	1.98 ± 0.09	9.87	2	351	4.66	2.39
20320	149	2.87	41	9.68 ± 0.82	4.20 ± 0.11	63 ± 1	1.54 ± 0.02	1.02	7	181	1.34	0.45
21997	170	3.07	39	9.34 ± 1.11	4.06 ± 0.10	63 ± 3	1.61 ± 0.07	33.4	37	83.5	17.9	0.47
110411	118	3.14	47	2.84 ± 0.26	3.93 ± 0.06	84 ± 4	1.78 ± 0.08	5.06	3	273	3.33	4.67
142091	127	3.53	46	1.37 ± 0.57	3.41 ± 0.07	69 ± 4	1.50 ± 0.08	5.40	...	...	...	8.16
102647	44	3.08	80	4.69 ± 0.16	4.40 ± 0.04	102 ± 5	1.28 ± 0.06	2.24	3	300	2.61	21.00
125162	116	3.88	51	1.97 ± 0.27	3.55 ± 0.04	84 ± 1	1.65 ± 0.02	4.24	6	217	2.08	4.76
216956	127	3.85	49	4.18 ± 0.40	3.45 ± 0.06	69 ± 1	1.42 ± 0.02	7.17	...	...	...	2.86
17848	223	3.90	37	8.67 ± 1.25	3.95 ± 0.12	63 ± 3	1.70 ± 0.08	4.19	20	124	1.92	3.38
9672	170	3.98	42	3.45 ± 0.61	3.66 ± 0.04	69 ± 2	1.63 ± 0.04	75.2	11	168	16.0	0.73
71722	128	4.43	48	2.41 ± 0.31	3.61 ± 0.06	84 ± 2	1.75 ± 0.04	9.75	4	258	4.77	1.99
182681	195	5.55	44	7.70 ± 1.52	4.05 ± 0.10	69 ± 3	1.56 ± 0.07	13.5	10	196	8.23	0.79
14055	164	5.54	48	4.18 ± 0.35	3.48 ± 0.03	69 ± 1	1.43 ± 0.02	6.42	13	170	2.54	2.59
161868	143	5.71	52	11.2 ± 1.14	3.89 ± 0.09	63 ± 2	1.20 ± 0.04	4.53	30	114	4.46	2.70
188228	102	5.83	62	1.10 ± 0.45	3.23 ± 0.09	84 ± 3	1.35 ± 0.05	0.42	...	...	...	1.60
10939	199	6.57	46	9.84 ± 1.37	3.61 ± 0.12	63 ± 2	1.35 ± 0.05	5.98	29	121	2.39	3.76
71155	85	7.24	73	6.52 ± 0.17	6.48 ± 0.12	102 ± 1	1.39 ± 0.01	1.52	15	174	1.84	1.75
172167	108	9.46	61	18.0 ± 1.45	3.77 ± 0.06	63 ± 1	1.02 ± 0.02	1.23	...	...	...	8.80
139006	61	8.49	98	9.15 ± 0.57	5.40 ± 0.38	92 ± 4	0.95 ± 0.04	0.78	19	177	0.72	2.33
95418	62	11.06	97	5.89 ± 0.51	4.12 ± 0.17	102 ± 3	1.05 ± 0.03	1.01	...	...	...	5.20
13161	154	7.80	65	21.3 ± 0.85	4.70 ± 0.21	57 ± 2	0.87 ± 0.02	1.15	43	123	2.24	3.25

Notes:
(1) The disc radii are given in AU, the temperatures in K and s_{min}, s_{blow} in µm and the fractional luminosity in 10^{-5}. (2) For the values of s_{blow} the equation of Burns et al. (1979) (see Equation (2.16)) was used with a material density of $\varrho = 2.25$ g/cm^3. Q_{pr} was averaged over the stellar spectrum. (3) The warm component is treated as blackbody. Therefore, the given R_{disc} and T_{d} are blackbody radius or temperature, respectively.

B.2 Astrosilicate and Vacuum

B.2.1 50% Astrosilicate and 50% Vacuum

	Cold Component								Warm Component			
HD	$R_{\rm disc}$	$s_{\rm blow}$	$T_{\rm BB}$	$s_{\rm min}$	q	$T_{\rm d}$	$T_{\rm d}/T_{\rm BB}$	$f_{\rm d}$	$R_{\rm disc}$	$T_{\rm d}$	$f_{\rm d}$	$\chi^2_{\rm red}$
GJ 581	38	...	15	0.03 ± 0.92	3.44 ± 0.20	43 ± 4	2.85 ± 0.23	7.23	...	...	...	0.90
197481	37	...	23	0.03 ± 0.30	3.26 ± 0.03	43 ± 2	1.87 ± 0.07	39.6	...	...	...	6.31
128311	58	...	27	0.14 ± 3.64	3.07 ± 0.22	35 ± 3	1.31 ± 0.12	3.13	...	...	...	1.56
192263	53	...	28	8.59 ± 1.98	5.35 ± 0.25	63 ± 5	2.20 ± 0.18	2.55	...	...	...	0.19
92945	72	...	25	5.89 ± 3.01	3.80 ± 0.49	47 ± 2	1.85 ± 0.08	58.1	...	...	...	2.72
23484	93	...	23	0.03 ± 0.43	3.24 ± 0.04	39 ± 2	1.68 ± 0.09	8.80	...	...	...	1.69
131511	74	...	27	0.06 ± 1.28	3.53 ± 0.19	69 ± 8	2.57 ± 0.28	0.74	...	...	...	14.00
166	40	...	39	2.55 ± 0.49	4.40 ± 0.22	92 ± 4	2.39 ± 0.11	4.68	0.2	512	20.2	1.23
104860	113	0.49	27	7.11 ± 0.82	3.58 ± 0.05	43 ± 2	1.57 ± 0.07	57.7	...	...	...	1.42
207129	144	0.55	24	3.37 ± 0.26	3.81 ± 0.03	57 ± 1	2.33 ± 0.04	8.73	...	...	...	4.29
10647	114	0.72	29	2.88 ± 0.35	3.56 ± 0.03	57 ± 2	1.98 ± 0.08	26.7	5	142	3.48	6.52
48682	129	0.87	28	0.03 ± 0.22	3.37 ± 0.03	63 ± 3	2.21 ± 0.09	7.23	...	...	...	2.94
50571	139	1.43	31	6.10 ± 0.77	3.75 ± 0.06	57 ± 3	1.82 ± 0.08	12.5	...	...	...	1.86
170773	203	1.53	26	5.26 ± 0.65	3.72 ± 0.05	52 ± 2	1.95 ± 0.06	52.9	...	...	...	2.87
218396	282	2.05	24	5.22 ± 0.34	3.78 ± 0.04	52 ± 2	2.11 ± 0.07	28.4	3	254	7.82	6.48
109085	142	2.12	35	7.58 ± 2.51	2.47 ± 0.13	35 ± 1	1.01 ± 0.03	1.53	3	253	14.0	3.05
27290	129	2.55	39	0.03 ± 0.43	3.21 ± 0.05	57 ± 4	1.48 ± 0.09	1.95	...	...	...	7.23
95086	272	2.74	27	1.39 ± 0.26	3.55 ± 0.03	63 ± 3	2.29 ± 0.10	137	7	170	16.3	1.32
195627	171	2.89	35	5.50 ± 0.44	3.73 ± 0.05	57 ± 2	1.64 ± 0.07	9.78	1	393	5.46	2.33
20320	149	3.82	41	9.61 ± 1.18	4.02 ± 0.11	63 ± 2	1.54 ± 0.06	1.09	7	184	1.33	0.41
21997	170	4.09	39	9.81 ± 1.23	3.91 ± 0.08	57 ± 2	1.47 ± 0.05	35.1	37	84	17.4	0.49
110411	118	4.18	47	4.70 ± 0.31	4.18 ± 0.10	84 ± 1	1.78 ± 0.02	4.44	6	212	3.06	5.10
142091	127	4.65	46	1.24 ± 0.58	3.36 ± 0.06	69 ± 3	1.50 ± 0.06	5.28	...	...	...	7.86
102647	44	4.67	80	5.37 ± 0.19	4.31 ± 0.03	112 ± 4	1.41 ± 0.06	2.15	3	300	2.61	19.50
125162	116	5.27	51	3.05 ± 0.32	3.56 ± 0.04	76 ± 3	1.50 ± 0.05	3.81	8	193	2.29	4.10
216956	127	5.21	49	4.44 ± 0.48	3.33 ± 0.05	63 ± 2	1.29 ± 0.03	7.04	...	...	...	2.77
17848	223	5.37	37	9.31 ± 1.88	3.83 ± 0.12	57 ± 2	1.54 ± 0.06	4.31	20	124	1.91	3.58
9672	170	5.42	42	3.27 ± 0.55	3.55 ± 0.03	69 ± 1	1.63 ± 0.02	77.8	10	171	14.3	1.22
71722	128	6.02	48	4.27 ± 0.39	3.80 ± 0.09	76 ± 2	1.59 ± 0.04	8.82	6	226	5.09	1.91
182681	195	7.55	44	3.92 ± 0.88	3.74 ± 0.07	76 ± 3	1.72 ± 0.07	18.6	9	210	7.11	0.88
14055	164	7.59	48	4.72 ± 0.40	3.37 ± 0.04	63 ± 1	1.30 ± 0.02	6.19	13	171	2.58	1.35
161868	143	7.78	52	12.40 ± 2.36	3.75 ± 0.13	63 ± 3	1.20 ± 0.06	4.84	29	116	4.29	2.91
188228	102	7.92	62	1.27 ± 0.73	3.20 ± 0.15	84 ± 5	1.35 ± 0.08	0.42	...	...	...	1.68
10939	199	8.94	46	6.19 ± 1.45	3.38 ± 0.07	63 ± 3	1.35 ± 0.06	7.24	17	157	1.83	3.14
71155	85	9.83	73	8.09 ± 0.24	6.84 ± 0.33	102 ± 1	1.39 ± 0.01	1.59	14	184	1.83	2.18
172167	108	12.85	61	15.30 ± 3.09	3.40 ± 0.08	69 ± 2	1.13 ± 0.03	1.30	...	...	...	8.40
139006	61	11.60	98	11.50 ± 0.54	5.47 ± 0.24	102 ± 1	1.05 ± 0.01	0.84	17	188	0.68	2.38
95418	62	15.12	97	7.59 ± 0.59	4.20 ± 0.14	112 ± 5	1.15 ± 0.05	1.00	...	...	...	5.21
13161	154	10.66	65	28.30 ± 1.55	4.55 ± 0.14	57 ± 3	0.87 ± 0.04	1.22	42	126	2.18	3.25

Notes:

(1) The disc radii are given in AU, the temperatures in K and $s_{\rm min}$, $s_{\rm blow}$ in µm and the fractional luminosity in 10^{-5}. (2) For the values of $s_{\rm blow}$ the equation of Burns et al. (1979) (see Equation (2.16)) was used with a material density of $\varrho = 1.65$ g/cm^3. $Q_{\rm pr}$ was averaged over the stellar spectrum. (3) The warm component is treated as blackbody. Therefore, the given $R_{\rm disc}$ and $T_{\rm d}$ are blackbody radius or temperature, respectively.

B.2.2 10% Astrosilicate and 90% Vacuum

	Cold Component								Warm Component			
HD	R_{disc}	s_{blow}	T_{BB}	s_{min}	q	T_{d}	$T_{\mathrm{d}}/T_{\mathrm{BB}}$	f_{d}	R_{disc}	T_{d}	f_{d}	χ^2_{red}
GJ 581	38	...	15	0.01 ± 2.62	3.46 ± 0.12	47 ± 2	3.14 ± 0.14	6.48	...	...	...	1.10
197481	37	...	23	0.23 ± 3.85	1.81 ± 0.13	43 ± 1	1.87 ± 0.04	38.7	...	...	...	25.00
128311	58	...	27	6.68 ± 2.44	1.61 ± 0.10	43 ± 1	1.59 ± 0.04	2.78	...	...	...	1.69
192263	53	...	28	45.50 ± 3.61	4.57 ± 0.30	63 ± 2	2.20 ± 0.08	2.83	...	...	...	0.20
92945	72	...	25	16.00 ± 2.83	2.78 ± 0.06	47 ± 1	1.85 ± 0.06	58.8	...	...	...	2.92
23484	93	...	23	0.05 ± 1.67	2.69 ± 0.07	47 ± 2	2.04 ± 0.09	7.32	...	...	...	4.61
131511	74	...	27	0.02 ± 1.17	3.33 ± 0.14	69 ± 4	2.57 ± 0.16	0.67	...	...	...	14.33
166	40	...	39	13.20 ± 3.07	3.94 ± 0.13	84 ± 4	2.17 ± 0.11	4.67	0.2	512	19.9	1.36
104860	113	...	27	2.31 ± 1.36	1.75 ± 0.08	47 ± 2	1.73 ± 0.07	50.4	...	...	...	8.00
207129	144	...	24	0.05 ± 0.48	3.06 ± 0.01	52 ± 1	2.11 ± 0.04	0.86	...	...	...	18.60
10647	114	...	29	17.20 ± 3.19	-1.68 ± 0.26	43 ± 2	1.48 ± 0.08	4.14	24	63	25.7	14.28
48682	129	...	28	0.05 ± 0.63	2.98 ± 0.02	57 ± 1	2.01 ± 0.04	5.89	...	...	...	23.86
50571	139	...	31	2.96 ± 5.36	2.25 ± 0.11	52 ± 1	1.65 ± 0.03	12.2	...	...	...	3.06
170773	203	...	26	0.09 ± 1.66	2.25 ± 0.07	47 ± 1	1.77 ± 0.04	54.2	...	...	...	6.39
218396	282	1.54	24	6.59 ± 2.79	2.77 ± 0.05	47 ± 1	1.92 ± 0.04	28.1	2	287	8.61	11.11
109085	142	0.93	35	5.29 ± 1.54	1.18 ± 0.27	52 ± 1	1.50 ± 0.03	1.50	1	347	20.2	48.25
27290	129	2.93	39	0.11 ± 2.25	1.69 ± 0.25	57 ± 3	1.48 ± 0.06	1.29	...	...	...	13.55
95086	272	4.68	27	3.97 ± 1.58	2.43 ± 0.07	47 ± 2	1.71 ± 0.07	85.4	29	84	54.9	5.23
195627	171	5.08	35	3.84 ± 2.48	2.28 ± 0.08	57 ± 2	1.64 ± 0.06	9.50	2	373	5.14	5.39
20320	149	10.88	41	24.60 ± 3.49	2.29 ± 0.13	63 ± 3	1.54 ± 0.07	1.19	6	205	1.38	0.43
21997	170	13.59	39	20.70 ± 7.37	-1.53 ± 0.17	52 ± 2	1.33 ± 0.06	27.7	42	78	22.6	1.08
110411	118	15.33	47	14.90 ± 1.81	3.19 ± 0.06	84 ± 1	1.78 ± 0.02	4.90	3	302	3.73	5.83
142091	127	9.19	46	0.11 ± 1.35	1.85 ± 0.17	63 ± 1	1.36 ± 0.02	3.86	...	...	...	27.90
102647	44	17.15	80	110.00 ± 3.20	5.92 ± 0.42	102 ± 5	1.28 ± 0.06	2.19	3	300	2.56	20.75
125162	116	21.11	51	15.70 ± 3.82	1.97 ± 0.33	69 ± 3	1.36 ± 0.06	2.49	16	137	2.90	8.58
216956	127	20.00	49	0.01 ± 2.20	-4.29 ± 0.90	57 ± 13	1.17 ± 0.27	6.34	...	...	...	9.94
17848	223	20.70	37	6.70 ± 3.14	1.23 ± 0.16	52 ± 1	1.40 ± 0.03	4.05	22	118	2.04	4.75
9672	170	21.97	42	36.60 ± 3.32	-1.42 ± 0.23	52 ± 3	1.22 ± 0.07	32.7	41	87	50.1	3.64
71722	128	25.29	48	5.11 ± 2.19	2.81 ± 0.05	76 ± 1	1.59 ± 0.02	9.02	5	248	4.76	1.04
182681	195	34.65	44	11.80 ± 1.56	2.21 ± 0.25	63 ± 1	1.41 ± 0.03	14.8	10	199	7.82	9.48
14055	164	34.22	48	5.79 ± 1.05	-1.30 ± 0.26	57 ± 2	1.18 ± 0.03	4.90	26	121	3.34	7.89
161868	143	35.09	52	13.20 ± 1.72	-0.84 ± 0.17	63 ± 1	1.20 ± 0.02	4.92	34	108	4.60	4.50
188228	102	36.82	62	0.02 ± 2.04	2.64 ± 0.05	84 ± 4	1.35 ± 0.06	0.43	...	...	...	3.12
10939	199	41.45	46	26.20 ± 8.13	-3.85 ± 0.79	57 ± 5	1.23 ± 0.10	6.62	26	129	2.17	6.08
71155	85	76.73	73	14.50 ± 8.03	3.39 ± 0.21	112 ± 1	1.53 ± 0.01	2.53	0.1	2050	72.8	19.43
172167	108	62.45	61	0.01 ± 17.76	-6.30 ± 0.78	76 ± 22	1.24 ± 0.36	1.46	...	...	...	9.76
139006	61	55.67	98	23.70 ± 3.18	2.65 ± 0.05	112 ± 4	1.15 ± 0.04	1.16	0.04	3830	172	6.63
95418	62	74.09	97	289.00 ± 1.76	9.04 ± 0.30	102 ± 1	1.05 ± 0.01	0.98	...	...	...	5.44
13161	154	49.59	65	58.80 ± 2.73	-2.26 ± 0.52	69 ± 3	1.06 ± 0.04	1.43	62	104	2.33	12.70

Notes:

(1) The disc radii are given in AU, the temperatures in K and s_{min}, s_{blow} in µm and the fractional luminosity in 10^{-5}. (2) For the values of s_{blow} the equation of Burns et al. (1979) (see Equation (2.16)) was used with a material density of $\varrho = 0.33$ g/cm^3. Q_{pr} was averaged over the stellar spectrum. (3) The warm component is treated as blackbody. Therefore, the given R_{disc} and T_{d} are blackbody radius or temperature, respectively.

B.3 Carbon (ACAR)

	Cold Component								Warm Component			
HD	R_{disc}	s_{blow}	T_{BB}	s_{min}	q	T_{d}	$T_{\mathrm{d}}/T_{\mathrm{BB}}$	f_{d}	R_{disc}	T_{d}	f_{d}	χ^2_{red}
GJ 581	38	...	15	1.28 ± 0.48	3.48 ± 0.27	26 ± 9	1.75 ± 0.61	8.72	...	...	...	0.79
197481	37	...	23	1.00 ± 0.15	3.55 ± 0.04	52 ± 3	2.27 ± 0.13	50.8	...	...	...	0.66
128311	58	0.46	27	2.52 ± 1.79	3.43 ± 0.52	35 ± 5	1.31 ± 0.18	3.20	...	...	...	1.57
192263	53	0.46	28	5.02 ± 0.84	6.46 ± 0.36	63 ± 7	2.20 ± 0.24	2.53	...	...	...	0.19
92945	72	0.51	25	4.52 ± 0.52	4.48 ± 0.25	52 ± 2	2.04 ± 0.09	57.6	...	...	...	2.76
23484	93	0.54	23	1.49 ± 0.35	3.56 ± 0.09	39 ± 3	1.68 ± 0.13	9.77	...	...	...	1.23
131511	74	0.61	27	0.03 ± 0.51	3.48 ± 0.11	124 ± 25	4.63 ± 0.93	2.28	...	...	...	5.63
166	40	0.68	39	3.30 ± 0.15	5.97 ± 0.12	92 ± 2	2.39 ± 0.04	4.76	0.2	512	21.3	1.14
104860	113	0.95	27	5.27 ± 0.20	4.22 ± 0.04	47 ± 1	1.73 ± 0.04	55.4	...	...	...	1.30
207129	144	1.00	24	3.31 ± 0.15	4.51 ± 0.05	57 ± 2	2.33 ± 0.08	9.08	...	...	...	3.90
10647	114	1.10	29	3.47 ± 0.13	4.21 ± 0.04	52 ± 3	1.79 ± 0.09	26.3	5	132	3.95	5.32
48682	129	1.24	28	2.28 ± 0.13	4.04 ± 0.03	57 ± 1	2.01 ± 0.04	7.13	...	...	...	3.44
50571	139	1.73	31	4.33 ± 0.27	4.37 ± 0.07	57 ± 3	1.82 ± 0.08	12.6	...	...	...	1.72
170773	203	1.82	26	4.15 ± 0.41	4.42 ± 0.10	52 ± 1	1.95 ± 0.04	52.9	...	...	...	3.13
218396	282	2.19	24	3.88 ± 0.15	4.40 ± 0.05	52 ± 1	2.11 ± 0.04	29.0	3	259	7.94	6.52
109085	142	2.28	35	11.90 ± 1.46	3.30 ± 0.10	35 ± 1	1.01 ± 0.03	1.27	3	220	12.6	2.05
27290	129	2.64	39	1.06 ± 0.22	3.51 ± 0.06	57 ± 3	1.48 ± 0.08	2.37	...	...	...	6.02
95086	272	2.78	27	2.82 ± 0.14	4.27 ± 0.05	57 ± 1	2.08 ± 0.04	135	8	163	17.9	1.10
195627	171	2.91	35	4.06 ± 0.18	4.38 ± 0.09	63 ± 3	1.80 ± 0.07	5.31	1	383	5.31	2.14
20320	149	3.64	41	4.82 ± 0.53	4.50 ± 0.25	63 ± 3	1.54 ± 0.07	1.16	7	193	1.36	0.45
21997	170	3.82	39	5.22 ± 0.48	4.51 ± 0.13	63 ± 3	1.61 ± 0.07	37.0	34	87	15.7	0.46
110411	118	3.89	47	3.53 ± 0.12	4.78 ± 0.15	84 ± 4	1.78 ± 0.09	4.61	5	223	3.24	5.47
142091	127	4.65	46	2.68 ± 0.17	3.85 ± 0.05	69 ± 3	1.50 ± 0.07	5.40	...	...	...	7.41
102647	44	3.88	80	3.55 ± 0.07	4.76 ± 0.03	112 ± 1	1.41 ± 0.01	2.09	3	300	2.67	17.75
125162	116	4.71	51	3.24 ± 0.13	4.12 ± 0.05	76 ± 3	1.50 ± 0.06	3.66	9	180	2.43	3.84
216956	127	4.73	49	3.57 ± 3.84	3.84 ± 0.06	69 ± 2	1.42 ± 0.04	7.41	...	...	...	2.96
17848	223	4.73	37	5.51 ± 0.51	4.50 ± 0.17	57 ± 2	1.54 ± 0.06	4.21	20	124	1.93	3.38
9672	170	4.79	42	3.48 ± 0.37	4.18 ± 0.05	69 ± 2	1.63 ± 0.04	74.8	13	156	17.7	0.52
71722	128	5.34	48	3.39 ± 0.14	4.28 ± 0.13	76 ± 4	1.59 ± 0.08	8.88	6	222	5.11	1.73
182681	195	6.50	44	2.23 ± 0.08	3.92 ± 0.04	76 ± 2	1.72 ± 0.05	19.6	4	303	5.06	22.00
14055	164	6.57	48	3.80 ± 0.14	3.92 ± 0.04	69 ± 1	1.43 ± 0.02	6.56	12	177	2.64	3.70
161868	143	6.72	52	6.12 ± 0.70	4.31 ± 0.17	63 ± 4	1.20 ± 0.07	4.75	29	116	4.35	2.50
188228	102	6.77	62	2.29 ± 0.22	3.58 ± 0.08	84 ± 4	1.35 ± 0.06	0.42	...	...	...	1.68
10939	199	7.59	46	4.19 ± 0.28	3.82 ± 0.07	63 ± 1	1.35 ± 0.02	7.27	18	156	1.87	3.64
71155	85	8.33	73	4.25 ± 0.11	6.59 ± 0.16	102 ± 4	1.39 ± 0.05	1.77	10	214	2.00	5.40
172167	108	10.94	61	9.29 ± 0.17	4.42 ± 0.03	63 ± 1	1.02 ± 0.02	1.20	...	...	...	9.20
139006	61	9.90	98	5.20 ± 0.16	5.81 ± 0.20	102 ± 1	1.05 ± 0.01	0.91	14	207	0.70	2.92
95418	62	12.85	97	4.25 ± 0.17	4.74 ± 0.09	112 ± 4	1.15 ± 0.04	1.03	...	...	...	5.43
13161	154	9.17	65	10.10 ± 0.37	5.32 ± 0.22	63 ± 2	0.96 ± 0.03	1.21	40	128	2.18	3.55

Notes:

(1) The disc radii are given in AU, the temperatures in K and s_{min}, s_{blow} in µm and the fractional luminosity in 10^{-5}. (2) For the values of s_{blow} the equation of Burns et al. (1979) (see Equation (2.16)) was used with a material density of $\varrho = 1.95$ g/cm^3. Q_{pr} was averaged over the stellar spectrum. (3) The warm component is treated as blackbody. Therefore, the given R_{disc} and T_{d} are blackbody radius or temperature, respectively.

B.4 Astrosilicate and Carbon (ACAR)

	Cold Component								Warm Component			
HD	R_{disc}	s_{blow}	T_{BB}	s_{min}	q	T_{d}	$T_{\mathrm{d}}/T_{\mathrm{BB}}$	f_{d}	R_{disc}	T_{d}	f_{d}	χ^2_{red}
GJ 581	38	...	15	1.38 ± 0.66	3.43 ± 0.24	25 ± 9	1.66 ± 0.63	8.83	...	...	...	0.78
197481	37	...	23	1.02 ± 0.16	3.55 ± 0.04	59 ± 3	2.59 ± 0.14	51.2	...	...	...	0.97
128311	58	0.35	27	2.70 ± 2.26	3.40 ± 0.56	35 ± 6	1.30 ± 0.21	3.23	...	...	...	1.57
192263	53	0.35	28	5.18 ± 1.01	5.71 ± 0.34	65 ± 6	2.28 ± 0.21	2.66	...	...	...	0.19
92945	72	0.38	25	5.95 ± 0.44	4.63 ± 0.11	51 ± 1	2.01 ± 0.05	55.4	...	...	...	2.84
23484	93	0.42	23	1.64 ± 0.37	3.54 ± 0.08	38 ± 4	1.66 ± 0.15	9.70	...	...	...	1.62
131511	74	0.46	27	0.01 ± 0.38	3.50 ± 0.10	124 ± 24	4.63 ± 0.90	2.15	...	...	...	6.30
166	40	0.51	39	3.57 ± 0.20	5.64 ± 0.17	92 ± 2	2.39 ± 0.04	4.72	0.2	512	21.3	1.08
104860	113	0.74	27	6.41 ± 0.25	4.25 ± 0.05	46 ± 1	1.71 ± 0.04	54.4	...	...	...	1.49
207129	144	0.78	24	4.04 ± 0.18	4.51 ± 0.06	56 ± 1	2.30 ± 0.05	8.78	...	...	...	4.70
10647	114	0.87	29	3.97 ± 0.17	4.21 ± 0.04	56 ± 1	1.95 ± 0.03	26.1	6	127	4.17	4.62
48682	129	0.98	28	2.39 ± 0.04	3.97 ± 0.04	59 ± 1	2.08 ± 0.05	7.18	...	...	...	3.14
50571	139	1.35	31	5.00 ± 0.54	4.36 ± 0.11	56 ± 2	1.79 ± 0.05	12.5	...	...	...	1.78
170773	203	1.40	26	6.07 ± 0.50	4.65 ± 0.09	51 ± 1	1.93 ± 0.05	48.8	...	...	...	3.57
218396	282	1.71	24	4.47 ± 0.22	4.40 ± 0.05	52 ± 1	2.11 ± 0.04	28.6	3	259	8.00	6.97
109085	142	1.74	35	12.60 ± 1.10	3.27 ± 0.08	35 ± 1	1.00 ± 0.03	1.21	4	212	12.3	2.70
27290	129	2.03	39	1.09 ± 0.24	3.50 ± 0.06	62 ± 4	1.60 ± 0.09	2.39	...	...	...	6.47
95086	272	2.12	27	3.00 ± 0.18	4.21 ± 0.05	59 ± 1	2.15 ± 0.04	134	8	160	17.9	1.49
195627	171	2.25	35	4.63 ± 0.17	4.39 ± 0.06	62 ± 1	1.77 ± 0.03	10.0	1	391	5.56	2.23
20320	149	2.80	41	5.97 ± 0.73	4.55 ± 0.26	62 ± 2	1.52 ± 0.06	1.08	7	186	1.35	0.46
21997	170	2.94	39	6.53 ± 0.56	4.62 ± 0.12	59 ± 2	1.52 ± 0.05	34.0	36	84	17.5	0.48
110411	118	2.95	47	3.99 ± 0.11	4.84 ± 0.08	87 ± 2	1.84 ± 0.04	4.58	5	219	3.20	4.90
142091	127	3.54	46	2.90 ± 0.23	3.85 ± 0.09	71 ± 3	1.55 ± 0.06	5.47	...	...	...	7.31
102647	44	3.23	80	3.96 ± 0.15	4.76 ± 0.13	112 ± 1	1.41 ± 0.01	2.09	3	300	2.67	17.75
125162	116	3.61	51	3.69 ± 0.14	4.15 ± 0.05	79 ± 2	1.54 ± 0.04	3.61	9	180	2.49	3.86
216956	127	3.55	49	4.04 ± 0.18	3.89 ± 0.05	68 ± 2	1.40 ± 0.03	7.50	...	...	...	3.01
17848	223	3.61	37	6.42 ± 0.67	4.51 ± 0.18	56 ± 2	1.52 ± 0.05	4.16	20	123	1.95	3.38
9672	170	3.61	42	4.02 ± 0.38	4.20 ± 0.05	71 ± 2	1.68 ± 0.05	73.0	13	153	18.7	0.49
71722	128	4.06	48	3.28 ± 0.21	3.91 ± 0.17	75 ± 3	1.56 ± 0.06	8.92	6	228	4.93	3.80
182681	195	4.97	44	3.67 ± 0.40	4.38 ± 0.08	79 ± 3	1.77 ± 0.06	19.7	9	209	7.19	2.56
14055	164	5.02	48	4.19 ± 0.14	3.94 ± 0.05	68 ± 1	1.41 ± 0.03	6.71	11	189	2.67	4.01
161868	143	5.03	52	7.39 ± 0.59	4.42 ± 0.11	62 ± 3	1.18 ± 0.05	4.58	29	115	4.41	2.50
188228	102	5.09	62	2.36 ± 0.35	3.55 ± 0.10	83 ± 3	1.33 ± 0.05	0.42	...	...	...	1.67
10939	199	5.70	46	4.61 ± 0.24	3.86 ± 0.05	65 ± 2	1.40 ± 0.03	7.39	16	162	1.84	3.90
71155	85	6.21	73	4.85 ± 0.14	6.59 ± 0.31	105 ± 2	1.43 ± 0.02	1.73	11	208	2.01	4.07
172167	108	8.26	61	10.50 ± 0.45	4.41 ± 0.06	62 ± 1	1.01 ± 0.02	1.16	...	...	...	9.60
139006	61	7.42	98	5.63 ± 0.27	5.48 ± 0.27	100 ± 3	1.02 ± 0.03	0.94	13	213	0.68	2.91
95418	62	9.61	97	4.84 ± 0.25	4.79 ± 0.24	110 ± 3	1.13 ± 0.03	1.03	...	...	...	5.41
13161	154	6.88	65	12.30 ± 0.36	5.88 ± 0.23	53 ± 1	0.82 ± 0.02	0.96	48	117	2.39	4.08

Notes:

(1) The disc radii are given in AU, the temperatures in K and s_{min}, s_{blow} in µm and the fractional luminosity in 10^{-5}. (2) For the values of s_{blow} the equation of Burns et al. (1979) (see Equation (2.16)) was used with a material density of $\varrho = 2.63$ g/cm^3. Q_{pr} was averaged over the stellar spectrum. (3) The warm component is treated as blackbody. Therefore, the given R_{disc} and T_{d} are blackbody radius or temperature, respectively.

AppendixC List of resolved debris discs

No	HD	HIP	SpT	*d* [pc]	Vmag	Reference
1	105	490	G0V	40.0	7.53	Donaldson et al. (2012)
2	166	544	K0V	14.0	6.13	Eiroa et al. (2013)
3	377	682	G2V	39.1	7.59	Choquet et al. (2016); Steele et al. (2016)
4	8907	6878	F8	34.8	6.66	Steele et al. (2016)
5	9672	7345	A1V	59.4	5.62	Roberge et al. (2013)
6	10647	7978	F9V	17.0	5.52	Liseau et al. (2010); Eiroa et al. (2013)
7	10700	8102	G8.5V	4.0	3.50	Greaves et al. (2004); Di Folco et al. (2004)
8	10939	8241	A1V	62.0	5.04	Moór et al. (2015)
9	13161	10064	A5III	39.0	3.00	Kennedy et al. (2012b); Booth et al. (2013)
10	14055	10670	A1Vnn	34.0	4.00	Booth et al. (2013)
11	15115	11360	F2D	45.0	6.80	Kalas et al. (2007b)
12	15745	11847	F2V	63.0	7.49	Kalas et al. (2007a)
13	16743	12361	F1III/IV4	58.9	6.77	Moór et al. (2015)
14	17848	13141	A2V	50.0	5.26	Moór et al. (2015)
15	17925	13402	K1V	10.0	6.00	Eiroa et al. (2013)
16	19994	14954	F8V	23.0	5.08	Eiroa et al. (2013)
17	20320	15197	kA4hA9mA9V	34.0	4.79	Booth et al. (2013)
18	20794	15510	G8III	6.1	4.27	Kennedy et al. (2015); Montesinos et al. (2016)
19	20807	15371	G0V	12.0	5.24	Liseau et al. (2010); Eiroa et al. (2013)
20	21997	16449	A3IV/V	72.0	6.37	Moór et al. (2013b)
21	22049	16537	K2Vk	3.0	3.73	Greaves et al. (1998)
22	22484	16852	F9IV/V	14.0	4.30	Montesinos et al. (2016)
23	23484	17439	K2V	16.0	7.00	Marshall et al. (2013); Eiroa et al. (2013)
24	27290	19893	F1V	20.0	4.20	Broekhoven-Fiene et al. (2013)
25	30447	22226	F3V	80.0	7.86	Soummer et al. (2014)
26	30495	22263	G1.5VCH-0.5	13.0	5.50	Eiroa et al. (2013); Marshall et al. (2014a)
27	31295	22845	A3Va	35.7	4.66	Draper et al. (2016b)
28	32297	23451	A0V	112.0	8.14	Kalas et al. (2006); Donaldson et al. (2013)
29	35650	25283	K5V	18.0	9.05	Choquet et al. (2016)
30	35841	...	F3V	96.0	8.90	Soummer et al. (2014)
31	38678	27288	A2IV-V(n)	22.0	3.55	Moerchen et al. (2007, 2010)
32	38858	27435	G2V	15.2	5.97	Krist et al. (2012); Kennedy et al. (2015)
33	39060	27321	A6V	19.0	3.86	Di Folco et al. (2004); Golimowski et al. (2006)
34	43834	29271	G7V	10.0	5.09	Eiroa et al. (2011)
35	48682	32480	G0V	17.0	5.25	Eiroa et al. (2013)
36	50571	32775	F5VFe+0.4	34.0	6.11	Moór et al. (2015)
37	53143	33690	G9V	18.0	6.80	Kalas et al. (2006)
38	61005	36948	G8Vk	35.0	8.22	Ricarte et al. (2013)
39	69830	40693	G8+V	12.5	5.95	Smith et al. (2009b); Beichman et al. (2011)
40	70313	41152	A3V	50.0	5.54	Morales et al. (2013)
41	71155	41307	A0V	38.0	3.90	Moerchen et al. (2010); Booth et al. (2013)
42	71722	41373	A0V	69.0	6.05	Morales et al. (2013)
43	76582	44001	F0IV	46.1	5.69	Marshall et al. (2016)
44	82943	47007	F9VFe+0.5	27.5	6.53	Kennedy et al. (2013)
45	84870	48164	A3	88.0	7.19	Eiroa et al. (2011)
46	88230	49908	K8V	5.0	6.61	Eiroa et al. (2013)
47	90089	51502	F2V	22.0	5.26	Eiroa et al. (2013)
48	90839	51459	F8V	13.0	4.83	Eiroa et al. (2013)
49	92945	52462	K1V	21.0	7.72	Golimowski et al. (2011)
50	95086	53524	A8III	90.0	7.36	Moór et al. (2013a)
51	95418	53910	A1IVps	24.0	2.35	Matthews et al. (2010); Booth et al. (2013)
52	98800	55505	K4V	45.0	9.11	Andrews et al. (2010)
53	102647	57632	A3Va	11.0	2.13	Matthews et al. (2010); Churcher et al. (2011a)
54	104860	58876	F8	45.0	7.91	Morales et al. (2013)
55	106906	59960	F5V	91.8	7.81	Lagrange et al. (2016)
56	107146	60074	G2V	27.0	7.01	Ardila et al. (2004)
57	109085	61174	F2V	18.0	4.31	Matthews et al. (2010); Duchêne et al. (2014)
58	109573	61498	A0	72.8	5.78	Schneider et al. (1999)

No	HD	HIP	SpT	d [pc]	Vmag	Reference
59	110411	61960	A0V	36.0	4.87	Booth et al. (2013)
60	110897	62207	G0V	17.0	6.00	Eiroa et al. (2013); Marshall et al. (2014a)
61	111520	62657	F5/6V	108.0	8.87	Draper et al. (2016a)
62	113337	63584	F6V	36.9	6.03	Su et al. (2013a)
63	113766	63975	F3/5V+F6V	122.5	7.56	Smith et al. (2012); Olofsson et al. (2013)
64	115617	64924	G7V	9.0	4.74	Wyatt et al. (2012)
65	125162	69732	A0p	30.0	4.18	Booth et al. (2013)
66	127821	70952	F4IV	31.8	6.11	Su et al. (2013a)
67	128311	71395	K3V	16.5	7.45	Jonathan P. Marshall, this work
68	131511	72848	K0V	11.5	6.01	Marshall et al. (2014a)
69	131835	73145	A2	122.0	7.86	Hung et al. (2015)
70	139006	76267	A0V	23.0	2.21	Kennedy et al. (2012b); Booth et al. (2013)
71	139664	76829	F5V	17.0	4.64	Kalas et al. (2006)
72	141569	77542	A0Ve	116.1	7.12	Augereau et al. (1999)
73	141943	...	G2V	67.0	7.85	Soummer et al. (2014)
74	142091	77655	K1IVa	30.0	4.80	Bonsor et al. (2012)
75	146897	79977	F2/F3V	122.7	9.11	Thalmann et al. (2013)
76	158633	85235	K0V	13.0	6.43	Eiroa et al. (2013)
77	159492	86305	A5IV-V	45.0	5.25	Morales et al. (2013)
78	161868	87108	A0V	32.0	3.75	Moór et al. (2015)
79	165908	88745	F7V	16.0	5.07	Kennedy et al. (2012a)
80	170773	90936	F5V	37.0	6.24	Moór et al. (2015)
81	172167	91262	A0V	8.0	0.03	Sibthorpe et al. (2010)
82	172555	92024	A7V	28.5	4.78	Smith et al. (2012)
83	173667	92043	F6V	19.0	4.20	Eiroa et al. (2013)
84	181296	95261	A0V	48.0	5.02	Smith et al. (2009a)
85	181327	95270	F6V	52.0	7.04	Schneider et al. (2006); Lebreton et al. (2013)
86	181869	95347	B8V	56.0	3.95	Moerchen et al. (2010)
87	182681	95619	B9V	70.0	5.65	Moór et al. (2015)
88	188228	98495	A0Va	32.0	3.95	Booth et al. (2013)
89	191089	99273	F5V	52.0	7.18	Churcher et al. (2011a); Soummer et al. (2014)
90	192263	99711	K2.5V	19.3	7.77	Jonathan P. Marshall, this work
91	195627	101612	F0V	28.0	4.76	Moór et al. (2015)
92	197481	102409	M1Ve	10.0	8.61	Krist et al. (2005)
93	202628	105184	G5V	24.0	6.75	Krist et al. (2012)
94	202917	105388	G7V	43.0	8.67	Soummer et al. (2014)
95	207129	107649	G2V	16.0	5.58	Krist et al. (2010)
96	216956	113368	A4V	8.0	1.16	Acke et al. (2012)
97	218396	114189	A5V	39.0	5.95	Su et al. (2009)
98	TWA 7	...	M3.2	34.5	10.91	Choquet et al. (2016)
99	GJ 581	74995	M5V	6.0	10.61	Lestrade et al. (2012)
100	TWA 25	...	M0.5	54.0	11.41	Choquet et al. (2016)

Table C.1: Resolved debris discs sorted by HD number. Column SpT gives the spectral type, d the distance to the observer and Vmag the apparent magnitude in the V band. We used values from SIMBAD (http://simbad.u-strasbg.fr/simbad/sim-fid). Spatially resolution of the discs is reported in the literature cited under Reference.

Bibliography

Acke, B., Min, M., Dominik, C., Vandenbussche, B., Sibthorpe, B., Waelkens, C., Olofsson, G., Degroote, P., Smolders, K., Pantin, E., Barlow, M. J., Blommaert, J. A. D. L., Brandeker, A., De Meester, W., Dent, W. R. F., Exter, K., Di Francesco, J., Fridlund, M., Gear, W. K., Glauser, A. M., Greaves, J. S., Harvey, P. M., Henning, T., Hogerheijde, M. R., Holland, W. S., Huygen, R., Ivison, R. J., Jean, C., Liseau, R., Naylor, D. A., Pilbratt, G. L., Polehampton, E. T., Regibo, S., Royer, P., Sicilia-Aguilar, A., and Swinyard, B. M. (2012). Herschel images of Fomalhaut. An extrasolar Kuiper belt at the height of its dynamical activity. *A& A*, 540:A125.

Alibert, Y., Mordasini, C., and Benz, W. (2011). Extrasolar planet population synthesis. III. Formation of planets around stars of different masses. *A& A*, 526:A63.

Allende Prieto, C., García López, R. J., Lambert, D. L., and Gustafsson, B. (1999). A Consistency Test of Spectroscopic Gravities for Late-Type Stars. *ApJ*, 527:879–892.

Anderson, T. and Darling, D. (1952). Asymptotic theory of certain "goodness of fit" criteria based on stochastic processes. *Ann. Math. Statist.*, 23(2):193–212.

Anderson, T. and Darling, D. (1954). A test of goodness of fit. *J. Am. Stat. Assoc.*, 49:765–769.

Andrews, S. M., Czekala, I., Wilner, D. J., Espaillat, C., Dullemond, C. P., and Hughes, A. M. (2010). Truncated Disks in TW Hya Association Multiple Star Systems. *ApJ*, 710:462–469.

Ardila, D. R., Golimowski, D. A., Krist, J. E., Clampin, M., Williams, J. P., Blakeslee, J. P., Ford, H. C., Hartig, G. F., and Illingworth, G. D. (2004). A resolved debris disk around the G2 V star HD 107146. *ApJ*, 617:L147–L150.

Augereau, J. and Beust, H. (2006). The AU Mic debris ring. Density profile and dynamics of the dust. *A& A*, 455:987–999.

Augereau, J.-C., Lagrange, A.-M., Mouillet, D., and Ménard, F. (1999). HST/NICMOS2 observations of the HD 141569 A circumstellar disk. *A& A*, 350:L51–L54.

Aumann, H. H., Beichman, C. A., Gillett, F. C., de Jong, T., Houck, J. R., Low, F. J., Neugebauer, G., Walker, R. G., and Wesselius, P. R. (1984). Discovery of a shell around Alpha Lyrae. *ApJ*, 278:L23–L27.

Backman, D., Marengo, M., Stapelfeldt, K., Su, K., Wilner, D., Dowell, C. D., Watson, D., Stansberry, J., Rieke, G., Megeath, T., Fazio, G., and Werner, M. (2009). Epsilon Eridani's Planetary Debris Disk: Structure and Dynamics Based on Spitzer and Caltech Submillimeter Observatory Observations. *ApJ*, 690:1522–1538.

Backman, D. and Paresce, F. (1993). Main-sequence stars with circumstellar solid material: The Vega phenomenon. In Levy, E. H. and Lunine, J. I., editors, *Protostars and Planets III*, pages 1253–1304. Univ. of Arizona Press.

Ballering, N. P., Rieke, G. H., Su, K. Y. L., and Montiel, E. (2013). A Trend between Cold Debris Disk Temperature and Stellar Type: Implications for the Formation and Evolution of Wide-orbit Planets. *ApJ*, 775:55.

Balog, Z., Müller, T., Nielbock, M., Altieri, B., Klaas, U., Blommaert, J., Linz, H., Lutz, D., Moór, A., Billot, N., Sauvage, M., and Okumura, K. (2013). The Herschel-PACS photometer calibration - Point-source flux calibration for scan maps. *Experimental Astronomy, arXiv:1309.6099.*

Beichman, C. A., Bryden, G., Rieke, G. H., Stansberry, J. A., Trilling, D. E., Stapelfeldt, K. R., Werner, M. W., Engelbracht, C. W., Blaylock, M., Gordon, K. D., Chen, C. H., Su, K. Y. L., and Hines, D. C. (2005). Planets and ir excesses: Preliminary results from a Spitzer/MIPS survey of solar-type stars. *ApJ*, 622:1160–1170.

Beichman, C. A., Lisse, C. M., Tanner, A. M., Bryden, G., Akeson, R. L., Ciardi, D. R., Boden, A. F., Dodson-Robinson, S. E., Salyk, C., and Wyatt, M. C. (2011). Multi-epoch Observations of HD 69830: High-resolution Spectroscopy and Limits to Variability. *ApJ*, 743:85.

Beichman, C. A., Tanner, A., Bryden, G., Stapelfeldt, K. R., Werner, M. W., Rieke, G. H., Trilling, D. E., Lawler, S., and Gautier, T. N. (2006). IRS Spectra of Solar-Type Stars: A Search for Asteroid Belt Analogs. *ApJ*, 639:1166–1176.

Benz, W. and Asphaug, E. (1999). Catastrophic disruptions revisited. *Icarus*, 142:5–20.

Bessell, M. S. (1979). UBVRI photometry. II - The Cousins VRI system, its temperature and absolute flux calibration, and relevance for two-dimensional photometry. *PASP*, 91:589–607.

Bode, J. (1772). *Anleitung zur Kenntnis des gestirnten Himmels auf jede einzele Monate des Jahrs eingerichtet*. 2 edition.

Bohren, C. F. and Huffman, D. R. (1983). *Absorption and Scattering of Light by Small Particles*. Wiley and Sons: New York – Chichester – Brisbane – Toronto – Singapore.

Bonsor, A., Augereau, J.-C., and Thebault, P. (2012). Scattering of small bodies by planets: a potential origin for exozodiacal dust ? *A& A*, 548:A104.

Bonsor, A., Kennedy, G. M., Crepp, J. R., Johnson, J. A., Wyatt, M. C., Sibthorpe, B., and Su, K. Y. L. (2013). Spatially resolved images of dust belt(s) around the planet-hosting subgiant κ CrB. *MNRAS*, 431:3025–3035.

Bonsor, A., Kennedy, G. M., Wyatt, M. C., Johnson, J. A., and Sibthorpe, B. (2014). Herschel observations of debris discs orbiting planet-hosting subgiants. *MNRAS*, 437:3288–3297.

Booth, M., Kennedy, G., Sibthorpe, B., Matthews, B. C., Wyatt, M. C., Duchêne, G., Kavelaars, J. J., Rodriguez, D., Greaves, J. S., Koning, A., Vican, L., Rieke, G. H., Su, K. Y. L., Moro-Martín, A., and Kalas, P. (2013). Resolved debris discs around A stars in the Herschel DEBRIS survey. *MNRAS*, 428:1263–1280.

Broekhoven-Fiene, H., Matthews, B. C., Kennedy, G. M., Booth, M., Sibthorpe, B., Lawler, S. M., Kavelaars, J. J., Wyatt, M. C., Qi, C., Koning, A., Su, K. Y. L., Rieke, G. H., Wilner, D. J., and Greaves, J. S. (2013). The Debris Disk around γ Doradus Resolved with Herschel. *ApJ*, 762:52.

Bronstein, I., Semendjajew, K., Musiol, G., and Mühlig, H. (1977). *Taschenbuch der Mathematik*. Verlag Harri Deutsch.

Brott, I. and Hauschildt, P. H. (2005). A PHOENIX Model Atmosphere Grid for Gaia. In C. Turon, K. S. O'Flaherty, & M. A. C. Perryman, editor, *The Three-Dimensional Universe with Gaia*, volume 576 of *ESA SP*, page 565.

Bruggeman, D. A. G. (1935). Berechnung verschiedener physikalischer Konstanten von heterogenen Substanzen I. *Annalen der Physik*, 24:636–664.

Bruggeman, D. A. G. (1936). Berechnung verschiedener physikalischer Konstanten von heterogenen Substanzen II. *Annalen der Physik*, 25:645–672.

Bryden, G., Beichman, C. A., Carpenter, J. M., Rieke, G. H., Stapelfeldt, K. R., Werner, M. W., Tanner, A. M., Lawler, S. M., Wyatt, M. C., Trilling, D. E., Su, K. Y. L., Blaylock, M., and Stansberry, J. A. (2009). Planets and Debris Disks: Results from a Spitzer/MIPS Search for Infrared Excess. *ApJ*, 705:1226–1236.

Burns, J. A., Lamy, P. L., and Soter, S. (1979). Radiation forces on small particles in the Solar System. *Icarus*, 40:1–48.

Castelli, F. and Kurucz, R. L. (2004). New Grids of ATLAS9 Model Atmospheres. *ArXiv:astro-ph/0405087*.

Chen, C. H., Mittal, T., Kuchner, M., Forrest, W. J., Lisse, C. M., Manoj, P., Sargent, B. A., and Watson, D. M. (2014). The Spitzer Infrared Spectrograph Debris Disk Catalog. I. Continuum Analysis of Unresolved Targets. *ApJS*, 211:25.

Chen, C. H., Pecaut, M., Mamajek, E. E., Su, K. Y. L., and Bitner, M. (2012). A Spitzer MIPS Study of 2.5-2.0 M $_\odot$ Stars in Scorpius-Centaurus. *ApJ*, 756:133.

Chen, C. H., Sargent, B. A., Bohac, C., and et al. (2006). Spitzer irs spectroscopy of iras-discovered debris disks. *ApJS*, 166:351–377.

Choquet, É., Perrin, M. D., Chen, C. H., Soummer, R., Pueyo, L., Hagan, J. B., Gofas-Salas, E., Rajan, A., Golimowski, D. A., Hines, D. C., Schneider, G., Mazoyer, J., Augereau, J.-C., Debes, J., Stark, C. C., Wolff, S., N'Diaye, M., and Hsiao, K. (2016). First Images of Debris Disks around TWA 7, TWA 25, HD 35650, and HD 377. *ApJL*, 817:L2.

Churcher, L., Wyatt, M., and Smith, R. (2011a). Resolved imaging of the HD 191089 debris disc. *MNRAS*, 410:2–12.

Churcher, L. J., Wyatt, M. C., Duchêne, G., Sibthorpe, B., Kennedy, G., Matthews, B. C., Kalas, P., Greaves, J., Su, K., and Rieke, G. (2011b). Multiwavelength modelling of the β Leo debris disc: one, two or three planetesimal populations? *MNRAS*, 417:1715–1734.

Cohen, M., Wheaton, W. A., and Megeath, S. T. (2003). Spectral Irradiance Calibration in the Infrared. XIV. The Absolute Calibration of 2MASS. *AJ*, 126:1090–1096.

Cutri, R. M., Skrutskie, M. F., van Dyk, S., Beichman, C. A., Carpenter, J. M., Chester, T., Cambresy, L., Evans, T., Fowler, J., Gizis, J., Howard, E., Huchra, J., Jarrett, T., Kopan, E. L., Kirkpatrick, J. D., Light, R. M., Marsh, K. A., McCallon, H., Schneider, S., Stiening, R., Sykes, M., Weinberg, M., Wheaton, W. A., Wheelock, S., and Zacarias, N. (2003). *2MASS All Sky Catalog of point sources.*

Darling, D. A. (1957). The kolmogorov-smirnov, cramer-von mises tests. *Ann. Math. Statist.*, 28(4):823–838.

Davis, D. R., Chapman, C. R., Weidenschilling, S. J., and Greenberg, R. (1985). Collisional history of asteroids – Evidence from Vesta and the Hirayama families. *Icarus*, 62:30–53.

Defrère, D., Absil, O., Augereau, J.-C., di Folco, E., Berger, J.-P., Coudé Du Foresto, V., Kervella, P., Le Bouquin, J.-B., Lebreton, J., Millan-Gabet, R., Monnier, J. D., Olofsson, J., and Traub, W. (2011). Hot exozodiacal dust resolved around Vega with IOTA/IONIC. *A& A*, 534:A5.

Di Folco, E., Thévenin, F., Kervella, P., Domiciano de Souza, A., Coudé du Foresto, V., Ségransan, D., and Morel, P. (2004). VLTI near-IR interferometric observations of Vega-like stars. Radius and age of α PsA, β Leo, β Pic, ϵ Eri and τ Cet. *A& A*, 426:601–617.

Dohnanyi, J. S. (1969). Collisional model of asteroids and their debris. *J. Geophys. Res.*, 74:2531–2554.

Donaldson, J. K., Lebreton, J., Roberge, A., Augereau, J.-C., and Krivov, A. V. (2013). Modeling the HD32297 Debris Disk with Far-IR Herschel Data. *ApJ*, 772:17.

Donaldson, J. K., Roberge, A., Chen, C. H., Augereau, J.-C., Dent, W. R. F., Eiroa, C., Krivov, A. V., Mathews, G. S., Meeus, G., Ménard, F., Riviere-Marichalar, P., and Sandell, G. (2012). Herschel PACS Observations and Modeling of Debris Disks in the Tucana-Horologium Association. *ApJ*, 753:147.

Dragomir, D., Kane, S. R., Henry, G. W., Ciardi, D. R., Fischer, D. A., Howard, A. W., Jensen, E. L. N., Laughlin, G., Mahadevan, S., Matthews, J. M., Pilyavsky, G., von Braun, K., Wang, S. X., and Wright, J. T. (2012). The HD 192263 System: Planetary Orbital Period and Stellar Variability Disentangled. *ApJ*, 754:37.

Draine, B. T. (2003a). Interstellar Dust Grains. *ARA& A*, 41:241–289.

Draine, B. T. (2003b). Scattering by Interstellar Dust Grains. II. X-Rays. *ApJ*, 598:1026–1037.

Draine, B. T. and Lee, H. M. (1984). Optical properties of interstellar graphite and silicate grains. *ApJ*, 285:89–108.

Draper, Z. H., Duchêne, G., Millar-Blanchaer, M. A., Matthews, B. C., Wang, J. J., Kalas, P., Graham, J. R., Padgett, D., Ammons, S. M., Bulger, J., Chen, C., Chilcote, J. K., Doyon, R., Fitzgerald, M. P., Follette, K. B., Gerard, B., Greenbaum, A. Z., Hibon, P., Hinkley, S., Macintosh, B., Ingraham, P., Lafrenière, D., Marchis, F., Marois, C., Nielsen, E. L., Oppenheimer, R., Patel, R., Patience, J., Perrin, M., Pueyo, L., Rajan, A., Rameau, J., Sivaramakrishnan, A., Vega, D., Ward-Duong, K., and Wolff, S. G. (2016a). The Peculiar Debris Disk of HD 111520 as Resolved by the Gemini Planet Imager. *ArXiv e-prints*.

Draper, Z. H., Matthews, B. C., Kennedy, G. M., Wyatt, M. C., Venn, K. A., and Sibthorpe, B. (2016b). IR excesses around nearby Lambda Boo stars are caused by debris discs rather than ISM bow waves. *MNRAS*, 456:459–476.

Duchêne, G., Arriaga, P., Wyatt, M., Kennedy, G., Sibthorpe, B., Lisse, C., Holland, W., Wisniewski, J., Clampin, M., Kalas, P., Pinte, C., Wilner, D., Booth, M., Horner, J., Matthews, B., and Greaves, J. (2014). Spatially Resolved Imaging of the Two-component η Crv Debris Disk with Herschel. *ApJ*, 784:148.

Dutrey, A., Semenov, D., Chapillon, E., X, X., Y, Y., and Z, Z. (2014). Physical and chemical structure of planet-forming disks probed by millimeter observations and modelling. In Beuther, H., Klessen, R., Dullemond, C., and Henning, T., editors, *Protostars and Planets VI*. Univ. of Arizona Press. in press, arXiv:1402.3503.

Edgeworth, K. E. (1943). The evolution of our planetary system. *Journal of the British Astronomical Association*, 53:181–188.

Edgeworth, K. E. (1949). The origin and evolution of the solar system. *MNRAS*, 109:600–609.

Eiroa, C., Marshall, J. P., Mora, A., Krivov, A. V., et al. (2011). Herschel discovery of a new class of cold, faint debris discs. *A& A*, 536:L4.

Eiroa, C., Marshall, J. P., Mora, A., Montesinos, B., Absil, O., Augereau, J. C., Bayo, A., Bryden, G., Danchi, W., del Burgo, C., Ertel, S., Fridlund, M., Heras, A. M., Krivov, A. V., Launhardt, R., Liseau, R., Löhne, T., Maldonado, J., Pilbratt, G. L., Roberge, A., Rodmann, J., Sanz-Forcada, J., Solano, E., Stapelfeldt, K., Thébault, P., Wolf, S., Ardila, D., Arévalo, M., Beichmann, C., Faramaz, V., González-García, B. M., Gutiérrez, R., Lebreton, J., Martínez-Arnáiz, R., Meeus, G., Montes, D., Olofsson, G., Su, K. Y. L., White, G. J., Barrado, D., Fukagawa, M., Grün, E., Kamp, I., Lorente, R., Morbidelli, A., Müller, S., Mutschke, H., Nakagawa, T., Ribas, I., and Walker, H. (2013). DUst around NEarby Stars. The survey observational results. *A& A*, 555:A11.

Elliot, J. L., Kern, S. D., Clancy, K. B., Gulbis, A. A. S., Millis, R. L., Buie, M. W., Wasserman, L. H., Chiang, E. I., Jordan, A. B., Trilling, D. E., and Meech, K. J. (2005). The Deep Ecliptic Survey: A Search for Kuiper Belt Objects and Centaurs. II. Dynamical Classification, the Kuiper Belt Plane, and the Core Population. *AJ*, 129:1117–1162.

Engle, S. G. and Guinan, E. F. (2011). Red Dwarf Stars: Ages, Rotation, Magnetic Dynamo Activity and the Habitability of Hosted Planets. In Qain, S., Leung, K., Zhu, L., and Kwok, S., editors, *9th Pacific Rim Conference on Stellar Astrophysics*, volume 451 of *Astronomical Society of the Pacific Conference Series*, page 285.

Ertel, S. (2012). *Modeling the spatial structure of debris disks: Simultaneous multi-wavelength modeling and predictions on the observability of planet-disk interaction (PhD Thesis).*

Ertel, S., Marshall, J. P., Augereau, J.-C., Krivov, A. V., Löhne, T., Eiroa, C., Mora, A., del Burgo, C., Montesinos, B., Bryden, G., Danchi, W., Kirchschlager, F., Liseau, R., Maldonado, J., Pilbratt, G. L., Schüppler, C., Thébault, P., White, G. J., and Wolf, S. (2014). Potential multi-component structure of the debris disk around HIP 17439 revealed by Herschel/DUNES. *A& A*, 561:A114.

Ertel, S., Wolf, S., Marshall, J. P., Eiroa, C., Augereau, J.-C., Krivov, A. V., Löhne, T., Absil, O., Ardila, D., Arévalo, M., Bayo, A., Bryden, G., del Burgo, C., Greaves, J., Kennedy, G., Lebreton, J., Liseau, R., Maldonado, J., Montesinos, B., Mora, A., Pilbratt, G. L., Sanz-Forcada, J., Stapelfeldt, K., and White, G. J. (2012). A peculiar class of debris disks from Herschel/DUNES. A steep fall off in the far infrared. *A& A*, 541:A148.

Ertel, S., Wolf, S., Metchev, S., Schneider, G., Carpenter, J. M., Meyer, M. R., Hillenbrand, L. A., and Silverstone, M. D. (2011). Multi-wavelength modeling of the spatially resolved debris disk of HD 107146. *A& A*, 533:A132.

Faramaz, V., Beust, H., Thébault, P., Augereau, J.-C., Bonsor, A., del Burgo, C., Ertel, S., Marshall, J. P., Milli, J., Montesinos, B., Mora, A., Bryden, G., Danchi, W., Eiroa, C., White, G. J., and Wolf, S. (2014). Can eccentric debris disks be long-lived?. A first numerical investigation and application to ζ^2 Reticuli. *A& A*, 563:A72.

Feigelson, E. and Babu, G. (2012). *Modern Statistical Methods for Astronomy.* Cambridge University Press.

Fitzgerald, M. P., Kalas, P. G., and Graham, J. R. (2007). A Ring of Warm Dust in the HD 32297 Debris Disk. *ApJ*, 670:557–564.

Frisch, P. C., Redfield, S., and Slavin, J. D. (2011). The Interstellar Medium Surrounding the Sun. *ARA& A*, 49:237–279.

Fujiwara, H., Ishihara, D., Onaka, T., Takita, S., Kataza, H., Yamashita, T., Fukagawa, M., Ootsubo, T., Hirao, T., Enya, K., Marshall, J. P., White, G. J., Nakagawa, T., and Murakami, H. (2013). AKARI/IRC 18 μm survey of warm debris disks. *A& A*, 550:A45.

Fujiwara, H., Onaka, T., Yamashita, T., Ishihara, D., Kataza, H., Fukagawa, M., Takeda, Y., and Murakami, H. (2012). Silica-rich Bright Debris Disk around HD 15407A. *ApJ*, 749:L29.

Gilman, J. (1960). Direct Measurements of the Surface Energies of Crystals. *Journal of Applied Physics*, 31:2208–2218.

Golimowski, D. A., Ardila, D. R., Krist, J. E., Clampin, M., Ford, H. C., Illingworth, G. D., Bartko, F., Benítez, N., Blakeslee, J. P., Bouwens, R. J., Bradley, L. D., Broadhurst, T. J., Brown, R. A., Burrows, C. J., Cheng, E. S., Cross, N. J. G., Demarco, R., Feldman, P. D., Franx, M., Goto, T., Gronwall, C., Hartig, G. F., Holden, B. P., Homeier, N. L., Infante, L., Jee, M. J., Kimble, R. A., Lesser, M. P., Martel, A. R., Mei, S., Menanteau, F., Meurer, G. R., Miley, G. K., Motta, V., Postman, M., Rosati, P., Sirianni, M., Sparks, W. B., Tran, H. D., Tsvetanov, Z. I., White, R. L., Zheng, W., and Zirm, A. W. (2006). Hubble Space Telescope ACS Multiband Coronagraphic Imaging of the Debris Disk around β Pictoris. *AJ*, 131:3109–3130.

Golimowski, D. A., Krist, J. E., Stapelfeldt, K. R., Chen, C. H., Ardila, D. R., Bryden, G., Clampin, M., Ford, H. C., Illingworth, G. D., Plavchan, P., Rieke, G. H., and Su, K. Y. L. (2011). Hubble and Spitzer Space Telescope Observations of the Debris Disk around the Nearby K Dwarf HD 92945. *ArXiv e-prints*.

Gomes, R., Levison, H. F., Tsiganis, K., and Morbidelli, A. (2005). Origin of the cataclysmic Late Heavy Bombardment period of the terrestrial planets. *Nature*, 435:466–469.

Gray, D. F. (1992). *The observation and analysis of stellar photospheres.*

Gray, R. O., Corbally, C. J., Garrison, R. F., McFadden, M. T., Bubar, E. J., McGahee, C. E., O'Donoghue, A. A., and Knox, E. R. (2006). Contributions to the Nearby Stars (NStars) Project: Spectroscopy of Stars Earlier than M0 within 40 pc-The Southern Sample. *AJ*, 132:161–170.

Gray, R. O., Corbally, C. J., Garrison, R. F., McFadden, M. T., and Robinson, P. E. (2003). Contributions to the Nearby Stars (NStars) Project: Spectroscopy of Stars Earlier than M0 within 40 Parsecs: The Northern Sample. I. *AJ*, 126:2048–2059.

Greaves, J. S., Holland, W. S., Moriarty-Schieven, G., and 8 colleagues (1998). A dust ring around ϵ Eridani: Analog to the young Solar system. *A& A*, 506:L133–L137.

Greaves, J. S., Kennedy, G. M., Thureau, N., Eiroa, C., Marshall, J. P., Maldonado, J., Matthews, B. C., Olofsson, G., Barlow, M. J., Moro-Martín, A., Sibthorpe, B., Absil, O., Ardila, D. R., Booth, M., Broekhoven-Fiene, H., Brown, D. J. A., Cameron, A. C., del Burgo, C., Di Francesco, J., Eislöffel, J., Duchêne, G., Ertel, S., Holland, W. S., Horner, J., Kalas, P., Kavelaars, J. J., Lestrade, J.-F., Vican, L., Wilner, D. J., Wolf, S., and Wyatt, M. C. (2014a). Alignment in star-debris disc systems seen by Herschel. *MNRAS*, 438:L31–L35.

Greaves, J. S., Sibthorpe, B., Acke, B., Pantin, E. E., Vandenbussche, B., Olofsson, G., Dominik, C., Barlow, M. J., Bendo, G. J., Blommaert, J. A. D. L., Brandeker, A., de Vries, B. L., Dent, W. R. F., Di Francesco, J., Fridlund, M., Gear, W. K., Harvey, P. M., Hogerheijde, M. R., Holland, W. S., Ivison, R. J., Liseau, R., Matthews, B. C., Pilbratt, G. L., Walker, H. J., and Waelkens, C. (2014b). Extreme Conditions in a Close Analog to the Young Solar System: Herschel Observations of epsilon Eridani. *ApJL*, 791:L11.

Greaves, J. S., Wyatt, M. C., Holland, W. S., and Dent, W. R. F. (2004). The debris disc around τ Ceti: a massive analogue to the Kuiper belt. *MNRAS*, 351:L54–L58.

Greenberg, R. (1978). Orbital resonance in a dissipative medium. *Icarus*, 33:62–73.

Griffin, M. J., Abergel, A., Abreu, A., Ade, P. A. R., André, P., Augueres, J.-L., Babbedge, T., Bae, Y., Baillie, T., Baluteau, J.-P., Barlow, M. J., Bendo, G., Benielli, D., Bock, J. J., Bonhomme, P., Brisbin, D., Brockley-Blatt, C., Caldwell, M., Cara, C., Castro-Rodriguez, N., Cerulli, R., Chanial, P., Chen, S., Clark, E., Clements, D. L., Clerc, L., Coker, J., Communal, D., Conversi, L., Cox, P., Crumb, D., Cunningham, C., Daly, F., Davis, G. R., de Antoni, P., Delderfield, J., Devin, N., di Giorgio, A., Didschuns, I., Dohlen, K., Donati, M., Dowell, A., Dowell, C. D., Duband, L., Dumaye, L., Emery, R. J., Ferlet, M., Ferrand, D., Fontignie, J., Fox, M., Franceschini, A., Frerking, M., Fulton, T., Garcia, J., Gastaud, R., Gear, W. K., Glenn, J., Goizel, A., Griffin, D. K., Grundy, T., Guest, S., Guillemet, L., Hargrave, P. C., Harwit, M., Hastings, P., Hatziminaoglou, E., Herman, M., Hinde, B., Hristov, V., Huang, M., Imhof, P., Isaak, K. J., Israelsson, U., Ivison, R. J., Jennings, D., Kiernan, B., King, K. J., Lange, A. E., Latter, W., Laurent, G., Laurent, P., Leeks, S. J., Lellouch, E., Levenson, L., Li, B., Li, J., Lilienthal, J., Lim, T., Liu, S. J., Lu, N., Madden, S., Mainetti, G., Marliani, P., McKay, D., Mercier, K., Molinari, S., Morris, H., Moseley, H., Mulder, J., Mur, M., Naylor, D. A., Nguyen, H., O'Halloran, B., Oliver, S., Olofsson, G., Olofsson, H.-G., Orfei, R., Page, M. J., Pain, I., Panuzzo, P., Papageorgiou, A., Parks, G., Parr-Burman, P., Pearce, A., Pearson, C., Pérez-Fournon, I., Pinsard, F., Pisano, G., Podosek, J., Pohlen, M., Polehampton, E. T., Pouliquen, D., Rigopoulou, D., Rizzo, D., Roseboom, I. G., Roussel, H., Rowan-Robinson, M., Rownd, B., Saraceno, P., Sauvage, M., Savage, R., Savini, G., Sawyer, E., Scharmberg, C., Schmitt, D., Schneider, N., Schulz, B., Schwartz, A., Shafer, R., Shupe, D. L., Sibthorpe, B., Sidher, S., Smith, A., Smith, A. J., Smith, D., Spencer, L., Stobie, B., Sudiwala, R., Sukhatme, K., Surace, C., Stevens, J. A., Swinyard, B. M., Trichas, M., Tourette, T., Triou, H., Tseng, S., Tucker, C., Turner, A., Vaccari, M., Valtchanov, I., Vigroux, L., Virique, E., Voellmer, G., Walker, H., Ward, R., Waskett, T., Weilert, M., Wesson, R., White, G. J., Whitehouse, N., Wilson, C. D., Winter, B., Woodcraft, A. L., Wright, G. S., Xu, C. K., Zavagno, A., Zemcov, M., Zhang, L., and Zonca, E. (2010). The Herschel-SPIRE instrument and its in-flight performance. *A& A*, 518:L3.

Gundlach, B., Kilias, S., Beitz, E., and Blum, J. (2011). Micrometer-sized ice particles for planetary-science experiments - I. Preparation, critical rolling friction force, and specific surface energy. *Icarus*, 214:717–723.

Heap, S. R., Lindler, D. J., Lanz, T. M., Cornett, R. H., Hubeny, I., Maran, S. P., and Woodgate, B. (2000). STIS coronagraphic observations of Beta Pictoris. *ApJ*, 539:435–444.

Hedderich, J. and Sachs, L. (1968). *Angewandte Statistik*. Springer Gabler.

Holmberg, J., Nordström, B., and Andersen, J. (2009). The Geneva-Copenhagen survey of the solar neighbourhood. III. Improved distances, ages, and kinematics. *A& A*, 501:941–947.

Hung, L.-W., Duchêne, G., Arriaga, P., Fitzgerald, M. P., Maire, J., Marois, C., Millar-Blanchaer, M. A., Bruzzone, S., Rajan, A., Pueyo, L., Kalas, P. G., De Rosa, R. J., Graham, J. R., Konopacky, Q., Wolff, S. G., Ammons, S. M., Chen, C. H., Chilcote, J. K., Draper, Z. H., Esposito, T. M., Gerard, B., Goodsell, S., Greenbaum, A., Hibon, P., Hinkley, S., Macintosh, B., Marchis, F., Metchev, S., Nielsen, E. L., Oppenheimer, R., Patience, J. L., Perrin, M. D., Rantakyrö, F. T., Sivaramakrishnan, A., Wang, J. J., Ward-Duong, K., and Wiktorowicz, S. J. (2015). First Scattered-light Image of the Debris Disk around HD 131835 with the Gemini Planet Imager. *ApJL*, 815:L14.

Ida, S. and Lin, D. N. C. (2005). Toward a Deterministic Model of Planetary Formation. III. Mass Distribution of Short-Period Planets around Stars of Various Masses. *ApJ*, 626:1045–1060.

Ishihara, D., Onaka, T., Kataza, H., Salama, A., Alfageme, C., Cassatella, A., Cox, N., García-Lario, P., Stephenson, C., Cohen, M., Fujishiro, N., Fujiwara, H., Hasegawa, S., Ita, Y., Kim, W., Matsuhara, H., Murakami, H., Müller, T. G., Nakagawa, T., Ohyama, Y., Oyabu, S., Pyo, J., Sakon, I., Shibai, H., Takita, S., Tanabé, T., Uemizu, K., Ueno, M., Usui, F., Wada, T., Watarai, H., Yamamura, I., and Yamauchi, C. (2010). The AKARI/IRC mid-infrared all-sky survey. *A&A*, 514:A1.

Janson, M., Brandt, T. D., Moro-Martin, A., Usuda, T., Thalmann, C., Carson, J. C., Goto, M., Currie, T., McElwain, M. W., Itoh, Y., Fukagawa, M., Crepp, J., Kuzuhara, M., Hashimoto, J., Kudo, T., Kusakabe, N., Abe, L., Brandner, W., Egner, S., Feldt, M., Grady, C. A., Guyon, O., Hayano, Y., Hayashi, M., Hayashi, S., Henning, T., Hodapp, K. W., Ishii, M., Iye, M., Kandori, R., Knapp, G. R., Kwon, J., Matsuo, T., Miyama, S., Morino, J.-I., Nishimura, T., Pyo, T.-S., Serabyn, E., Suenaga, T., Suto, H., Suzuki, R., Takahashi, Y., Takami, M., Takato, N., Terada, H., Tomono, D., Turner, E. L., Watanabe, M., Wisniewski, J., Yamada, T., Takami, H., and Tamura, M. (2013). The SEEDS Direct Imaging Survey for Planets and Scattered Dust Emission in Debris Disk Systems. *ArXiv e-prints*.

Jewitt, D., Luu, J., and Marsden, B. G. (1992). 1992 QB1. *IAU Circ.*, 5611.

Johnson, J. A., Aller, K. M., Howard, A. W., and Crepp, J. R. (2010). Giant Planet Occurrence in the Stellar Mass-Metallicity Plane. *PASP*, 122:905–915.

Kalas, P. (2005). First optical images of circumstellar dust surrounding the debris disk candidate HD 32297. *ApJ*, 635:L169–L172.

Kalas, P., Duchene, G., Fitzgerald, M. P., and Graham, J. R. (2007a). Discovery of an Extended Debris Disk around the F2 V Star HD 15745. *ApJL*, 671:L161–L164.

Kalas, P., Fitzgerald, M. P., and Graham, J. R. (2007b). Discovery of Extreme Asymmetry in the Debris Disk Surrounding HD 15115. *ApJL*, 661:L85–L88.

Kalas, P., Graham, J. R., Chiang, E., Fitzgerald, M. P., Clampin, M., Kite, E. S., Stapelfeldt, K., Marois, C., and Krist, J. (2008). Optical Images of an Exosolar Planet 25 Light-Years from Earth. *Science*, 322:1345–.

Kalas, P., Graham, J. R., and Clampin, M. (2005). A planetary system as the origin of structure in Fomalhaut's dust belt. *Nature*, 435:1067–1070.

Kalas, P., Graham, J. R., Clampin, M. C., and Fitzgerald, M. P. (2006). First Scattered Light Images of Debris Disks around HD 53143 and HD 139664. *ApJ*, 637:L57–L60.

Kennedy, G. M. (2015). Nature or nurture of coplanar Tatooines: the aligned circumbinary Kuiper belt analogue around HD 131511. *MNRAS*, 447:L75–L79.

Kennedy, G. M. and Kenyon, S. J. (2008). Planet Formation around Stars of Various Masses: The Snow Line and the Frequency of Giant Planets. *ApJ*, 673:502–512.

Kennedy, G. M., Matrà, L., Marmier, M., Greaves, J. S., Wyatt, M. C., Bryden, G., Holland, W., Lovis, C., Matthews, B. C., Pepe, F., Sibthorpe, B., and Udry, S. (2015). Kuiper belt structure around nearby super-Earth host stars. *MNRAS*, 449:3121–3136.

Kennedy, G. M. and Wyatt, M. C. (2010). Are debris disks self-stirred? *MNRAS*, 405:1253–1270.

Kennedy, G. M. and Wyatt, M. C. (2014). Do two-temperature debris discs have multiple belts? *MNRAS*, 444:3164–3182.

Kennedy, G. M., Wyatt, M. C., Bryden, G., Wittenmyer, R., and Sibthorpe, B. (2013). Star-planet-debris disc alignment in the HD 82943 system: is planetary system coplanarity actually the norm? *MNRAS*.

Kennedy, G. M., Wyatt, M. C., Sibthorpe, B., Duchêne, G., Kalas, P., Matthews, B. C., Greaves, J. S., Su, K. Y. L., and Fitzgerald, M. P. (2012a). 99 Herculis: host to a circumbinary polar-ring debris disc. *MNRAS*, 421:2264–2276.

Kennedy, G. M., Wyatt, M. C., Sibthorpe, B., Phillips, N. M., Matthews, B. C., and Greaves, J. S. (2012b). Coplanar circumbinary debris discs. *MNRAS*, 426:2115–2128.

Kenyon, S. J. and Bromley, B. C. (2001). Gravitational Stirring in Planetary Debris Disks. *AJ*, 121:538–551.

Kenyon, S. J. and Bromley, B. C. (2004a). Collisional cascades in planetesimal disks. II. Embedded planets. *AJ*, 127:513–530.

Kenyon, S. J. and Bromley, B. C. (2004b). Detecting the dusty debris of terrestrial planet formation. *ApJ*, 602:L133–L136.

Kenyon, S. J. and Bromley, B. C. (2004c). The size distribution of Kuiper Belt objects. *AJ*, 128:1916–1926.

Kenyon, S. J. and Bromley, B. C. (2008). Variations on Debris Disks: Icy Planet Formation at 30-150 AU for 1-3 $M_\odot$ Main-Sequence Stars. *ApJS*, 179:451–483.

Kirchschlager, F. and Wolf, S. (2013). Porous dust grains in debris disks. *A& A*, 552:A54.

Kobayashi, H., Kimura, H., Watanabe, S.-i., Yamamoto, T., and Müller, S. (2011). Sublimation temperature of circumstellar dust particles and its importance for dust ring formation. *Earth, Planets, and Space*, 63:1067–1075.

Kolmogorov, A. (1933). Sulla determinazione empirica di una legge di distriutione. *Giornale dell'Istituto Italiano deglo Attuari*, 4:1–11.

Krijt, S. and Kama, M. (2014). A dearth of small particles in debris disks. An energy-constrained smallest fragment size. *A& A*, 566:L2.

Krist, J. E., Ardila, D. R., Golimowski, D. A., and 38 colleagues (2005). Hubble Space Telescope advanced camera for surveys coronagraphic imaging of the AU Microscopii debris disk. *AJ*, 129:1008–1017.

Krist, J. E., Stapelfeldt, K. R., Bryden, G., and Plavchan, P. (2012). Hubble Space Telescope Observations of the HD 202628 Debris Disk. *AJ*, 144:45.

Krist, J. E., Stapelfeldt, K. R., Bryden, G., Rieke, G. H., Su, K. Y. L., Chen, C. C., Beichman, C. A., Hines, D. C., Rebull, L. M., Tanner, A., Trilling, D. E., Clampin, M., and Gáspár, A. (2010). HST and Spitzer Observations of the HD 207129 Debris Ring. *AJ*, 140:1051–1061.

Krivov, A. V. (2010). Debris disks: Seeing dust, thinking of planetesimals and planets. *Research in Astron. Astrophys.*, 10:383–414.

Krivov, A. V., Eiroa, C., Löhne, T., Marshall, J. P., Montesinos, B., del Burgo, C., Absil, O., Ardila, D., Augereau, J.-C., Bayo, A., Bryden, G., Danchi, W., Ertel, S., Lebreton, J., Liseau, R., Mora, A., Mustill, A. J., Mutschke, H., Neuhäuser, R., Pilbratt, G. L., Roberge, A., Schmidt, T. O. B., Stapelfeldt, K. R., Thébault, P., Vitense, C., White, G. J., and Wolf, S. (2013). Herschel's "Cold Debris Disks": Background Galaxies or Quiescent Rims of Planetary Systems? *ApJ*, 772:32.

Krivov, A. V., Löhne, T., and Sremčević, M. (2006). Dust distributions in debris disks: Effects of gravity, radiation pressure and collisions. *A& A*, 455:509–519.

Krivov, A. V., Mann, I., and Krivova, N. A. (2000). Size distributions of dust in circumstellar debris disks. *A& A*, 362:1127–1137.

Krivov, A. V., Müller, S., Löhne, T., and Mutschke, H. (2008). Collisional and thermal emission models of debris disks: Toward planetesimal population properties. *ApJ*, 687:608–622.

Krivov, A. V., Sremčević, M., and Spahn, F. (2005). Evolution of a keplerian disk of colliding and fragmenting particles: A kinetic model and application to the Edgeworth-Kuiper Belt. *Icarus*, 174:105–134.

Kuiper, G. P. (1951). On the Origin of the Solar System. *Proceedings of the National Academy of Science*, 37:1–14.

Laarhoven, P. and Aarts, E. (1987). *Simulated Annealing: Theory and Applications*. Springer Science and Business Media.

Lagage, P. O. and Pantin, E. (1994). Dust depletion in the inner disk of Beta-Pictoris as a possible indicator of planets. *Nature*, 369:628–630.

Lagrange, A.-M., Bonnefoy, M., Chauvin, G., Apai, D., Ehrenreich, D., Boccaletti, A., Gratadour, D., Rouan, D., Mouillet, D., Lacour, S., and Kasper, M. (2010). A Giant Planet Imaged in the Disk of the Young Star β Pictoris. *Science*, 329:57–.

Lagrange, A.-M., Langlois, M., Gratton, R., Maire, A.-L., Milli, J., Olofsson, J., Vigan, A., Bailey, V., Mesa, D., Chauvin, G., Boccaletti, A., Galicher, R., Girard, J. H., Bonnefoy, M., Samland, M., Menard, F., Henning, T., Kenworthy, M., Thalmann, C., Beust, H., Beuzit, J.-L., Brandner, W., Buenzli, E., Cheetham, A., Janson, M., le Coroller, H., Lannier, J., Mouillet, D., Peretti, S., Perrot, C., Salter, G., Sissa, E., Wahhaj, Z., Abe, L., Desidera, S., Feldt, M., Madec, F., Perret, D., Petit, C., Rabou, P., Soenke, C., and Weber, L. (2016). A narrow, edge-on disk resolved around HD 106906 with SPHERE. *A& A*, 586:L8.

Lamy, P. L. (1974). Interaction of interplanetary dust grains with the solar radiation field. *A& A*, 35:197–207.

Laor, A. and Draine, B. T. (1993). Spectroscopic constraints on the properties of dust in active galactic nuclei. *ApJ*, 402:441–468.

Lebouteiller, V., Barry, D. J., Spoon, H. W. W., Bernard-Salas, J., Sloan, G. C., Houck, J. R., and Weedman, D. W. (2011). CASSIS: The Cornell Atlas of Spitzer/Infrared Spectrograph Sources. *ApJS*, 196:8.

Lebreton, J., Augereau, J.-C., Thi, W.-F., Roberge, A., Donaldson, J., Schneider, G., Maddison, S. T., Ménard, F., Riviere-Marichalar, P., Mathews, G. S., Kamp, I., Pinte, C., Dent, W. R. F., Barrado, D., Duchêne, G., Gonzalez, J.-F., Grady, C. A., Meeus, G., Pantin, E., Williams, J. P., and Woitke, P. (2012). An icy Kuiper belt around the young solar-type star HD 181327. *A& A*, 539:A17.

Lebreton, J., van Lieshout, R., Augereau, J.-C., Absil, O., Mennesson, B., Kama, M., Dominik, C., Bonsor, A., Vandeportal, J., Beust, H., Defrère, D., Ertel, S., Faramaz, V., Hinz, P., Kral, Q., Lagrange, A.-M., Liu, W., and Thébault, P. (2013). An interferometric study of the Fomalhaut inner debris disk. III. Detailed models of the exozodiacal disk and its origin. *A& A*, 555:A146.

Leonard, F. C. (1930). The New Planet Pluto. *Leaflet of the Astronomical Society of the Pacific*, 1:121.

Lestrade, J.-F., Matthews, B. C., Sibthorpe, B., Kennedy, G. M., Wyatt, M. C., Bryden, G., Greaves, J. S., Thilliez, E., Moro-Martín, A., Booth, M., Dent, W. R. F., Duchêne, G., Harvey, P. M., Horner, J., Kalas, P., Kavelaars, J. J., Phillips, N. M., Rodriguez, D. R., Su, K. Y. L., and Wilner, D. J. (2012). A DEBRIS disk around the planet hosting M-star GJ 581 spatially resolved with Herschel. *A& A*, 548:A86.

Lestrade, J.-F. and Thilliez, E. (2015). MAMBO image of the debris disk around ϵ Eridani: robustness of the azimuthal structure. *A& A*, 576:A72.

Li, A. and Greenberg, J. M. (1998). A comet dust model for the β pictoris disk. *A& A*, 331:291–313.

Liseau, R., Eiroa, C., Fedele, D., Augereau, J., Olofsson, G., González, B., Maldonado, J., Montesinos, B., Mora, A., Absil, O., Ardila, D., Barrado, D., Bayo, A., Beichman, C. A., Bryden, G., Danchi, W. C., Del Burgo, C., Ertel, S., Fridlund, C. W. M., Heras, A. M., Krivov, A. V., Launhardt, R., Lebreton, J., Löhne, T., Marshall, J. P., Meeus, G., Müller, S., Pilbratt, G. L., Roberge, A., Rodmann, J., Solano, E., Stapelfeldt, K. R., Thébault, P., White, G. J., and Wolf, S. (2010). Resolving the cold debris disc around a planet-hosting star . PACS photometric imaging observations of q^1 Eridani (HD 10647, HR 506). *A& A*, 518:L132.

Liseau, R., Risacher, C., Brandeker, A., Eiroa, C., Fridlund, M., Nilsson, R., Olofsson, G., Pilbratt, G. L., and Thébault, P. (2008). q^1 eridani: a solar-type star with a planet and a dust belt. *A& A*, 480:L47–L50.

Lissauer, J. J. and Stewart, G. R. (1993). Planetary accretion in circumstellar disks. In Phillips, J. A., Thorsett, J. E., and Kulkarni, S. R., editors, *Planets around Pulsars (ASP Conf. Series, vol. 36)*, pages 217–233.

Lisse, C. M., Beichman, C. A., Bryden, G., and Wyatt, M. C. (2007). On the Nature of the Dust in the Debris Disk around HD 69830. *ApJ*, 658:584–592.

Löhne, T., Augereau, J.-C., Ertel, S., Marshall, J. P., Eiroa, C., Mora, A., Absil, O., Stapelfeldt, K. R., Thébault, P., del Burgo, C., Danchi, W., Krivov, A. V., Lebreton, J., Letawe, G., Magain, P., Maldonado, J., Montesinos, B., Pilbratt, G. L., White, G. J., and Wolf, S. (2012). Modelling the huge, Herschel-resolved debris ring around HD 207129. *A& A*, 537:A110.

Löhne, T., Krivov, A. V., and Rodmann, J. (2008). Long-term collisional evolution of debris disks. *ApJ*, 673:1123–1137.

MacGregor, M. A., Wilner, D. J., Andrews, S. M., and Hughes, A. M. (2015). Resolved Millimeter Emission from the HD 15115 Debris Disk. *ApJ*, 801:59.

Mamajek, E. E. and Bell, C. P. M. (2014). On the age of the β Pictoris moving group. *MNRAS*, 445:2169–2180.

Marois, C., Zuckerman, B., Konopacky, Q. M., Macintosh, B., and Barman, T. (2010). Images of a fourth planet orbiting HR 8799. *Nature*, 468:1080–1083.

Marshall, J. P., Booth, M., Holland, W., Matthews, B. C., Greaves, J. S., and Zuckerman, B. (2016). Far-infrared and sub-millimetre imaging of HD 76582's circumstellar disk. *MNRAS*.

Marshall, J. P., Kirchschlager, F., Ertel, S., Augereau, J.-C., Kennedy, G. M., Booth, M., Wolf, S., Montesinos, B., Eiroa, C., and Matthews, B. (2014a). Interpreting the extended emission around three nearby debris disc host stars. *A& A*, 570:A114.

Marshall, J. P., Krivov, A. V., del Burgo, C., Eiroa, C., Mora, A., Montesinos, B., Ertel, S., Bryden, G., Liseau, R., Augereau, J.-C., Bayo, A., Danchi, W., Löhne, T., Maldonado, J., Pilbratt, G. L., Stapelfeldt, K., Thebault, P., White, G. J., and Wolf, S. (2013). Herschel observations of the debris disc around HIP 92043. *A& A*, 557:A58.

Marshall, J. P., Löhne, T., Montesinos, B., Krivov, A. V., Eiroa, C., Absil, O., Bryden, G., Maldonado, J., Mora, A., Sanz-Forcada, J., Ardila, D., Augereau, J.-C., Bayo, A., Del Burgo, C., Danchi, W., Ertel, S., Fedele, D., Fridlund, M., Lebreton, J., González-García, B. M., Liseau, R., Meeus, G., Müller, S., Pilbratt, G. L., Roberge, A., Stapelfeldt, K., Thébault, P., White, G. J., and Wolf, S. (2011). A Herschel resolved far-infrared dust ring around HD 207129. *A& A*, 529:A117.

Marshall, J. P., Moro-Martín, A., Eiroa, C., Kennedy, G., Mora, A., Sibthorpe, B., Lestrade, J.-F., Maldonado, J., Sanz-Forcada, J., Wyatt, M. C., Matthews, B., Horner, J., Montesinos, B., Bryden, G., del Burgo, C., Greaves, J. S., Ivison, R. J., Meeus, G., Olofsson, G., Pilbratt, G. L., and White, G. J. (2014b). Correlations between the stellar, planetary, and debris components of exoplanet systems observed by Herschel. *A& A*, 565:A15.

Massey, F. J. (1951). The kolmogorov-smirnov test for goodness of fit. *Journal of the American Statistical Association*, 46(253):68–78.

Matthews, B., Kennedy, G., Sibthorpe, B., Booth, M., Wyatt, M., Broekhoven-Fiene, H., Macintosh, B., and Marois, C. (2014a). Resolved Imaging of the HR 8799 Debris Disk with Herschel. *ApJ*, 780:97.

Matthews, B. C., Kennedy, G., Sibthorpe, B., Holland, W., Booth, M., Kalas, P., MacGregor, M., Wilner, D., Vandenbussche, B., Olofsson, G., Blommaert, J., Brandeker, A., Dent, W. R. F., de Vries, B. L., Di Francesco, J., Fridlund, M., Graham, J. R., Greaves, J., Heras, A. M., Hogerheijde, M., Ivison, R. J., Pantin, E., and Pilbratt, G. L. (2015). The AU Mic Debris Disk: Far-infrared and Submillimeter Resolved Imaging. *ApJ*, 811:100.

Matthews, B. C., Krivov, A. V., Wyatt, M. C., Bryden, G., and Eiroa, C. (2014b). Observations, modeling and theory of debris disks. In Beuther, H., Klessen, R., Dullemond, C., and Henning, T., editors, *Protostars and Planets VI*. U. Arizona Press. in press, arXiv:1401.0743.

Matthews, B. C., Sibthorpe, B., Kennedy, G., Phillips, N., Churcher, L., Duchêne, G., Greaves, J. S., Lestrade, J., Moro-Martin, A., Wyatt, M. C., Bastien, P., Biggs, A., Bouvier, J., Butner, H. M., Dent, W. R. F., di Francesco, J., Eislöffel, J., Graham, J., Harvey, P., Hauschildt, P., Holland, W. S., Horner, J., Ibar, E., Ivison, R. J., Johnstone, D., Kalas, P., Kavelaars, J., Rodriguez, D., Udry, S., van der Werf, P., Wilner, D., and Zuckerman, B. (2010). Resolving debris discs in the far-infrared: Early highlights from the DEBRIS survey. *A& A*, 518:L135.

Mittal, T., Chen, C. H., Jang-Condell, H., Manoj, P., Sargent, B. A., Watson, D. M., and Lisse, C. M. (2015). The Spitzer Infrared Spectrograph Debris Disk Catalog. II. Silicate Feature Analysis of Unresolved Targets. *ApJ*, 798:87.

Moerchen, M. M., Telesco, C. M., and Packham, C. (2010). High Spatial Resolution Imaging of Thermal Emission from Debris Disks. *ApJ*, 723:1418–1435.

Moerchen, M. M., Telesco, C. M., Packham, C., and Kehoe, T. J. J. (2007). Mid-Infrared Resolution of a 3 AU Radius Debris Disk around ζ Leporis. *ApJ*, 655:L109–L112.

Montesinos, B., Eiroa, C., Krivov, A. V., Marshall, J. P., Pilbratt, G. L., Liseau, R., Mora, A., Maldonado, J., Wolf, S., Ertel, S., Bayo, A., Augereau, J.-C., Heras, A. M., Fridlund, M., Danchi, W. C., Solano, E., Kirchschlager, F., del Burgo, C., and Montes, D. (2016). Incidence of debris discs around FGK stars in the solar neighbourhood. *ArXiv e-prints*.

Moór, A., Ábrahám, P., Derekas, A., Kiss, C., Kiss, L. L., Apai, D., Grady, C., and Henning, T. (2006). Nearby Debris Disk Systems with High Fractional Luminosity Reconsidered. *ApJ*, 644:525–542.

Moór, A., Ábrahám, P., Juhász, A., Kiss, C., Pascucci, I., Kóspál, Á., Apai, D., Henning, T., Csengeri, T., and Grady, C. (2011). Molecular Gas in Young Debris Disks. *ApJL*, 740:L7.

Moór, A., Ábrahám, P., Kóspál, Á., Szabó, G. M., Apai, D., Balog, Z., Csengeri, T., Grady, C., Henning, T., Juhász, A., Kiss, C., Pascucci, I., Szulágyi, J., and Vavrek, R. (2013a). A Resolved Debris Disk around the Candidate Planet-hosting Star HD 95086. *ApJL*, 775:L51.

Moór, A., Juhász, A., Kóspál, Á., Ábrahám, P., Apai, D., Csengeri, T., Grady, C., Henning, T., Hughes, A. M., Kiss, C., Pascucci, I., Schmalzl, M., and Gabányi, K. (2013b). ALMA Continuum Observations of a 30 Myr Old Gaseous Debris Disk around HD 21997. *ApJL*, 777:L25.

Moór, A., Kóspál, Á., Ábrahám, P., Apai, D., Balog, Z., Grady, C., Henning, T., Juhász, A., Kiss, C., Krivov, A. V., Pawellek, N., and Szabó, G. M. (2015). Stirring in massive, young debris discs from spatially resolved Herschel images. *MNRAS*, 447:577–597.

Morales, F. Y., Bryden, G., Werner, M. W., and Stapelfeldt, K. R. (2013). Herschel-resolved Outer Belts of Two-belt Debris Disks around A-type Stars: HD 70313, HD 71722, HD 159492, and F-type: HD 104860. *ApJ*, 776:111.

Morales, F. Y., Rieke, G. H., Werner, M. W., Bryden, G., Stapelfeldt, K. R., and Su, K. Y. L. (2011). Common Warm Dust Temperatures Around Main-sequence Stars. *ApJL*, 730:L29.

Mordasini, C., Alibert, Y., Benz, W., Klahr, H., and Henning, T. (2012). Extrasolar planet population synthesis . IV. Correlations with disk metallicity, mass, and lifetime. *A& A*, 541:A97.

Moro-Martín, A., Malhotra, R., Bryden, G., Rieke, G. H., Su, K. Y. L., Beichman, C. A., and Lawler, S. M. (2010). Locating Planetesimal Belts in the Multiple-planet Systems HD 128311, HD 202206, HD 82943, and HR 8799. *ApJ*, 717:1123–1139.

Moro-Martín, A., Marshall, J. P., Kennedy, G., Sibthorpe, B., Matthews, B. C., Eiroa, C., Wyatt, M. C., Lestrade, J.-F., Maldonado, J., Rodriguez, D., Greaves, J. S., Montesinos, B., Mora, A., Booth, M., Duchêne, G., Wilner, D., and Horner, J. (2015). Does the Presence of Planets Affect the Frequency and Properties of Extrasolar Kuiper Belts? Results from the Herschel Debris and Dunes Surveys. *ApJ*, 801:143.

Müller, S., Löhne, T., and Krivov, A. V. (2010). The Debris Disk of Vega: A Steady-State Collisional Cascade, Naturally. *ApJ*, 708:1728–1747.

Müller, T., Nielbock, M., Balog, Z., Klaas, U., and Vilenius, E. (2011). PACS Photometer - Point Source Flux Calibration.

Mustill, A. J. and Wyatt, M. C. (2009). Debris disc stirring by secular perturbations from giant planets. *MNRAS*, 399:1403–1414.

Najita, J. and Williams, J. P. (2005). An 850 micron survey for dust around solar mass stars. *ApJ*, 635:625–635.

Nielsen, E. L., Liu, M. C., Wahhaj, Z., Biller, B. A., Hayward, T. L., Close, L. M., Males, J. R., Skemer, A. J., Chun, M., Ftaclas, C., Alencar, S. H. P., Artymowicz, P., Boss, A., Clarke, F., de Gouveia Dal Pino, E., Gregorio-Hetem, J., Hartung, M., Ida, S., Kuchner, M., Lin, D. N. C., Reid, I. N., Shkolnik, E. L., Tecza, M., Thatte, N., and Toomey, D. W. (2013). The Gemini NICI Planet-Finding Campaign: The Frequency of Giant Planets around Young B and A Stars. *ApJ*, 776:4.

Nilsson, R., Liseau, R., Brandeker, A., Olofsson, G., Pilbratt, G. L., Risacher, C., Rodmann, J., Augereau, J.-C., Bergman, P., Eiroa, C., Fridlund, M., Thébault, P., and White, G. J. (2010). Kuiper belts around nearby stars. *A& A*, 518:A40.

Olofsson, J., Henning, T., Nielbock, M., Augereau, J.-C., Juhàsz, A., Oliveira, I., Absil, O., and Tamanai, A. (2013). The twofold debris disk around HD 113766 A. Warm and cold dust as seen with VLTI/MIDI and Herschel/PACS. *A& A*, 551:A134.

Ortega, V. G., de la Reza, R., Jilinski, E., and Bazzanella, B. (2004). New Aspects of the Formation of the β Pictoris Moving Group. *ApJ*, 609:243–246.

Ott, S. (2010). The Herschel Data Processing System - HIPE and Pipelines - Up and Running Since the Start of the Mission. In Mizumoto, Y., Morita, K.-I., and Ohishi, M., editors, *Astronomical Data Analysis Software and Systems XIX*, volume 434 of *ASP Conf. Series*, page 139.

Pan, M. and Schlichting, H. E. (2012). Self-consistent Size and Velocity Distributions of Collisional Cascades. *ApJ*, 747:113.

Paunzen, E., Schnell, A., and Maitzen, H. M. (2006). An empirical temperature calibration for the Δ a photometric system. II. The A-type and mid F-type stars. *A& A*, 458:293–296.

Pawellek, N. and Krivov, A. V. (2015). The dust grain size-stellar luminosity trend in debris discs. *MNRAS*, 454:3207–3221.

Pawellek, N., Krivov, A. V., Marshall, J. P., Montesinos, B., Ábrahám, P., Moór, A., Bryden, G., and Eiroa, C. (2014). Disk Radii and Grain Sizes in Herschel-Resolved Debris Disks. *ArXiv e-prints*.

Piazzi, G. (1802). *Della scoperta del nuovo pianeta Cerere Ferdinandea, ottavo tra i primari del nostro sistema solare*.

Pilbratt, G. L., Riedinger, J. R., Passvogel, T., Crone, G., Doyle, D., Gageur, U., Heras, A. M., Jewell, C., Metcalfe, L., Ott, S., and Schmidt, M. (2010). Herschel Space Observatory. An ESA facility for far-infrared and submillimetre astronomy. *A& A*, 518:L1.

Planck, M. (1900). Zur Theorie des Gesetzes der Energieverteilung im Normalspectrum. *Verhandlungen der Deutschen physikalischen Gesellschaft*, 17:237–245.

Planck Collaboration, Ade, P. A. R., Aghanim, N., Arnaud, M., Ashdown, M., Aumont, J., Baccigalupi, C., Banday, A. J., Barreiro, R. B., Bartolo, N., and et al. (2015). Planck intermediate results. XXV. The Andromeda galaxy as seen by Planck. *A& A*, 582:A28.

Poglitsch, A., Waelkens, C., Geis, N., Feuchtgruber, H., Vandenbussche, B., Rodriguez, L., Krause, O., Renotte, E., van Hoof, C., Saraceno, P., Cepa, J., Kerschbaum, F., Agnèse, P., Ali, B., Altieri, B., Andreani, P., Augueres, J.-L., Balog, Z., Barl, L., Bauer, O. H., Belbachir, N., Benedettini, M., Billot, N., Boulade, O., Bischof, H., Blommaert, J., Callut, E., Cara, C., Cerulli, R., Cesarsky, D., Contursi, A., Creten, Y., De Meester, W., Doublier, V., Doumayrou, E., Duband, L., Exter, K., Genzel, R., Gillis, J.-M., Grözinger, U., Henning, T., Herreros, J., Huygen, R., Inguscio, M., Jakob, G., Jamar, C., Jean, C., de Jong, J., Katterloher, R., Kiss, C., Klaas, U., Lemke, D., Lutz, D., Madden, S., Marquet, B., Martignac, J., Mazy, A., Merken, P., Montfort, F., Morbidelli, L., Müller, T., Nielbock, M., Okumura, K., Orfei, R., Ottensamer, R., Pezzuto, S., Popesso, P., Putzeys, J., Regibo, S., Reveret, V., Royer, P., Sauvage, M., Schreiber, J., Stegmaier, J., Schmitt, D., Schubert, J., Sturm, E., Thiel, M., Tofani, G., Vavrek, R., Wetzstein, M., Wieprecht, E., and Wiezorrek, E. (2010). The Photodetector Array Camera and Spectrometer (PACS) on the Herschel Space Observatory. *A& A*, 518:L2.

Pontoppidan, K. M., Salyk, C., Bergin, E. A., Brittain, S., Marty, B., Mousis, O., and Öberg, K. I. (2014). Volatiles in Protoplanetary Disks. *Protostars and Planets VI*, pages 363–385.

Press, W. H., Teukolsky, S. A., Vetterling, W. T., and Flannery, B. P. (2002). *Numerical Recipes in C++*. Cambridge University Press. 1032 pp.

Quillen, A. C. (2006). Reducing the probability of capture into resonance. *MNRAS*, 365:1367–1382.

Reffert, S., Bergmann, C., Quirrenbach, A., Trifonov, T., and Künstler, A. (2015). Precise radial velocities of giant stars. VII. Occurrence rate of giant extrasolar planets as a function of mass and metallicity. *A& A*, 574:A116.

Reis, W., Corradi, W., de Avillez, M. A., and Santos, F. P. (2011). Interstellar Reddening in the Local Bubble and Loop I Region: Insight from Strömgren Photometry Analysis and Three-dimensional Modeling. *ApJ*, 734:8.

Rhee, J. H., Song, I., Zuckerman, B., and McElwain, M. (2007). Characterization of Dusty Debris Disks: The IRAS and Hipparcos Catalogs. *ApJ*, 660:1556–1571.

Ricarte, A., Moldvai, N., Hughes, A. M., Duchêne, G., Williams, J. P., Andrews, S. M., and Wilner, D. J. (2013). Resolving the Moth at Millimeter Wavelengths. *ApJ*, 774:80.

Rieke, G. H. and Lebofsky, M. J. (1985). The interstellar extinction law from 1 to 13 microns. *ApJ*, 288:618–621.

Riviere-Marichalar, P., Barrado, D., Montesinos, B., Duchêne, G., Bouy, H., Pinte, C., Menard, F., Donaldson, J., Eiroa, C., Krivov, A. V., Kamp, I., Mendigutía, I., Dent, W. R. F., and Lillo-Box, J. (2014). Gas and dust in the beta Pictoris moving group as seen by the Herschel Space Observatory. *A& A*, 565:A68.

Roberge, A., Kamp, I., Montesinos, B., Dent, W. R. F., Meeus, G., Donaldson, J. K., Olofsson, J., Moór, A., Augereau, J.-C., Howard, C., Eiroa, C., Thi, W.-F., Ardila, D. R., Sandell, G., and Woitke, P. (2013). Herschel Observations of Gas and Dust in the Unusual 49 Ceti Debris Disk. *ApJ*, 771:69.

Schneider, G., Grady, C. A., Hines, D. C., Stark, C. C., Debes, J. H., Carson, J., Kuchner, M. J., Perrin, M. D., Weinberger, A. J., Wisniewski, J. P., Silverstone, M. D., Jang-Condell, H., Henning, T., Woodgate, B. E., Serabyn, E., Moro-Martin, A., Tamura, M., Hinz, P. M., and Rodigas, T. J. (2014). Probing for Exoplanets Hiding in Dusty Debris Disks: Disk Imaging, Characterization, and Exploration with HST/STIS Multi-roll Coronagraphy. *AJ*, 148:59.

Schneider, G., Silverstone, M. D., and Hines, D. C. (2005). Discovery of a Nearly Edge-on Disk around HD 32297. *ApJ*, 629:L117–L120.

Schneider, G., Silverstone, M. D., Hines, D. C., Augereau, J.-C., Pinte, C., Ménard, F., Krist, J., Clampin, M., Grady, C., Golimowski, D., Ardila, D., Henning, T., Wolf, S., and Rodmann, J. (2006). Discovery of an 86 AU Radius Debris Ring around HD 181327. *ApJ*, 650:414–431.

Schneider, G., Smith, B. A., Becklin, E. E., Koerner, D. W., Meier, R., Hines, D. C., Lowrance, P. J., Terrile, R. J., Thompson, R. I., and Rieke, M. (1999). NICMOS imaging of the HR 4796A circumstellar disk. *ApJ*, 513:L127–L130.

Scholz, F.-W. and Stephens, M. A. (1987). *k*-sample Anderson–Darling tests. *J. Am. Stat. Assoc.*, 82(399):918–924.

Schüppler, C., Löhne, T., Krivov, A. V., Ertel, S., Marshall, J. P., and Eiroa, C. (2014). Collisional modelling of the debris disc around HIP 17439. *ArXiv: 1404.6144*.

Schüppler, C., Löhne, T., Krivov, A. V., Ertel, S., Marshall, J. P., Wolf, S., Wyatt, M. C., Augereau, J.-C., and Metchev, S. A. (2015). Collisional modelling of the AU Microscopii debris disc. *A& A*, 581:A97.

Selsis, F., Kasting, J. F., Levrard, B., Paillet, J., Ribas, I., and Delfosse, X. (2007). Habitable planets around the star Gliese 581? *A& A*, 476:1373–1387.

Sheret, I., Dent, W. R. F., and Wyatt, M. C. (2004). Submillimetre observations and modelling of Vega-type stars. *MNRAS*, 348:1282–1294.

Sibthorpe, B., Vandenbussche, B., Greaves, J. S., Pantin, E., Olofsson, G., Acke, B., Barlow, M. J., Blommaert, J. A. D. L., Bouwman, J., Brandeker, A., Cohen, M., De Meester, W., Dent, W. R. F., di Francesco, J., Dominik, C., Fridlund, M., Gear, W. K., Glauser, A. M., Gomez, H. L., Hargrave, P. C., Harvey, P. M., Henning, T., Heras, A. M., Hogerheijde, M. R., Holland, W. S., Ivison, R. J., Leeks, S. J., Lim, T. L., Liseau, R., Matthews, B. C., Naylor, D. A., Pilbratt, G. L., Polehampton, E. T., Regibo, S., Royer, P., Sicilia-Aguilar, A., Swinyard, B. M., Waelkens, C., Walker, H. J., and Wesson, R. (2010). The Vega debris disc: A view from Herschel. *A& A*, 518:L130.

Sitko, M. L., Grady, C. A., Lynch, D. K., Russell, R. W., and Hanner, M. S. (1998). Cometary Dust in the Debris Disks of HD 31648 and HD 163296: Two “Baby” Beta Pictoris Stars. In *Bulletin of the American Astronomical Society*, volume 30, page 1096.

Smirnov, N. (1939). Sur les écarts de la courbe de distribution empirique. *Recueil Mathématique (Matematiceskii Sbornik)*, 6:3–26.

Smirnov, N. (1948). Table for estimating the goodness of fit of empirical distributions. *Annals of Mathematical Statistics*, 19:279–281.

Smith, R., Churcher, L. J., Wyatt, M. C., Moerchen, M. M., and Telesco, C. M. (2009a). Resolved debris disc emission around η Telescopii: a young solar system or ongoing planet formation? *A& A*, 493:299–308.

Smith, R., Wyatt, M. C., and Haniff, C. A. (2009b). Resolving the hot dust around HD69830 and η Corvi with MIDI and VISIR. *A& A*, 503:265–279.

Smith, R., Wyatt, M. C., and Haniff, C. A. (2012). Resolving the terrestrial planet forming regions of HD113766 and HD172555 with MIDI. *ArXiv e-prints*.

Song, I., Caillault, J.-P., Barrado y Navascués, D., and Stauffer, J. R. (2001). Ages of A-Type Vega-like Stars from uvbyβ Photometry. *ApJ*, 546:352–357.

Song, I., Zuckerman, B., Weinberger, A. J., and Becklin, E. E. (2005). Extreme collisions between planetesimals as the origin of warm dust around a Sun-like star. *Nature*, 436:363–365.

Soummer, R., Perrin, M. D., Pueyo, L., Choquet, É., Chen, C., Golimowski, D. A., Brendan Hagan, J., Mittal, T., Moerchen, M., N’Diaye, M., Rajan, A., Wolff, S., Debes, J., Hines, D. C., and Schneider, G. (2014). Five Debris Disks Newly Revealed in Scattered Light from the Hubble Space Telescope NICMOS Archive. *ApJL*, 786:L23.

Stapelfeldt, K. R., Bryden, G., Su, K. Y., Krist, J. E., Plavchan, P., and Herschel/SKARPS Project Team (2013). Herschel-resolved Debris Disks around Nearby Late-type Stars: HD 202628, HD 92945, and HD 53143. In *American Astronomical Society Meeting Abstracts #221*, volume 221 of *American Astronomical Society Meeting Abstracts*, page 144.14.

Steele, A., Hughes, A. M., Carpenter, J., Ricarte, A., Andrews, S. M., Wilner, D. J., and Chiang, E. (2016). Resolved Millimeter-wavelength Observations of Debris Disks around Solar-type Stars. *ApJ*, 816:27.

Stern, S. A. (1996). Signatures of collisions in the Kuiper Disk. *A& A*, 310:999–1010.

Stewart, S. T. and Leinhardt, Z. M. (2009). Velocity-Dependent Catastrophic Disruption Criteria for Planetesimals. *ApJL*, 691:L133–L137.

Stock, N. D., Su, K. Y. L., Liu, W., Hinz, P. M., Rieke, G. H., Marengo, M., Stapelfeldt, K. R., Hines, D. C., and Trilling, D. E. (2010). The Structure of the β Leonis Debris Disk. *ApJ*, 724:1238–1255.

Strubbe, L. E. and Chiang, E. I. (2006). Dust dynamics, surface brightness profils, and thermal spectra of debris disks: The case of AU Mic. *ApJ*, 648:652–665.

Su, K. Y., Bryden, G., Rieke, G., Stapelfeldt, K. R., and Balog, Z. (2013a). Herschel-resolved Debris Disks around Nearby F-type Stars: HD 139664, HD 127821 and HD 113337. In *American Astronomical Society Meeting Abstracts #221*, volume 221 of *American Astronomical Society Meeting Abstracts*, page 144.19.

Su, K. Y. L., Morrison, S., Malhotra, R., Smith, P. S., Balog, Z., and Rieke, G. H. (2015). Debris Distribution in HD 95086 - A Young Analog of HR 8799. *ApJ*, 799:146.

Su, K. Y. L., Rieke, G. H., Malhotra, R., Stapelfeldt, K. R., Hughes, A. M., Bonsor, A., Wilner, D. J., Balog, Z., Watson, D. M., Werner, M. W., and Misselt, K. A. (2013b). Asteroid Belts in Debris Disk Twins: Vega and Fomalhaut. *ApJ*, 763:118.

Su, K. Y. L., Rieke, G. H., Stansberry, J. A., Bryden, G., Stapelfeldt, K. R., Trilling, D. E., Muzerolle, J., Beichman, C. A., Moro-Martin, A., Hines, D. C., and Werner, M. W. (2006). Debris disk evolution around A stars. *ApJ*, 653:675–689.

Su, K. Y. L., Rieke, G. H., Stapelfeldt, K. R., Malhotra, R., Bryden, G., Smith, P. S., Misselt, K. A., Moro-Martin, A., and Williams, J. P. (2009). The Debris Disk Around HR 8799. *ApJ*, 705:314–327.

Thébault, P. and Augereau, J.-C. (2007). Collisional processes and size distribution in spatially extended debris discs. *A& A*, 472:169–185.

Thébault, P. and Wu, Y. (2008). Outer edges of debris discs: how sharp is sharp? *A& A*, 481:713–724.

Thalmann, C., Janson, M., Buenzli, E., Brandt, T. D., Wisniewski, J. P., Dominik, C., Carson, J., McElwain, M. W., Currie, T., Knapp, G. R., Moro-Martín, A., Usuda, T., Abe, L., Brandner, W., Egner, S., Feldt, M., Golota, T., Goto, M., Guyon, O., Hashimoto, J., Hayano, Y., Hayashi, M., Hayashi, S., Henning, T., Hodapp, K. W., Ishii, M., Iye, M., Kandori, R., Kudo, T., Kusakabe, N., Kuzuhara, M., Kwon, J., Matsuo, T., Mayama, S., Miyama, S., Morino, J.-I., Nishimura, T., Pyo, T.-S., Serabyn, E., Suto, H., Suzuki, R., Takami, M., Takato, N., Terada, H., Tomono, D., Turner, E. L., Watanabe, M., Yamada, T., Takami, H., and Tamura, M. (2013). Imaging Discovery of the Debris Disk around HIP 79977. *ApJL*, 763:L29.

Thebault, P. (2016). Dust production in debris discs: constraints on the smallest grains. *A& A*, 587:A88.

Thébault, P., Augereau, J.-C., and Beust, H. (2003). Dust production from collisions in extrasolar planetary systems. The inner β Pictoris disc. *A& A*, 408:775–788.

Thi, W. F., Blake, G. A., van Dishoeck, E. F., van Zadelhoff, G. J., Horn, J. M. M., Becklin, E. E., Mannings, V., Sargent, A. I., van den Ancker, M., and Natta, A. (2001). Substantial reservoirs of molecular hydrogen in the debris disks around young stars. *Nature*, 409:60–63.

Thureau, N. D., Greaves, J. S., Matthews, B. C., Kennedy, G., Phillips, N., Booth, M., Duchêne, G., Horner, J., Rodriguez, D. R., Sibthorpe, B., and Wyatt, M. C. (2014). An unbiased study of debris discs around A-type stars with Herschel. *MNRAS*, 445:2558–2573.

Tombaugh, C. W. (1946). The search for the ninth planet, pluto. *Leaflet of the Astronomical Society of the Pacific*, 5:73.

Torres, G. (2010). On the Use of Empirical Bolometric Corrections for Stars. *AJ*, 140:1158–1162.

Trilling, D. E., Bryden, G., Beichman, C. A., Rieke, G. H., Su, K. Y. L., Stansberry, J. A., Blaylock, M., Stapelfeldt, K. R., Beeman, J. W., and Haller, E. E. (2008). Debris disks around Sun-like stars. *ApJ*, 674:1086–1105.

Trilling, D. E., Stansberry, J. A., Stapelfeldt, K. R., Rieke, G. H., Su, K. Y. L., Gray, R. O., Corbally, C. J., Bryden, G., Chen, C. H., Boden, A., and Beichman, C. A. (2007). Debris disks in main-sequence binary systems. *ApJ*, 658:1289–1311.

Valenti, J. A. and Fischer, D. A. (2005). Spectroscopic Properties of Cool Stars (SPOCS). I. 1040 F, G, and K Dwarfs from Keck, Lick, and AAT Planet Search Programs. *ApJS*, 159:141–166.

van Leeuwen, F. (2007). Validation of the new Hipparcos reduction. *A& A*, 474:653–664.

Vandenbussche, B., Sibthorpe, B., Acke, B., Pantin, E., Olofsson, G., Waelkens, C., Dominik, C., Barlow, M. J., Blommaert, J. A. D. L., Bouwman, J., Brandeker, A., Cohen, M., De Meester, W., Dent, W. R. F., Exter, K., di Francesco, J., Fridlund, M., Gear, W. K., Glauser, A. M., Gomez, H. L., Greaves, J. S., Hargrave, P. C., Harvey, P. M., Henning, T., Heras, A. M., Hogerheijde, M. R., Holland, W. S., Huygen, R., Ivison, R. J., Jean, C., Leeks, S. J., Lim, T. L., Liseau, R., Matthews, B. C., Naylor, D. A., Pilbratt, G. L., Polehampton, E. T., Regibo, S., Royer, P., Sicilia-Aguilar, A., Swinyard, B. M., Walker, H. J., and Wesson, R. (2010). The β Pictoris disk imaged by Herschel PACS and SPIRE. *A& A*, 518:L133.

Vican, L. (2012). Age Determination for 346 Nearby Stars in the Herschel DEBRIS Survey. *AJ*, 143:135.

Vitense, C., Krivov, A. V., Kobayashi, H., and Löhne, T. (2012). An improved model of the Edgeworth-Kuiper debris disk. *A& A*, 540:A30.

Vitense, C., Krivov, A. V., and Löhne, T. (2010). The Edgeworth-Kuiper Debris Disk. *A& A*, 520:A32.

von Braun, K., Boyajian, T. S., Kane, S. R., van Belle, G. T., Ciardi, D. R., López-Morales, M., McAlister, H. A., Henry, T. J., Jao, W.-C., Riedel, A. R., Subasavage, J. P., Schaefer, G., ten Brummelaar, T. A., Ridgway, S., Sturmann, L., Sturmann, J., Mazingue, J., Turner, N. H., Farrington, C., Goldfinger, P. J., and Boden, A. F. (2011). Astrophysical Parameters and Habitable Zone of the Exoplanet Hosting Star GJ 581. *ApJL*, 729:L26.

Wada, K., Tanaka, H., Suyama, T., Kimura, H., and Yamamoto, T. (2007). Numerical Simulation of Dust Aggregate Collisions. I. Compression and Disruption of Two-Dimensional Aggregates. *ApJ*, 661:320–333.

Wahhaj, Z., Koerner, D. W., and Sargent, A. I. (2007). High-Resolution Imaging of the Dust Disk around 49 Ceti. *ApJ*, 661:368–373.

Werner, M. W., Roellig, T. L., Low, F. J., Rieke, G. H., Rieke, M., Hoffmann, W. F., Young, E., Houck, J. R., Brandl, B., Fazio, G. G., Hora, J. L., Gehrz, R. D., Helou, G., Soifer, B. T., Stauffer, J., Keene, J., Eisenhardt, P., Gallagher, D., Gautier, T. N., Irace, W., Lawrence, C. R., Simmons, L., Van Cleve, J. E., Jura, M., Wright, E. L., and Cruikshank, D. P. (2004). The Spitzer Space Telescope Mission. *ApJS*, 154:1–9.

Wien, W. (1896). Über die Energievertheilung im Emissionsspectrum eines schwarzen Körpers. *Annalen der Physik*, 294(8):662–669.

Williams, D. R. and Wetherill, G. W. (1994). Size distribution of collisionally evolved asteroidal populations - Analytical solution for self-similar collision cascades. *Icarus*, 107:117.

Williams, J. P. and Andrews, S. M. (2006). The Dust Properties of Eight Debris Disk Candidates as Determined by Submillimeter Photometry. *ApJ*, 653:1480–1485.

Williams, J. P. and Cieza, L. A. (2011). Protoplanetary Disks and Their Evolution. *ARA& A*, 49:67–117.

Williams, J. P., Najita, J., Liu, M. C., Bottinelli, S., Carpenter, J. M., Hillenbrand, L. A., Meyer, M. R., and Soderblom, D. R. (2004). Detection of cool dust around the G2V star HD 107146. *ApJ*, 604:414–419.

Witt, A. (1989). Visible/uv Scattering by Interstellar Dust. In Allamandola, L. J. and Tielens, A. G. G. M., editors, *Interstellar Dust*, volume 135 of *IAU Symposium*, page 87.

Wolf, S. and Hillenbrand, L. A. (2003). Model spectral energy distributions of circumstellar debris disks. I. Analytic disk density distributions. *ApJ*, 596:603–620.

Wright, E. L., Eisenhardt, P. R. M., Mainzer, A. K., Ressler, M. E., Cutri, R. M., Jarrett, T., Kirkpatrick, J. D., Padgett, D., McMillan, R. S., Skrutskie, M., Stanford, S. A., Cohen, M., Walker, R. G., Mather, J. C., Leisawitz, D., Gautier, T. N., McLean, I., Benford, D., Lonsdale, C. J., Blain, A., Mendez, B., Irace, W. R., Duval, V., Liu, F., Royer, D., Heinrichsen, I., Howard, J., Shannon, M., Kendall, M., Walsh, A. L., Larsen, M., Cardon, J. G., Schick, S., Schwalm, M., Abid, M., Fabinsky, B., Naes, L., and Tsai, C.-W. (2010). The Wide-field Infrared Survey Explorer (WISE): Mission Description and Initial On-orbit Performance. *AJ*, 140:1868–1881.

Wyatt, M. C. (2005). The insignificance of P-R drag in detectable extrasolar planetesimal belts. *A& A*, 433:1007–1012.

Wyatt, M. C. (2008). Evolution of Debris Disks. *ARA& A*, 46:339–383.

Wyatt, M. C., Clarke, C. J., and Booth, M. (2011). Debris disk size distributions: Steady state collisional evolution with P-R drag and other loss processes. *Celest. Mech. Dynam. Astron.*, 111:1–28.

Wyatt, M. C., Kennedy, G., Sibthorpe, B., Moro-Martin, A., Lestrade, J.-F., Ivison, R. J., Matthews, B., Udry, S., Greaves, J. S., Kalas, P., Lawler, S., Su, K. Y. L., Rieke, G. H., Booth, M., Bryden, G., Horner, J., Kavelaars, J. J., and Wilner, D. (2012). Herschel imaging of 61 Vir: implications for the prevalence of debris in low-mass planetary systems. *MNRAS*, 424:1206–1223.

Wyatt, M. C., Smith, R., Greaves, J. S., Beichman, C. A., Bryden, G., and Lisse, C. M. (2007a). Transience of hot dust around sun-like stars. *ApJ*, 658:569–583.

Wyatt, M. C., Smith, R., Su, K. Y. L., Rieke, G. H., Greaves, J. S., Beichman, C. A., and Bryden, G. (2007b). Steady State Evolution of Debris Disks around A Stars. *ApJ*, 663:365–382.

Zubko, V. G., Mennella, V., Colangeli, L., and Bussoletti, E. (1996). Optical constants of cosmic carbon analogue grains - I. Simulation of clustering by a modified continuous distribution of ellipsoids. *MNRAS*, 282:1321–1329.

Zuckerman, B., Forveille, T., and Kastner, J. H. (1995). Inhibition of giant-planet formation by rapid gas depletion around young stars. *Nature*, 373:494–496.

Zuckerman, B., Song, I., Bessell, M. S., and Webb, R. A. (2001). The β Pictoris moving group. *ApJ*, 562:L87–L90.

Ehrenwörtliche Erklärung

Ich erkläre hiermit ehrenwörtlich, dass ich die vorliegende Arbeit selbstständig, ohne unzulässige Hilfe Dritter und ohne Benutzung anderer als der angegebenen Hilfsmittel und Literatur angefertigt habe. Die aus anderen Quellen direkt oder indirekt übernommenen Daten und Konzepte sind unter der Angabe der Quellen gekennzeichnet.
Bei der Auswahl und Auswertung folgenden Materials haben mir die nachstehend aufgeführten Personen in der jeweils beschriebenen Weise unentgeltlich geholfen:

1. Prof. Dr. Alexander Krivov
2. Dr. Jonathan P. Marshall
3. Dr. Benjamin Montesinos
4. Dr. Steve Ertel

Weitere Personen waren an der inhaltlich-materiellen Erstellung der vorliegenden Arbeit nicht beteiligt. Insbesondere habe ich hierfür nicht die entgeltliche Hilfe von Vermittlungs- bzw. Beratungsdiensten (Promotionsberater oder andere Personen) in Anspruch genommen. Niemand hat von mir unmittelbar oder mittelbar geldwertige Leistungen für die Arbeiten erhalten, die im Zusammenhang mit dem Inhalt der vorgelegten Dissertation stehen.
Die Arbeit wurde bisher weder im In- noch im Ausland in gleicher oder ähnlicher Form einer anderen Prüfungsbehörde vorgelegt.
Die geltende Promotionsordnung der Physikalisch-Astronomischen Fakultät ist mir bekannt. Ich versichere ehrenwörtlich, dass ich nach bestem Wissen die reine Wahrheit gesagt und nichts verschwiegen habe.

Jena, den

Nicole Pawellek

Lebenslauf

Zur Person

Name:	Nicole Pawellek
Geburtsdatum:	06. Dezember 1988
Geburtsort:	Meiningen/Thüringen
Staatsangehörigkeit	Deutsch

Werdegang

1995 – 1999:	Grundschule in Meiningen/Thüringen
1999 – 2003:	Gymnasium in Meiningen/Thüringen
2003 – 2007:	Gymnasium mit mathematisch-naturwissenschaftlichen Spezialklassen Ilmenau/Thüringen
20.06.2007	Allgemeine Hochschulreife (Abitur) mit besonderer Leistungsüberprüfung für Spezialklassen (Spezialklassenabitur)
2007 – 2010	Studium der Physik an der Friedrich-Schiller-Universität Jena (Abschluss: Bachelor of science)
2010 – 2012	Studium der Physik an der Friedrich-Schiller-Universität Jena (Abschluss: Master of science)
2011	Teilnahme an der Sommerschule der ESA mit dem Thema "Star formation across the universe"
seit 01.10.2012	Graduiertenstudium an der Friedrich-Schiller-Universität Jena als wiss. Mitarbeiterin am AIU unter Betreuung durch Prof. A.V. Krivov
2013 – 2014	Betreuung von Studenten als Assistentin im Physikalischen Grundpraktikum
2014 – 2015	Leitung der Übung zur Vorlesung "Einführung in die Radioastronomie"